Recombination dynamics in (In,Ga)N/GaN heterostructures: Influence of localization and crystal polarity

D I S S E R T A T I O N

zur Erlangung des akademischen Grades

doctor rerum naturalium
(Dr. rer. nat.)
im Fach Physik

eingereicht an der
Mathematisch-Naturwissenschaftlichen Fakultät
Humboldt-Universität zu Berlin

von
M. Sc. Phys. Felix Ihbo Feix (geb. Felgenträger)

Präsidentin der Humboldt-Universität zu Berlin:
Prof. Dr.-Ing. Dr. Sabine Kunst

Dekan der Mathematisch-Naturwissenschaftlichen Fakultät:
Prof. Dr. Elmar Kulke

Gutachter:
(i) Prof. Dr. Henning Riechert
(ii) Prof. Dr. Oliver Benson
(iii) Prof. Dr. Eoin O'Reilly

Tag der mündlichen Prüfung: 13. April 2018

"To raise new questions, new possibilities, to regard old problems from a new angle, requires creative imagination and marks real advance in science."

A. Einstein and L. Infeld, *The Evolution of Physics*,
Cambridge University Press, 1938 p. 95.

Abstract

(In,Ga)N/GaN light-emitting diodes have been commercialized more than one decade ago. However, the knowledge about the influence of the localization on the recombination dynamics and on the diffusivity in the (In,Ga)N/GaN quantum wells (QWs) is still incomplete. In this thesis, we employ temperature-dependent steady-state and time-resolved photoluminescence (PL) spectroscopy to investigate the impact of localization on the recombination dynamics of a typical Ga-polar, planar (In,Ga)N/GaN QW structure. In addition, we extend our study to N-polar, axial (In,Ga)N/GaN quantum disks, nonpolar core/shell GaN/(In,Ga)N µ-rods, and Ga-polar, sub-monolayer InN/GaN superlattices. While we observe a single exponential decay of the PL intensity in the nonpolar QWs, indicating the recombination of excitons, the decay of the PL intensity in polar QWs asymptotically obeys a power law. This power law reveals that recombination occurs between individually localized, spatially separated electrons and holes. No unique PL lifetime can be defined for such a decay, which impedes the estimation of the internal quantum efficiency and the determination of a diffusion length. In order to extract useful recombination parameters and diffusivities for the polar QWs, we analyze the PL transients with position-dependent diffusion-reaction equations, efficiently solved by a Monte Carlo algorithm. From these simulations, we conclude that the power law asymptote is preserved despite efficient nonradiative recombination in the nanowires. Moreover, we find that the InN/GaN superlattices behave electronically as conventional (In,Ga)N/GaN QWs, but with a strong, thermally-activated nonradiative channel. Furthermore, we demonstrate that the ratio of localization and exciton binding energy, both of which are influenced by the magnitude of the internal electric fields in the QWs, determines the recombination mechanism to be either dominated by tunneling of electrons and holes or by the decay of excitons.

Keywords: (In,Ga)N/GaN, heterostructures, time-resolved photoluminescence spectroscopy, localization, power law decay, individual charge carriers, polarity, diffusion, internal quantum efficiency, Monte Carlo, short-period superlattices, nanowires

Zusammenfassung

(In,Ga)N/GaN-Leuchtdioden wurden vor mehr als 10 Jahren kommerzialisiert, dennoch ist das Verständnis über den Einfluss von Lokalisierung auf die Rekombinationsdynamik in den (In,Ga)N/GaN Quantengräben (QG) unvollständig. In dieser Arbeit nutzen wir die temperaturabhängige stationäre und zeitaufgelöste Spektroskopie der Photolumineszenz (PL), um diesen Einfluss in einer typischen Ga-polaren, planaren (In,Ga)N/GaN-QG-Struktur zu untersuchen. Zusätzlich dehnen wir unsere Studie auf N-polare, axiale (In,Ga)N/GaN Quantumscheiben, nichtpolare Kern/Mantel GaN/(In,Ga)N µ-Drähte und Ga-polare, submonolage InN/GaN Übergitter aus. Während wir einen einfach exponentiellen Abfall der PL-Intensität in den nichtpolaren QG beobachten (Hinweise auf die Rekombination von Exzitonen), folgen die PL-Transienten in polaren QG asymptotisch einem Potenzgesetz. Dieses Potenzgesetz weist auf eine Rekombination zwischen individuell lokalisierten, räumlich getrennten Elektronen und Löchern hin. Für einen solchen Zerfall kann keine eindeutige PL-Lebensdauer definiert werden, was die Schätzung der internen Quanteneffizienz und die Bestimmung einer Diffusionslänge erschwert. Um nützliche Rekombinationsparameter und Diffusivitäten für die polaren QG zu extrahieren, analysieren wir die PL-Transienten mit positionsabhängigen Diffusionsreaktionsgleichungen, die durch einen Monte-Carlo-Algorithmus effizient gelöst werden. Aus diesen Simulationen ergibt sich, dass das asymptotische Potenzgesetz auch bei effizienter nichtstrahlender Rekombination (z. B. in den Nanodrähten) erhalten bleibt. Zudem stellen wir fest, dass sich die InN/GaN Übergitter elektronisch wie konventionelle (In,Ga)N/GaN QG verhalten, aber mit starkem, thermisch aktiviertem nichtstrahlenden Kanal. Des Weiteren zeigen wir, dass das Verhältnis von Lokalisierungs- und Exzitonenbindungsenergie bestimmt, dass die Rekombination entweder durch das Tunneln von Elektronen und Löchern oder durch den Zerfall von Exzitonen dominiert wird.

Stichwörter: (In,Ga)N/GaN, Heterostrukturen, zeitaufgelöste Photolumineszenzspektroskopie, Lokalisierung, Potenzgesetzzerfall, individuelle Ladungsträger, Polarität, Diffusion, interne Quanteneffizienz, Monte Carlo, kurzperiodische Übergitter, Nanodrähte

List of publications

Publications of parts of this work

F. Feix, T. Flissikowski, K. K. Sabelfeld, V. M. Kaganer, M. Wölz, L. Geelhaar, H. T. Grahn, and O. Brandt, *Ga-polar (In,Ga)N/GaN quantum wells versus N-polar (In,Ga)N quantum disks in GaN nanowires: A comparative analysis of carrier recombination, diffusion, and radiative efficiency*, Phys. Rev. Applied **8**, 014032 (2017)

F. Feix, T. Flissikowski, C. Chèze, R. Calarco, H. T. Grahn, and O. Brandt, *Individual electron and hole localization in submonolayer InN quantum sheets embedded in GaN*, Appl. Phys. Lett. **109**, 042104 (2016)

Further publications

J. Kamimura, P. Bogdanoff, M. Ramsteiner, P. Corfdir, F. Feix, L. Geelhaar, and H. Riechert, *p-type doping of GaN nanowires characterized by photoelectrochemical measurements*, Nano Lett. **17**, 1529 (2017)

C. Chèze, F. Feix, M. Anikeeva, T. Schulz, M. Albrecht, H. Riechert, O. Brandt, and R. Calarco, *In/GaN(0001)-($\sqrt{3}\times\sqrt{3}$)$R30°$ adsorbate structure as a template for embedded (In,Ga)N/GaN monolayers and short-period superlattices*, Appl. Phys. Lett. **110**, 072104 (2017)

C. Chèze, M. Siekacz, F. Isa, B. Jenichen, F. Feix, J. Buller, T. Schulz, M. Albrecht, C. Skierbiszewski, R. Calarco, and H. Riechert, *Investigation of interface abruptness and In content in (In,Ga)N/GaN superlattices*, J. Appl. Phys. **120**, 125307 (2016)

J. Lähnemann, P. Corfdir, F. Feix, J. Kamimura, T. Flissikowski, H. T. Grahn, L. Geelhaar, and O. Brandt, *Radial Stark effect in (In,Ga)N nanowires*, Nano Lett. **16**, 917 (2016)

P. Corfdir, F. Feix, J. K. Zettler, S. Fernández-Garrido, and O. Brandt, *Importance of the dielectric contrast for the polarization of excitonic transitions in single GaN nanowires*, New J. Phys. **17**, 033040 (2015)

Conference presentations

F. Feix, T. Flissikowski, K. K. Sabelfeld, V. M. Kaganer, M. Wölz, L. Geelhaar, H. T. Grahn, and O. Brandt, *Power law photoluminescence transients from polar (In,Ga)N/GaN quantum wells: Impact of nonradiative recombination and diffusion of electrons*, Compound Semiconductor Week 2017, Berlin, Germany

F. Feix, T. Flissikowski, C. Chèze, R. Calarco, H. T. Grahn, and O. Brandt, *Localization of Individual Electrons and Holes in Submonolayer InN Quantum Sheets Embedded in GaN*, International Conference on Nitride Semiconductors 2016, Orlando, United States of America

F. Feix, T. Flissikowski, C. Chèze, R. Calarco, H. T. Grahn, and O. Brandt, *Charge carrier localization in submonolayer InN/GaN superlattices*, Deutsche Physikalische Gesellschaft-Frühjahrstagung der Sektion Kondensierte Materie 2016, Regensburg, Germany

F. Feix, P. Corfdir, J. Lähnemann, J. Kamimura, O. Brandt, and L. Geelhaar, *Origin of the long wavelength emission of (In,Ga)N nanowires with low In content*, 582. WE-Heraeus-Seminar: III-V Nanowire Photonics, March 2015, Bad Honnef, Germany

List of abbreviations

CB	conduction band
EL	electroluminescence
EQE	external quantum efficiency
FWHM	full width at half maximum
IQE	internal quantum efficiency
LED	light-emitting diode
MBE	molecular beam epitaxy
ML	monolayer
MOCVD	metalorganic chemical vapor deposition
PL	photoluminescence
QB	quantum barrier
QD	quantum disk
QS	quantum sheet
QW	quantum well
SPSL	short-period superlattice
SRH	Shockley-Read-Hall
TPA	two-photon absorption
UV	ultraviolet
VB	valence band
WZ	wurtzite
ZB	zincblende

List of symbols

symbol	name	unit/value
A	Shockley-Read-Hall coefficient	s^{-1}
a	tunneling parameter	m
a_B	Bohr radius	$0.529 \times 10^{-10}\,\mathrm{m}$
a_X	exciton Bohr radius	m
α	absorption	
B, B_0	radiative coefficient	$\mathrm{m}^3\,\mathrm{s}^{-1}$
$b_{n,p}$	electron, holes capture coefficients	s^{-1}
C	Auger coefficient	$\mathrm{m}^6\,\mathrm{s}^{-1}$
C_{ij}	elastic constant	Pa
c_0	vacuum speed of light	$2.998 \times 10^8\,\mathrm{m/s}$
d	thickness/depth	m
D	diffusivity	m^2/s
$\hat{\mathrm{D}}$	dimensionality	
e	elementary charge	$1.602 \times 10^{-19}\,\mathrm{C}$
e_{ij}	element of the piezoelectric tensor	$\mathrm{C/m}^2$
E_0	effective Rydberg energy	eV
$E_\mathrm{a,\,g,\,laser}$	activation, band gap, laser photon energy	eV
$E_\mathrm{barrier,\,loc}$	barrier, localization energy	eV
E_BX	binding energy of excitons to impurities	eV
$E_\mathrm{D,A}$	donor, acceptor level	eV
E_X	exciton binding energy	eV
ε_0	permittivity	$8.854 \times 10^{-12}\,\mathrm{A\,s/(V\,m)}$
ε	relative permittivity	
ϵ	strain components	
η	(internal quantum) efficiency	
F	electric field	V/cm
f	Fermi–Dirac distribution	
G	generation (rate)	s^{-1}
γ, γ_c, γ_D	recombination, capture, dissociation rate	s^{-1}
$\hbar$	Planck constant h divided by 2π	$1.054 \times 10^{-34}\,\mathrm{J\,s}$
$\mathcal{H}$	Hamiltonian	

symbol	name	unit/value
I_{exc}	excitation power density	$\mathrm{W/cm^2}$
I_{PL}	(integrated) photoluminescence intensity	arb. units
k_{B}	Boltzmann constant	$1.380 \times 10^{-23}\,\mathrm{J\,K^{-1}}$
κ	kinetic energy	eV
L	diffusion length	m
λ	wavelength	m
m_0	electron mass	$9.109 \times 10^{-31}\,\mathrm{kg}$
$m_{e,hh,lh}$	effective electron, heavy, light hole mass	kg
μ	effective mass	kg
μ^*	mobility	$\mathrm{cm^2/(V\,s)}$
N, ($N_\bigcirc$, $N_\times$)	density of nonradiative centers (empty, filled)	$\mathrm{m^{-2}}$
(Δ)n	(excess) density of electrons/excitons	$\mathrm{m^{-2}}$
$n_{\mathrm{d},\,\ell}$	density of localized, delocalized excitons	$\mathrm{m^{-2}}$
N_{D}	donor density	$\mathrm{m^{-2}}$
n_{F}	density of free excitons	$\mathrm{m^{-2}}$
$\hat{n}$	refractive index	
(Δ)p	(excess) number density of holes	$\mathrm{m^{-2}}$
Φ	photon flux	$\mathrm{nm^{-2}\,ns^{-1}}$
ψ	wave function	
$P_{\mathrm{sp,\,pz}}$	spontaneous, piezoelectric polarization	$\mathrm{C/m^2}$
Q	(cation) charge	
$\mathbf{r}$	spatial location	m
R_{H}	Rydberg energy	eV
$R_{\mathrm{sp,\,SRH,\,total}}$	spontaneous, SRH, total emission rate	$\mathrm{s^{-1}}$
ρ	Pearson correlation coefficient	
$\tau_{\mathrm{eff,\,r,\,nr}}$	effective, radiative, nonradiative lifetime	s
$\tau_{\mathrm{c,\,e,\,esc}}$	capture, emission, escape time	s
$\tau_{\mathrm{d},\,\ell}$	lifetime of de-, localized excitons	s
$\tau_{\mathrm{TE,\,T}}$	thermionic, tunneling emission time	s
T	temperature	K
t	time	s
U	potential profile	eV
u	internal parameter	
ω	radial frequency	$\mathrm{s^{-1}}$
x	concentration	
$\lvert\mathbf{x}\rvert$, z	distance	m

Given values have been taken from CODATA.[1]

Contents

Chapter 1

Introduction

GaN was synthesized for the first time by Johnson *et al.*[2] in 1932 by passing ammonia over hot Ga, resulting in GaN in the form of a dark gray powder. In subsequent work by other researchers,[3–6] small GaN needles and platelets were obtained that could be used to study some of the basic properties of the material. More than 35 years later, Maruska and Tietjen[7] obtained single-crystal GaN thin-film[8] on Al_2O_3 by hydride vapor-phase epitaxy. Metal-insulator-semiconductor light-emitting diodes (LEDs) fabricated from these films by Maruska and Pankove exhibited extremely low external quantum efficiencies (EQEs) of about 0.001 %.[9] Pioneered by Manasevit *et al.*,[10] metalorganic chemical vapor deposition (MOCVD) was used to grow GaN layers on foreign substrates in the 1970s. However, the EQEs of GaN LEDs remained low, and p-doping, i. e., a significant hole concentration and mobility, of the intrinsic n-type GaN was believed to be impossible.[11,12] For this reason, the industry shut down research and development on GaN around the globe in the late 1970s.[13] Two breakthroughs of the group of Akasaki in Nagoya University paved the way for blue LEDs in the late 1980s. First, they improved the quality of GaN layers significantly by using low temperature buffers.[14] Second, Amano *et al.*[15] achieved p-type GaN:Mg by utilizing a postgrowth low-energy electron beam irradiation treatment in 1989. A similar effect was obtained utilizing postgrowth annealing.[16] Nakamura *et al.*[17] ascribed the observed effect to a thermal activation of hydrogen-passivated Mg in 1992. Later, this hypothesis was confirmed by first-principles calculations.[18] The successful realization of p-GaN paved the way for the first demonstration of an (In,Ga)N/GaN LED by Nakamura *et al.*[19] Since this first demonstration, the EQE of the LED increased from 0.22 % to a record-high value of about 84 % in 2010.[19,20] For their pioneering achievements, Isamu Akasaki, Hiroshi Amano, and Shuji Nakamura received the Nobel Prize in Physics in 2014.[21] The total market volume of (In,Ga)N-based solid-state lighting was estimated to amount to more than 5 billion dollars in 2014 and was forecasted to quadruple until 2019.[22] Moreover, the search for the keywords (In,Ga)N and InGaN yielded more than 150,000 patents[23] and 9,500 research articles in July 2017.[24]

Despite the everyday presence of (In,Ga)N-based LEDs and the impressive research

activities on future concepts of (In,Ga)N-based lighting, the present LEDs suffer from two drawbacks: First, a reduction of the efficiency at high current densities and, second, a decrease of the efficiency with increasing In content in particular in the green spectral range. Both effects are discussed extensively in the literature, but no general agreement as to their origin has been reached (see, e. g., Refs. 25–30). While the first observation may be attributed to Auger recombination[31] or density-activated defect recombination,[27] potential reasons for the second observation may be a deterioration of the crystal quality resulting in an increase of nonradiative processes,[32–35] a reduced radiative rate due to an increasing magnitude of the polarization fields,[36] or an increase of the Auger recombination coefficient.[37,38]

Another important contribution to both effects may originate from carrier or exciton localization.[29,39] Localization in (In,Ga)N/GaN quantum wells (QWs) manifests itself by broad bands in photoluminescence (PL) spectra or by a plethora of narrow lines in PL spectra of individual nanowires.[40–43] Additional indications for localization in (In,Ga)N/GaN QWs are the high internal quantum efficiency (IQE) despite the high density of structural defects,[44,45] the characteristic S-shape temperature dependence of the PL peak energy,[46] the rather large line width of the transition,[47] and the strongly retarded recombination dynamics.[48–51] In the 2000s, it was generally accepted that excitons localize at In clusters in the (In,Ga)N/GaN QWs.[45,47,52–56] However, recent microscopic investigations reveal that the In atoms in standard (In,Ga)N/GaN QWs are indeed homogeneously distributed, resulting in a random alloy.[57–65] The absence of significant compositional fluctuations led to the assumption that localization may be negligible.[66,67] Recent theoretical calculations, though, demonstrated the significance of localization even in a perfect random alloy and initiated a renaissance of the investigation of localization in (In,Ga)N.[29,30,58,68] Taking into account both, the strong internal electric fields and localization, Morel *et al.*[48] phenomenologically explained the nonexponential PL transients of polar (In,Ga)N/GaN QWs (that asymptotically obey a power law) by the donor-acceptor-pair-like recombination of individually localized electrons and holes. However, the general understanding of the (radiative and nonradiative) recombination dynamics in (In,Ga)N/GaN heterostructures as well as the influence of localization, nonradiative recombination, and diffusion on the same or on the IQE is still incomplete.

The main aim of this thesis is to investigate the presence and consequences of localization in (In,Ga)N/GaN QWs. Moreover, the nature of the localized species, being either excitons or individual electrons and holes, as well as its dependence of the crystal polarity is examined. In order to understand the influence of localization on the recombination dynamics, on the diffusion, and on the IQE in a standard industry-grade, planar (In,Ga)N/GaN multi-QW reference sample, we utilize temperature-dependent time-resolved PL spectroscopy. In addition, we extend our study of the recombination dynamics to three different categories of possible future (In,Ga)N-based light emitters and compare the results to the reference sample. The three categories are: First, axial, N-polar (In,Ga)N quantum disks (QDs) in self-assembled GaN nanowires,[69] which allow the compensation of lattice mismatch of the (In,Ga)N QDs with high In contents via

the relaxation of strain at the sidewalls of sufficiently thin nanowires.[70–72] Moreover, the nanowires naturally exhibit a much higher extraction efficiency compared to planar samples (see Ref. 73 and references therein). Second, we examine nonpolar GaN/(In,Ga)N QW core/shell µ-rods,[74] which are beneficial because of the absence of the internal electric fields and their large effective area. The latter reduces the current density and hence the decrease of the efficiency compared to planar samples.[75] As a third category, we choose short-period superlattices (SPSLs) consisting of Ga-polar, sub-monolayer (ML) InN quantum sheets (QSs) embedded between GaN quantum barriers (QBs) to eliminate the influence of the alloy disorder of the random ternary alloy.[76,77] These heterostructures only contain the binary compounds InN and GaN, but exhibit the possibility to tune the band gap similar to (In,Ga)N/GaN.[78] Furthermore, these so-called digital alloys should not exhibit localization effects.

Subsequent to this introduction, the thesis is organized as follows: Chapter 2 provides a brief introduction into the basic properties of group III–nitrides as well as of recombination processes in semiconductors. We also present the current state of the literature about localization and carrier diffusion in (In,Ga)N in this chapter. Furthermore, we discuss the current understanding of the reduction of the efficiency of (In,Ga)N/GaN LEDs at high current densities and the application of the so-called *ABC* model for the extraction of the IQE.

In Chap. 3, we briefly categorize the samples investigated in this thesis and describe the experimental setups for steady-state and time-resolved PL spectroscopy. We also specify the parameters used for the Schrödinger-Poisson simulations. Subsequently, we present a basic electro-optical characterization of representative samples to demonstrate that they exhibit electro-optical properties as commonly reported in the literature.

In Chap. 4, we investigate the central question of this thesis: What is the influence of localization on the recombination dynamics, the diffusivity, and the IQE of polar (In,Ga)N/GaN QWs and QDs? In particular, we conduct a side-by-side comparison of the steady-state PL spectra of the Ga-polar, planar reference QWs and the N-polar, axial QDs in the nanowires. While the thermal quenching of the PL intensities is basically identical for both samples, the absolute PL intensities differ by two orders of magnitude. In order to understand this discrepancy, we analyze the initial part of the PL transients as well as their power law asymptote. A model employing the tunneling recombination of individually localized, spatially separated electrons and holes is utilized to explain the observed PL decay in the polar (In,Ga)N/GaN heterostructures. The corresponding system of position-dependent rate equations is solved efficiently by a Monte Carlo algorithm,[79] which is also employed to theoretically investigate the peculiarities of the power law transients. In view of our results of the simulation of the experimental temperature-dependent PL transients, the chapter concludes with the finding that the nanowires exhibit negligible diffusivities even at room temperature and suffer from high nonradiative recombination rates, as well as that the radiative tunneling recombination is only enabled by the strong localization.

We compare the findings obtained for the polar (In,Ga)N/GaN QWs to the ones for

nonpolar QWs in Chap. 5. For this purpose, we investigate the temperature-dependent steady-state and time-resolved PL intensities of GaN/(In,Ga)N core/shell µ-rods. In contrast to the tunneling recombination of individual charge carriers, we observe the recombination of localized excitons. We explain this result by a comparison of the localization and the exciton binding energies, which are both influenced by the magnitude of the internal electric fields.

To exclude that the distinct difference of the recombination mechanism originates from various localization strengths in the different samples investigated in the previous chapter, we study the impact of the internal electric field on the recombination mechanism in one and the same sample in Chap. 6. To this end, we apply a reverse bias to the Ga-polar LED and analyze the resulting PL transients. The experimentally observed change from tunneling recombination of electrons and holes to the radiative decay of excitons is supported by simulations of the band structure and the exclusion of classic escape mechanisms of charge carriers from the QWs.

In Chap. 7, we study the PL properties of a digital alloy consisting of the binary components InN and GaN in the form of Ga-polar, ML-thick InN QSs separated by thin GaN QBs. In contrast to the expectation of sharp transitions and a fast exponential decay, the PL spectra and transients are reminiscent of conventional Ga-polar (In,Ga)N/GaN QWs, which additionally suffer from a severe quenching of the PL intensity once delocalization sets in at elevated temperatures.

Finally, we summarize our conclusions in Chap. 8 and offer a general outlook for further investigations of recombination dynamics in polar (In,Ga)N/GaN QWs as well as the prospective of future concepts of (In,Ga)N-based emitters for solid-state lighting.

In Appendix A, we analyze the contrast pattern of µ-electroluminescence (EL) maps of (In,Ga)N/GaN LEDs within the framework of a drift-diffusion model. In Appendix B, we present investigations of the giant anti-Stokes PL intensity of (In,Ga)N/GaN heterostructures.

Chapter 2

Fundamentals and background

In this chapter, we give a brief introduction into the crystal structure of wurtzite GaN as well as into the concept of strain and polarization in group III–nitride heterostructures. Furthermore, we introduce the fundamental recombination processes of charge carriers as well as the formation and annihilation of excitons in direct semiconductors. In a second part, we review the present state of the literature of (In,Ga)N concerning localization, diffusion, and the decrease of the quantum efficiency due to an increasing current and In content. In addition, we discuss the modeling of the internal quantum efficiency by the so-called ABC model. The basic physics presented in this chapter are adapted in parts from the books of Kittel,[80] Ashcroft and Mermin,[81] and Hunklinger.[82] Parts directly related to GaN are based on the series authored by Morkoç.[83–85]

2.1 Crystal structure of the direct semiconductor GaN

Single-crystal solids exhibit a highly ordered lattice of their atomic constituents. The strict periodicity enables the description of the energy eigenstates of the overlapping electron wave functions of the crystal by periodic Bloch waves within the first Brillouin zone (primitive Wigner-Seitz cell in reciprocal space). The resulting energy bands are separated by a band gap. For direct band gap semiconductors, the valence band (VB) maximum and the conduction band (CB) minimum are located at the same position in the reciprocal space (typically at the center of the Brillouin zone, the so-called Γ-point). Semiconductors exhibit a negative temperature coefficient of the resistance, and their conductivity can be controlled by the introduction of dopants (i. e., a shift of the Fermi level due to donor or acceptor atoms).

Based on the concept of the ionicity of chemical bonds,[86] it was shown that tetrahedrally coordinated close-packed crystal structures of the binary compounds of $A^N B^{8-N}$-type crystallize either in the cubic zincblende (ZB) or the hexagonal wurtzite (WZ) structure.[87] The equilibrium phase of GaN with its comparatively high ionicity is the WZ structure, but a meta-stable ZB polytype also exists. While distance and angle of nearest and next-nearest neighbor are identical for both configurations, the bond angle to the third-nearest neighbor is different. The resulting simplified WZ and ZB stacking se-

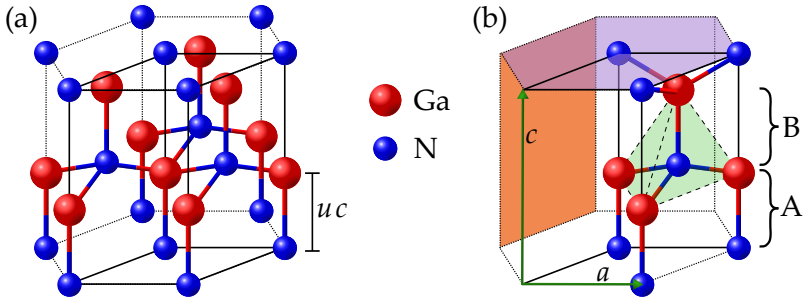

Figure 2.1: (a) Stick-and-ball model of the hexagonal crystal structure of wurtzite GaN along the [0001] direction with the unit cell indicated by solid lines. The size of the balls represents the covalent atomic radii. (b) The tetrahedral coordination geometry is highlighted by light green surfaces. The stacking sequence AB as well as the lattice parameters a and c are indicated. Orange and violet surfaces indicate exemplary nonpolar $(1\bar{1}00)$ and polar $(000\bar{1})$ crystal planes.

quences* along the [0001] and [111] direction are denoted as ABAB... and ABCABC..., respectively.

In the following, we will focus on the stable WZ phase of GaN. A schematic stick-and-ball model with the primitive unit cell (solid lines), containing four atoms, is shown in Fig. 2.1(a). The tetrahedral coordination, exemplary polar and nonpolar lattice planes as well as the WZ unit cell with the two basis vectors a and c are shown schematically in Fig. 2.1(b). The ideal values for the ratio of c/a as well as the internal parameter u, which can be calculated by $u = \frac{1}{3}(a/c)^2 + \frac{1}{4}$,[88] are $\sqrt{8/3}$ and 3/8, respectively. Experimental values for WZ GaN amount to $a = 3.1884\,\text{Å}$, $c = 5.1852\,\text{Å}$, and $u = 0.376$ and reveal that the real crystal structure deviates from the ideal hexagonal close-packed model.[89] A compilation of material parameters for (In,Ga)N/GaN heterostructures is given in Ref. 90.

2.2 Polarization fields and their influence on the band diagram

GaN in its WZ modification belongs to the space group $P6_3mc$ and the point group 6mm (Hermann-Mauguin notation). It exhibits a singular polar axis in the ⟨0001⟩ direction, resulting in spontaneous polarization (P_{sp}) along this polar axis even at equilibrium.[91] In addition, any deviation from the ideal tetrahedral coordination, i. e., due to strain induced by the lattice mismatch to the underlying layer, leads to piezoelectric polarization (P_{pz}) due to the lack of inversion symmetry. For (In,Ga)N/GaN heterostructures, the total macroscopic polarization is the sum of both, P_{pz} and P_{sp}. The values of P_{pz} are typically larger than that of P_{sp}.[90]

*Because a cation-anion-pair shares the same in-plane lattice position, AB instead of AaBb is used.

The spontaneous polarization can be described in a point-charge model as[92]

$$P_{\mathrm{sp}} = -\frac{4Q}{\sqrt{3}a^2}(u - \frac{3}{8}). \tag{2.1}$$

However, the cation charge Q is not properly defined for structures with partially ionic bonds.[93] Commonly, P_{sp} is calculated *ab initio* by the density functional theory with the Berry phase approach.[94] In a quantum mechanical picture, the point charges are replaced by charge distributions, and the modern definition of polarization is based on an adiabatic flow of current through the crystal.[95] Very recently, Dreyer *et al.*[96] reported a refined implementation of spontaneous and piezoelectric polarization constants in wurtzite materials.

The vector of the piezoelectric polarization can be calculated by utilizing the piezoelectric tensor for the space group $P6_3mc$ as[97]

$$\mathbf{P}_{\mathrm{pz}} = \begin{pmatrix} 0 & 0 & 0 & 0 & \mathrm{e}_{15} & 0 \\ 0 & 0 & 0 & \mathrm{e}_{15} & 0 & 0 \\ \mathrm{e}_{31} & \mathrm{e}_{31} & \mathrm{e}_{33} & 0 & 0 & 0 \end{pmatrix} \begin{pmatrix} \epsilon_{xx} \\ \epsilon_{yy} \\ \epsilon_{zz} \\ \epsilon_{yz} \\ \epsilon_{xz} \\ \epsilon_{xy} \end{pmatrix} \tag{2.2}$$

with e_{ij}, ϵ_{ii}, and ϵ_{ij} being piezoelectric constants as well as uniaxial and shear strain components, respectively. For the heteroepitaxy of planar (In,Ga)N/GaN on foreign substrates along the polar or nonpolar direction, it is expected that shear strains are absent. Thus,

$$\mathbf{P}_{\mathrm{pz}} = \mathrm{e}_{31}(\epsilon_{xx} + \epsilon_{yy}) + \mathrm{e}_{33}\epsilon_{zz}. \tag{2.3}$$

Strain (deformation of the crystal) and stress (pressure applied to the crystal) are linked by the stress-strain tensor (pseudo-second rank in the Voigt scheme[98]) with the elastic constants C_{ij}. Experimental and theoretical values for C_{ij} of InN and GaN are given in Refs. 99–101. Because the layer is free of stress along the growth direction, we obtain

$$\epsilon_{yy} = \frac{-C_{12}\epsilon_{xx} - C_{13}\epsilon_{zz}}{C_{11}} \quad \text{and} \quad \epsilon_{zz} = -2\frac{C_{13}}{C_{33}}\epsilon_{xx} \tag{2.4}$$

(Poisson effect) for the strain along the $[1\bar{1}00]$ and [0001] direction, respectively. Moreover, for growth along the polar axis on substrates with a lattice constant a_s, the in-plane strain in a sufficiently thin epitaxial layer with a lattice constant a_l is isotropic ($\epsilon_{xx} = \epsilon_{yy}$) and does not relax (pseudomorphic growth). Hence,

$$\epsilon_{xx} = \epsilon_{yy} = (a_s - a_l)/a_l. \tag{2.5}$$

While the direction of the polarization is normal to the growth axis for growth along the $[1\bar{1}00]$ direction, it is parallel for the growth along the [0001] direction [cf. combination of

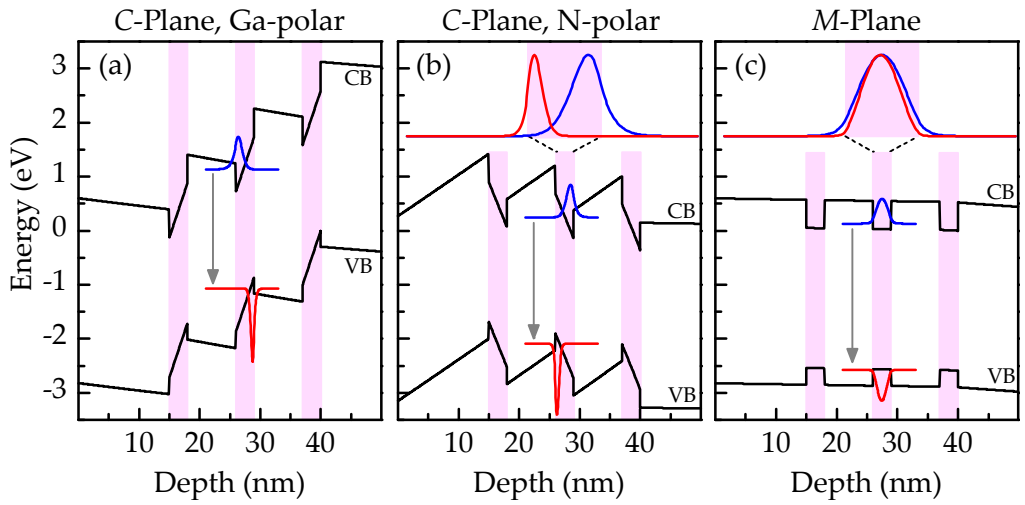

Figure 2.2: Band diagram of an $In_{0.2}Ga_{0.8}N/GaN$ heterostructure with three 3-nm-thick QWs (highlighted by pink rectangles) for growth along the (a) [0001], (b) [000$\bar{1}$], and (c) [1$\bar{1}$00] direction. The structure is n-type doped with a concentration of 5×10^{16} cm^{-3}. The transition energy of the electron (blue) and hole ground state (red) for the central QW is indicated by the arrow. To visualize the different overlap of the electron and hole wave functions, the central QW is enlarged in the top part of (b) and (c).

Eqs. (2.3)–(2.5)]. Thus, for layers grown on the C-plane, a discontinuity in the polarization ΔP (especially at interfaces) introduces a sheet charge density resulting in opposing internal electrostatic fields in the different layers. In a heterostructure grown along the polar direction, the internal electric fields E_i inside the QB or the QW with thicknesses d_i, the permittivity of the vacuum ε_0, and relative permittivities ε_i can be calculated for an infinite superlattice by utilizing the dielectric displacement conservation of the polarization P_i

$$\Delta P = (P_{\mathrm{QB}} - P_{\mathrm{QW}}) = (\varepsilon_{\mathrm{QW}} E_{\mathrm{QW}} - \varepsilon_{\mathrm{QB}} E_{\mathrm{QB}})\varepsilon_0 \tag{2.6}$$

and the periodic boundary conditions ($d_{\mathrm{QW}} E_{\mathrm{QW}} + d_{\mathrm{QB}} E_{\mathrm{QB}} = 0$).[102–105] Consequently,

$$E_{\mathrm{QW}} = \frac{d_{\mathrm{QB}}(P_{\mathrm{QB}} - P_{\mathrm{QW}})}{(\varepsilon_{\mathrm{QW}} d_{\mathrm{QB}} - \varepsilon_{\mathrm{QB}} d_{\mathrm{QW}})\varepsilon_0}. \tag{2.7}$$

In order to accurately determine the electric fields, we utilize a self-consistent approach and solve the Poisson and Schrödinger equations in the effective mass approximation and take the polarization charges at the interfaces into account (see Sec. 3.3 for more details and material parameters).

In Fig. 2.2, the resulting profiles of the VB and CB edge as well as electron and hole wave functions are shown for three $In_{0.2}Ga_{0.8}N$ QWs embedded between GaN QBs for growth along the polar and nonpolar crystal directions. Note the significantly different band profiles for the structures grown along the [0001] and [000$\bar{1}$] direction. According

growth direction	transition energy	overlap
[0001]	2.21 eV	0.11
[000$\bar{1}$]	2.34 eV	0.17
[1$\bar{1}$00]	2.70 eV	0.98

Table 2.1: Transition energy and overlap of electron and hole wave functions for (In,Ga)N/GaN QWs grown along various crystal directions. The band gap of the 3-nm-thick $In_{0.2}Ga_{0.8}N$/GaN QWs amounts to 2.59 eV.

to the termination of the surface with either Ga or N atoms, these directions are referred to as Ga- and N-polar, respectively. A major difference for the growth along these polar axes is the direction of the internal electric fields and the value at which the Fermi level is pinned.[106] Along the polar axes, the strong internal electric fields, caused by the polarization charges at the QW/QB interfaces, lead to the so-called quantum-confined Stark effect. As a consequence, the transition energy is lower than the band gap [cf. Tab. 2.1 and Figs. 2.2(a) and 2.2(b)]. Moreover, electron and hole wave functions are pulled to the opposite sides of the QW, which reduces their overlap. This separation and the reduction of the transition energy is the strongest for the [0001] direction. In contrast, no electric fields are present along the nonpolar direction, leading to a transition energy larger than the band gap and a large overlap of the wave functions [see Fig. 2.2(c)]. We have summarized the quantitative results from the Schrödinger-Poisson calculations in Tab. 2.1.

2.3 Recombination processes and lifetimes

2.3.1 Exciton binding energy

The lowest energy state in an ideal crystal is the free exciton-polariton. From a quantum mechanical point of view, an exciton-polariton is a coherent elementary excitation over the whole *ideal* crystal.[107] However, for real crystals, the classical description is often more appropriate: Due to Coulomb interaction, electron and hole form a quasi-particle, the so-called exciton. In inorganic semiconductors, the exciton binding energy is low (several meV; Wannier-Mott exciton) while the binding energy is higher in organic semiconductors (several hundred meV; Frenkel exciton).[108,109] Following the derivation in Ref. 110 and treating the exciton as a hydrogen-like atom, the discrete exciton bound-state energies E_n can be obtained from a hydrogenic Schrödinger equation in an $\hat{D}$-dimensional space in the framework of the fractional-dimensional model. Neglecting the vanishing kinetic energy of the relaxed exciton, we obtain

$$E_n = E_g - \frac{E_0}{\left[n + \frac{\hat{D}-3}{2}\right]^2} \tag{2.8}$$

with the energy of the band gap (E_g) and the effective Rydberg energy (E_0) which can be calculated by

$$E_0 = \frac{\mu/m_0}{\varepsilon^2} R_H. \tag{2.9}$$

Here $\mu = (1/m_e + 1/m_h)^{-1}$ and $R_H = 13.6\,\text{eV}$ denote the reduced effective exciton mass and the Rydberg energy, respectively. Finally, the exciton binding energies E_X with

$$E_X = \left(\frac{2}{\hat{D} - 1}\right)^2 E_0 \tag{2.10}$$

result in $E_X = E_0,\ 4E_0,$ or ∞ for the dimensions $\hat{D} = 3,\ 2,$ or 1. We note that the lower E_X the larger the exciton Bohr radius (a_X). Analogously to the derivation of Eq. (2.9), a_X can be defined as:

$$a_X = \frac{\varepsilon}{\mu/m_0} a_B. \tag{2.11}$$

In comparison to GaAs, the comparatively low value of ε and the large effective masses result in a large value of E_X for GaN.[111] Using the relative permittivity $\varepsilon = 9.5$[102] and the effective electron ($m_e = 0.2m_0$) and hole ($m_h = 1.6m_0$) masses[112] for wurtzite GaN, we obtain a bulk exciton binding energy ($\hat{D} = 3$) of $E_X \approx 27\,\text{meV}$ and an exciton Bohr radius of $a_X \approx 3\,\text{nm}$. Due to the large value of E_X, free excitons in GaN are stable up to room temperature ($\approx 25\,\text{meV}$). The calculated value of E_X is in good agreement with reported experimental values for bulk GaN.[108,113–116] In addition, $E_X(\hat{D} = 2) = 4E_0$ for QWs embedded between infinite barriers is on the same order of magnitude as the experimental value, which was found to amount to about 60 meV.[117] Without additional confinement, the wave functions of the excitons leak into the surrounding material for finite barriers, reducing E_X.[107] The same applies for $E_X(\hat{D} = 1) = \infty$, which may be obtained only theoretically for infinite barriers. Thus, the exciton experiences a binding energy close to the one of the barrier material for extremely thin QWs. This fact is considered by the approach of the fractional-dimension[118,119] or the exact theoretical description by Andreani and Pasquarello.[120] However, this analytical solution is not applicable for semiconductor heterostructures with strong internal electric fields such as (In,Ga)N/GaN. Alternatively, the variational approach (following the seminal work of Miller *et al.*[121]) is used for calculating the exciton binding energy of QWs with infinite[122] and finite[123] barriers including excitonic effects.[124,125] In general, the determination of the exciton binding energy becomes more complex in the presence of localization centers such as alloy fluctuations or impurities, which bind the excitons.

2.3.2 Excitonic recombination

The recombination processes of excitons are schematically depicted in Fig. 2.3(a). After the excitation of electron-hole pairs into the energy continuum $|C\rangle$ of a semiconductor

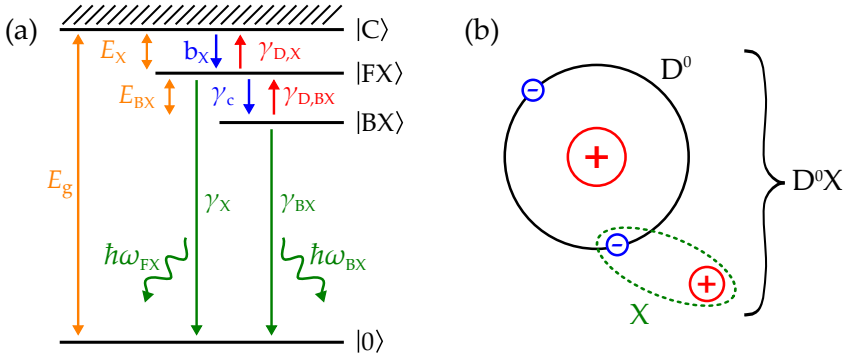

Figure 2.3: (a) Schematic representation of the energy levels for free and bound exciton states in a semiconductor with the band gap E_g. After excitation of an electron-hole pair to the energy continuum $|C\rangle$, excitons form (populating the free-exciton state $|FX\rangle$) and bind to impurities or alloy fluctuations (bound states $|BX\rangle$) (blue arrows). Transitions from either of these levels to the ground state $|0\rangle$ are indicated by green arrows with the respective photon energies (in case of a radiative decay). Depending on the thermal energy, the exciton may delocalize or dissociate (red arrows). (b) Exciton (X) indicated by the dashed ellipse bound to a neutral donor (D^0) forming a donor-bound exciton (D^0X).

with the band gap E_g, free excitons form with a capture rate b_X, gaining the exciton binding energy E_X (see Sec. 2.3.1). The resulting transition energy $\hbar\omega_{FX}$ for the radiative decay of the exciton from the free exciton state ($|FX\rangle$) to the ground state ($|0\rangle$) equals $E_g - E_X$. In the presence of alloy fluctuations or impurities, it is energetically favorable for excitons to localize at these crystal imperfections. Schematically, an exciton bound to a neutral donor D_0 (such as Si or O in GaN[126]) is shown in Fig. 2.3(b). In GaN, the energy gained by the binding of an exciton to a donor or an acceptor amounts to 7 and 12 meV, respectively.[127],† Thus, bound excitons exhibit transition energies $\hbar\omega_{BX} = E_g - E_X - E_{BX}$, but may be observed only at low temperatures, for which the kinetic energy of the excitons ($3k_BT/2$) is lower than the binding energy E_{BX}.

In unintentionally doped semiconductors, the impurity concentration is typically on the order of $1 \times 10^{14}\,\mathrm{cm}^{-3}$ for GaAs and $1 \times 10^{16}\,\mathrm{cm}^{-3}$ for GaN, i. e., in the ppb to ppm range. Still, bound excitons dominate the emission spectra of bulk semiconductors. The reason for this fact lies in the very inefficient decay of free excitons in bulk crystal. In fact, free excitons form a coupled state with the photon, which, in principle, does not decay in an ideal crystal because of momentum conservation, resulting in an exciton lifetime determined by the scattering with phonons at low temperatures.[128] In addition, bound excitons exhibit a very efficient radiative decay (giant oscillator strength; see, e. g., Ref. 129–132).

In almost dislocation-free and high-purity QWs, the free excitons exhibit large radiative recombination rates[133,134],‡ even at low temperatures, because the coupling between the exciton and the photon is enhanced by the breakdown of the translational invariance in

†For example, the donor binding energy can be approximated simply by using $\hat{D} = 3$ and $\mu = m_e$ in Eq. (2.10).

‡Originally, the concept of superradiance was introduced by Dicke.[135]

the growth direction.[134] This behavior can be explained in the picture of the coherence area of the exciton introduced by Rashba and Gurgenishvili.[129] The larger the coherence area, the larger the coherent extension of the exciton's center-of-mass wave function and thus the shorter the radiative lifetime.[136] However, even in these systems, localization of excitons[137,138] for example at well-width fluctuations lead to a lower limit of the radiative lifetime.[134,139] Note that this effect must not be confused with quantum confinement of the exciton, because only its translational motion becomes localized.[140]

Summarizing, the excitonic recombination processes under steady-state conditions result in the following rate equations for free (n_F) and bound (n_b) excitons for an n-type semiconductor with the total donor concentration $N_\mathrm{D} = N_\mathrm{D}^0 + n_\mathrm{b}$:

$$0 = \frac{\mathrm{d}n_\mathrm{F}}{\mathrm{d}t} = b_\mathrm{X} np - \gamma_\mathrm{X} n_\mathrm{F} - \gamma_\mathrm{c} n_\mathrm{F} N_\mathrm{D}^0 + \gamma_\mathrm{D,BX} n_\mathrm{b} - \gamma_\mathrm{D,X} n_\mathrm{F} \tag{2.12}$$

$$0 = \frac{\mathrm{d}n_\mathrm{b}}{\mathrm{d}t} = \gamma_\mathrm{c} n_\mathrm{F} N_\mathrm{D}^0 - \gamma_\mathrm{D,BX} n_\mathrm{b} - \gamma_\mathrm{BX} n_\mathrm{b} \tag{2.13}$$

with the capture rate of free excitons (γ_c) by unoccupied donors (N_D^0) as well as the dissociation rates ($\gamma_\mathrm{D,BX}$) of exciton-donor complexes (n_b) and free excitons ($\gamma_\mathrm{D,X}$). The recombination rates of free (γ_X) and bound (γ_BX) excitons include radiative and nonradiative recombination. In general, the recombination processes are not purely excitonic, but are, depending on temperature, mixed with free-carrier recombination (see, e. g., Ref. 128).

2.3.3 Free-carrier recombination

In semiconductors, the excitation of an electron from the valence to the conduction band leaves behind a hole in the valence band. The excited charge carrier recombine radiatively or nonradiatively as shown schematically in Fig. 2.4. Besides the transitions of free carriers involving donor or acceptor levels or nonradiative three-particle processes (i. e., Auger recombination), which become important at high charge carrier densities, bimolecular radiative band-to-band recombination and trap-assisted nonradiative recombination occur. The latter two processes describe the simplest case for the simultaneous radiative and nonradiative recombination. For these two processes, we obtain the following rate equations for electrons (n) and holes (p), which are generated with a rate G:

$$\frac{\mathrm{d}n}{\mathrm{d}t} = G - Bnp - b_n n N_\times \tag{2.14}$$

$$\frac{\mathrm{d}p}{\mathrm{d}t} = G - Bnp - b_p p N_\bigcirc \tag{2.15}$$

with B and b being the radiative recombination and capture coefficients. The density of nonradiative centers (N) equals the sum of empty ($N_\bigcirc$) and filled ($N_\times$) centers. The experimental observable PL intensity is given by Bnp. Assuming steady-state conditions,

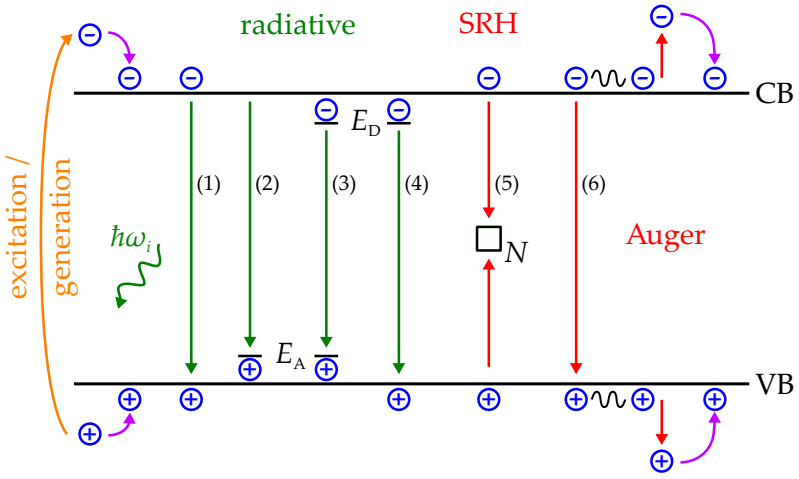

Figure 2.4: Schematic of generation and recombination of free charge carriers in a semiconductor. After excitation of electrons from the VB to the CB (orange), the excited electrons and holes relax (violet) to the band edges. Radiative band-to-band (1), band-to-acceptor (2), donor-acceptor (3), and donor-band (4) transitions (with photon energies $\hbar\omega_i$) are indicated in green. Nonradiative SRH recombination (5), mediated by mid-gap states which act as nonradiative recombination centers (N), as well as nonradiative nnp- or npp-Auger recombination (6) are indicated in red.

for which Eqs. (2.14) and (2.15) are identical, we obtain for the nonradiative recombination rate

$$R_{\mathrm{SRH}} = b_n n N_\times = b_p p N_\bigcirc = \frac{b_n b_p N n p}{b_n n + b_p p}, \tag{2.16}$$

the classical Shockley-Read-Hall (SRH) expression.[141]

For an n-type semiconductor, $n = n_0 + \Delta n$ and $p = \Delta p$ with n_0 being the concentration of dark electrons (e. g. from donors). From the equations above the neutrality condition in the presence of active nonradiative recombination centers reads

$$n_0 + \Delta n = \Delta p + N_D^+ + N_\times \tag{2.17}$$

with the concentration of ionized donors (N_D^+), which equals n_0. Consequently, the equality of the excess carrier densities ($\Delta n = \Delta p$) is justified only for purely radiative recombination.[142] For the general case, an asymmetry in Eq. (2.16) causes a nonlinear increase of the PL intensity with increasing values of G due to the saturation of recombination centers.

The situation is even more complex for transient conditions, because R_{SRH} includes the time-dependent concentration of empty centers.[142] Assuming that N and $N_\bigcirc$ balance each other (at a value N^*) and that N^* is small compared to n_0 or Δn, we can derive approximations for low and high excitation densities. In the case of low excitation densities

(i. e., $\Delta n = \Delta p \ll n_0$), the radiative and nonradiative rates are described by

$$Bnp = Bn_0\Delta p = \tau_{\mathrm{r}}^{-1}\Delta p \quad \text{and} \quad R_{\mathrm{SRH}} = b_p N^* \Delta p = \tau_{\mathrm{nr}}^{-1}\Delta p, \tag{2.18}$$

respectively. Because the coefficients are independent of n and p, the PL decay is exponential, and a constant lifetime (τ_i) can be defined for both processes. For high excitations ($\Delta n = \Delta p \gg n_0$), the equation for the nonradiative recombination reads

$$R_{\mathrm{SRH}} = \frac{b_p b_n}{b_p + b_n} N^* \Delta p = \tau_{\mathrm{nr}}^{-1}\Delta p. \tag{2.19}$$

For radiative recombination, we obtain

$$Bnp = B\Delta p^2 \tag{2.20}$$

which does not contain a unique lifetime. Hence, in the nondegenerate case (Boltzmann statistics), the decay is hyperbolic for $R_{\mathrm{SRH}} = 0$ or hyperbolic with an exponential asymptote for $R_{\mathrm{SRH}} \neq 0$.

2.3.4 Temperature dependence of the radiative lifetime

In this subsection, we will derive the temperature dependence of the radiative lifetime of charge carriers experiencing confinement in various dimensions. Already in 1927, Dirac[143] introduced a formula which is now known as *Fermi's Golden Rule*.[144] In our picture, we modify *Fermi's Golden Rule* with its Hamiltonian $\mathcal{H}$ to describe the total emission rate R_{total} of photons with a wavelength λ and an energy $\hbar\omega_\lambda$.

$$R_{\mathrm{total}} = \frac{2\pi}{\hbar} \sum_{\lambda} \sum_{\mathrm{CB,VB}} |\langle \mathrm{VB}|\mathcal{H}|\mathrm{CB}\rangle|^2 \delta(E_{\mathrm{VB}} - E_{\mathrm{CB}} + \hbar\omega_\lambda) \tag{2.21}$$

for the respective energy levels E of electrons from the CB annihilating with holes from the VB. Following the derivation given by Bebb and Williams,[145] we use Eq. (2.21) to relate the spontaneous emission rate R_{sp} to the absorption $\alpha(\hbar\omega)$. We sum over the total number of CB and VB states as well as over the radiation modes λ between ω and $\omega + \mathrm{d}\omega$. By introducing the optical density of states[§] and with the knowledge that in a dielectric medium the energy velocity equals the group velocity,[146] we arrive at

$$R_{\mathrm{sp}} = \alpha(\hbar\omega) \frac{\hat{n}^2 E_{\mathrm{g}}^2}{\pi^2 c^2 \hbar^3} \frac{f_{\mathrm{CB}} f'_{\mathrm{VB}}}{[1 - f'_{\mathrm{VB}}][1 - f_{\mathrm{CB}}] - f_{\mathrm{CB}} f'_{\mathrm{VB}}} \tag{2.22}$$

for materials with a band gap of E_{g} and a refractive index $\hat{n}$. For the Fermi-Dirac distribution, the sum of the probabilities of filled (f) and empty (f') states is unity. For optical transitions, impurities due to donors or acceptors can introduce an additional degeneracy because of their charge state.[145] As we are only interested in the dependence on temper-

[§]Here, the wave vector is converted to the wave number and the group velocity is introduced.[145]

ature, we omit this degeneracy and stick to the case of the band-to-band recombination. Assuming that the density of states is proportional to the distribution function for the respective particle, which in turn follows a Boltzmann distribution for the nondegenerate case, we obtain for the spontaneous emission rate

$$R_{\mathrm{sp}} = \alpha(\hbar\omega)\frac{\hat{n}^2 E_{\mathrm{gap}}^2}{\pi^2 c^2 \hbar^3}\left[e^{(\hbar\omega-\Delta f)/(k_{\mathrm{B}}T)} - 1\right]^{-1} \tag{2.23}$$

which is known as Roosbroeck-Shockley relation[147] with Δf being the difference of the quasi-Fermi levels. At thermal equilibrium, $\Delta f = 0$, and, for optical transitions, $\hbar\omega/k_{\mathrm{B}}T \gg 1$. With the intrinsic carrier concentrations n_0 and p_0, we can link the spontaneous emission rate to the radiative recombination rate and hence to the inverse of the radiative lifetime (τ_{r}).[148] In the case of an n-type semiconductor, we obtain

$$\frac{R_{\mathrm{sp}}}{n_0^2} = \frac{\hat{n}^2 E_{\mathrm{gap}}^2}{\pi^2 c^2 n_i^2 \hbar^3}\int_0^\infty \alpha(\hbar\omega)e^{-\hbar\omega/(k_{\mathrm{B}}T)}\mathrm{d}\hbar\omega = \frac{1}{\tau_{\mathrm{r}}}. \tag{2.24}$$

Because $\alpha(\hbar\omega)$ depends on the density of unoccupied states[82] and thus on the dimensionality of the system, we obtain

$$\hat{\mathrm{D}} = 3 \;\rightarrow\; \alpha(\hbar\omega) \propto \sqrt{\hbar\omega} \;\rightarrow\; \tau_{\mathrm{r}} \propto T^{3/2}, \tag{2.25}$$

$$\hat{\mathrm{D}} = 2 \;\rightarrow\; \alpha(\hbar\omega) \propto \text{const.} \;\rightarrow\; \tau_{\mathrm{r}} \propto T^{2/2} = T, \tag{2.26}$$

$$\hat{\mathrm{D}} = 1 \;\rightarrow\; \alpha(\hbar\omega) \propto 1/\sqrt{\hbar\omega} \;\rightarrow\; \tau_{\mathrm{r}} \propto T^{1/2}, \text{ and} \tag{2.27}$$

$$\hat{\mathrm{D}} = 0 \;\rightarrow\; \alpha(\hbar\omega) \propto \delta(E) \;\rightarrow\; \tau_{\mathrm{r}} \propto T^{0/2} = \text{const.} \tag{2.28}$$

For excitons in QWs, the linear dependence of the radiative lifetime[137,139,149–151] has also been derived from the polariton picture developed by Hopfield.[152] The theoretically predicted decrease of the radiative lifetime in bulk crystals down to low temperatures is usually not seen in the experiment. Instead, a constant radiative lifetime of localized excitons is approached at low temperatures due to an inefficient decay of free excitons (see Sec. 2.3.2).

2.4 Localization in the random alloy (In,Ga)N

Localization at In clusters[153] or In-N-In chains[45,56,154] has been suggested to explain the high efficiency of (In,Ga)N/GaN despite the high density of structural defects. In early studies of (In,Ga)N/GaN by transmission electron microscopy, nanoscopic clusters with high In concentration have been observed.[153] This observation was supported by theoretical calculations of the spinodal decomposition.[155] However, these calculations do not account for strain in the QW and between the In- and Ga-rich regions.[156] Moreover, it turned out that the clusters were in fact artificially produced by electron beam irradiation[57] (see review about this topic in Ref. 157). Recent investigations by the

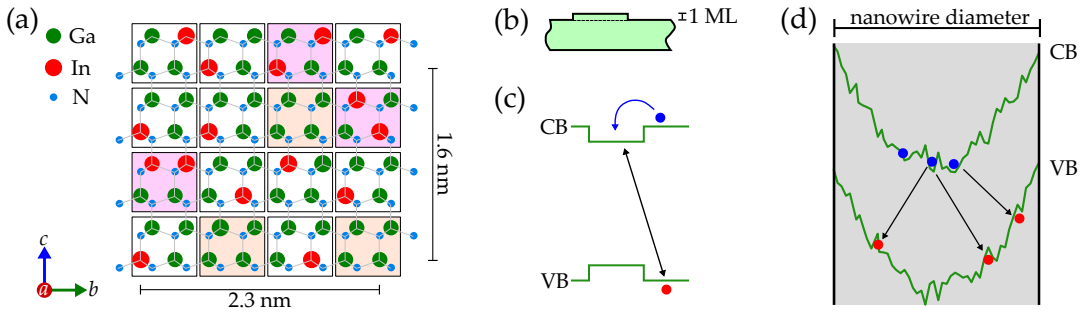

Figure 2.5: (a) Slice of an $In_{0.25}Ga_{0.75}N$ crystal along the [0001] direction with randomly distributed In atoms. Groups of four metal atoms are framed by rectangles to visualize regions with higher than average (pink) and lower than average (orange) In content. (b) Schematic of a well-width fluctuation with a typical thickness of 1 ML and (c) in-plane band profile indicating the in-plane separation of electrons (blue) and holes (red). (d) Schematic of the radial Stark effect[162] in (In,Ga)N nanowires at room temperature as explained in the text.

combination of aberration-corrected high-resolution transmission electron microscopy and atom-probe tomography reveal that polar (In,Ga)N/GaN QWs constitute random alloys.[59–65] We schematically present such a random distribution for $In_{0.25}Ga_{0.75}N$ in Fig. 2.5(a). Assuming that the local band profile depends directly on the number of In atoms in every "unit" cell, we observe areas with higher and lower band gap. In the free-carrier picture, predominantly holes localize at these atomistic potential fluctuations because of their larger effective mass.[68,158] In addition, monolayer fluctuations of the well-width[159,160] or the interface roughness,[59,161] occurring commonly at the upper interface of the QWs [see schematic in the upper part of Fig. 2.5(b)], constitute an additional localization center for electrons in Ga-polar (In,Ga)N/GaN QWs.[50,68] Due to the polarization charges (see Sec. 2.1), electrons are attracted to the upper interface in these samples. Because of the resulting polarization fields causing the quantum-confined Stark effect, the transition energy in the region of a well-width fluctuation is reduced, and the electrons get trapped in these potential minima [see Fig. 2.5(c)]. Consequently, the different localization mechanisms of individual electrons and holes introduce a horizontal separation of the charge carriers in addition to the vertical one.

For GaN and other III–V semiconductors, a band bending is induced by the pinning of the Fermi level at the free surface.[163,164] In nanowires (with their large free surface), this band bending leads to a radial separation of charge carriers. In analogy to the quantum-confined Stark effect, it is called radial Stark effect.[162] This effect is detrimental for (In,Ga)N/GaN nanowire heterostructures with large diameters or thin QDs.[165,166] However, this band bending is superimposed by the potential fluctuations of the random alloy as schematically shown in Fig. 2.5(d). Consequently, localization prevents the complete radial separation of charge carriers at room temperature, resulting in an increase of the efficiency as well as a redshift of the PL energy and of the absorption edge in pure (In,Ga)N nanowires compared to (In,Ga)N/GaN QDs.[162,167] This behavior is beneficial

for the application of these nanowires as photoanodes for solar water splitting.[168,169]

2.4.1 Localization energy

As the localization of charge carriers seems to be important in (In,Ga)N, it is crucial to estimate the localization energy for different samples. A commonly employed method is the analysis of the temperature-dependent peak PL energy $E_{\mathrm{PL}}(T)$. With increasing temperature, the peak energy of the PL band of the QWs exhibits the frequently observed so-called S-shape.[46,53,170] Often, the blue shift of the peak energy at intermediate temperatures is explained by localization of charge carriers and a thermally-induced redistribution in the occupation of states. More specifically, localized charge carriers are randomly distributed over the density of states at low temperatures. For slightly higher temperatures, relaxation to lower energy states sets in (initial redshift). At even higher temperatures, a redistribution of the charge carriers lead to a thermal population of higher states (blue shift), until the shrinkage of the band gap dominates the peak energy (redshift).[46,53,171] By fitting the band gap with simple empirical models such as the Varshni-formula,[172] models which are based on lattice vibrations,[173–175] or sophisticated semi-empirical theories as proposed by Pässler,[176,177] the difference between the fit and the dip of the S-shape of $E_{\mathrm{PL}}(T)$ is attributed to the localization energy. However, the internal electric fields (see also Sec. 2.1) complicate this analysis. Moreover, Langer *et al.*[170] proposed another explanation for the S-shape of $E_{\mathrm{PL}}(T)$ by attributing it to the competition between the spectrally dependent radiative and nonradiative recombination. In view of these results, the estimation of localization energies from the PL energy seems to be rather questionable.[170] In addition, we note that the apparent absence of the S-shape of $E_{\mathrm{PL}}(T)$ does not automatically imply an absence of localization.

For a system of free and localized excitons, the measured (effective) radiative lifetime (τ_{r}) depends on the lifetimes of localized and free excitons as well as on their concentrations.[137,178,179] Hence, the analysis of the temperature-dependent value of τ_{r} can be used to determine the influence of the localization energy E_{loc}. In the case of GaN or nonpolar (In,Ga)N with low to moderate In content, we can neglect the dissociation of excitons up to room temperature. Thus, the recombination can be described by using a system of rate equations similar to Eqs. (2.12) and (2.13) for delocalized (n_{d}) and localized excitons (n_ℓ). Under the assumption that capture and emission processes are much faster than the radiative transitions, the density of occupied localized states can be expressed in terms of a thermal equilibrium cross section for the capture of excitons by localized states.[180] In the limit of small-signal excitation, the temperature-dependent effective radiative lifetime becomes[180]

$$\tau_{\mathrm{r}}(T) = \frac{1 + \frac{n_\ell}{n_{\mathrm{d}}} e^{E_{\mathrm{loc}}/(k_{\mathrm{B}}T)}}{\frac{1}{\tau_{\mathrm{d}}(T)} + \frac{1}{\tau_\ell}\frac{n_\ell}{n_{\mathrm{d}}} e^{E_{\mathrm{loc}}/(k_{\mathrm{B}}T)}}. \tag{2.29}$$

While $\tau_{\mathrm{d}}(T)$ is the lifetime of the delocalized excitons in a quantum well (analogous to Sec. 2.3.4, $\tau_{\mathrm{d}}(T) \propto T$), τ_ℓ is the temperature-independent lifetime of the localized exciton.

Hence, by fitting the measured values of τ_r with Eq. (2.29), we have the possibility to extract the localization energy E_{loc}.

2.5 Carrier and exciton diffusion in (In,Ga)N/GaN

The epitaxial growth of (In,Ga)N/GaN on foreign substrates (such as Si or Al_2O_3), which are typically used in commercial LEDs,[181] triggers the creation of threading dislocations to compensate for the lattice mismatch.[182] The lateral transport of charge carriers to the cores of the dislocations may cause a vertical (shunt) current, which has been investigated theoretically in Refs. 183–185. For the experimental investigation of the lateral/in-plane transport of charge carriers in (In,Ga)N/GaN QWs, we have to take into account both the drift and the diffusion of charge carriers. In general, diffusion is the omnidirectional motion of particles to balance concentration gradients, and drift describes the motion of charged particles due to electric fields. Furthermore, quasi-electric fields induced by gradients of the band gap in semiconductors influence also neutral particles such as excitons. The classical experiment to determine both, the carrier mobility and the diffusivity, is the one designed by Haynes and Shockley.[186] However, this classical experiment is difficult to perform in GaN which exhibits ns lifetimes and comparatively small diffusivities. In addition, polar (In,Ga)N/GaN QWs exhibit random microscopic compositional fluctuations as well as macroscopic inhomogeneities in the In content and the well width caused by the growth (see also Sec. 2.4). As shown in Sec. 2.1, the growth along a polar direction induces polarization charges at the interfaces of the QWs and internal electric fields. Screening of these internal polarization fields induced by high optical excitation or band gap gradients caused by the strain field of the dislocations or fluctuations in In content and well width will generate a significant drift of charge carriers. To distinguish drift and diffusion in this situation is not straightforward. Hence, the measurement of the diffusion length L_D, which is linked to the diffusion coefficient D and lifetime of the charge carriers τ via $L_D = \sqrt{D\tau}$, is not straightforward.

There is a clear agreement in the literature that ambipolar diffusion is essentially absent at low temperatures in (In,Ga)N due to carrier or exciton localization.[187,188] At higher temperatures, carriers may delocalize, but the compositional fluctuations in the random alloy (In,Ga)N manifest themselves by a strong alloy scattering that reduces carrier mobility and hence diffusivity, if the validity of the Einstein relation is assumed. Note that this relation is strictly valid only in equilibrium and needs also to be viewed with caution in disordered materials such as (In,Ga)N.[189,190] From mobility measurements of transistors containing an (In,Ga)N channel, we expect a clear decrease of the diffusivity for an increasing In content because of the enhanced scattering.[183,191,192]

To circumvent the limitation of the classical Haynes-Shockley experiment, many researchers have employed contactless, purely optical approaches like near-field scanning optical microscopy, cathodoluminescence spectroscopy, electron beam-induced current, time-of-flight measurements, the four-wave mixing method, and the transient grating method.[193–198] For the binary material GaN, it is possible to measure a unique lifetime

due to the decay of excitons. For GaN grown on sapphire, values for the typical diffusion lengths scatter in the range of 60–200 nm, depending on doping concentration and dislocation density.[195,199–207],¶ Thus, already for GaN, it is experimentally extremely difficult to directly observe carrier or exciton diffusion by spatially resolved techniques. Moreover, the strain fields of the threading dislocations[209] cause a long range potential in the band gap and lead to a drift of charge carriers,[210,211] which further complicates the analysis. The values for the diffusivity D of (In,Ga)N seem to scatter between 0–3 cm^2/s depending on the temperature, the excitation condition, and the measurement technique.[193,194,196–198,212–216],‖ In addition, the diffusion coefficient in (In,Ga)N seems to depend on the excitation density as demonstrated in Refs. 198 and 218.

All the above mentioned methods have in common that they may give just an upper limit of the diffusivity due to their limited possibility to spatially resolve and disentangle drift and diffusion processes that presumably occur on a scale of a few of nanometers (cf. calculations in Refs. 58 and 188). In addition, the evaluation of the experiments designed to measure the diffusion length for polar (In,Ga)N/GaN QWs becomes more complex due to the inevitable random compositional fluctuations and the internal piezoelectric fields. The combination of both effects causes a nonexponential decay of individual electrons and holes without a unique lifetime[48,51] and hence without a unique diffusion length as a material parameter. Consequently, one may consult only experiments based on the analysis of the impact of diffusion to obtain parameters for the diffusivity in polar (In,Ga)N. Such an experiment, for which the spatial resolution is no limiting factor, will be presented in Chap. 4.

2.6 Droop and green gap in (In,Ga)N/GaN light emitting diodes

Since the first demonstration of an electrically-driven blue (In,Ga)N/GaN LED with an efficiency of about 0.2 % by Nakamura *et al.*[19] in 1993, industry and research focus on the ultimate goal of achieving extremely efficient devices for solid-state lighting. Mainly due to advantages in growth, the peak external efficiency of blue (In,Ga)N/GaN LEDs was increased up to record-high values of about 85 % already in 2010.[20] Since the early days, however, LEDs exhibit a decrease of their efficiency for large current densities, the so-called *droop*. The origin of this droop is an active topic in LED research.

(In,Ga)N-based LEDs face an additional drawback. Although LEDs containing the ternary alloy (In,Ga)N as their active region are advertised to cover the full visible spectrum, which was also demonstrated experimentally (see, e. g., Ref. 180), the efficiency decreases remarkably towards the green spectral range. This reduction of the efficiency with increasing In content is often referred to as the *green gap*. In Fig. 2.6, the IQE is shown as a function of the current density and the peak wavelength. In this figure, the droop and green gap are highlighted by dashed-dotted and dotted lines, respectively. In contrast to the droop, which seems to constitute a fundamental problem for (In,Ga)N/GaN QWs, the

¶ For high-quality bulk GaN values up to 2 µm have been reported.[208]
‖ Actually, even a singular value of D = 3,000 cm^2/s has been reported.[217]

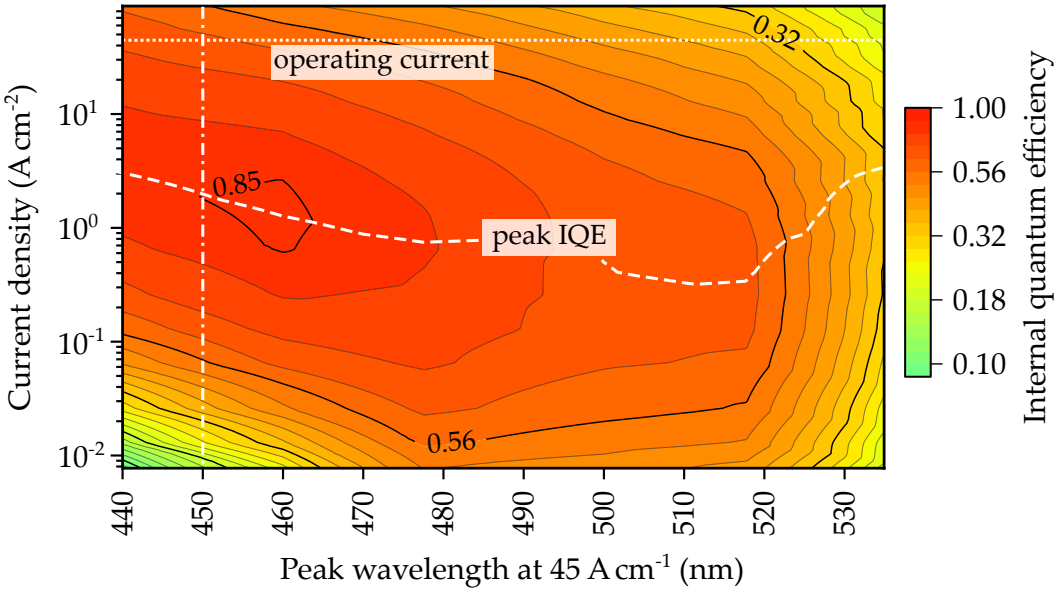

Figure 2.6: Color-coded IQE of LEDs as a function of the peak wavelength and current density. The peak IQE and the operating current are indicated by a dashed and a dotted line, respectively. The dashed-dotted line (at the commonly-used peak wavelength of blue LEDs) highlights the decrease of the IQE for current densities larger than about 2 A/cm^2. The figure was adapted from Ref. 26.

green gap originates at least partly from the fact that the current density at the peak IQE (dashed line) deviates from the operating current for higher In contents (see Fig. 2.6). The senior director of chip research as well as development at OSRAM Opto Semiconductors GmbH, Hahn, attributed the majority of the difference in efficiency of blue and green LED to the very limited industrial research and development efforts and reported recent values of the EQE of about 50 % for green LEDs.[219] The progress in development may be reflected by the fact that very similar nonradiative recombination coefficients have been reported for blue- and green-emitting LEDs recently,[220] while earlier works observe an increase of the nonradiative recombination coefficient for higher In contents.[221] However, Pristovsek *et al.*[222] have reported very recently and in contradiction to the observation in Ref. 220 that the increasing nonradiative rate is an important factor for the green gap even for samples with a low threading dislocation density, i. e., a high crystal perfection. Note that not only (In,Ga)N/GaN QWs exhibit a droop, but also the phosphor material for the photon conversion in white-light-emitting (In,Ga)N/GaN LEDs.[223]

2.6.1 Internal quantum efficiency and ABC model

In order to be independent of the different electrical injection and light extraction efficiencies for devices of different designs, the comparison of the IQEs (instead of EQEs) has been established. However, the extraction of the IQE is experimentally challenging and requests a sound understanding of the recombination processes. Apparently simple

solutions such as the ratio of the integrated PL intensities at low and high temperatures are frequently used in the community, but are to be viewed with caution.[224–229] In fact, as demonstrated by the measurement of the absolute PL intensities at low temperatures using an integrating sphere, the assumption of an IQE of unity at 10 K is not valid in general.[230] Additionally, effects such as photon recycling impede the estimation of the IQE.[231]

More elaborated approaches utilize time-resolved PL spectroscopy,[45,180] differential carrier lifetime measurements,[232,233] or bias-dependent PL spectroscopy[234] to determine the IQE at room temperature. Furthermore, the combination of PL spectroscopy with bolometric or photo-acoustic measurements has been used to determine the IQE by detecting radiative emission and generated heat simultaneously.[235,236] However, the IQE is most commonly deduced from the current-dependent EQE by the so-called *ABC* model introduced by Shen *et al.*[31] for (In,Ga)N/GaN LEDs. A recent review of this model is given in Ref. 237. Summarizing, the model assumes constant SRH (A), radiative (B), and Auger (C) recombination coefficients to relate the IQE (η) with the charge carrier density (n)

$$\eta = \frac{Bn^2}{An + Bn^2 + Cn^3}. \tag{2.30}$$

Note that it is all but trivial to convert the applied current density into a charge carrier density in the QWs because n depends on the carrier capture[238–240] as well as on the lifetime of the charge carriers under steady-state conditions. Moreover, the distribution of the carriers between different QWs in commonly fabricated multi-QW heterostructures is not clear a priori, but requires sophisticated transport simulations and experiments.[241–246]

In the frame of the *ABC* model [Eq. (2.30)], the droop in (In,Ga)N/GaN LEDs is solely attributed to Auger recombination at high charge carrier densities. This interpretation has been met with skepticism (see, e.g., Ref. 247). Compared to narrow band gap III–V semiconductors, direct Auger recombination is insignificant in wide-gap materials such as (In,Ga)N with In contents below 30 %.[248] However, C coefficients extracted from experiments with the *ABC* model are actually by several orders of magnitude larger than expected.[25] In 2009, Delaney *et al.*[37] reported an enhancement of the direct Auger coefficient in the green spectral range, but corrected their result to an about three orders of magnitude lower value seven years later.[249] In order to explain the rather large experimental values of C, indirect Auger processes, mediated by electron-phonon and alloy scattering, were taken into account.[38,250,251]

Recently, Iveland *et al.*[252] reported the direct experimental observation of Auger recombination by electron emission spectroscopy. They suggested that the L-valley population originates from an nnp-Auger process.[253] Additionally, Binder *et al.*[254] reported the direct observation of hot carriers generated by Auger recombination via PL spectroscopy on structures containing alternating green and ultraviolet emitting (In,Ga)N/GaN QWs. However, both experiments have received some criticism. For example, Bertazzi *et al.*[255] suggested to include (thermionic) leakage[256] as well as drift-induced leakage[257] of elec-

trons, which overcome the electron blocking layer, to result in the emission of electrons.** Moreover, free carrier absorption[262] should be considered too. In order to explain the observations made by Binder *et al.*,[254] excitation-induced dephasing, for which the subsequent polarization to population conversion results in a broad distribution of carrier energies, was suggested.[263] However, the observation of hot carriers may be also explained by localization and a subsequent two-step two-photon absorption (TPA) process (see Appendix B).

Temperature-dependent measurements of the droop (see, e. g., Refs. 264–266) indicate a reduction of the Auger coefficient over several orders of magnitude with increasing temperature.[267] This observation is in contrast to the assumed increase of Auger losses with temperature. Therefore, Hader *et al.*[27] propose density-activated defect recombination as the origin of the droop. Other possibilities are a phonon-assisted transport of holes along threading dislocation.[268] Because of the relaxation of stress during the heteroepitaxy, so-called V-pits may form at the end of dislocations (see Ref. 182 and references therein). Hangleiter *et al.*[269] have reported that the transport of charge carriers to the dislocations (acting as nonradiative centers) is efficiently screened by semipolar QWs with low In content at the sidewalls of these V-pits. By adjusting the parameters of the In-containing SPSL in the buffer region, which is grown before the active region, V-pits and the efficiency of the resulting LED can be optimized.[270,271]

All things considered, the prevailing belief that the droop is exclusively caused by Auger recombination seems to be questionable. Moreover, the standard *ABC* model given in Eq. (2.30) is *not* valid over the complete range of current densities, for which it is commonly used. For example, for low current densities, the background carrier concentration n_0 [resulting from unintentional doping; n-type for (In,Ga)N] has to be considered (see also Sec. 2.3).[272] Note that n and p are not equal for low excess carrier densities in the presence of SRH centers [cf. Eq. (2.17)]. Additionally, the background carrier concentration influences both, nonradiative and radiative processes, at low carrier densities. Hence, the standard term for purely bimolecular radiative recombination Bn^2 is actually given by $B(n + n_0)p$ for an n-type material.[272,273] A similar transformation applies to the nnp- and npp-Auger coefficients. Consequently, the total recombination rate for low carrier densities should read

$$\frac{b_n b_p N(n_0 + n)}{b_n(n_0 + n) + b_p p}p + B(n_0 + n)p + C_{\mathrm{nnp}}(n_0 + n)^2 p + C_{\mathrm{npp}}(n_0 + n)p^2. \tag{2.31}$$

Note that A has been replaced by the classical SRH expression given in Eq. (2.16). At moderate to high current densities, B, C_{nnp}, and C_{nnp} are no constants either.[274] David *et al.*[275] have reported that the three "constants" increase quadratically with increasing overlap of electron and hole wave functions and attributed this behavior to a screening of the internal electric fields, which typically occurs for carrier densities larger than

** Actually, the overflow of electrons despite an electron blocking layer has been confirmed experimentally by conductive atomic force microscopy.[258] Moreover, trap-assisted tunneling escape may be important too.[259–261]

$1 \times 10^{19}\,\mathrm{cm}^{-3}$.[276] Note that typical charge carrier densities of high-power (In,Ga)N/GaN LEDs amount to about $5 \times 10^{19}\,\mathrm{cm}^{-3}$. The observed quadratic increase of A, B, and C in Eq. (2.30) with charge carrier density is in agreement with recent theoretical calculations.[277] Moreover, at carrier densities larger than $1 \times 10^{18}\,\mathrm{cm}^{-3}$, degeneracy in the conduction band sets in,[278] and the Fermi-Dirac statistics cannot be approximated by a Boltzmann-like behavior anymore. The so-called phase-space filling causes a decrease of the radiative and the Auger recombination coefficient.[221,233,251,279–281] In general, the assumption of constant coefficients, although in fact the coefficients are not constant at all, may explain the large variation of the reported values.

In all previous considerations, the impact of the diffusion and the localization of charge carriers in the random alloy on the IQE and on the green gap has not been considered, but is in fact significant.[29,30,51] Recently, Auf der Maur *et al.* [29] have calculated that random alloy fluctuations account for a reduction of the IQE by about 0.1 in the green spectral range. Moreover, they speculated that the effect of random alloy fluctuations in nonpolar QWs is considerably reduced due to the absence of the quantum-confined Stark effect. In addition, Shahmohammadi *et al.* [39] suggested that localization and the large internal fields in polar (In,Ga)N/GaN heterostructures enhance Auger recombination.

Summarizing, the standard *ABC* model is neither appropriate to determine the IQE nor to analyze the recombination processes in (In,Ga)N/GaN QWs, because several effects such as the background doping density, the internal electric fields, the band degeneracy, and the localization are neglected altogether.

Chapter 3

Samples, methods, and basic electro-optical characterization

In this chapter, we introduce the employed methods and experimental setups. Additionally, we present a basic characterization of a representative Ga-polar (In,Ga)N/GaN QW heterostructure and an exemplary N-polar GaN nanowire ensemble containing (In,Ga)N QDs by temperature-dependent steady-state PL spectroscopy. Moreover, we investigate the basic electro-optical characteristics of Ga-polar (In,Ga)N/GaN LEDs. The properties of our samples are close to those reported for similar structures in the literature, and we can thus be sure that they constitute representative examples for their classes.

3.1 Growth methods

According to the crystal structure of GaN, (In,Ga)N may principally be grown along polar, semipolar or nonpolar crystal directions. Due to the different binding of the atoms for the various crystallographic planes, the growth kinetics and modus, the incorporation of impurities and defects as well as the homogeneity of the random alloy are different. The main difference for the band profiles between the various crystal orientations is the presence and magnitude of the internal electric fields (see Sec. 2.1), for which the semipolar direction represent the intermediate case between the polar and nonpolar direction. In order to focus our attention on the cases of maximum and minimum internal electric fields, we investigate in this thesis (In,Ga)N/GaN heterostructures grown along the polar and nonpolar direction. Along the polar direction, the different polarities, being either Ga- or N-polar, have to be considered. In principle, the N-polar direction is favorable because of the higher thermal stability of InN along this direction than along the Ga-polar direction. Thus, the incorporation of a higher amount of In and the growth at higher substrate temperatures are possible.[282,283] Both are beneficial to obtain efficient emitters in the green spectral range. Additionally, the direction of the polarization fields along the N-polar growth direction is reversed compared to the Ga-polar direction, which in turn may lead to an improved efficiency of LEDs.[284]

In general, crystalline (In,Ga)N/GaN is fabricated with MOCVD[285] or molecular beam epitaxy (MBE).[286] Both methods have benefits and drawbacks.[287] Technical limitations of the size and the fluence of effusion and plasma cells restrict the scalability of conventional MBE reactors. Additionally, the low growth rates impede a comparable high throughput as in MOCVD. Therefore, MBE growth of (In,Ga)N/GaN structures is mainly used in research. However, in contrast to MOCVD, the employed ultra-high vacuum in MBE (which is technically demanding too) enables the utilization of powerful in-situ characterization tools such as reflection high-energy electron diffraction. Moreover, as MBE does not use metalorganic compounds (i. e., precursors), the incorporation of impurities such as C and especially H is much lower than in to MOCVD. Compared to MOCVD, the growth temperatures for group-III-nitrides are about 300 K lower in MBE.[288] Nowadays, the efficiency of Ga-polar, planar (In,Ga)N/GaN heterostructures grown by MOCVD defines the state-of-the-art in industry and research.[20]

3.2 Categorization of the samples

In this thesis, we investigate the PL properties of the active region of (In,Ga)N/GaN heterostructures. For our main conclusions, we utilize an industry-grade planar, Ga-polar (In,Ga)N/GaN multi-QW sample grown by MOCVD as the standard reference. In addition, we compare the PL properties of possible future (In,Ga)N-based light emitters to the results obtained from the reference. The different samples classes are:

1) planar, Ga-polar (In,Ga)N/GaN QWs grown by MOCVD as our standard reference (similar to the ones investigated in Ref. 289),
2) axial (In,Ga)N QDs in N-polar GaN nanowires grown by MBE (similar to the ones described in Refs. 69 and 290),
3) (In,Ga)N QWs around GaN µ-rods in a core/shell configuration grown by MOCVD (similar to the ones investigated in Ref. 74), and
4) SPSLs with sub-ML InN QSs embedded between GaN barriers grown by MBE (and characterized in Ref. 77).

The potential advantages and further details of these samples will be introduced in the relevant chapters of this thesis. At this point, we only present the working principle of (In,Ga)N/GaN-based solid-state LEDs. A schematic of such an LED is shown in Fig. 3.1. The active region contains (In,Ga)N/GaN QWs, which are commonly 3 nm thick (similar to the exciton Bohr radius in GaN as shown in Sec. 2.3.1) to avoid the separation of charge

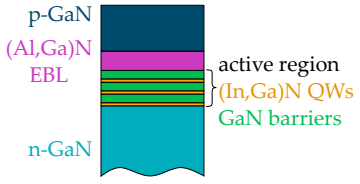

Figure 3.1: Schematic of a GaN-based LED containing a heterostructure of (In,Ga)N QWs and GaN barriers. The active region is separated from the p-doped region by an electron blocking layer (EBL) consisting of (Al,Ga)N.

carriers along the polar crystal direction. In order to increase the active volume, multiple QWs are separated by GaN barriers (with typical thicknesses in the range of 5–20 nm). The complete active region is embedded between p- and n-doped GaN region. In general, p- and n-type doping of group-III-nitrides are realized by the incorporation of Mg (several 10^{19} cm^{-3}) and Si (about 10^{19} cm^{-3}), respectively.[291,292] Recently, the superiority of Ge as a dopant as compared to Si with regard to achievable free carrier concentrations has been demonstrated by Fritze *et al.*[293] Optionally, the Mg-doped cap* may be separated by an about 20-nm-thick, p-doped (Al,Ga)N electron blocking layer (Al content of about 20 %) from the active region to prevent the overflow of electrons.[298–300] For PL spectroscopy, however, the injection (here: excitation) of charge carriers into the active region occurs not electrically but optically. Hence, for a first characterization of new device concepts, doping and contacting are not necessary, which in turn reduces the complexity of the structure under investigation.

3.3 Schrödinger-Poisson calculations

In order to obtain the band profiles of unbiased structures, we have used Snider's[301] one-dimensional Schrödinger-Poisson solver taking polarization charges at the interfaces into account.[302,303] However, this solver is not appropriate to simulate the band structure of biased samples,† for which we have used the free one-dimensional device simulator by Wu.[305] For unbiased structures, the results are identical to the ones obtained with Snider's program. For biased structures, we have obtained band profiles which are in perfect agreement with the commercial device simulator Atlas from Silvaco.[306]

To calculate the transition energies, the overlap of electron and hole wave functions as well as the band structure of our (In,Ga)N/GaN heterostructures with In contents up to 25 %, we employ the following material parameters:

For the effective masses of electrons, heavy holes (hh), and light holes (lh) perpendicular to the c-axis of wurtzite GaN, we utilize $m_e = 0.2\,m_0$, $m_{hh} = 1.6\,m_0$ and $m_{lh} = 0.26\,m_0$, respectively.[112,307] We interpolate the effective electron mass of (In,Ga)N with Vergard's law[308] using $m_e = 0.068\,m_0$ for InN and obtain $m_e = 0.168\,m_0$ for $In_{0.25}Ga_{0.75}N$.‡ Because the data for the effective hole masses of GaN and InN do not differ significantly (see, e. g., Refs. 112, 307, and 309), we avoid the interpolation via Vergard's law and use the value mentioned above for GaN also for (In,Ga)N QWs. The value of the relative permittivity perpendicular to the c-axis of wurtzite GaN is similar to the corresponding one in InN, and we use a value of $\varepsilon = 9.5$ for our calculations.[310,311] Interpolating between the band

*High Mg concentrations are required to obtain a sufficient number density of holes in the p-doped region because of the high thermal activation energy of Mg.[294,295] This fact, in combination with the lower growth temperature, leads to a lower crystal perfection of Mg-doped GaN.[296,297] Consequently, the thin p-doped region is grown as the final layer of the p-i-n structure.

†Biased band diagrams may be calculated with the free device simulator SimWindows[304] from Winston. However, the polarization charges have to be simulated by heavily doped ultrathin layers. Moreover, the calculation of wave functions is not implemented.

‡Note that the conduction band of InN is highly nonparabolic.[307]

gap (E_g) of wurtzite GaN and the one of wurtzite InN (i.e., 0.68 eV[310],§) by using the bowing parameter of Schley *et al.*,[310] we arrive at

$$E_g(x)[\mathrm{eV}] = 3.45(1-x) + 0.68x - 1.72x(1-x). \tag{3.1}$$

for the band gap of the wurtzite $In_xGa_{1-x}N$ alloy. For the band offset ratio, we use a value of 60:40 determined with x-ray photoelectron spectroscopy by Martin *et al.* [313] for the simulation of (In,Ga)N/GaN QWs with up to 25 % of In.¶

Finally, we have to consider the spontaneous (P_{sp}) and piezoelectric (P_{pz}) polarization at the (In,Ga)N/GaN heterointerfaces grown along the polar crystal axis of wurtzite GaN. The calculation of P_{pz} based on material parameters has been shown in Sec. 2.1. However, in our simulations, we employ the commonly used fitted dependence of the polarization on the In content with[90]

$$P_{sp}[\mathrm{C/m^2}] = -0.042x - 0.034(1-x) + 0.037x(1-x). \tag{3.2}$$

Originally the parameters were reported by Fiorentini *et al.* [317] We note that improved values for P_{sp} of group-III nitrides have been reported by Belabbes *et al.* [93] For the sake of consistency we use the values for P_{pz} from Ref. 90:

$$P_{pz}[\mathrm{C/m^2}] = 0.148x - 0.0424x(1-x). \tag{3.3}$$

To account for our experimental data, we multiplied P_{pz} by a factor of about 0.62. Such a reduction of the theoretical values of P_{pz} is frequently used to describe experimental results.[318–322]

3.4 Signal acquisition and processing

The analysis of the recombination processes of charge carriers in semiconductors (i. e., the spectroscopy of the emitting radiation) is commonly based on the energy of the respective transition. However, the optical grating inside the monochromator correlates the measured PL intensity with the wavelength λ of the emitted photons. Thus, we have to convert the photon wavelength into the photon energy E by utilizing a conversion factor of

$$E[\mathrm{eV}] = \frac{hc_0}{\hat{n}_{air}\lambda} = \frac{1{,}239.489}{\lambda[\mathrm{nm}]} \tag{3.4}$$

with the refractive index of air ($\hat{n}_{air}$), Planck's constant (h), and the vacuum speed of light (c_0) (see list of symbols for the respective constants). The value of $\hat{n}_{air}$ amounts to 1.000285 close to the band edge emission of GaN.[127,323] Although $\hat{n}_{air}$ actually depends

§Note that a band gap as low as 0.65 eV has been reported.[312]

¶Note that more recent experimental measurements[314] and theoretical calculations[315,316] tend to a band offset ratio of 80:20.

on λ, the introduced deviation of the conversion factor given in Eq. (3.4) is well below our experimental resolution even for λ = 1,000 nm. Thus, we employ one and the same conversion factor, namely 1,239.489, throughout the whole spectral range investigated in this thesis.

3.4.1 Steady-state photo- and electroluminescence spectroscopy

For steady-state PL and EL spectroscopy, we have utilized the three different setups listed below. Their general working principle is schematically depicted in Fig. 3.2(a).

i) We have used a Horiba Jobin Yvon Labram HR 800 UV setup for steady-state µ-PL spectroscopy. For PL experiments with nonresonant excitation, the 325-nm line (3.814 eV) of a Kimmon IK 3552R-G HeCd laser with a maximum power of 30 mW was used. For excitation of the (In,Ga)N/GaN QWs, we have employed an Ondax LM-402-PLR-180 multi-mode (In,Ga)N/GaN diode laser emitting at 402 nm (3.08 eV) with a maximum power of 180 mW. The PL signal was dispersed by a monochromator with a focal length of 80 cm, which is equipped with a 600-lines/mm grating. The spectrally dispersed signal was recorded with a liquid-nitrogen-cooled ISA SPECTRUM ONE charge-coupled device camera with 1024 × 256 pixels. The spectral resolution amounts to at least 1 meV in the ultraviolet (UV) to visible range. In order to obtain a spatial resolution in the range of at least one µm, the setup is equipped with a 50× Mitutoyo Plan Apo NUV HR microscope objective with an numerical aperture of 0.65.

ii) We have employed a Horiba Jobin Yvon Labram HR Evolution setup with a micro-positioning system for µ-EL mappings. For current injection into the investigated LEDs, a Manson HCS 3302 power supply was used. We have obtained a high spatial resolution of 0.25 µm by utilizing a 100× Mitutoyo Plan Apo NIR HR objective with a numerical aperture of 0.7. In order to record corresponding steady-state µ-PL maps, we have excited the (In,Ga)N/GaN QWs with an Ondax LM-405-PLR-40 single-mode (In,Ga)N/GaN diode laser emitting at 405 nm (3.06 eV) with a maximum power of 40 mW. The detection system is similar to the one of the HR 800 setup (also the same spectral resolution), except for the charge-coupled device camera, which is a liquid-nitrogen-cooled Horiba Symphony II charge-coupled device camera with 1024 × 256 pixels.

iii) We have utilized a home-built steady-state PL setup to simultaneously excite the samples under investigation with two lasers with different photon energies. Therefore, we have employed a Coherent Innova 400-K3 Kr^+-ion laser using the 413.1-nm line (3.000 eV) with a maximum output power of 1.8 W as the main excitation source. Additionally, we have coupled a DL640-070-S diode laser from CrystaLaser emitting at 642 nm (1.93 eV) with a maximum power of 70 mW or a diode-pumped Nd:YAG solid-state laser emitting at 1,064 nm (1.165 eV) with a maximum power of 40 mW via a 10:90 beamsplitter into the optical path. Using one stage of the TriVista triple

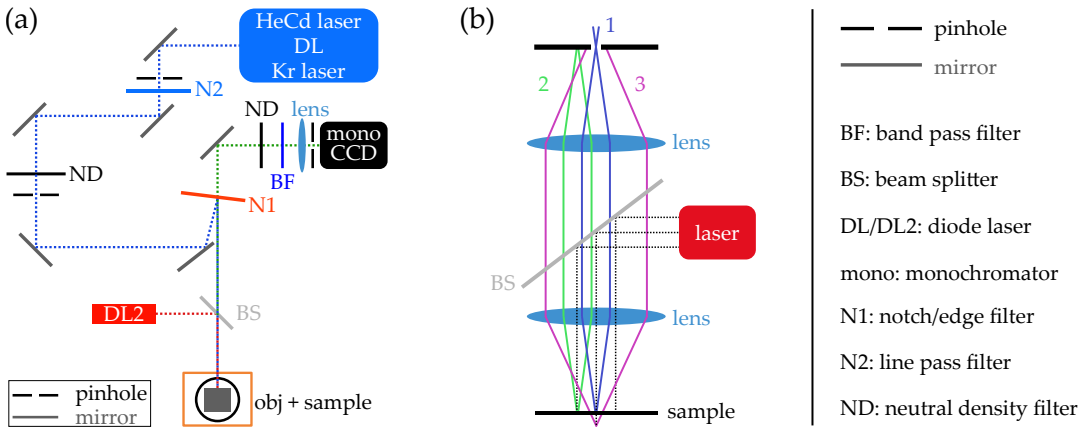

Figure 3.2: (a) Schematic (top view) of the confocal steady-state PL setup equipped with a charge-coupled device (CCD) camera and a microscope objective (obj) to obtain a spatial resolution at least one µm. (b) Working principle (side view) of a confocal microscope. The detailed description of the figures is given in the text.

spectrometer from Princeton Instruments in conjunction with a Horiba Symphony II charge-coupled device camera, the setup exhibits a spectral resolution on the order of 1 meV for the used spectral range. Again, we have utilized the 50× Mitutoyo Plan Apo NUV HR objective.

For the temperature-dependent PL measurements, the samples were mounted on a copper cold finger of a He-flow cryostat from CryoVac. Using a resistive heater and a temperature controller (CryoVac ITC 304), the temperature can be adjusted between 4 and 300 K. The cryostat is evacuated with a Balzers turbo molecular pump to a pressure of approximately 3×10^{-6} mbar.

In order to suppress plasma lines of the Kr^+-ion laser or direct laser radiation of the additional diode laser, a line pass or a band pass filter are used, respectively [see Fig. 3.2(a)]. The excitation power density as well as the intensity of the detected signal can by attenuated by standard neutral density filters.

All our detection systems are controlled by the LabSpec software, which automatically performs a stitching process for spectra recorded over a large spectral range (e. g. from 3.54 eV to 1.90 eV), for which the grating of the monochromator has to rotate. To correct the measured spectra for the spectral response of the system, we have calibrated the system with a Bentham CL2 light source.

Confocal arrangement and spatial resolution

In order to obtain a confocal arrangement [schematically depicted in Fig. 3.2(b)], the light of the main excitation laser is coupled into the optical path via an edge or notch filter for the respective laser line [see Fig. 3.2(a)] or a beamsplitter. The spectral resolution increases when reducing the aperture of the pinhole in front of the monochromator (ideal case: point source). Moreover, the pinhole allows the transmission of the light originating

from a small volume (beam 1) only, while other parts (beams 2 and 3) are blocked [see Fig. 3.2(b)]. Hence, the minimal lateral resolution as well as the axial resolution are reduced by a factor of about 0.7 compared to a conventional microscope for a completely closed pinhole.[324]

In Fig. 3.3(a), we present the experimental results of determining the actual spatial resolution of the LABRAM EVOLUTION setup with the knife edge method. For this purpose, we have scanned across the edge of a razor blade with the microscope objective with an appropriate size of the pinhole, i. e., balanced between resolution and intensity of the single, for different step sizes. The resulting intensity profile has been fitted with a sigmoidal function as explained in Ref. 325. We have obtained a lateral resolution of about 0.25 µm, which is close to the maximum expected resolution.

Automated map analysis

Acquiring µ-EL and µ-PL maps over an area of $20 \times 20\,\mu m^2$ with a step size of 0.25 µm produces more than 6,500 individual spectra per map. Thus, we have utilized an automated analysis procedure, exemplarily shown for two spectra in Fig. 3.3(b). During this procedure, we have applied a fast Fourier transform low-pass filtering to the spectra to remove interference fringes. The commonly observed asymmetry of the band impedes a simply Gaussian fit. Hence, we have extracted the peak energy at the maximum intensity of the band. To extract the full width at half maximum (FWHM) of the band, we have divided the peak intensity by a factor of two and have extracted the corresponding photon energies. The smaller absolute difference of these values to the peak energy was multiplied by a factor two and was used as the FWHM.

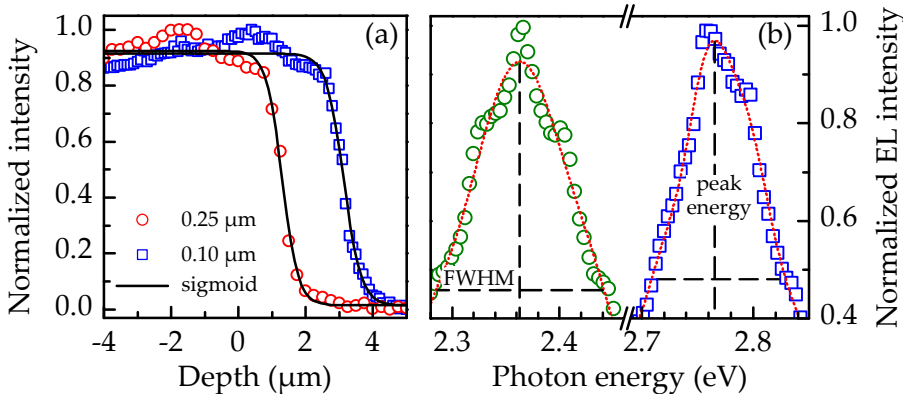

Figure 3.3: (a) Edge of a razor blade scanned with an objective with a magnification of 100× and a numerical aperture of 0.7. The intensity of the reflected light (symbols) is normalized for the two different step sizes. A fixed value of the confocal hole was used. The spatial resolution was extracted by a fit of the data (solid line) with a sigmoid function as described in the text. (b) Exemplary µ-EL spectra from a map of a blue- and green-emitting LED (symbols) with automated fast Fourier transform filtering (dotted lines) and analysis of peak energy and FWHM (dashed lines).

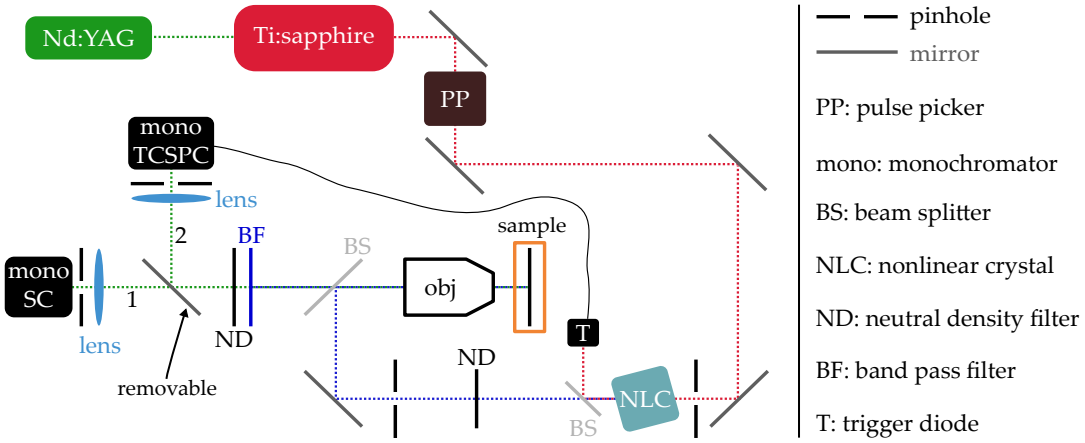

Figure 3.4: Schematic (top view) of the time-resolved PL setup as described in the text to acquire spectrally resolved PL transients either with the streak camera (SC) or with time-correlated single photon counting (TCSPC). The setup is equipped with a microscope objective (obj) to obtain a spatial resolution on the order of µm.

3.4.2 Time-resolved photoluminescence spectroscopy

A schematic of the home-built time-resolved PL setup is shown in Fig. 3.4. The ultra-short laser pulses (200 fs) are produced by a Coherent Mira 900 Ti:Sapphire femtosecond oscillator (emission: 700–980 nm). This Kerr-lens passively mode-locked oscillator is optically pumped by a Coherent Verdi V10 Nd:YAG diode-pumped solid-state laser emitting at 532 nm with 10 W. To reduce the repetition rate of the fs-pulses of about 76 MHz (measured with a HAMEG HM8123 programmable counter), we have used a Coherent 9200 pulse picker. The second harmonic of the laser radiation is generated by a β-Bariumborat nonlinear crystal.

The ThorLabs 20× LMU-NUV microscope objective with a numerical aperture of 0.4 is mounted on a x-y-z translation stage Owis Limes. The laser spot can be scanned with µm-precision over the sample and exhibits a diameter of about 5 µm. The sample itself is mounted on the copper cold finger of a liquid-He flow cryostat from Oxford whose temperature is controlled by an Oxford ITC 503s. The pressure of about 5×10^{-7} mbar inside the cryostat is obtained with an Oerlikon Leybold Vacuum PT70. PL transients can be recorded in two different ways by utilizing a removable mirror (see Fig. 3.4):

1) The PL signal is dispersed by a Jobin Yvon Spex 1681 0.22 m spectrometer and detected by a Hamamatsu C5680 streak camera equipped with a slow single sweep unit (Hamamatsu M5677) and an ORCA-R^2 digital charge-coupled device camera (C10600). We have used a Hamamatsu C4792 trigger unit to adjust the time delay.

2) The PL signal is dispersed by a Horiba iHR 320 monochromator. We have used a PicoHarp 300 system in conjunction with a Hamamatsu photomultiplier tube for time-correlated single photon counting. The trigger signal for the counting process is obtained by a PicoHarp TDA 200 photodiode placed after the nonlinear crystal.

More details about the technical aspects of a streak camera or time-correlated single photon counting can be found in Refs. 326 and 327, respectively.

In order to obtain high signal-to-noise ratios and because the (In,Ga)N-related PL bands are rather broad, we have used spectral resolutions of 5 and 20 meV for measurements with the streak camera and time-correlated single photon counting, respectively. While the temporal resolution of the slow sweep unit of the streak camera amounts to 150 ps, we have obtained a temporal resolution of about 45 ps (500 ps) with time-correlated single photon counting for transients recorded up to 1 µs (33 µs).

3.5 Basic electro-optical characterization

In this section, we present a basic temperature-dependent steady-state PL characterization of (In,Ga)N/GaN QWs and QDs as well as a basic EL characterization of (In,Ga)N/GaN LEDs with various emission colors.

3.5.1 Temperature-dependent photoluminescence spectroscopy

The investigated planar Ga-polar (In,Ga)N/GaN QW heterostructure (reference sample) was grown by MOCVD on a Si(111) substrate. In contrast, the N-polar (In,Ga)N QDs were embedded in GaN nanowires grown by MBE on a Si(111) substrate. Both, the planar sample and the nanowires, contain active regions consisting of five and four about 3-nm-thick (In,Ga)N/GaN QWs and QDs, respectively. The undoped GaN barriers have thicknesses larger than 7 nm, and the In content in the QWs amounts to approximately 15 %, while it is on the order of 25 % for the QDs. The nanowires exhibit a length of about 1 µm, a mean diameter of 80 nm, and a surface coverage of about 50 %. Side- and top-view scanning electron micrographs of the nanowire ensemble are shown in Figs. 3.5(a) and 3.5(b), respectively. By performing x-ray diffraction and transmission electron microscopy on these types of nanowire samples, it was demonstrated that the (In,Ga)N/GaN interfaces are coherent and exhibit no misfit dislocations.[69] The density of threading dislocations is in the 10^8 cm^{-2} range for the planar sample (confirmed by

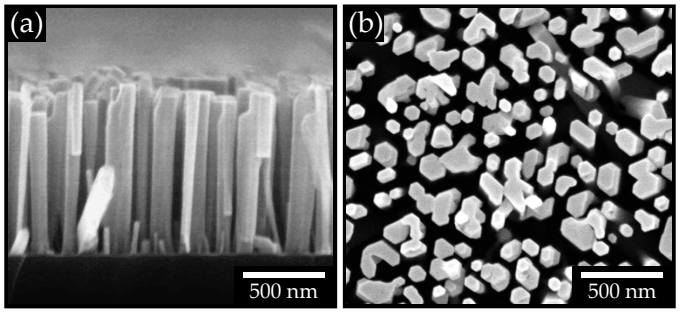

Figure 3.5: (a) Side-view and (b) top-view scanning electron micrographs of unintentionally doped GaN nanowires with (In,Ga)N QDs. The micrographs were recorded by A.-K. Bluhm.

atomic-force microscopy) and is basically zero within the top part (containing the QDs) of the nanowire ensemble. Additionally, we observe that the nanowires exhibit a hexagonal shape and are not significantly tilted, but partly coalesced.

In Figs. 3.6(a) and 3.6(b), we present temperature-dependent steady-state PL spectra of the QWs and the nanowire LED, respectively. As the temperature increases from 10 to 300 K, the PL intensity quenches by about a factor of three for both samples, indicating the presence of nonradiative recombination. We observe an intense emission from the (In,Ga)N/GaN QWs centered at about 2.79 eV [see Fig. 3.6(a)]. At low temperatures, the longitudinal optical phonon replica, separated by about 92 meV[328,329] from the main band in GaN, can be identified, while the modulation due to interference effects impede the analysis at elevated temperatures. By exciting the complete heterostructure of the nanowire LED, we detect a broad (In,Ga)N-related PL band centered at about 2.35 eV [see Fig. 3.6(b)]. The observed individual spikes at low temperatures and at low excitation densities are related to individual localized states in the QDs.[43]

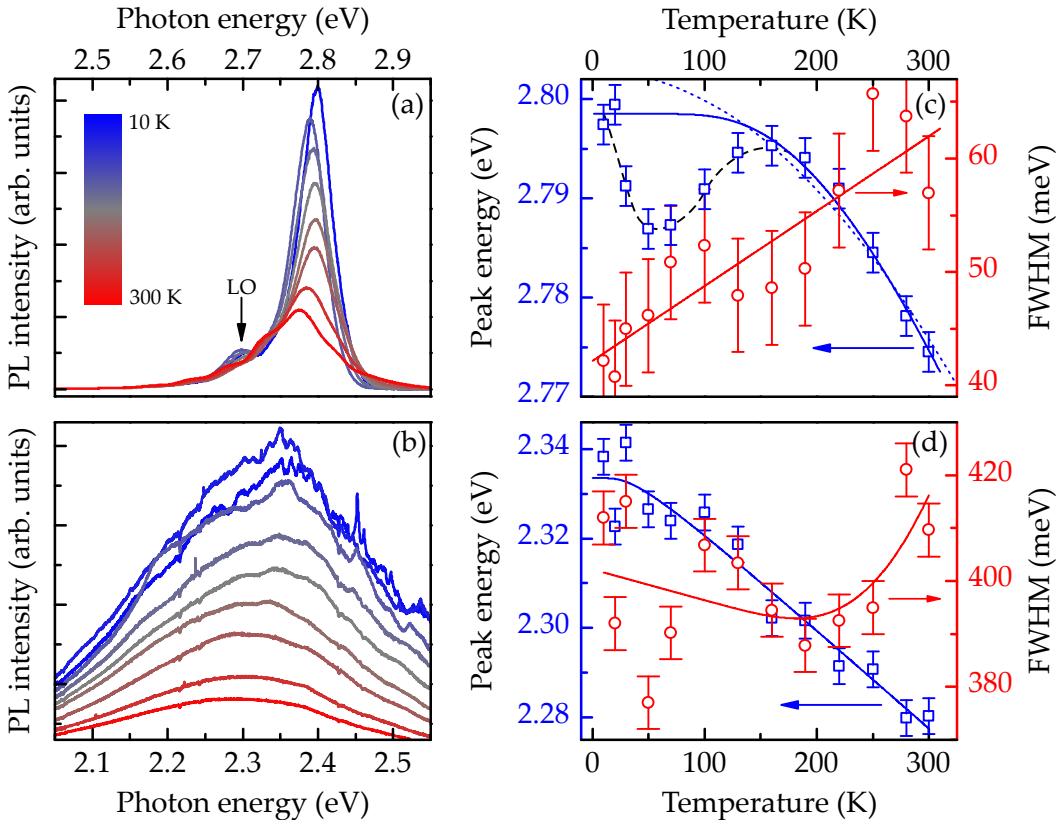

Figure 3.6: Temperature-dependent steady-state PL spectra of (a) (In,Ga)N/GaN QWs and (b) (In,Ga)N/GaN QDs excited with E_{laser} = 3.08 eV. The longitudinal optical phonon (LO) in (a) is indicated by the arrow. The respective analysis of the temperature-dependent peak energy and FWHM is shown in (c) and (d). The dotted and solid lines in (c) and (d) represent fits of the peak energy and the FWHM as described in the text. The dashed line in (c) is a guide to the eye and highlights the S-shape dependence of the peak energy.

In the following, we analyze the shift of the peak energy and the evolution of the FWHM of the (In,Ga)N-related PL band with increasing temperature. We extract both parameters by a fit of the emission band of the QWs and QDs with a Gaussian function.

With increasing temperature, the peak energy of the PL band of the QWs, shown in Fig. 3.6(c), exhibits the so-called S-shape, frequently observed for (In,Ga)N (see also Sec. 2.4.1).[46,53,170] However, the S-shape of $E_{\mathrm{PL}}(T)$ is absent for the QDs in the nanowires [see Fig. 3.6(d)]. In order to reproduce the temperature dependence of the peak energy of the PL band, we have employed the model of Korona *et al.* [175] (solid line) and Pässler [176] (dotted line). In the case of the nanowires, both fits overlap perfectly and result in similar phonon temperatures of about 100 K. In contrast, the temperature dependence of the peak energy for the planar QWs is only partially reproduced by both models. As outlined in Sec. 2.4.1, the modeling of the temperature-dependent peak energy of (In,Ga)N is, in fact, even more complex than for GaN, and an extraction of the localization energy is rather questionable.[170] Consequently, the temperature dependence of the peak energy is not a reliable fingerprint for a comparison of different types of (In,Ga)N-containing samples.

We show the extracted FWHM of the (In,Ga)N-related PL band for (In,Ga)N QWs and QDs in Figs. 3.6(c) and 3.6(d), respectively. The FWHM increases monotonically from 40 meV at 10 K to 60 meV at 300 K for the sample containing QWs. In contrast, the FWHM of the QDs is much larger (about 400 meV at 10 K) and almost constant up to 300 K [see Fig. 3.6(d)]. Taking into account the zero temperature broadening parameter, the coupling strength of exciton-acoustic-phonon interaction, and the exciton-LO-phonon interaction, the temperature dependence of the linewidth of semiconductors in general[330,331] and of GaN[175] in particular can be reproduced. However, for a ternary alloy such as (In,Ga)N, the total broadening is dominated by alloy disorder (see, e. g., Ref. 332) and in the case of the nanowires by QD-to-QD as well as ensemble fluctuations.[333] Although the model of Korona *et al.* [175] reproduces the data well [see Figs. 3.6(c) and 3.6(d)], the parameters may be misleading, because effects of alloy disorder and localization are not included. As a rule of thumb, values for the FWHM of about 50 meV for conventional blue emitting (In,Ga)N/GaN heterostructures at room temperature reflect a low compositional fluctuations of the In content.

3.5.2 Current-dependent electroluminescence spectroscopy

For µ-EL measurements, custom-made research and development (In,Ga)N-based LEDs emitting in the blue and green spectral range were fabricated at OSRAM Opto Semiconductors GmbH using the UX:3 technique. More details about the growth by MOCVD and the processing, utilizing a thin-film flip-chip technique,[334] can be found in Refs. 181, 335, and 336. The usual processing steps generate a rough surface, which is beneficial for light extraction. In the present thesis, the surface of the investigated LEDs was polished to avoid scattering and to obtain a high spatial resolution in µ-EL experiments. We have mounted the LEDs with a conductive epoxy (EPO-TEK® H20E) on a Cu-supported 8-pin chip carrier (for thermal management) and contacted the individual LED chips with 12.5-µm-thick Au wires as shown in the photograph in Fig. 3.7(a). According to OSRAM Opto

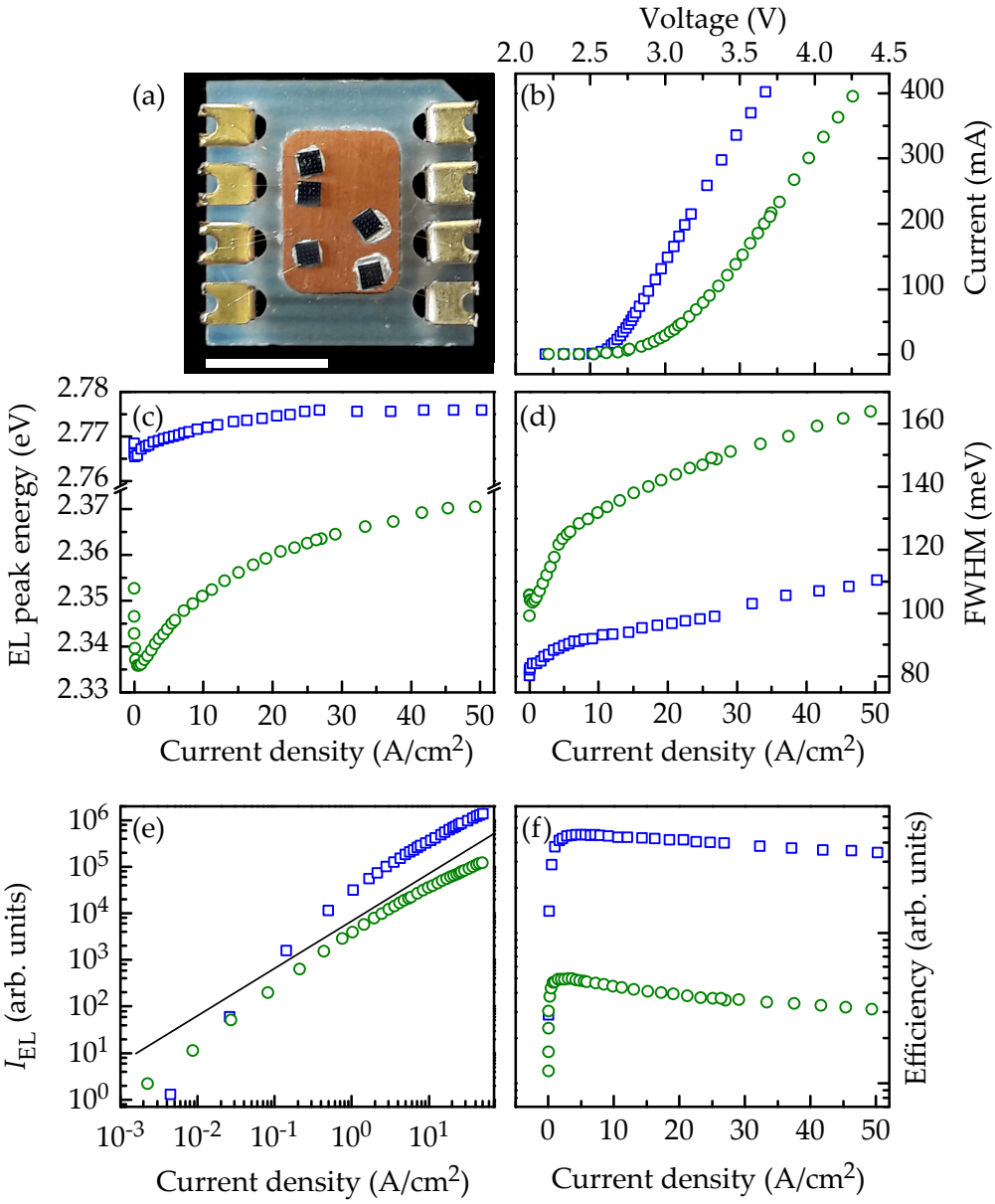

Figure 3.7: (a) Photograph of electrically connected (In,Ga)N/GaN LED chips on a Cu-supported chip mount. The scale bar is 5 mm. (b) Current-voltage diagram as well as current-dependent (c) peak energy, (d) FWHM, (e) integrated EL intensity (I_{EL}), and (f) efficiency of (In,Ga)N/GaN LEDs, emitting in the blue (squares) and the green (circles) spectral range. The solid line in the double-logarithmic representation in (e) exhibits a slope of one. All measurements have been performed at room temperature.

Semiconductors, the current density under normal operation conditions for these LEDs amounts to 45 A/cm^2.

Figure 3.7(b) shows *I*-*V* curves of the LEDs, which indicate a turn-on at about 2.6 V for the blue and 3.0 V for the green LED. The slightly larger threshold for the green LED does not only arise from the larger number of QWs, but is also due to our suboptimal

contacting process. The dark current is generally low and amounts to only 350 nA at −20 V (not shown). We have summarized the EL properties of the blue and the green emitting LED in Figs. 3.7(c)–3.7(f). The peak energy of the EL band blueshifts slightly (10 meV) with increasing current density in the blue LED. In contrast, the peak energy first decreases by 20 meV and then increases monotonically by 35 meV above a current density of 0.125 A/cm^2 in the green LED [see Fig. 3.7(c)]. This behavior may be explained by the competition between an increasing internal electric field with increasing forward bias in Ga-polar LEDs and the screening of the electric fields induced by the charge carriers. In agreement with this explanation, the effect is less pronounced in the blue LED due to the lower In content, which in turn reduces the internal electric fields. Nonetheless, even for the green LED, the spectral position is stable within 5 nm in the investigated current range. Typical for (In,Ga)N-based light emitters, the FWHM is rather large [around 100 meV in the blue and 150 meV in the green spectral range as shown in Fig. 3.7(d)] and increases even further with increasing current density. We ascribe this increase mainly to band filling caused by the increasing density of charge carriers.

We present the integrated EL intensity (I_{EL}) as a function of the current density in a double-logarithmic representation in Fig. 3.7(e). As indicated by the solid line, the values of I_{EL} increase superlinearly up to a current density of 2 A/cm^2 for both LEDs. For higher current densities, the increase of I_{EL} is almost linear in the blue LED, but slightly sublinear in the green one. Dividing the measured values of I_{EL} by the applied current density, we obtain the (external) efficiency of the LED as a function of the current density as presented in the semilogarithmic representation in Fig. 3.7(f). We attribute the initial steep rise of the efficiency (corresponding to the superlinear increase of I_{EL} at low current densities) to the saturation of nonradiative SRH recombination (see, e. g., Ref. 142, 337 and Sec. 2.3.3). At standard operating conditions, the efficiency is about 20 % and 35 % lower than the maximum efficiency for the blue and the green LED, respectively. To date, this decrease of the efficiency is inherent to (In,Ga)N/GaN LEDs and referred to as *droop*.[289,338–340] The impact of different effects, such as electron leakage,[256] Auger recombination[31] or localization,[29] on this efficiency decrease is still under discussion (see also Sec. 2.6). Since we have measured I_{EL} in arbitrary units, the evaluation of the data presented in Fig. 3.7(f) with the commonly used *ABC* model[31] does not result in meaningful parameters.

3.6 Summary

In this chapter, we have introduced the growth methods and samples, the parameters for the Schrödinger-Poisson simulation as well as the employed setups for the analysis of PL and EL spectra. In addition, we have categorized the different classes of samples investigated in this thesis.

General statements about localization or the actual performance of (In,Ga)N/GaN heterostructures, deduced from temperature-dependent steady-state PL spectroscopy, have to be viewed with caution. Nonetheless, the presented temperature dependence of the PL properties for planar and nanowire sample are representative for their respective

class (cf. Refs. 229 and 338). Moreover, the investigated custom-made (In,Ga)N/GaN LEDs exhibit EL properties very similar to those found in commercial LEDs (cf. Ref. 181). Thus, we believe that the conclusions drawn in the subsequent chapters are not only valid for these samples, but reflect the general characteristics of (In,Ga)N/GaN heterostructures.

Chapter 4

Tunneling recombination of charge carriers in polar (In,Ga)N/GaN

We investigate the eligibility of N-polar (In,Ga)N/GaN nanowires for future light emitters by comparing the radiative and nonradiative recombination processes to a Ga-polar planar (In,Ga)N/GaN heterostructure. Utilizing steady-state PL spectroscopy, we observe the discrepancy between the apparently high IQE and low EQE also reported in the literature. Time-resolved analysis of the PL decay reveals transients that are nonexponential and independent of temperature. Moreover, the transients approach a power law, reflecting the fact that recombination occurs between individual electrons and holes with different spatial separation. To simulate and reproduce the transients, we set up a system of stochastic integro-differential equations taking into account both radiative and nonradiative tunneling recombination of spatially separate electrons and holes as well as their diffusion. Employing a Monte Carlo method, we solve these equations to theoretically investigate the influence of the recombination parameters on the power law decay. Additionally, the reproduction of the experimentally obtained transients allows us to draw the conclusions that the power law is preserved even despite dominant nonradiative recombination, that the diffusivity is low in polar (In,Ga)N/GaN QWs, and that the investigated nanowires suffer from a very high nonradiative recombination rate instead of a high density of nonradiative centers. Parts of this chapter have been published in Ref. 51.

4.1 N-polar nanowires versus Ga-polar layers

The majority of today's consumer products using high-brightness LEDs (e. g. automotive headlights or smartphone flashlights) is based on (In,Ga)N/GaN heterostructures grown along the polar direction because substrates facilitating the growth along the nonpolar directions are expensive and not suitable for mass production. Despite the fact that (In,Ga)N/GaN LEDs have a high market penetration and the Nobel prize has been awarded in 2014 to Isamu Akasaki, Hiroshi Amano, and Shuji Nakamura "for the invention of efficient blue light-emitting diodes which has enabled bright and energy-saving white light sources",[21] the recombination dynamics in (In,Ga)N/GaN are not entirely understood to date. At low charge carrier densities (below the Mott-transition[278]), excitons should form in (In,Ga)N/GaN because of the large exciton binding energy (see

Sec. 2.3.1). In conjunction with the compositional fluctuations of the alloy, the localization of excitons is believed to enable the high IQE in (In,Ga)N/GaN.[45,47,52–56] However, the resulting nonexponential PL transients cannot be fitted by a stretched exponential (see, e. g., Ref. 49 and references therein). Thus, the assumption of an excitonic PL decay is questionable.

Starting from scratch with physically motivated rate-equations, we will investigate in this chapter the recombination dynamics of charge carriers in (In,Ga)N/GaN heterostructures grown along the technologically important polar direction. Especially, we will focus on heterostructures for devices for future white light emission.

The active region in devices for solid-state lighting,[20,341] display technologies,[342] and diode lasers[343] is formed by QWs consisting of the ternary alloy (In,Ga)N embedded in GaN and commonly grown along the polar crystal direction. A record-high EQE of about 84 % for a blue (In,Ga)N-based LED has been achieved already in 2010.[20] However, the realization of phosphor-free white LEDs with both, a high luminous efficiency and a high color rendering index, requires the use of efficient narrow-band emitters not only in the blue, but also in the green and red spectral ranges.[344,345] For this reason, the U.S. Department of Energy has released a research and development plan that, amongst others, prioritizes the development of efficient green-emitter materials[346] to overcome the so-called green gap, which denotes the drastic reduction of the luminous efficiency of (In,Ga)N- as well as (Al,In,Ga)P-based LEDs in the green spectral range.[347,348] For both materials, this phenomenon is caused by a steep decline of the IQE for wavelengths approaching the green spectral range (see also Sec. 2.6). In (In,Ga)N-based LEDs, the potential reasons for this decline with increasing In content are manifold and include a possible deterioration of the crystal quality resulting in an increase of defect-assisted nonradiative processes[32–35] as well as a reduced radiative rate due to an increasing magnitude of the polarization fields,[36] an increase of the Auger recombination coefficient,[37,38] and localization phenomena.[29]

Since the two first issues are directly related to the increasing magnitude of strain in the (In,Ga)N layer, axial (In,Ga)N/GaN$(000\bar{1})$ nanowire heterostructures are considered as a promising alternative to planar structures for long-wavelength emission.[227] In MBE, N-polar GaN nanowires spontaneously form[349] on various technologically attractive substrates such as Si, see Ref. 350 and references therein, or metal foils[351,352] while retaining their single-crystal nature. Using MBE, (In,Ga)N QD can subsequently be synthesized on the GaN nanowires. The growth of such heterostructures has been extensively studied and optimized in recent years (see Ref. 353 and references therein). In sufficiently thin nanowires, the lattice mismatch between the (In,Ga)N QD and GaN is partly accommodated elastically due to strain relaxation at the nanowire sidewalls, see Refs. 70–72. This strain relief facilitates the incorporation of high In contents without the formation of extended defects, reduces the driving force to generate point defects, and decreases the magnitude of the polarization field in the (In,Ga)N QD embedded within the nanowire. Moreover, nanowires naturally exhibit a much higher extraction efficiency compared to planar samples, see Ref. 73 and references therein. Indeed, several groups

have reported nanowire LEDs on Si emitting in the green and even red spectral range with IQEs of up to 50 %.[225–229] At the same time, the EQE of these devices has thus far remained significantly lower than that of conventional planar LEDs at comparable wavelengths. For example, yellow LEDs were reported in Ref. 354 with values for the IQE and the EQE of 40 % and 0.014 %, respectively. It is crucial to elucidate the origin of this blatant discrepancy for a realistic assessment of the potential of axial nanowire heterostructures for efficient full-color emitters.

For comparison, we use the planar (In,Ga)N/GaN(0001) QW structure with an In content of about 0.15 which was grown by MOCVD on a Si(111) substrate as a reference sample and whose basic steady-state PL was characterized in Sec. 3.5.1. The sample was fabricated in an LED production reactor and has an IQE close to the state of the art for blue emitting LEDs in 2012.[289] The axial (In,Ga)N/GaN(000$\bar{1}$) nanowire heterostructure we have chosen for this study is representative for this type of samples and was grown by MBE on a Si(111) substrate. The nanowires exhibit a length of about 500 nm and a mean diameter of 50 nm [see Figs. 3.5(a) and 3.5(b)]. The In content in the QDs was determined by x-ray diffraction[355,356] to amount to 0.26 ± 0.1. The sample was selected by virtue of its comparatively high luminous efficiency and the fact that is has been very thoroughly investigated by both structural and spectroscopic techniques.[43]

Both samples contain similar active regions, consisting of five (six) 3-nm-thick (In,Ga)N QWs (QDs) separated by undoped GaN barriers with thicknesses larger than 7 nm for the planar (nanowire) structure. The nanowire ensemble has a surface coverage of around 50 %. Hence, the active volume of both samples differs by less than a factor of two.

In contrast to planar (In,Ga)N/GaN QWs that reach their maximum performance in the blue spectral range,[289] axial insertions in nanowires show a higher luminous efficiency in the green because of a complex interplay of surface potentials and polarization fields.[165] We have selected the two samples used in this study accordingly: Both belong to the brightest emitters for their class. The two samples were measured side by side, and the PL signal was corrected for the spectral response of the detection system to obtain a meaningful comparison. The measured PL intensity also depends on the absorbance of the structure at the wavelength of the laser used for excitation as well as on the efficiency with which the internally emitted radiation is extracted. Owing to light scattering and diffraction, both of these quantities are enhanced for nanowires, particularly the extraction efficiency.[73,357] For simplicity, however, we assume henceforth that light absorption and extraction are comparable for the two samples under investigation. Thus, when comparing external luminous efficiencies, we are overestimating the IQE of the nanowire sample.

4.2 Basic steady-state photoluminescence characterization

To compare the basic PL characteristics of the N-polar (In,Ga)N QDs in the nanowires and of the Ga-polar planar reference sample, we have performed temperature-dependent steady-state PL spectroscopy of the samples utilizing a diode laser (E_{laser} = 3.083 eV)

with excitation power densities ranging from W/cm^2 to MW/cm^2. The samples were measured side-by-side. We also conducted experiments with nonresonant excitation (E_{laser} = 3.814 eV) and obtained essentially identical results (not shown). More details about the excitation and collection of the PL signal and the experimental setups can be found in Sec. 3.4.

Figure 4.1(a) shows exemplary steady-state PL spectra of the planar and the nanowire sample on a semilogarithmic scale (see also Sec. 3.5.1). The most obvious and striking difference between the two samples is the PL intensity, which is two orders of magnitude higher for the planar sample at both low (10 K) and high (300 K) temperatures. The low-temperature PL band of the QWs of the planar sample peaks at 2.795 eV with a FWHM of 70 meV. Compared to the binary compound GaN, the PL band is broad reflecting the inherent alloy disorder in the ternary compound (In,Ga)N.[358] The band redshifts with increasing temperature by about 20 meV, which is about 45 meV less than compared to the temperature-induced shift of the transition energy of the free exciton in GaN,[359] broadens to 130 meV, and decreases in intensity. The broad luminescence band at 2.2 eV is caused by yellow luminescence in the GaN buffer layer, as is commonly observed in

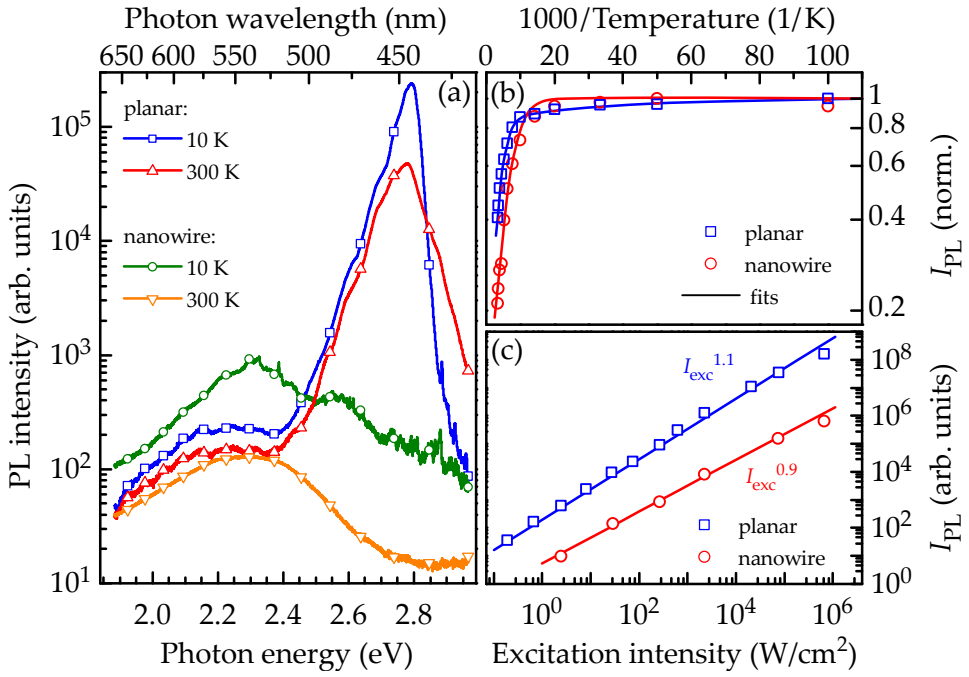

Figure 4.1: (a) steady-state PL spectra of the planar and the nanowire sample excited with an intensity of approximately 50 W/cm^2 at a temperature of 10 and 300 K in a semilogarithmic representation. (b) Semilogarithmic normalized Arrhenius representation of the integrated PL intensity I_{PL} (symbols) measured with an excitation power density of approximately 100 W/cm^2. Solid lines show fits to the data as discussed in the text. The extracted activation energies amount to 48 and 34 meV for the planar and the nanowire sample, respectively. (c) I_{PL} versus the excitation intensity I_{exc} acquired at 300 K in a double-logarithmic. The solid lines indicate fits whose slopes correspond to the given exponents of I_{exc}.

MOCVD-grown GaN.[127] The dominant, broad PL band of the MBE-grown (In,Ga)N QDs in the GaN nanowires peaks at 2.32 eV and exhibits a FWHM of 300 meV at 10 K. This large linewidth is not only caused by alloy disorder, but also by variations in the In content and the QD width between the individual nanowires.[333] Because of the small number of nanowires probed in these steady-state PL experiments with a µm-sized excitation spot, we observe individual spikes at low temperatures and low excitation densities due to localized states, particularly on the high-energy side of the spectrum. For even lower excitation densities, these spikes can dominate the spectrum entirely as was found in a previous study of the same sample.[43] With increasing temperature, the band redshifts by 30 meV and decreases in intensity with a factor similar to the one of the planar reference sample.

The temperature-induced decrease in intensity observed for both samples reflects the presence of nonradiative recombination channels at elevated temperatures. In fact, analyzing the temperature-dependent PL intensity is a frequently employed method to study the impact of nonradiative recombination in semiconductors. Nonradiative recombination is often assumed to be thermally activated and to be negligible at low temperatures.[66] The latter assumption is not based on any sound physical arguments, but if we accept it for the moment, a quenching of the PL intensity at elevated temperatures is directly related to the IQE of the investigated sample. In Fig. 4.1(b), we show the temperature-dependent evolution of the normalized integrated PL intensity I_{PL} of the planar and the nanowire sample. For both samples, a moderate thermal quenching of the PL intensity is observed. The activation energies, deduced from fits employing the common three-level model of a thermally activated PL quenching,[360] are similar and amount to 48 and 34 meV for the planar and the nanowire sample, respectively [see Fig. 4.1(b)].

If we proceed in the usual fashion and take the ratio of $I_{\mathrm{PL}}(300\,\mathrm{K})/I_{\mathrm{PL}}(10\,\mathrm{K})$ as the IQE η at room temperature (thus implicitly assuming an IQE of unity at 10 K or any other low temperature),[66,224,229,354,361–363] we obtain $\eta = 0.41$ for the planar and $\eta = 0.21$ for the nanowire sample directly from the normalized I_{PL} shown in Fig. 4.1(b). Obviously, the latter value for the nanowire sample is meaningless considering that the integrated PL intensity of this sample is more than two orders of magnitude lower than that of the planar sample [see Figs. 4.1(a) and 4.1(c)]. This result shows that the ratio $I_{\mathrm{PL}}(300\,\mathrm{K})/I_{\mathrm{PL}}(10\,\mathrm{K})$ cannot be taken as a sensible measure for the IQE of samples for which no independent data support the assumption of an IQE of 1 at 10 K.

In Fig. 4.1(c), we show the excitation-dependent integrated PL intensity of the planar and the nanowire sample recorded at 300 K. The spectrally integrated PL intensity I_{PL} of the nanowire sample amounts to 1.4 % of the value of the planar sample at low excitation densities, and this ratio decreases to 0.3 % at high excitation densities. Nevertheless, the increase of I_{PL} with excitation intensity I_{exc} is close to linear for both samples over six orders of magnitude ($I_{\mathrm{PL}} \propto I_{\mathrm{exc}}^{1.1}$ for the planar and $I_{\mathrm{PL}} \propto I_{\mathrm{exc}}^{0.9}$ for the nanowire sample). We observe neither a superlinear increase of I_{PL} due to a saturation of SRH centers[142,364] nor a noticeable sublinear increase at high excitation densities because of an increasing contribution of carrier leakage[365] or the onset of Auger recombination.[212]

4.3 Initial part of the photoluminescence transients

The results discussed in Sec. 4.2 show that the temperature and excitation dependence of the steady-state PL intensity are not necessarily sensitive to the actual IQE of a given sample. For binary bulk semiconductors such as GaN, for which a unique radiative lifetime exists,[366] a reliable measure of the IQE is the minority carrier lifetime determined by time-resolved PL experiments.[367] However, in (In,Ga)N/GaN{0001} QWs, the radiative lifetime depends strongly on the well width and In content due to the presence of large piezoelectric fields.[68] Additionally, the inevitable compositional fluctuations in the random alloy (In,Ga)N lead to the localization of charge carriers,[45,50,68,368] making the definition of a unique radiative lifetime all but impossible. Still, time-resolved PL measurements in conjunction with a comparative measurement of the absolute emission intensities enable one to disentangle radiative and nonradiative contributions to the PL decay.

For the time-resolved PL spectroscopy, we have employed nonresonant excitation with the frequency-doubled, femtosecond Ti:sapphire laser ($E_{\mathrm{laser}} = 3.55\,\mathrm{eV}$). More details about the time-resolved PL setup can be found in Sec. 3.4.2. The transients were recorded with time-correlated single photon counting at the respective peak energies integrated over a spectral range of about 20 meV.* The energy fluence per pulse amounted to approximately $3\,\mu\mathrm{J\,cm^{-2}}$, corresponding to a maximum charge carrier density of about $3 \times 10^{11}\,\mathrm{cm^{-2}}$. The excitation density was chosen such that no spectral diffusion of the PL band was detected, i. e., a screening of the internal electric fields and hence a dynamically changing overlap of the electron and hole wave functions was avoided. In addition, the low repetition rate (9.3 kHz for recording the transients up to 33 µs in a temperature range from 10 to 250 K) of the laser pulses prevented the accumulation of charge carriers created by consecutive laser pulses. By employing time-correlated single photon counting in conjunction with an appropriate binning in the time domain and a careful subtraction of the background, we achieve a dynamic range in the detection of six orders of magnitude. The temporal resolution amounted to 45 ps for the investigation of the initial decay.

We first focus on the initial part of the PL transients that accounts for a decay in the PL intensity over two decades after pulsed excitation. This dynamic range is typical for time-resolved PL experiments for which a streak camera is used for detection as reported, for example, in Refs. 170, 197, 362, and 369–371. Figure 4.2(a) displays PL transients of the planar and the nanowire sample recorded at 10 K in a semilogarithmic representation. Evidently, this initial decay of the PL intensity is significantly faster for the nanowire as compared to the planar sample: While it takes 80 ns for the PL intensity of the latter to decrease by two orders of magnitude, it only requires 20 ns for that of the former. Note that the decay cannot be described by a single exponential [see the dashed lines in Fig. 4.2(a)], particularly so for the nanowire sample. We emphasize that this nonexponential decay is not caused by a screening of the piezoelectric fields, since the transients were acquired

*Transients recorded at the low- or high-energy tails of the PL band (that do not substantially contribute to the integrated PL intensity) will change the shape of the transient slightly, as we probe localization centers with different confining potential.

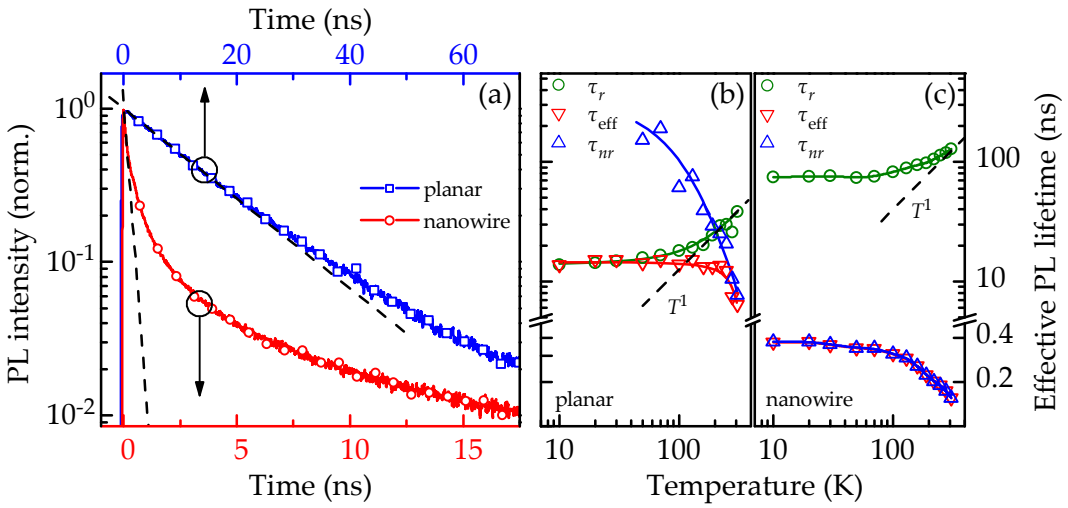

Figure 4.2: (a) Semilogarithmic representation of the normalized PL transients of the planar and the nanowire sample recorded at 10 K. Note the different time scales for the planar and the nanowire sample. The dashed lines are fits with single exponentials with different effective lifetimes. Temperature-dependent effective (τ_{eff}), radiative (τ_{r}), and nonradiative (τ_{nr}) PL lifetimes of (b) the planar and (c) the nanowire sample. The solid lines are guides to the eye. The dashed lines illustrate the linear increase of τ_{r} with increasing temperature T. Note the axis break in the axis of the effective PL lifetimes of the double-logarithmic representation.

with excitation densities well below the onset of this effect.

To derive a decay time despite the nonexponential nature of the transients, we define a phenomenological effective PL lifetime τ_{eff} as the time at which I_{PL} has decreased to $1/e$ ($\approx 37\,\%$) of its initial value. In addition, we assume that

$$\frac{1}{\tau_{\mathrm{eff}}} = \frac{1}{\tau_{\mathrm{r}}} + \frac{1}{\tau_{\mathrm{nr}}} \tag{4.1}$$

with the radiative and nonradiative lifetimes being τ_{r} and τ_{nr}, respectively. Figures 4.2(b) and 4.2(c) show the temperature dependence of τ_{eff} for the planar and the nanowire sample, respectively. For the planar sample, the effective PL lifetime is constant up to 220 K with a value of about 14 ns and decreases subsequently to 6 ns at 300 K. A similar temperature dependence is observed for the nanowire sample, for which τ_{eff} amounts to about 0.37 ns between 10 K and 70 K and decreases to 0.16 ns at 300 K.

To distinguish the radiative and nonradiative contributions to τ_{eff}, we first determine the temperature dependence of τ_{r} from the inverse peak PL intensity of the transient just after the laser pulse.[142] To deduce absolute values for τ_{r} and τ_{nr}, some additional information is required. Since τ_{eff} and τ_{r} are related by

$$\eta = \frac{\tau_{\mathrm{eff}}}{\tau_{\mathrm{r}}}, \tag{4.2}$$

the required information is the IQE η at, for example, 10 K. This quantity is often indis-

criminately assumed to be unity regardless of the sample. In the present case, we use the planar (In,Ga)N/GaN(0001) QWs as reference, whose IQE is known to be high even at room temperature: LEDs with these QWs as active region exhibit an EQE between 0.1 and 0.7 at low injection levels.[289] For this sample, it thus seems justified to assign a value of unity to its IQE at 10 K. To obtain a corresponding value for the (In,Ga)N/GaN(000$\bar{1}$) QD, we recall that the IQE is proportional to the time-integrated intensity of the transient. Since this intensity is 200 times lower for the nanowire sample than for the planar reference, we thus obtain $\eta \approx 0.005$ for the nanowire sample at 10 K.

Figures 4.2(b) and 4.2(c) show the temperature dependence of the radiative and nonradiative lifetimes determined as described above for the planar and the nanowire sample, respectively. The PL lifetimes and the values of the IQEs at 10 K and 250 K are also compiled in Tab. 4.1. Regardless of the absolute values, we obtain a qualitative understanding of the decay processes by examining the temperature dependence of τ_r. For both samples, τ_r is constant up to a certain temperature and then smoothly approaches a linear increase as indicated by the dashed lines. Hence, emission takes place from zero-dimensional localized states at low temperatures and approaches the behavior expected for a two-dimensional system (i. e., a QW) at higher temperatures[372] (see also Sec. 2.3.4 for derivation). The transition from a zero- to two-dimensional system occurs at a higher temperature and is more gradual for the nanowire sample, indicating that carriers in the QDs experience stronger localization than those in the planar QWs.

Regarding the absolute values of the lifetimes, we first see that the radiative lifetimes measured for the nanowire sample are significantly longer than those of the planar sample. This finding is consistent with the stronger polarization fields in the QDs expected from the higher In content, but also with stronger localization. Second, we see that τ_{nr} becomes shorter than τ_r at about 200 K for the planar sample, while τ_{nr} is always drastically shorter than τ_r for the nanowire sample. Thus, the recombination in the latter sample is dominated by nonradiative recombination over the entire temperature range.

sample	T (K)	τ_{eff} (ns)	τ_r (ns)	τ_{nr} (ns)	η
planar	10	14	14	∞	1
planar	250	12	30	21	0.40
nanowire	10	0.37	75	0.37	0.005
nanowire	250	0.19	114	0.19	0.002

Table 4.1: Effective τ_{eff}, radiative τ_r and nonradiative τ_{nr} PL lifetimes extracted for different temperatures T from the analysis of the initial decay of the PL intensity. The IQE η at 250 K is estimated from the initial PL decay.

4.4 Photoluminescence transients over the full time range

The analysis of the initial PL decay discussed in Sec. 4.3 has provided useful information, but did not yield any insights into the nonexponential nature of the PL decay. In earlier studies, this nonexponential decay invariably observed for (In,Ga)N/GaN(0001) QWs was proposed to be represented by a stretched exponential.[370] This observation was attributed to strong compositional fluctuations in the ternary alloy (In,Ga)N, creating In-rich regions resembling "quantum dots" that confine excitons with different energies and, consequently, different lifetimes.[55]

Alternatively, Morel *et al.*[48] attributed the nonexponential decay to the recombination of individually localized electrons and holes that are separated spatially in the two-dimensional QW plane. Their model was inspired by the seminal work of Thomas *et al.*,[373] which describes the kinetics of radiative recombination of electrons and holes bound to randomly distributed donor-acceptor pairs (DAPs) in a bulk crystal and is therefore known as the two-dimensional-DAP model.

More recently, Brosseau *et al.*[49] recorded PL transients of (In,Ga)N/GaN(0001) QWs over six decades in intensity. These measurements demonstrated that only the initial decay follows an exponential or stretched exponential dependence. For longer times, the decay was observed to deviate from this dependence and to asymptotically become a power law. The authors analyzed their data by a phenomenological model based on the coexistence of a radiative state and a metastable charge-separated state.[374] This model also described the experimentally observed asymptotic slowdown of the decay, which cannot be accounted for by the model of Morel *et al.*[48] Recently, Cardin *et al.*[375] extended this study by investigating the PL decay kinetics of (In,Ga)N/GaN(000$\bar{1}$) nanowire heterostructures at room temperature and observed a power law decay for these structures as well.

A power law decay of the PL intensity is by no means restricted to polar (In,Ga)N, but is actually observed for the majority of solids.[376] The unifying characteristics of these materials is topological disorder as observed, for example, in solids with randomly situated traps such as found in various amorphous semiconductors. A wealth of studies is available on this subject, and its understanding is in fact much more mature than in the case of (In,Ga)N.[377–384] For example, the impact of carrier diffusion on the PL decay has been studied in great detail already decades ago.[379] However, nonradiative processes have not been taken into consideration in these previous studies, but are obviously essential for a full understanding of the PL decay in polar (In,Ga)N.

Figures 4.3(a) and 4.3(b) show exemplary PL transients of our samples over the full time range of 33 µs.[†] The double-logarithmic representation of the transients demonstrates that the initial decay analyzed in Fig. 4.2 amounts only to a fraction of the entire decay. Furthermore, this representation facilitates the direct identification of a power law decay (straight line).

Several important observations can be made from the experimental PL transients shown in Figs. 4.3(a) and 4.3(b). First, we observe a PL decay that obeys a power law asymp-

[†]To investigate the PL transients over the technically maximum possible time range of 33 µs, the temporal resolution was decreased to 400 ps.

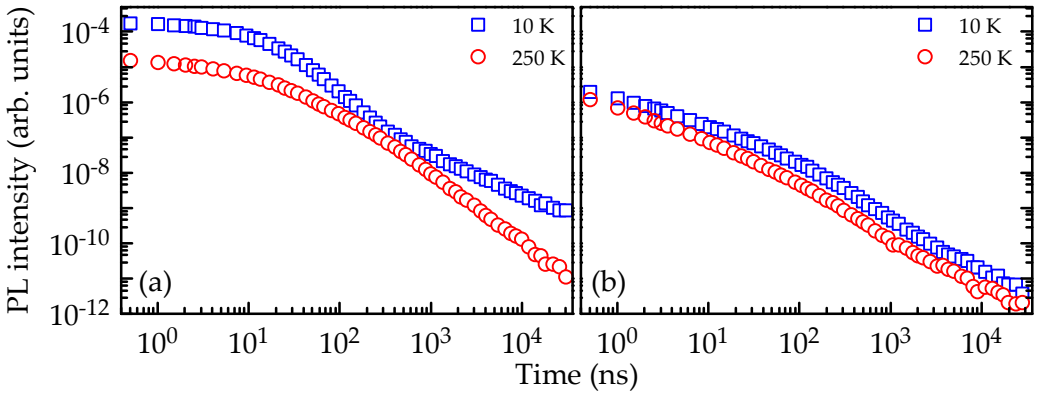

Figure 4.3: Double-logarithmic representation of exemplary experimental PL transients over the full time range of 33 µs recorded at the PL peak energy of the (a) planar and (b) nanowire sample at 10 and 250 K. The intensity has been scaled by the same factor to facilitate a direct comparison with the simulated transients in Fig. 4.12. The transients were recorded by T. Flissikowski.

totically for both samples and independently of temperature. At 10 K, the pronounced slowdown of the decay of the planar sample after about 400 ns closely resembles the asymptotic behavior reported by Brosseau *et al.*[49] Second, we observe a reduction of the time-integrated PL intensity (area under the PL transients) with increasing temperature for both samples, reflecting the presence of nonradiative recombination at elevated temperatures. Despite this fact, the decay does not become exponential, but still obeys a power law for both samples at elevated temperatures. For the planar sample, the decay accelerates with temperature (the absolute value of the exponent of the t^{β} asymptote increases from $\beta = -1.1$ at 10 K to $\beta = -1.9$ at 250 K), while the shape of the PL decay of the nanowire sample hardly changes at all between 10 and 250 K.

4.5 Recombination model

For a quantitative understanding of these transients, we consider the processes schematically depicted in Fig. 4.4. First of all, we assume that the power law decay is fundamentally related to the recombination of spatially separated electrons and holes. We also assume that (In,Ga)N constitutes a perfect random alloy[61,385] whose inherent compositional fluctuations, together with the associated inhomogeneous strain and fluctuations in the resulting piezoelectric fields, are sufficient to localize charge carriers individually.[50,56,158,386] This complex potential landscape is represented in the following by randomly situated localization sites with a randomly varying energy depth, as visualized in Fig. 4.4 by circles with different diameters. Due to the presence of nonradiative recombination, we include SRH recombination centers with a density N that are also assumed to be randomly distributed. These centers are either in state $N_{\times}$ (represented by squares) and interact with electrons or in state $N_{\circ} = N - N_{\times}$ (represented by triangles) and interact with holes.

Initially, electrons (minus) and holes (plus) are distributed randomly at localization sites

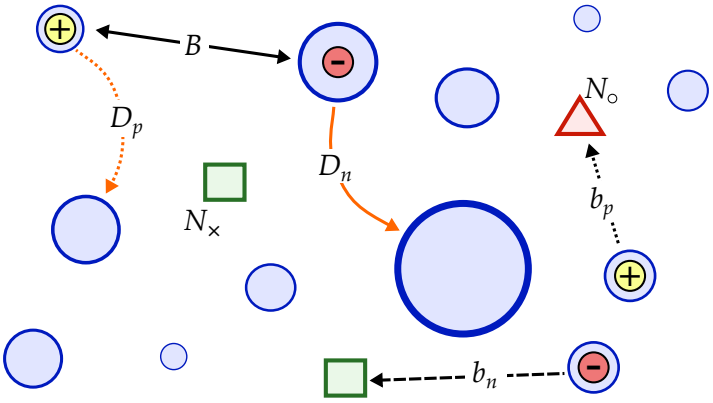

Figure 4.4: Schematic representation of the model for simulating the PL transients of (In,Ga)N/GaN{0001} QWs. The potential landscape of the random alloy (In,Ga)N is assumed to create localization sites (◯) for electrons (⊖) and holes (⊕) with varying energy depth (represented by the diameter). In addition, nonradiative recombination centers (□ and △) exist. Initially, electrons and holes are randomly distributed. Radiative recombination occurs via tunneling with a coefficient B. The recombination centers capture electrons and holes by tunneling with coefficients b_n and b_p, respectively. Diffusion (curved arrows) of electrons and holes allows them to migrate in the potential landscape with coefficients D_n and D_p, respectively. All coefficients are random functions of location $\mathbf{r}$ and, for recombination events, of spatial distance $\mathbf{x}$.

(see Fig. 4.4). The charge carriers can recombine radiatively via tunneling over distances $|\mathbf{x}|$ with a rate coefficient $B(|\mathbf{x}|, \mathbf{r}) = B_0 \exp[-|\mathbf{x}|/a(\mathbf{r})]$. Likewise, electrons and holes can be captured by recombination centers with rate coefficients $b_n(|\mathbf{x}|, \mathbf{r}) = b_{n0} \exp[-|\mathbf{x}|/a(\mathbf{r})]$ and $b_p(|\mathbf{x}|, \mathbf{r}) = b_{p0} \exp[-|\mathbf{x}|/a(\mathbf{r})]$, respectively. The tunneling parameter $a(\mathbf{r})$ depends on the localization energy and is thus a function of the spatial location $\mathbf{r}$.[‡] Finally, electrons and holes are given the possibility to diffuse within this potential landscape with diffusivities $D_n(\mathbf{r})$ and $D_p(\mathbf{r})$, respectively. The diffusivity is influenced by the potential depth of the localization site and thus explicitly depends on $\mathbf{r}$.

The three processes considered above (radiative recombination, SRH recombination, and carrier diffusion) are those considered in the classical diffusion-recombination equations of semiconductor physics.[387] Here, we generalize these equations by taking into account the stochastic nature of the recombination coefficients (i. e., the random dependence on position or distance of the respective process). We thus arrive at the following coupled system of integro-differential equations (4.3)–(4.5) for electrons n, holes p, and nonradiative centers N:

$$\begin{aligned}\frac{\partial n(\mathbf{r},t)}{\partial t} = D_n(\mathbf{r})\Delta n(\mathbf{r},t) - n(\mathbf{r},t)\int B(|\mathbf{x}|,\mathbf{r})p(\mathbf{r}+\mathbf{x},t)\mathrm{d}\mathbf{x} \\ - n(\mathbf{r},t)\int b_n(|\mathbf{x}|,\mathbf{r})N_\times(\mathbf{r}+\mathbf{x},t)\mathrm{d}\mathbf{x}\end{aligned} \tag{4.3}$$

[‡]In fact, a may be equivalent to the spread of the wave function of the respective particle in the confining potential.

$$\begin{aligned}\frac{\partial p(\mathbf{r},t)}{\partial t} &= D_p(\mathbf{r})\Delta p(\mathbf{r},t) - p(\mathbf{r},t)\int B(|\mathbf{x}|,\mathbf{r})n(\mathbf{r}+\mathbf{x},t)\mathrm{d}\mathbf{x} \\ &\quad - p(\mathbf{r},t)\int b_p(|\mathbf{x}|,\mathbf{r})[N(\mathbf{r}+\mathbf{x}) - N_\times(\mathbf{r}+\mathbf{x},t)]\,\mathrm{d}\mathbf{x}\end{aligned} \tag{4.4}$$

$$\begin{aligned}\frac{\partial N_\times(\mathbf{r},t)}{\partial t} &= -\,n(\mathbf{r},t)\int b_n(|\mathbf{x}|,\mathbf{r})N_\times(\mathbf{r}+\mathbf{x},t)\mathrm{d}\mathbf{x} \\ &\quad + p(\mathbf{r},t)\int b_p(|\mathbf{x}|,\mathbf{r})[N(\mathbf{r}+\mathbf{x}) - N_\times(\mathbf{r}+\mathbf{x},t)]\,\mathrm{d}\mathbf{x}\end{aligned} \tag{4.5}$$

The first term in Eqs. (4.3) and (4.4) represents the diffusion of electrons and holes, respectively, while the second and third terms represent the radiative and the nonradiative recombination of the respective type of charge carrier (either electrons or holes). The temporal evolution of the recombination centers in state $N_\times$ [Eq. (4.5)] is determined by the capture of an electron (first term) and the capture of a hole (second term) resulting in the nonradiative annihilation of both particles.

To solve these Smoluchowski-type equations[388] numerically, we employ the Monte Carlo algorithm developed and described in detail in Ref. 79. Since the out-of-plane separation of electrons and holes is limited by the width of the QWs, which is on the order of the exciton Bohr radius, the distance between the recombination partners will be governed by their lateral (in-plane) separation, particularly when the decay of the PL approaches the power law asymptotically. We can thus simplify the problem considerably by reducing it to two dimensions.

4.6 Monte Carlo simulation of the power law decay

Prior to attempting to fit the experimental data depicted in Fig. 4.3, we theoretically investigate the individual influence of the simulation parameters on the intensity transients, highlight some peculiarities of the power law decay, and identify the set of parameters reproducing the experimental transients best. Therefore, we have performed over 30,000 simulations covering a large parameter space. For this purpose, we have adapted the Fortran 95 code from Ref. 79 to efficiently solve Eqs. (4.3)–(4.5) in two dimensions. The execution of the code on a 4-way Intel® Xeon® E5-4627v2 with *parallel*,[389] has allowed us to track the radiative and nonradiative annihilation of 400 randomly situated electrons and holes as well as their diffusion. For each parameter set, the computation was repeated at least 1,000 times with a random seed to obtain sufficient statistics and smooth transients. The complete simulation of a transient typically required about 10 min on a single core of our system. For the simulation of large diffusivities, the size of the box in which the simulation takes place was enlarged to avoid an influence of the of periodic boundaries.

4.6.1 Tunneling distance and recombination coefficients

In the simulations, the average density of localization sites is set to a value of $1\,\mathrm{nm}^{-2}$, which translates into one localization site every three by three unit meshes in the wurtzite lattice of (In,Ga)N. This density is roughly equivalent to the density of localized states obtained by means of atomistic tight-binding calculations for $In_{0.25}Ga_{0.75}N$.[158] The initial density of excess charge carriers amounts to $\Delta n = \Delta p = 2.5 \times 10^{-3}\,\mathrm{nm}^{-2}$ and corresponds to an excitation density typically employed for the time-resolved experiments. The charge carriers are randomly distributed at localization sites at $t = 0$, and we do not allow one site to be occupied by more than one particle.

Starting with the simulation of purely radiative (tunneling) recombination, hence $N = 0$ and $D_n = D_p = 0$, the tunneling parameter $a(\mathbf{r})$ attributed to the localization sites and the radiative recombination rate B_0 are the remaining parameters that vary the simulated transients. In a first step, we choose $a(\mathbf{r})$ to be constant, but at the end of this subsection, we will investigate values of $a(\mathbf{r})$ being randomly distributed around an average value.

In Fig. 4.5(a), we show simulated transients with a constant a increasing from $a = 2\,\mathrm{nm}$ (blue) to $a = 20\,\mathrm{nm}$ (red) with a fixed value of $B_0 = 0.04\,\mathrm{ns}^{-1}$. In contrast, we fix a at a value of 4 nm and use values of B_0 increasing from $B_0 = 1 \times 10^{-3}\,\mathrm{ns}^{-1}$ (blue) to $B_0 = 1 \times 10^{1}\,\mathrm{ns}^{-1}$ (red) in Fig. 4.5(b). Obviously, all transients enter a power law behavior asymptotically that follows $t^{-1}\log(t)^{-2}$ [dashed lines in Figs. 4.5(a) and 4.5(b)] as analytically derived in Ref. 79.

The initial photon flux increases, and the initial phase of the decay (i. e., the part of the decay which can be approximated by an exponential function) becomes faster with increasing a or B_0. Both changes are expected since the recombination rate naturally increases for larger tunneling distances, i. e., similar to a larger spread of the wave functions, or for higher recombination rates. However, the shape of the initial phase of the decay develops in different ways for increasing a or B_0. For increasing a over a meaningful range, the initial phase of the decay amounts to about 100 ns and shortens only slightly. In contrast, when increasing B_0 over a larger range, the initial phase of the decay reduces from more than 1,000 ns to 1 ns and almost completely vanishes for large values of B_0 [see Fig. 4.5(b)]. Thus, B_0 seems to influence the initial phase of the decay of the decay more strongly than a. Moreover, large values of B_0 cause a transient which can be approximated by a single power law right after excitation. Finally, we observe a rather unique transient for the largest values of a. This transient exhibits a slowdown of the power law asymptote after approximately 100 ns as indicated by the dotted lines in Fig. 4.5(a). Thus, the slope of the asymptote cannot be fitted by a single power law anymore.

In a next step, we use the same parameters for a and B_0, but introduce nonradiative recombination centers with a density N and enable nonradiative tunneling recombination. For simplicity, we assume that $b_{n0} = b_{p0} = b_0$ and that $N = N_\times$ at $t = 0$. Additionally, charge carriers, once captured by a nonradiative center, will not be released again. With $b_0 = 0.02\,\mathrm{ns}^{-1}$ and $N = 1.25 \times 10^{-3}\,\mathrm{nm}^{-2}$, we obtain the transients presented in Figs. 4.5(c) and 4.5(d) for increasing a and B_0, respectively. In the presence of active nonradiative recombination centers, the decay accelerates, but the transients conserve their power law

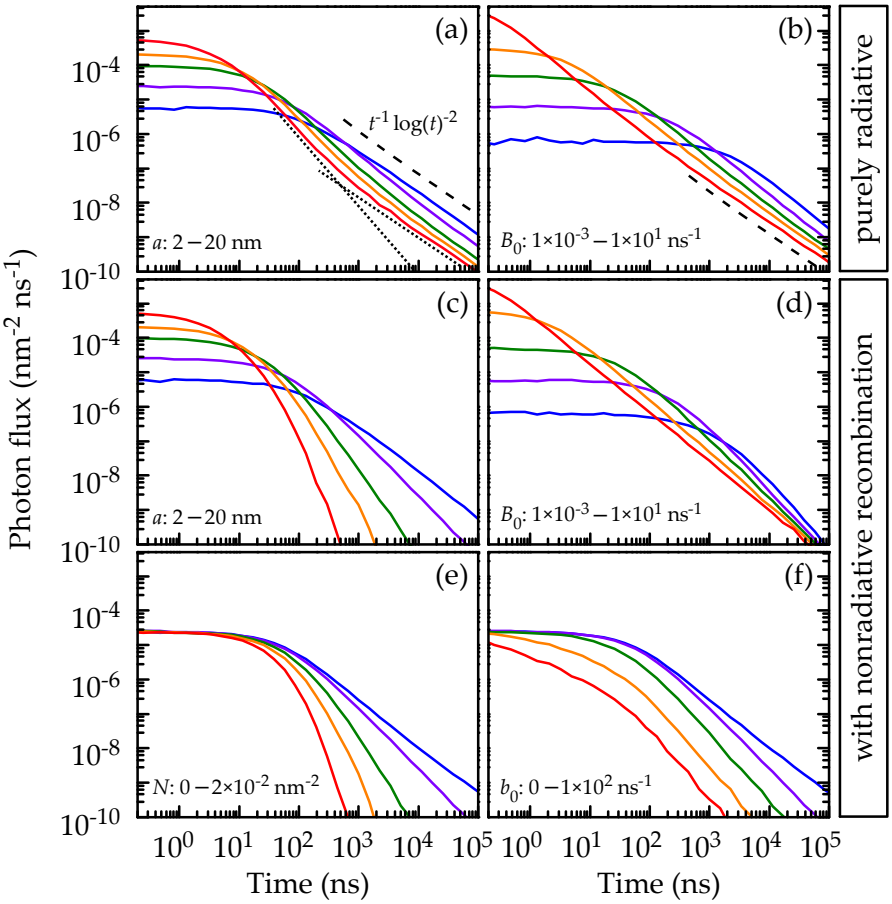

Figure 4.5: Double-logarithmic representation of simulated intensity transients with variation of one parameter per subfigure. The parameters increase in equidistant steps from low values (blue) to high values (red) as indicated. The remaining parameters are fixed at values described in the text. Purely radiative recombination with (a) increasing tunneling distance a and (b) increasing radiative recombination coefficient B_0. The photon flux with time t of purely radiative decays follows $t^{-1} \times \log t^{-2}$ asymptotically,[79] as indicated by the dashed lines in (a) and (b). The dotted lines highlight the different slopes of the decay for large a. (c)–(f) Variation of the parameters in the presence of nonradiative recombination centers with density N and recombination coefficient b_0.

asymptote. Compared to the case without nonradiative recombination, the transients are hardly influenced by the presence of nonradiative centers for increasing values of B_0. In contrast, increasing values of a with nonradiative centers present lead to a drastic increase of the absolute value of the slope of the power law asymptote from $t^{-1.3}$ to t^{-4}. The integrated photon flux (area under the transient) is reduced with increasing a according to the larger overlap of the electron and hole wave functions with nonradiative centers [see Fig. 4.5(c)]. Note that the slowdown of the power law asymptote for large values of a as observed in Fig. 4.5(a) is not detectable when active nonradiative centers are present.

In a last step, we have varied the density of nonradiative recombination centers N

and the nonradiative recombination rate b_0 in Figs. 4.5(e) and 4.5(f), respectively. As above, we set to remaining parameters to $a = 4\,\mathrm{nm}$, $B_0 = 0.04\,\mathrm{ns}^{-1}$, $b_0 = 0.02\,\mathrm{ns}^{-1}$, and $N = 1.25 \times 10^{-3}\,\mathrm{nm}^{-2}$. We observe that increasing N has a similar effect as increasing a in the presence of nonradiative recombination centers, which is plausible as the overlap between nonradiative center and particle increases accordingly. Increasing b_0 causes shapes of the transients similar to ones for increasing B_0, as the slope of the power law asymptote stays constant. However, the initial photon flux decreases only slightly for increasing values of b_0. For large values of b_0, the initial phase vanishes, and the complete transients can be approximated by a single power law. Thus, it is hardly possible to distinguish large values of B_0 from large values of b_0 without additional knowledge about the absolute photon flux of the investigated sample.

4.6.2 Influence of diffusion on the power law decay

Due to their thermal energy, particles are able to conduct an undirected motion (along a gradient) called diffusion. In accordance with recent theoretical results for (In,Ga)N,[50,68] we assume that the holes are localized due to their large effective mass at all temperatures ($D_p = 0$), but allow for a finite diffusivity of electrons ($D_n = D$) at elevated temperatures. The diffusion of electrons is implemented in the Monte Carlo algorithm by a hopping process[§] between the different localization sites as explained in Ref. 79. In case an electron hops into a localization sites filled with a hole, the pair instantaneously recombines radiatively. For a localization site being a nonradiative center (filled with a hole), the mobile electron becomes captured (and the electron-hole pair recombines nonradiatively). In Figs. 4.6(a) and 4.6(b), we present the influence of the diffusivity D of electrons ranging from 0–200 $\mathrm{nm}^2\,\mathrm{ns}^{-1}$ on the power law decay without nonradiative recombination and in the presence of nonradiative centers with a density of $N = 1.25 \times 10^{-3}\,\mathrm{nm}^{-2}$, respectively. For the remaining simulation parameters, we again use $a = 4\,\mathrm{nm}$, $B_0 = 0.04\,\mathrm{ns}^{-1}$ and $b_0 = 0.02\,\mathrm{ns}^{-1}$. Obviously, diffusion accelerates the decay (higher initial photon flux and shorter initial phase), but the transients still obey a power law. In the case of purely radiative recombination and the diffusion of both electrons and holes, it can be shown analytically that the transients asymptotically follow $t^{-3/2}$.[79] Approximately, this proportionality is valid also in the case of electron diffusion [see dotted line in Fig. 4.6(a)]. In the presence of active nonradiative centers, an increasing diffusivity causes significantly steeper slopes of the power law asymptote. Mobile electrons exhibit an effectively larger interaction distance with nonradiative centers and holes. Thus, the recombination processes involving electrons become more efficient. Although the integrated photon flux seems to decrease with increasing values of D [see Fig. 4.6(b)], a quantitative analysis reveals that it stays almost constant for this set of parameters, because the (immobile) holes are not affected by increasing values of D and constitute the rate-limiting process.

[§] A phonon-induced hopping was proposed by Conwell [390] and Mott [391] already in 1956. The existence of localized charge carriers that perform a hopping process is also well-known from polymer LEDs. [392]

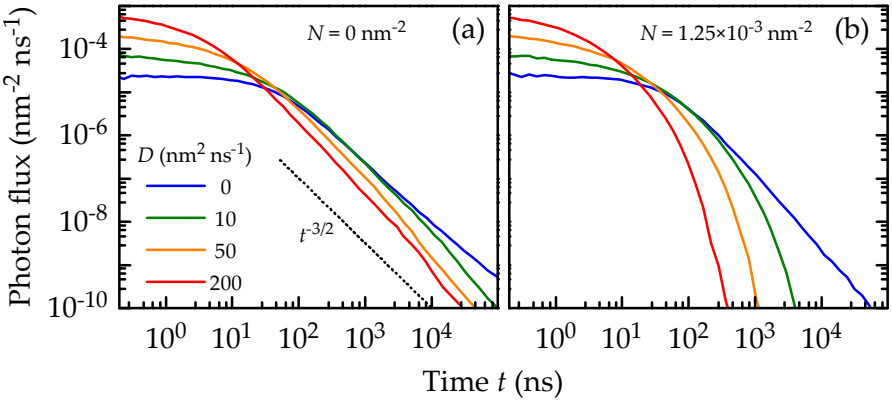

Figure 4.6: Double-logarithmic representation of simulated PL transients including the diffusion of electrons with diffusivity D for (a) purely radiative recombination and (b) in the presence of nonradiative centers with a density N. In the case of purely radiative recombination and the diffusion of both electrons and holes, the transient asymptotically follows $t^{-3/2}$ (dotted line).[79]

4.6.3 Influence of the diffusivity on the hopping distance and the IQE

If particles are able to diffuse or hop with a given diffusivity or hopping frequency, it is interesting to determine the diffusion length or hopping distance. As outlined in Sec. 2.5, the PL decay of polar (In,Ga)N is nonexponential, and thus, a unique lifetime cannot be defined. Hence, a diffusion length as a material parameter cannot be defined either. However, within our simulations, we simulate transients with a given diffusivity (material parameter). Moreover, we are able to track the hopping motion (number of hops) of particles, i. e. electrons in our case, between the individual localization sites and compare the resulting average hopping distance for standardized initial excitation conditions for different samples.

We present the analysis of such a hopping motion in Fig. 4.7. The particle hops 10^5 steps with a step size of 1 arb. unit for two different random seeds [see Figs. 4.7(a) and 4.7(b)]. During the random hopping process, the particle may hop into the same localization site several times. The distance the particle covers may be characterized either by the maximum radius from the starting point or the radial distance from the starting point to the final position. As electrons exhibit quasi-infinite lifetimes,[393] electrons can be trapped by nonradiative centers or annihilate with holes only. Thus, we define the maximum radius as the hopping distance.

We show an exemplary distribution of the maximum radii for 10^6 steps for a pure diffusion process in Fig. 4.7(c). The distribution follows a log-normal function and exhibits an average value at 1,171. The median of the distribution amounts to 1,115 and is close to the mean value as the standard deviation is comparatively small in our exemplary distribution. Utilizing a large number of repetitions of the simulations (here 10^4), the average maximum radii depend on the square root of the steps/hops (solid lines) as shown Fig. 4.7(d). To determine the exact mean maximum radii, the square root of

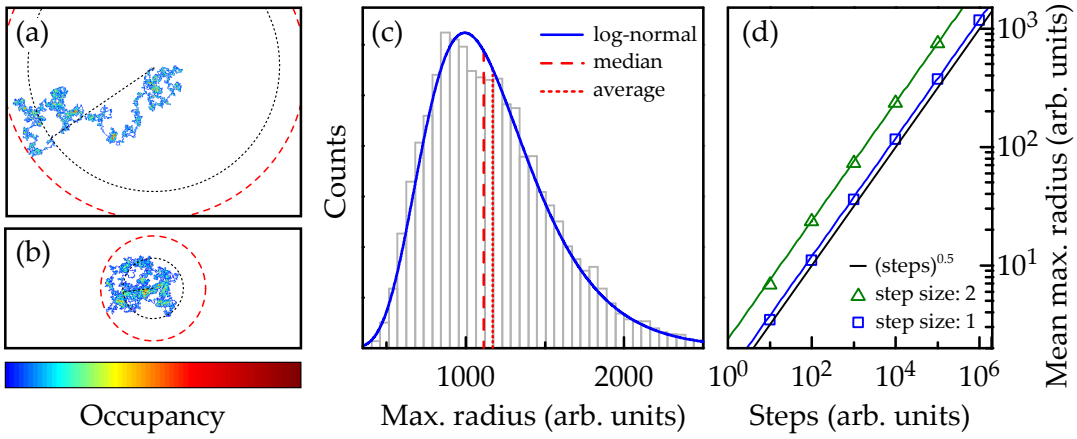

Figure 4.7: (a) and (b) Simulations of a hopping process with 10^5 step with a step size of 1 arb. unit and with different random seeds. The maximum hopping radius for the starting point in the center is encircled by the dashed line. The stop point of the particle is marked by the dotted circle. Positions can be occupied several times ranging from once (blue) to often (red). (c) Distribution of the mean maximum radius of 10^4 simulations with 10^6 steps and a step size of 1 arb. unit. Average and median of the maximum hopping radius are indicated by dotted and dashed lines, respectively. The distribution of the maximum hopping radius follows a log-normal distribution (solid line). (d) Semilogarithmic representation of the correlation between the number of steps and the mean maximum radii for step sizes as indicated and 10^4 repetitions of the simulation. The mean distances are proportional to the square root of the hops as visualized by the solid lines.

the steps has to be multiplied by the size of the steps (i. e., the diffusivity or hopping frequency) and by a prefactor that amounts to $\sqrt[4]{2}$. Thus, we have established a method to determine the mean electron hopping distance for a specific power law directly from our simulations.

In the following, we investigate the influence of the diffusivity and the density of nonradiative centers on the electron hopping distance and the IQE in detail. Therefore, we utilize arbitrary parameters listed as "star" in Tab. 4.2. From the simulated transients, we observe again that, regardless of the magnitude of the D or N, the power law asymptotes of the decay are conserved [see Figs. 4.8(a) and 4.8(b)]. However, for large densities of nonradiative centers, the deviation from an exponential decay is not easy to detect as highlighted by the dotted line in Fig. 4.8(b). While we obtain the electron hopping distance as described above, we deduce the IQE directly by dividing the number of radiative events by the total number of recombination events.

Both, the electron hopping distance and the IQE increase significantly with increasing diffusivity as shown in Fig. 4.8(c). While the first observation is intuitive, the latter is caused by an enhanced radiative recombination of neighboring electrons and holes in the initial phase of the PL decay which dominates over the nonradiative processes at a later stage. Due to the localization of the holes,[50,68] the capture of holes via tunneling into nonradiative centers remains the reaction-limiting process. The maximum electron hopping distance tends to saturate for large diffusivities [see Fig. 4.8(c)] as the decay

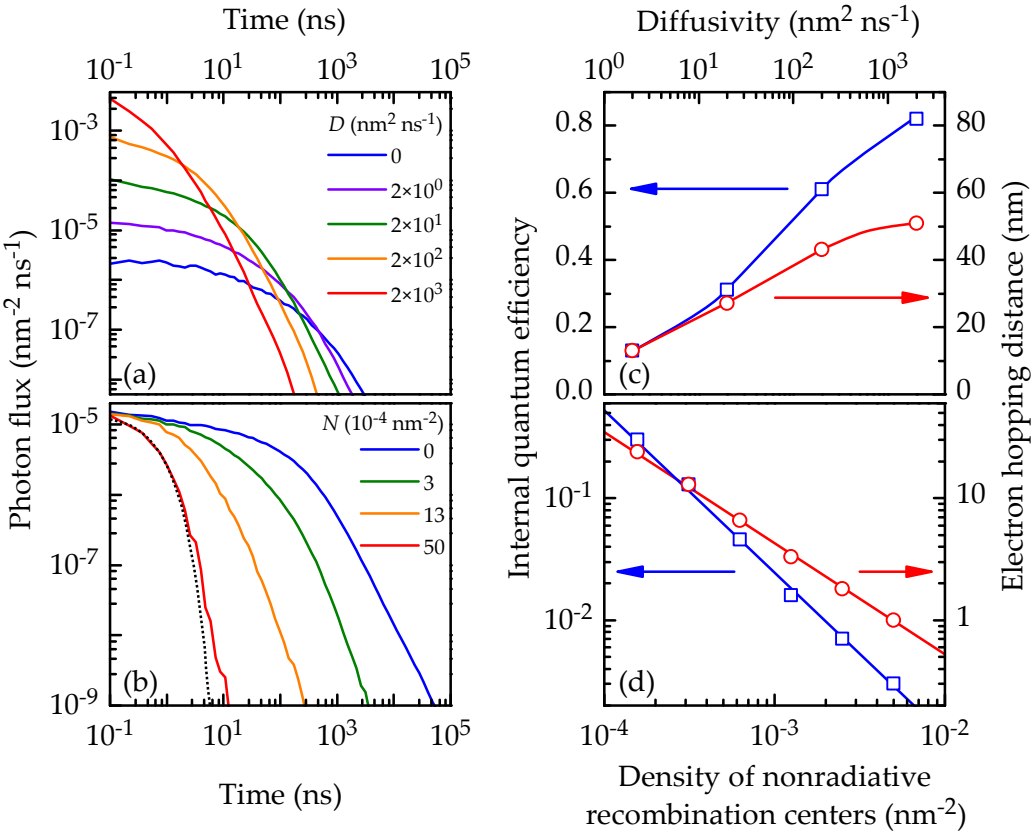

Figure 4.8: Detailed simulations of the influence of diffusion and nonradiative recombination processes on the transients as well as on the IQE and the hopping distance for arbitrary parameters listed as "star" in Tab. 4.2. Double-logarithmic representation of the simulated photon flux for (a) varying diffusivity D and (b) varying density of nonradiative centers N. The dotted line in (b) represents a single exponential function. Corresponding dependence of the IQEs (squares) and the electron hopping distances (circles) on (c) the diffusivity and (d) the density of nonradiative centers. Solid lines in the (c) semi- and the (d) double-logarithmic representation are guides to the eyes.

becomes faster and the times the electrons are able to diffuse are reduced. Accordingly, the reduced electron recombination times explain the reduced hopping distances for an increasing number of nonradiative centers as shown in Fig. 4.8(d). As intuitively expected, the IQE decreases for increasing densities of nonradiative centers [see Fig. 4.8(d)].

4.6.4 Distribution of recombination events

From the preceding simulations, we conclude that even the presence of nonradiative recombination centers or diffusion leads to power law asymptotes in our model. The slopes of the asymptotes become steeper, but the decays may persist up to µs after the initial excitation. However, considering the effect of nonradiative SRH recombination in GaN (see Sec. 2.3), one might expect at a first glance that the decay has to become exponential in (In,Ga)N as well. Starting with the rate equation for a purely radiative

monomolecular recombination process of charge carriers with a density $n(t)$ and adding the prefactor t^{a-1}, we obtain

$$\frac{\mathrm{d}n}{\mathrm{d}t} = -t^{a-1}\frac{n}{\tau_\mathrm{r}} \rightarrow n(t) = n_0 e^{-\frac{t^a}{a\tau_\mathrm{r}}} \tag{4.6}$$

with the radiative lifetime τ_r and the initial charge carrier density $n(t = 0) = n_0$. The intensity (calculated by means of $I = n(t)/\tau_\mathrm{r}$) obeys a stretched-exponential, but approaches a power law for $a \rightarrow 0$. Including a term for nonradiative SRH recombination with a nonradiative lifetime τ_nr in a second step, the asymptote of the resulting transient follows a single exponential function. Thus, the calculations predict an asymptote which is dominated by the exponential nonradiative component. To resolve this contradiction between these simple considerations and the observations from the simulations, we have to investigate the difference between the recombination of excitons and the stochastic tunneling recombination of our model (resulting in the power law asymptote). Therefore, we directly compare the radiative and nonradiative recombination events in Fig. 4.9.

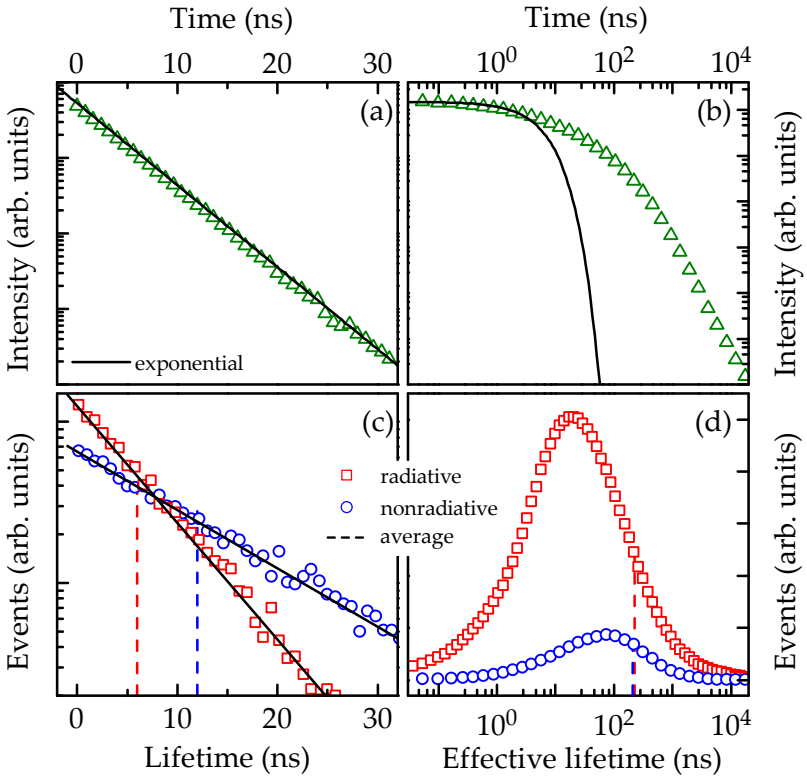

Figure 4.9: Comparison of the intensity decay in the presence of nonradiative recombination of (a) excitonic and (b) tunneling recombination in a semi- and double-logarithmic representation, respectively. The corresponding lifetimes of radiative (blue) and nonradiative (red) events are shown in below the respective transient. Dashed lines indicate the average lifetime of the respective recombination process. The parameters for the simulations as well as the lifetimes of the single exponential fits (solid lines) are given in the text.

For the excitonic case, we select an arbitrary single exponential decay with an effective, radiative, and nonradiative lifetime of $\tau_{\mathrm{eff}} = 4\,\mathrm{ns}$, $\tau_{\mathrm{r}} = 12\,\mathrm{ns}$, and $\tau_{\mathrm{nr}} = 6\,\mathrm{ns}$, respectively. We show the resulting transient in a semilogarithmic representation in Fig. 4.9(a). In Fig. 4.9(b), we use the arbitrary parameters "star" (cf. Tab. 4.2) for the simulation of an representative power law decay. Only a minimal part (up to 2 ns) of the decay can be approximated by an exponential decay with $\tau_{\mathrm{eff}} = 4\,\mathrm{ns}$. The effective lifetime determined as time t for which $I_{\mathrm{PL}}(t) = I_{\mathrm{PL}}(0)/e$ amounts to a value of $\tau_{\mathrm{eff}} \approx 6\,\mathrm{ns}$.

In contrast to the experiment, we have here the direct possibility to separately analyze radiative and nonradiative events, i. e., the annihilation of excitons or electrons and holes in the simulations. In the excitonic picture, the particles are indistinguishable. Both the radiative and nonradiative events are *uncorrelated* and distributed single exponentially. Averaging the lifetimes of all events (dashed lines) or determining the decay coefficient of the respective exponential functions (solid lines) results in $\tau_{\mathrm{r}} = 12\,\mathrm{ns}$ and $\tau_{\mathrm{nr}} = 6\,\mathrm{ns}$ as shown in Fig. 4.9(c). By using Eq. (4.1), we obtain $\tau_{\mathrm{eff}} = 4\,\mathrm{ns}$ as extracted from the corresponding single exponential transient. Although τ_{r} and τ_{nr} are distributed exponentially, we are able to determine useful average lifetimes.

The distribution of the radiative and nonradiative events of the power law decay is reminiscent of a Gaussian distribution at first glance [see Fig. 4.9(d)]. However, the actual distribution is much more complex because the effective lifetimes are displayed on a logarithmic scale. Moreover, the radiative and the nonradiative events are *correlated* and depend on the time-dependent charge carrier density as well as on the history of the stochastic recombination process. Thus, for this decay type, effective radiative and nonradiative lifetimes (i. e., recombination times) can be determined only. The numerical evaluation of the average effective radiative and nonradiative lifetime results in values of 211 ns and 223 ns, respectively. The combined effective recombination time (numerically deduced from the simulations) with a value of 221 ns is more than one order of magnitude larger than the value estimated from the transient. The median recombination time amounts to 22 ns and is therefore almost a factor of 4 larger than $\tau_{\mathrm{eff}} \approx 6\,\mathrm{ns}$. Hence, the correlation between the charge carriers impedes the characterization of a power law with useful average lifetimes, and only the simulation parameters (a, B_0, b_0, N and D) allow a feasible comparison of different samples.

4.6.5 Carrier density dependence

In Fig. 4.10(a), we increase $\Delta n = \Delta p$ in our simulation over two orders of magnitude for the arbitrary parameter set "star" (cf. Tab. 4.2). For increasing Δn, the initial photon flux increases, the length of the initial phase of the decay decreases, but the asymptotes stay identical. Since the interaction distance of electrons and holes decrease with increasing Δn, the results are similar to larger values of a, but without increasing the interaction distance with the nonradiative centers.

In a next step, we utilize various combinations of parameters as listed in Tab. 4.2 to theoretically investigate the dependence of the IQE on the charge carrier density. In Fig. 4.10(b), we obtain an IQE of unity for purely radiative recombination (blue squares)

set	a (nm)	D (nm^2 ns^{-1})	B_0 (ns^{-1})	b_0 (ns^{-1})	N (nm^{-2})
star	8	2	0.001	1	3.125×10^{-4}
circle	6	0	0.04	0.08	5×10^{-3}
triangle	6	0	0.04	0.08	6.25×10^{-4}
diamond	25	10	0.02	0.01	6.25×10^{-4}
square	6	0	0.04	0	0

Table 4.2: Parameters for the simulation of the IQE presented in Fig. 4.10.

as expected. In the presence of nonradiative centers and regardless of the diffusivity, the IQE monotonically increases with increasing initial charge carrier density. Thus, nonradiative processes become saturated. A decrease of the IQE for high initial charge carrier densities, commonly observed in (In,Ga)N-based heterostructures (droop), is obviously not inherent to our model. Additionally, a decrease of the IQE is also not observed in the case of steady-state excitation.[394] Depending on the density of nonradiative centers, the slope the increasing IQE differs for varying simulation parameters. Qualitatively, the simulated slopes are in agreement with experimental data from LEDs with different emission wavelengths.[289] However, our model is designed for low carrier densities, and effects of high carrier density are not included. For example, at high carrier densities, localization sites may be occupied by more than one charge carrier, causing the formation of localized (charged) excitons with an intrinsic lifetime. At even higher concentrations of charge carriers (i. e., above 1×10^{12} cm^{-2} in GaN[278,280]), degeneracy sets in and limits the radiative lifetime.[395–397] In the case of a fast nonradiative channel, both effects might cause a decrease of the IQE similar to the model of the "density-activated defect recombination" proposed by Hader *et al.*[27] For more information of higher-order effects

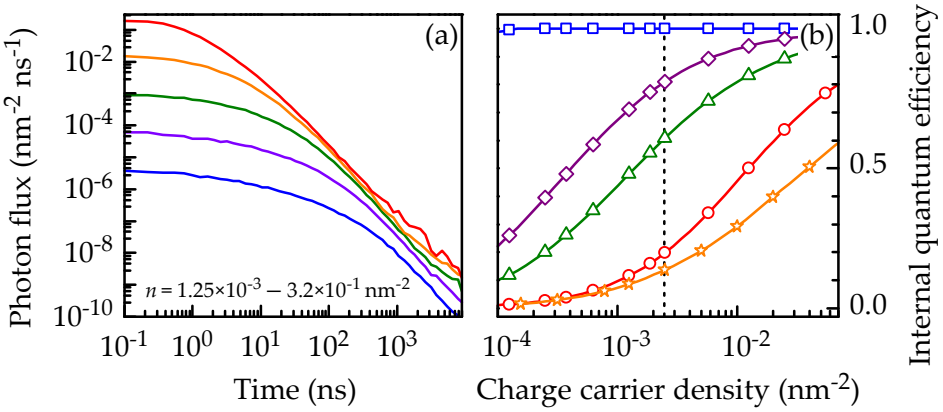

Figure 4.10: (a) Double-logarithmic representation of the influence of the initial carrier density Δn on the simulated transients with Δn increasing from low (blue) to high (red) values. (b) Simulation of the IQE for different parameters as listed in Tab. 4.2. The dotted line indicates the charge carrier density typically used in the experiment.

such as Auger recombination that may be relevant for the decrease of the IQE, the reader is referred to Sec. 2.6. In any case, the experimental investigation of transients recorded with time-correlated single photon counting for high initial charge carrier densities is hardly possible, as the screening of the internal electric fields significantly complicate the acquisition and interpretation of the transients.

In the last paragraph of this subsection, we will discuss the influence of the correlation between the radiative and nonradiative recombination time, observed and discussed in Sec. 4.6.4, on excitation-dependent simulations of power law transients. We start with an excitonic recombination process whose initial photon flux ϕ is proportional to the initial exciton/charge carrier density Δn. Dividing Δn by a factor of β results in a single exponential transient with an effective lifetime τ_{eff}, which we also obtain by starting the simulation with a certain delay t_0 after the excitation with n_0. According to

$$\phi\left(\frac{\Delta n}{\beta}, t\right) = \Delta n \frac{\exp(-t/\tau_{\text{eff}})}{\beta} = n \exp[-(t + t_0)/\tau_{\text{eff}}], \tag{4.7}$$

we calculate t_0 to be equal to $\tau_{\text{eff}} \ln(\beta)$ for all t. Thus, by shifting the time axis, it is possible to produce transients with different initial exciton densities. This behavior is also valid for a simplified pure free-carrier recombination characterized by a hyperbolic function[398] with a radiative recombination coefficient B:

$$\frac{B(\Delta n/\beta)^2}{(1 + B\Delta n/\beta t)^2} = \frac{B\Delta n^2}{(1 + B\Delta n(t + t_0))^2} \text{ with } t_0 = \frac{\beta - 1}{B\Delta n} \tag{4.8}$$

However, this behavior is valid only for the recombination of uncorrelated particles. In contrast, for the recombination of correlated particles characterized by a power law,

$$\phi\left(\frac{\Delta n}{\beta}, t\right) \neq \phi(n, t + t_0) \;\; \forall t. \tag{4.9}$$

We illustrate the issue graphically for the exemplary transients in Fig. 4.11. Clearly, the transient with the higher excitation density exhibits the larger initial photon flux. Obviously, it is not possible to achieve a complete overlap of the two transients by shifting

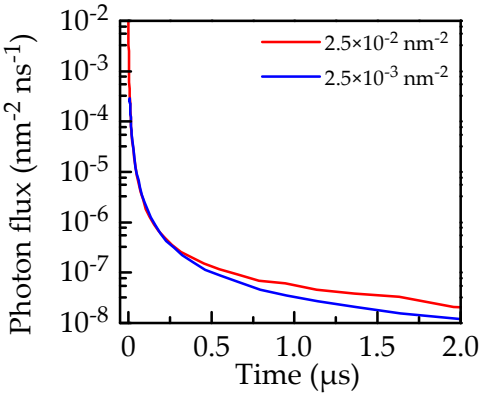

Figure 4.11: Semilogarithmic representation of exemplary simulated transients using the parameters "star" in Tab. 4.2, but with initial charge carrier densities as indicated in the graph. The transient with the lower excitation density is shifted by a delay time of $t_0 = 9\,\text{ns}$ to achieve overlapping transients for small times after the excitation. However, at long time delays, the transients diverge.

the time axis by a certain delay (here $t_0 = 9\,\text{ns}$) as shown in the semilogarithmic representation in Fig. 4.11. Due to the correlation between the charge carriers, a certain shape of a power law decay is not only related to (a, B_0, b_0, N and D), but also to the initial charge carrier density Δn, which in turn explains the variety of reported shapes, especially for the initial PL decay.[197,370,371]

4.6.6 Summary: power law simulations

By utilizing the Monte Carlo algorithm described in Ref. 79, we have solved the position-dependent diffusion-reaction Eqs. (4.3)–(4.5), which provide the basis of our recombination model for (In,Ga)N/GaN QWs. By a comparison with an excitonic decay, we highlighted the correlation between radiative and nonradiative recombination, which is a peculiarity of our model. Moreover, we have established a method to determine the hopping distance by tracking the diffusion of particles.

Finally, we summarize the influence of the individual recombination parameters (within their typical range) on the simulated power law transients in Tab. 4.3.

parameter	symbol	typical range	influence on the transient
tunneling distance	a	0.1–20 nm	initial photon flux; power law asymptote in the presence of nonradiative centers
radiative rate	B_0	10^{-4}–$10^{1}\,\text{ns}^{-1}$	length of the initial phase; initial photon flux
nonradiative centers	N	0–$10^{-2}\,\text{nm}^{-2}$	power law asymptote
nonradiative rate	b_0	0–$10^{2}\,\text{ns}^{-1}$	length of the initial phase; initial photon flux
diffusivity	D	0–$10^{2}\,\text{nm}^2\,\text{ns}^{-1}$	initial photon flux; power law asymptote in the presence of nonradiative centers
electron density	Δn	$2.5\times10^{-3}\,\text{nm}^{-2}$	effects similar to a

Table 4.3: Comparison and summary of the influence of the simulation parameters of the Monte Carlo algorithm on the power law transients as discussed in detail in Sec. 4.6

4.7 Analysis of the full time range

After we have studied the influence of the simulation parameters on the power law transients in detail in the previous section, we will focus on the reproduction of the

experimental transients in this section to understand and compare the recombination dynamics in our polar (In,Ga)N/GaN samples.

To recall, the average density of localization sites is set to a value of $1\,\mathrm{nm}^{-2}$ as discussed in Sec 4.6.1. From the excitation density employed for the time-resolved experiments, we estimate a charge carrier density of $\Delta n = \Delta p = 2.5 \times 10^{-3}\,\mathrm{nm}^{-2}$. The charge carriers are randomly distributed at localization sites at $t = 0$, and we do not allow one site to be occupied by more than one particle. Furthermore, as discussed in Sec. 4.6.2, the holes are localized at all temperatures ($D_p = 0$), but we allow for a finite diffusivity of electrons ($D_n = D$) at elevated temperatures. For simplicity, the nonradiative recombination coefficients for electrons and holes are set to be equal ($b_{n0} = b_{p0} = b_0$), and we assume that $N = N_\times$ at $t = 0$. Additionally, charge carriers, once captured by a nonradiative center, will not be released again.

Figures 4.12(a) and 4.12(b) show simulated transients (lines) in comparison to the experimental ones (symbols) displayed in Figs. 4.3(a) and 4.3(b), respectively. The input parameters used for these simulations are listed in Tab. 4.4. For a direct comparison with the simulated photon flux ϕ, the experimentally measured, spectrally integrated PL intensity I_{PL} is scaled by the same factor for both samples.

Let us first discuss the results for each sample separately. For the planar sample at 10 K, the experimental transient with its pronounced slowdown at 400 ns is only reproduced adequately when setting both the diffusivity and the nonradiative rate to zero, i. e., the simulated transient corresponds to the purely radiative recombination of localized electrons and holes [cf. Tab. 4.4 and Fig. 4.12(a)]. Thus, the peculiar slowdown of the decay is indeed a fingerprint for an IQE of unity, in agreement with our assumption in Secs. 4.2

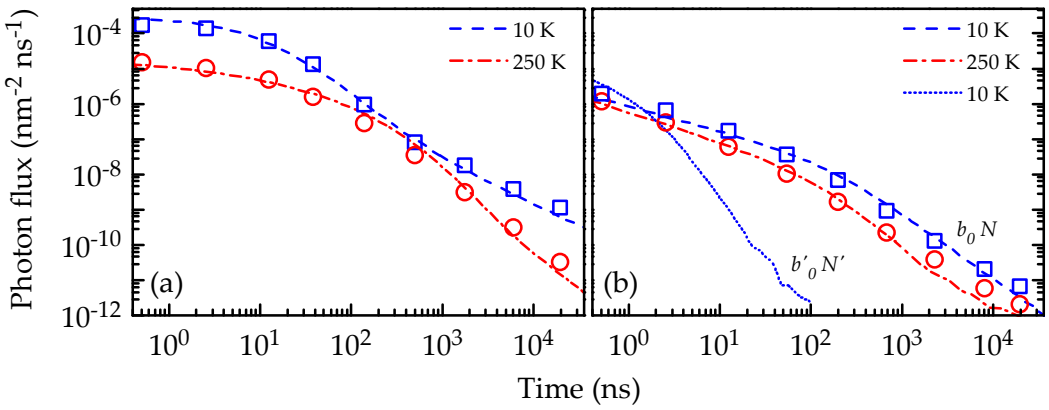

Figure 4.12: Double-logarithmic representation of simulated PL transient (lines) for the (a) planar and (b) nanowire sample. The transients were computed by means of Eqs. (4.3)–(4.5). The dotted line in (b) shows a transient for the nanowire sample at 10 K obtained with values for b_0 and N (namely, b'_0 and N') that keep the product constant (i. e., $b'_n N' = b_n N$). For comparison, a reduced number of experimental data points from the PL transients shown in Fig. 4.3 is added for 10 K (squares) and 250 K (circles) for both samples.

sample	T (K)	a (nm)	D (nm^2 ns^{-1})	B_0 (ns^{-1})	b_0 (ns^{-1})	N (nm^{-2})
planar	10	20	0	2×10^{-2}	0	3.1×10^{-4}
planar	250	8	2.00	1×10^{-3}	1.0×10^{0}	3.1×10^{-4}
nanowire	10	5 ± 2	0	1×10^{-2}	2.8×10^{2}	9.4×10^{-4}
nanowire	250	5 ± 1	0.05	1×10^{-2}	4.0×10^{2}	9.4×10^{-4}

Table 4.4: Parameters used for the Monte Carlo simulation of the temperature-dependent PL transients of the planar and the nanowire sample shown in Figs. 4.12(a) and 4.12(b), respectively.

and 4.3.[¶] At 250 K, the simultaneous loss in intensity and the acceleration of the decay are obtained by decreasing the radiative rate and enabling both electron diffusion and nonradiative recombination (see Tab. 4.4). The temperature dependence for the radiative and nonradiative processes are consistent with the respective lifetimes depicted in Fig. 4.2(b). Note that, although the power law decay is preserved, the nonradiative process eliminates the slowdown at 400 ns as also observed experimentally.

Regardless of temperature, the experimental transients of the nanowire sample are characterized by a complete absence of an initial exponential phase [see Fig. 4.2(a)]. The shape and intensity of these transients can only be reproduced by a dominant nonradiative process. We obtain the transients by assuming capture coefficients that are more than two orders of magnitude larger than those of the planar sample, while the density of the nonradiative centers is similar (this finding will be discussed in more detail below). The almost rigid downshift of the transient recorded at 250 K in Fig. 4.12(b) is obtained by a further increase of the capture rate, while the radiative recombination rate does not change at all. Note that the radiative rate is smaller than that observed for the planar sample, in agreement with the results in Tab. 4.1. In contrast to the more homogeneous planar sample, we include random variations of a (denoted by ±-sign in Tab. 4.4) to obtain better fits of the power law asymptote and to represent the strong ensemble fluctuations of the nanowires. Furthermore, diffusion is almost absent even at 250 K (see Tab. 4.4), which directly reflects that carrier localization is significantly stronger in the (In,Ga)N/GaN QDs than in the planar (In,Ga)N/GaN QWs. This result confirms the conclusions drawn from the results presented in Figs. 4.1(a) and 4.2(c) and is also in agreement with the study of Lähnemann *et al.* [43] on the same nanowire sample.

Finally, we discuss four important issues in connection with these simulations: (i) the physical origin of the slowdown in the experimental and simulated PL transients of the planar sample shown in Figs. 4.3(a) and 4.12(a), (ii) the different role of b_0 and N for the total nonradiative rate, (iii) the definition of a minority carrier diffusion length for (In,Ga)N, and (iv) the impact of carrier diffusion on the IQE.

(i) Figure 4.13 shows snapshots of the spatial distribution of electrons and holes during their radiative recombination resulting in the simulated PL transient at 10 K as shown in

[¶] As the In content is homogeneously distributed, large random fluctuations of a, resulting in a similar slowdown, can be excluded.

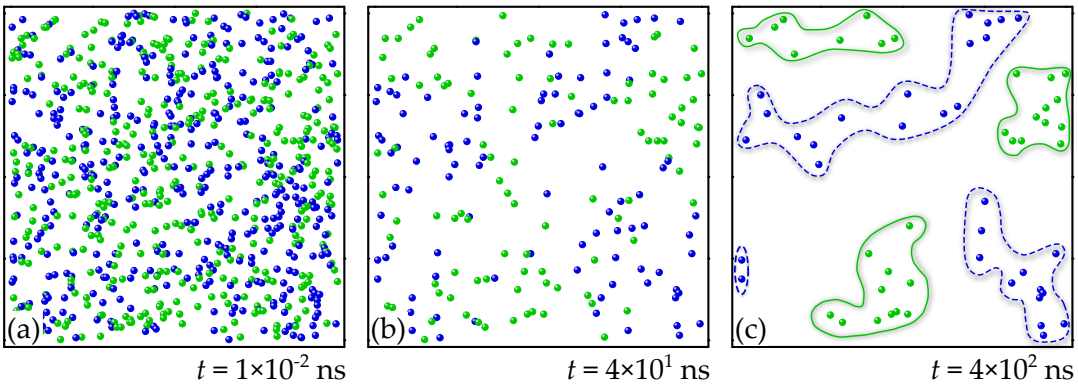

Figure 4.13: Snapshots of the distribution of electrons (green) and holes (blue) during the simulated decay of the PL intensity of the planar sample at 10 K. The snapshots are 400×400 nm^2 in size and were taken (a) right after excitation, (b) at 40 ns, and (c) at 400 ns, after which the decay slows down significantly. The emerging clusters of electrons and holes are encircled in (c) by solid and dashed lines, respectively. For clarity, we do not display the (inactive) nonradiative recombination centers, and we show electrons and holes as spheres of uniform size.

Fig. 4.12(a). Immediately after their excitation, electrons and holes are distributed randomly [see Fig. 4.13(a)]. Obviously, the electrons and holes most likely to recombine first are those with the least spatial separation. Hence, electrons in close vicinity to holes will disappear and vice versa. As a consequence, clusters of each individual species emerge from the initial random distribution as indeed seen in the snapshot shown in Fig. 4.13(b). These clusters become entirely spatially separated with subsequent recombination [see Fig. 4.13(c)], and it is at this point where the recombination slows down. This segregation phenomenon (resulting in the observed slowdown of the PL transient) only occurs in the absence of nonradiative recombination, since nonradiative centers (randomly distributed) couple the individual reservoirs, and of diffusion, which constantly redistributes the electrons and constitutes the rate-limiting step determining the speed of recombination.

(ii) For classical Shockley-Read-Hall recombination (see Sec. 2.3), the steady-state recombination rate is proportional to the product bN, and one cannot distinguish an increase in the density of nonradiative recombination centers from an increase of the capture coefficient.[142] In the present case, however, the impacts of $b = b_n = b_p$ and N is different and can be distinguished. This fact is illustrated by the simulated transient labeled $b_0'N'$ in Fig. 4.12(b), for which we assumed the same value for the capture coefficient as for the planar sample ($b_0 = 1\times10^0$ ns^{-1}), but increased N to the value required (2×10^{-2} nm^{-2}) to keep the product bN constant (taking into account that $|\mathbf{x}|$ equals asymptotically $1/2\sqrt{N}$). Evidently, the two transients computed with the same value of bN are drastically different. The origin of this different impact of b and N lies in the fact that the capture rate b depends exponentially on the density of the centers as well as of the carriers. A higher prefactor for the nonradiative capture coefficient is thus not equivalent to a higher density of nonradiative centers.

(iii) The precise shape of the power law decay depends sensitively on the carrier diffusiv-

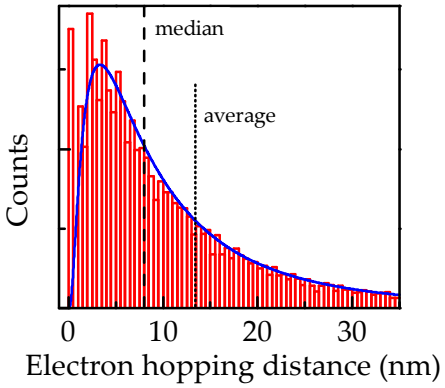

Figure 4.14: Simulated electron hopping distance corresponding to the planar sample measured at 250 K. Median and average value of the hopping distance are indicated by dashed and dotted lines, respectively. The solid line represents the probability density function of a log-normal distribution.

ity as was already discussed in Sec. 4.6.2 and shown in Fig. 4.8(a). Analyzing experimental transients by our recombination-diffusion model allows us to assess diffusion processes taking place on a nanometer scale without requiring any spatial resolution. In fact, even diffusivities as small as $10^{-5}\,\mathrm{cm^2\,s^{-1}}$ can be detected, a value too small to be resolved by most other techniques (see also Sec. 2.5). Note that this diffusivity cannot be translated into a diffusion length in the conventional sense since the diffusing species (i. e., the electrons) do not have a unique recombination time. Instead, both the recombination time of the electrons and their hopping distance within this recombination time are instantaneous quantities that vary over orders of magnitude with time. As shown in Sec. 4.6.2, we keep track of each individual electron including all of their elementary hops and recombination events in the frame of our Monte Carlo simulation. Averaging over all electrons in the simulation for a time up to 100 µs, we obtain an average hopping distance of 13 nm for the planar sample at 250 K. Note, however, that this hopping distance is not distributed normally as demonstrated in Fig. 4.14. Some electrons migrate over distances larger the 50 nm, whereas a noticeable portion of electrons do not hop even once before they recombine.[‖] In the nanowires, the average hopping distance (on the order of 1 nm) is negligible due to the smaller value of D and the much faster (nonradiative) recombination process limiting the recombination times of the electrons.

Utilizing the relationship of $L = \sqrt{D\tau}$ with $D = 2\,\mathrm{nm^2\,ns^{-1}}$ and the average (median) effective lifetime of the electrons of $\tau_{\mathrm{avg}} \approx 221$ ns ($\tau_{\mathrm{median}} \approx 22$ ns) for the planar sample at 250 K [see Fig. 4.9(d)] results in the average (median) hopping distance of the electrons of $L_{\mathrm{avg}} \approx 21$ nm ($L_{\mathrm{median}} \approx 7$ nm). Both values are close, but not identical to the ones extracted from Fig. 4.14. Again, this indicates that average lifetimes are only crude approximations to a power law decay.

(iv) Intuitively, one expects a monotonic increase of the IQE with increasing excitation density [see Fig. 4.10(b)], decreasing density of recombination centers [see Fig. 4.8(c)], or smaller (nonradiative) capture coefficients. Our model actually confirms this expectation. However, the impact of diffusion on the IQE is not as straightforward. In general, diffusion processes accelerate the decay of the PL intensity as shown in Fig. 4.6 in Sec. 4.6.2. For

[‖] In contrast to the distribution of the hopping distance of particles without additional recombination mechanisms [see Fig. 4.7(d)], the distribution of the electron hopping distance corresponding to power law transients cannot be approximated by a log-normal distribution.

the parameters used for simulating the transient for the planar sample at 250 K, the diffusion of electrons is found to *enhance* the IQE since it favors radiative recombination of neighboring electrons and holes in the initial phase of the PL decay over a capture by the nonradiative centers at a later stage [see Figs. 4.8(a) and 4.8(c) in Sec. 4.6.2]. The opposite situation occurs for a sufficiently high density of nonradiative recombination centers and the simultaneous diffusion of electrons and holes, for which diffusion enhances nonradiative over radiative recombination and thus results in a *reduction* of the IQE.

4.8 Summary, conclusions, and outlook

Our comparison of the recombination dynamics of Ga-polar planar (In,Ga)N/GaN QWs and N-polar (In,Ga)N/GaN QDs in nanowires has resulted in several important insights. First of all, we have shown that the recombination dynamics in the latter structures is characterized by both strong carrier localization and a highly efficient nonradiative decay channel. Using the ratio of the PL intensities at high and low temperatures as a measure for the IQE may result in grossly overestimated values, and may thus be entirely misleading. The actual IQE of the (In,Ga)N/GaN QDs is low ($\approx 0.5\,\%$) even at 10 K, but decreases only slightly to about 0.2 % at 250 K thanks to the fact that localization prevails up to high temperatures. These values are consistent with the low EQEs reported for (In,Ga)N/GaN$(000\bar{1})$-based nanowire LEDs.[354,399,400] They are also consistent with the peak EQE of 0.055 % measured for LEDs that have been fabricated from nanowire ensembles comparable to the one investigated in this thesis.[401]

An alternative and more reliable method to quantitatively investigate the IQE as well as carrier diffusion is the analysis of the PL transient recorded with time-correlated single photon counting over a time interval sufficient to yield a high dynamic range in intensity. For both (In,Ga)N/GaN(0001) QWs and (In,Ga)N/GaN$(000\bar{1})$ QDs, a power law decay is observed, reflecting that recombination occurs between individual electrons and holes with different spatial separation. The PL transient of the QWs at 10 K exhibits a characteristic slowdown after about 400 ns, which we have found to be a fingerprint of purely radiative recombination. Nonradiative recombination and carrier diffusion set in at 250 K and eliminate this slowdown, but the power law decay is preserved. Even the much faster nonradiative recombination in the QDs does not result in a faster overall decay. A slow decay is thus not a reliable indicator for a high IQE. However, the shape of the transients observed for the QDs is quite different from that of the QWs and can be reproduced in simulations only when assuming recombination centers with very high capture coefficients. It seems likely that these centers are identical to those hypothesized to be responsible for the complete lack of an (In,Ga)N$(000\bar{1})$-related band in the PL spectra of planar (In,Ga)N/GaN$(000\bar{1})$ QWs grown by MBE.[402–404] In both cases, these centers are most probably related to native point defects or defect complexes, but their actual nature still remains to be identified. In any case, the strong localization effects observed for QDs in nanowires[43] may help a small fraction of the carrier population to evade nonradiative annihilation and may thus prevent the total dominance of nonradiative

processes observed for homogeneous (In,Ga)N/GaN(000$\bar{1}$) QWs.

Our study in this chapter has, however, not only provided insights into the eligibility of N-polar (In,Ga)N/GaN nanowires for the use in future light emitters, but has also contributed to the understanding of the recombination processes of materials used presently for commercial devices. Just as in (In,Ga)N/GaN(000$\bar{1}$) QDs, the dominating recombination in (In,Ga)N/GaN(0001) QWs occurs between individually localized, spatially separated electrons and holes. The recombination rates, whether radiative or nonradiative, thus depend strongly (in fact exponentially) on the carrier density. This dependence manifests itself in the highly nonexponential nature of the PL decay with its power law asymptote. Obviously, analyzing the luminous efficiency of a material with these characteristics by means of a model with constant recombination coefficients (i. e., the popular *ABC* model [31,405]) will lead to misleading results, as was recently also pointed out by Badcock *et al.* [272] In addition, carrier diffusion has been found to occur at elevated temperatures and to affect the IQE, but is neglected in the *ABC* model (see Sec. 2.6.1) altogether. For understanding the origin of the droop of the EQE as well as the green gap in actual LEDs, models are required that go beyond the crude approximation offered by the *ABC* model and properly describe the carrier dynamics in the material under consideration. The diffusion-reaction equations employed in this chapter constitute a clear physical framework on which such a more general model could be based.

Chapter 5

Comparison of localization mechanism

Due to the absence of the internal electric field, (In,Ga)N/GaN heterostructures grown along the nonpolar crystal direction of GaN have attracted considerable attention. However, nonpolar GaN substrates are expensive and not suited for mass production. Recently, the growth of (In,Ga)N/GaN QWs on the nonpolar side facets of GaN µ-rods has led to the fabrication of cost-effective and efficient LEDs. The PL transients are single exponential in such core-shell heterostructures, indicating that the recombination is excitonic. This finding is in striking contrast to the recombination of individual electrons and holes in polar QWs characterized by a power law PL decay. We suggest that the reduced influence of well-width fluctuations on the individual localization of charge carriers in nonpolar QWs prevents the dissociation of localized excitons.

5.1 Nonpolar (In,Ga)N/GaN heterostructures

5.1.1 Planar layers versus core-shell µ-rods

In the previous chapter, we have analyzed the effect of the localization of charge carriers in polar (In,Ga)N/GaN heterostructures on the PL properties in detail. We have found that recombination takes place via tunneling between spatially separated electrons and holes. According to Schulz *et al.*,[68] we attribute the dissociation of excitons and the subsequent individual, spatially separated localization of electrons and holes in polar (In,Ga)N/GaN QWs to the enhanced influence of well-width fluctuations and the reduced exciton binding energy. Both effects are a consequence of the large internal electric fields in the polar QWs. However, internal electric fields are absent in QWs grown along the nonpolar crystal direction, e. g., on *M*-plane GaN.[406] Without spontaneous and piezoelectric polarization fields (see, e.g., Ref. 407 and references therein), also the quantum-confined Stark effect does not exist in nonpolar QWs. Thus, the transition energy as well as the overlap of the electron and hole wave functions and accordingly the recombination rates increase significantly for a given In content.[406],* Recently, exponential PL decays with lifetimes on

*See also the one-dimensional Schrödinger-Poisson calculations in Fig. 2.2 in Sec. 2.1.

the order of 0.5 ns have been reported for nonpolar GaN and (In,Ga)N/GaN QWs.[408–414] Thus, (In,Ga)N/GaN QWs grown along the nonpolar direction are an interesting test bed to study the recombination of charge carriers in the random alloy (In,Ga)N without the complications due to the internal electric fields.

Nonpolar GaN buffer layers for the subsequent growth of (In,Ga)N/GaN QWs can be grown on either γ-$LiAlO_2$(100),[406,407] resulting in films with a high density of stacking faults, or on expensive and small *M*-plane bulk GaN substrates diced from around 6 mm-thick GaN(0001) wafers. These free-standing GaN layers, grown by hydride vapor phase epitaxy, exhibit a high crystal quality with dislocation densities on the order of $10^5\,cm^{-2}$,[7,415,416] enabling the growth of (In,Ga)N/GaN heterostructures with high structural perfection. Although nonpolar LEDs and laser diodes based on (In,Ga)N/GaN QWs have been demonstrated already in 2005[417,418] and 2007,[419] the lack of suitable substrates has limited the application of nonpolar, planar LEDs to basic research up to now.[420–422]

It has been reported that, for a given substrate temperature, the incorporation of In is lower along the nonpolar crystal direction than for the polar or the semipolar ones.[423–426] In contrast, the authors in Ref. 427–430 have shown that the incorporation of In during growth is similar for the polar and nonpolar crystal directions. By comparing the experimentally measured transition energies with results obtained from $\mathbf{k}\cdot\mathbf{p}$-calculations, Wernicke *et al.*[429] concluded that the absence of the quantum-confined Stark effect and the effect of anisotropic strain in the (In,Ga)N/GaN QWs cause the high transition energies in nonpolar QWs compared to their polar counterparts (i. e., 3.0 eV instead of 2.6 eV for an In content of 18 %).

In order to fabricate coherently strained, nonpolar (In,Ga)N/GaN heterostructures in the desired green spectral range, partially relaxed (Al,In)N interlayers have recently been used to allow for an In incorporation of up to 40 %.[422] Thus, the fabrication of nonpolar, planar LEDs emitting in the green spectral range is technologically even more difficult than for polar LEDs. Recently, Davies *et al.*[431] have reported that droop occurs in optimized (In,Ga)N/GaN structures grown along the polar as well as along the nonpolar crystal direction. The sum of these complications makes nonpolar, planar (In,Ga)N-based LEDs unattractive for standard applications in solid-state lighting when compared to their optimized polar counterparts grown on inexpensive six-inch sapphire substrates.[†]

The situation is different for nonpolar GaN/(In,Ga)N core/shell heterostructures. Here, (In,Ga)N QWs are grown around GaN µ-rods as shown schematically in Fig. 5.1. Commonly, Ga-polar GaN µ-rods are realized by selective-area growth using a patterned SiO_x mask on a GaN buffer on sapphire substrates.[433,434],[‡] Extended defects such as strain-induced dislocations propagate to the sidewalls of the µ-rods during the initial phase of the growth,[438,439] leading to a high structural perfection of the upper parts of the µ-rod.

[†]Note that SORAA® produces and sells LEDs grown on polar bulk GaN for advanced illumination purposes. Benefiting from the high quality of the substrate, these LEDs are characterized by extremely high EQEs especially at high current densities.[340,432]

[‡]GaN µ-rods can be also produced by Au-assisted vapor-liquid-solid growth[435] or by wet chemical etching of thick GaN buffers using a colloidal mask.[436,437]

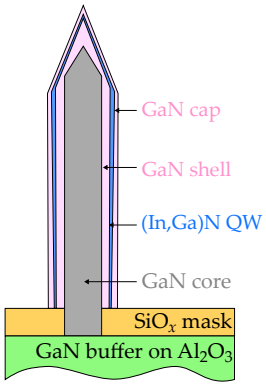

Figure 5.1: Schematic of an GaN/(In,Ga)N core/shell heterostructure in the form of a µ-rod grown by selective-area epitaxy on a GaN buffer on an Al_2O_3 substrate.

After the growth of the core, QWs are deposited on the nonpolar sidewalls of the µ-rods by MBE (see, e. g., Ref. 440) or MOCVD (see, e. g., Ref. 75). A review on LEDs based on µ-rods can be found in Ref. 441.

In addition to the low cost of the substrates and the high structural perfection of the µ-rods, these structures exhibit a large surface area since an aspect ratio of 40 can be realized.[75] The larger surface area leads to a reduced carrier density inside the QWs and hence a reduced droop per device area compared to planar structures. Moreover, the µ-rod LEDs exhibit a superior light extraction efficiency of 30 % without any additional structuring.[439] Another advantage of GaN/(In,Ga)N core/shell µ-rods is the realization of full-color emission on a single substrate by adjusting the diameter of the µ-rods.[442] A first commercialization of monolithic (red, green, and blue) RGB LED chips is expedited by glō®.[443] White-light emission can be achieved by utilizing optimized micrograin phosphors with blue emitting µ-rods as the pump source.[439] At present, however, the EQE of the µ-rods with a 5-nm-thick nonpolar single (In,Ga)N QW is estimated to be about 10 %, which is partly attributed to high reabsorption.[75] Additionally, the small radiative recombination coefficient and the short nonradiative lifetime cause an IQE below 40 %.[444] Recently, higher IQEs of about 70 % have been reported for µ-rods with a multi-QW core-shell structure.[445]

5.1.2 Photoluminescence spectroscopy of GaN/(In,Ga)N core/shell µ-rods

As outlined above, GaN/(In,Ga)N core/shell µ-rods are a promising alternative to planar LEDs. However, the origin of the low IQE has to be identified and carefully investigated to optimize these core-shell structures. Therefore, an understanding of the underlying recombination processes and the localization mechanism is essential. We utilize steady-state and pulsed excitation to explore the PL properties of GaN/(In,Ga)N core/shell µ-rods containing a single QW and emitting in the blue spectral range. The sample was grown by MOCVD in an industrial reactor at OSRAM Opto Semiconductors GmbH in 2015. More details about the growth and the sample as schematically depicted in Fig. 5.1 can be found in Refs. 74 and 433.

In the following, we present the results of steady-state µ-PL spectroscopy of single GaN/(In,Ga)N core/shell µ-rods, dispersed on a Si substrate, using nonresonant excita-

tion ($E_{\text{laser}} = 3.814\,\text{eV}$) with a power density of $I_{\text{exc}} \approx 200\,\text{W/cm}^2$. A color-coded, spatially resolved map of the PL peak energy is presented in Fig. 5.2(a). The peak energy decreases by about 100 meV from the bottom to the pencil-shaped tip of the Ga-polar µ-rod. Detailed investigations with various techniques (e. g. transmission electron microscopy or nanofocus x-ray diffraction) on similar samples have correlated this effect with an increase of In content and thickness of the QW along the µ-rod.[74,444,446–450] The reduced incorporation of In due to the reduced gas diffusion down to the base of the µ-rods, especially at low growth temperatures, has been identified to be the main reason for the increasing transition energy at the bottom of the µ-rod (see Ref. 448 and references therein).

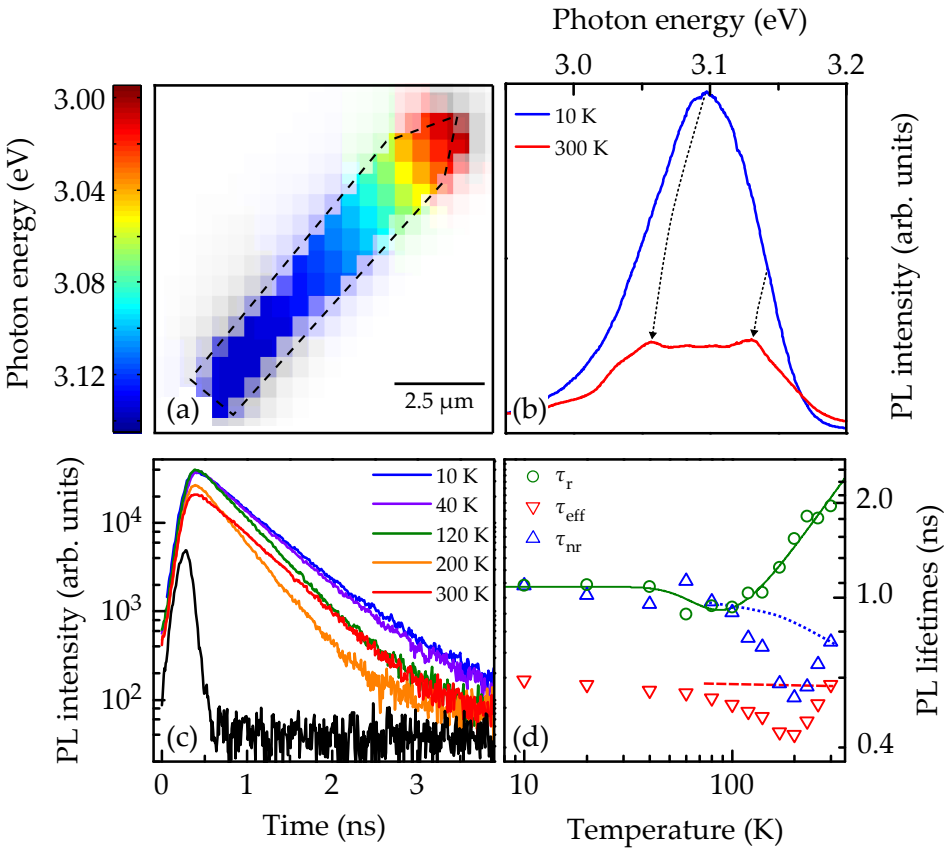

Figure 5.2: (a) Color-coded map of the spatially resolved peak energy measured with steady-state PL at 10 K. The profile of the µ-rod is indicated by the dashed line. The redshift of the PL band due to the quantum-confined Stark effect in the semipolar facets is visible at the pencil-shaped top of the µ-rod. (b) Representative steady-state PL spectra of the center of a µ-rod recorded at 10 and 300 K. The dotted arrows indicate the evolution of two dominant PL bands with increasing temperature. (c) Temperature-dependent PL transients of a single µ-rod on a semilogarithmic scale. The response of the system to the laser is given in black. (d) Temperature-dependent effective (τ_{eff}), radiative (τ_{r}), and nonradiative (τ_{nr}) PL lifetimes. The behavior of τ_{r} with temperature is fitted using Eq. (2.29) (solid line). Dashed and dotted lines indicate the assumed temperature-dependent lifetimes for a homogenous QW with a low In content as explained in the text.

At low temperatures, we observe an asymmetric PL band with a rather large FWHM of 80 meV [see Fig. 5.2(b)] which can be explained by the fact that we spatially average the PL signal over an area in the center of the μ-rod of as large as 1 μm^2. At 300 K, the asymmetric PL band splits into two bands with a combined FWHM of about 160 meV. Thus, the individual PL bands do not broaden significantly. The dashed lines in Fig. 5.2(b) indicate a severe quenching of the low energy band compared to the peak at higher energy. This finding may, analogously to polar QWs, be a direct consequence of a lower structural quality of (In,Ga)N with higher In content.[444] By raising the temperature from 10 to 300 K, the spectrally integrated PL intensity is reduced by a factor of 2 only.

In Fig. 5.2(c), we show temperature-dependent PL transients of a single μ-rod dispersed on Si utilizing a streak camera. For the time-resolved PL measurements presented in this chapter, the samples have been excited nonresonantly with a photon energy of 3.55 eV and an energy fluence per pulse of about 2 $\mu J/cm^2$ by utilizing the setup described in detail in Sec. 3.4.2. Due to the limited spatial resolution ($6 \times 4\ \mu m^2$), the transient originates from almost the entire μ-rod. However, by a careful positioning of the laser spot and simultaneously monitoring the PL spectrum, we avoid the excitation of the semipolar facets. The PL transients reveal a single exponential decay,[§] indicating the recombination of excitons as also observed by other groups.[421,451] Based on the atomistic theory for polarization fields in the random alloy (In,Ga)N,[386] Schulz *et al.* [368] have shown that localized excitons are predominant in QWs grown along the nonpolar direction due to Coulomb interactions and reduced localization mechanism for electrons.[68,368] The formation of excitons in the random alloy (In,Ga)N is in sharp contrast to the recombination of individual electrons and holes in polar (In,Ga)N/GaN QWs as shown in Sec. 4.1.

By fitting the PL transient with a single exponential function, we extract an effective PL lifetime τ_{eff} of 0.5 ns at 10 K. The value of τ_{eff} decreases slightly to 0.4 ns with increasing temperature up to 200 K [see Fig. 5.2(d)]. Above 200 K, τ_{eff} surprisingly increases which we will discuss at the end of this section. Lifetimes of 1 ns, obtained with time-resolved cathodoluminescence, have been reported for μ-rods similar in QW width and In content.[410] Assuming that IQE = 1 for these rods measured at 4 K, τ_r = 1 ns. Note that for an excitonic recombination the assumption of a material-dependent value of τ_r is justified. Utilizing the absolute value of τ_r = 1 ns, we obtain an IQE of η = 0.5 at 10 K by using Eq. (4.2). We deduce the temperature dependence of τ_r from the inverse of the maximum PL intensity[180] which results in an IQE of 0.25 at 300 K. Note that the extracted values for the IQE are average values as the actual IQE depends on the In content and hence on the position along the μ-rod.[444,445] We note that the nonradiative lifetime (τ_{nr}), calculated by means of Eq. (4.1), becomes faster than τ_r above 100 K.

Independent of the absolute values, we observe in Fig. 5.2(d) that τ_r is independent of temperature up to 150 K and increases linearly thereafter. According to the relationship between the radiative lifetime and the dimensionality of the system as derived in Sec. 2.3.4, excitons are localized in a zero-dimensional potential (at random compositional

[§]In Sec. 5.2, we show transients recorded with time-correlated single photon counting with a high dynamic range.

fluctuations or In clusters[65]) below 150 K. Above this temperature the excitons are delocalized and experience the two-dimensional confinement of the QW. Additionally, our findings of localized excitons up to 150 K are in agreement with atomistic simulations indicating localization not only for the ground state, but also for excited states.[452,453] As we are dealing with excitons, we utilize Eq. (2.29) to deduce a localization energy of $E_{\mathrm{loc}} = 30\,\mathrm{meV}$ from τ_{r} [solid line in Fig. 5.2(d)].

The picture of excitonic recombination influenced by random compositional fluctuations is underlined by recent time-resolved cathodoluminescence data of core-shell µ-rods. Utilizing a tunneling model for excitons,[454,455] Shahmohammadi *et al.*[410] explain their spectrally and spatially resolved cathodoluminescence transients by a thermalization of excitons through a hopping/diffusion process between localization centers.[410] Furthermore, they exclude a significant drift of charge carrier to regions with higher In content. However, the diffusion of electrons without significant drift is possible only, when excitons exhibit a limited mobility in the form of a hopping process between potential minima in a fluctuating potential landscape. Hence, localization does not influence the recombination mechanism which stays excitonic as in the case of GaN, but affects the diffusion of excitons.

As mentioned above, our PL signal is spatially averaged. Thus, the effective PL lifetime may be a superposition of different regions of the µ-rod which were found to exhibit different IQEs.[444] When the excitons become mobile above 150 K, regions with higher In content (lower IQE) should attract excitons, which recombine predominantly nonradiative. Accordingly, the decrease of τ_{eff} above 100 K is attributed to excitons causing the low energy peak that dominates the PL spectrum up to 200 K. Above 200 K, however, the slowly decaying excitons in regions of low In content (high IQE / high peak energy) dominate τ_{eff}. This argument is in agreement with the minor decrease of the intensity of the high-energy PL band compared to that of the low-energy PL band observed in Fig. 5.2(b). Accordingly, τ_{eff} and τ_{nr} of the excitons recombining at the bottom part of the µ-rod actually follow the dashed and dotted lines indicated in Fig. 5.2(d), respectively. Hence, the dip of τ_{eff} originates from the spatial averaging over the inhomogeneous µ-rod and the suppression of the diffusion due to the potential landscape.

5.2 Influence of electric fields and exciton binding energy

Both polar and nonpolar (In,Ga)N/GaN heterostructures are influenced by localization, but the recombination mechanisms are fundamentally different. In the following, we will show that it is energetically favorable for the excited electrons and holes to form excitons in nonpolar (In,Ga)N/GaN QWs, while electrons and holes localize at individual and spatially separated positions in polar (In,Ga)N/GaN QWs.

The relevant physical mechanism to form excitons is the gain of energy in the form of exciton binding energy E_{X} (see Sec. 2.3.1). Hence, excitons will dissociate if E_{X} is lower than the energy gained by the individual localization of electrons and holes into spatially

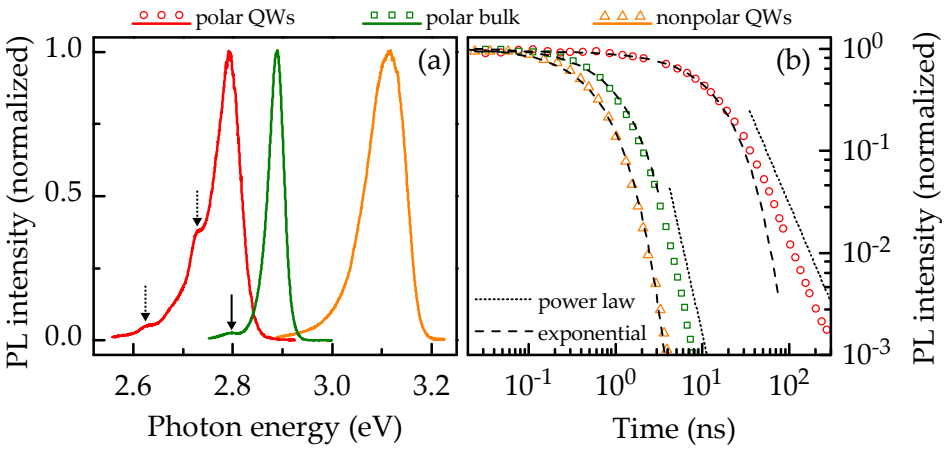

Figure 5.3: Low-temperature (a) steady-state PL spectra and (b) PL transients of polar and nonpolar (In,Ga)N/GaN QWs as well as Ga-polar bulk (In,Ga)N grown on GaN-buffered Al_2O_3. The samples have been excited nonresonantly with moderate excitation densities to avoid a screening of the internal electric fields. The dotted and solid arrows in (a) indicate oscillations due to interference effects and a longitudinal optical phonon replica, respectively. In (b), the dotted lines indicate the power law asymptote, while the dashed lines represent single exponential fits to the data.

separated potential minima E_{loc}.[48,456,457],¶ According to Schulz *et al.*,[68] electrons localize predominately at monolayer fluctuations of the well-width in polar (In,Ga)N/GaN QWs, while holes localize at In clusters of atomic size (caused by random compositional fluctuations) due to their large effective mass.[68,368] Thus, we assume E_{loc} to be the sum of the different contributions of electron ($E_{\mathrm{e,loc}}$) and hole ($E_{\mathrm{h,loc}}$) localization energy. If the In content is distributed randomly in the QWs (i. e., no significant In clustering), the hole localization energy should be the same for polar and nonpolar crystal orientation, as it is not influenced by the internal electric fields.[368] However, the influence of well-width fluctuations, causing the localization of electrons, is much stronger in Ga-polar QWs compared to nonpolar ones (see Sec. 2.4). In the case of a (In,Ga)N bulk grown along the polar direction, charge carriers experience the influences of internal electric fields and thickness fluctuations only close to the interfaces, which represent only a minor fraction of the active volume.

Therefore, we select three samples for our comparison: A Ga-polar (In,Ga)N/GaN heterostructure with five QWs, the nonpolar GaN/(In,Ga)N core/shell µ-rod investigated in the preceding section, and a 40-nm-thick Ga-polar (In,Ga)N bulk. The selected samples are representative for their respective type and exhibit comparable concentrations of In. Therefore, the PL bands peak in a similar spectral region, ranging from violet to blue.‖ The normalized low-temperature steady-state PL spectra of these three samples are shown in

¶Note that the exciton may localize as entity at low temperatures, gaining exciton localization energy. In the following, this fact is neglected for simplicity.

‖Because of the absence of the quantum-confined Stark effect, the nonpolar QWs emits at higher energies than the polar ones with a similar In content.[429]

Fig. 5.3(a). The FWHM of the polar QWs and the polar bulk sample are comparable. The nonpolar QWs seem to exhibit larger compositional fluctuations as indicated by the rather large FWHM. This observation is in agreement with recent findings by a transmission electron microscope-cathodoluminescence study on similar samples.[65,448] However, a significant contribution to the FWHM of the PL spectrum directly originates from the fact that the In content exhibits a macroscopic gradient along the axis of the µ-rod as shown in Sec. 5.1.2. Thus, we believe that the magnitude of the random compositional fluctuations is similar in all samples.

Figure 5.3(b) shows PL transients of the three samples recorded with time-correlated single photon counting at 10 K. The transients were recorded at the respective peak energies integrated over a spectral range of about 20 meV. While the transients of the nonpolar QWs clearly follow a single exponential function (dashed line) over at least three orders of magnitude, the transients of the polar QWs obey a power law (dotted line) after an initial exponential phase. As mentioned in Secs. 4.7 and 5.1.2, the decay is dominated by tunneling recombination of spatially separated electrons and holes for polar (In,Ga)N/GaN QWs, but by exciton recombination for nonpolar ones. As expected from the discussion in this subsection, the thick, but fully strained,[458,459] polar (In,Ga)N bulk reflects an intermediate case. The transient is single exponential over 1–2 orders of magnitude and subsequently obeys a steep power law decay. The recombination may be caused predominantly by (localized) excitons (far from the interfaces) recombining in the first 3–4 ns of the decay. As the decay proceeds, spatially separated electrons and holes close to the interface cause the power law asymptote. A slower power law decay may be excluded, because threading dislocation in the (In,Ga)N bulk sample are not entirely screened by V-shaped pits as in the case of optimized QWs[269,458] and therefore act as nonradiative centers. Our experimental observations of the decay shape are summarized in Tab. 5.1.

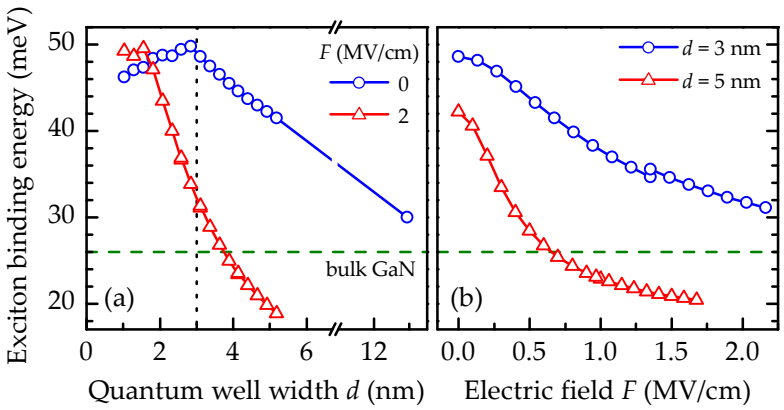

Figure 5.4: Dependence of the exciton binding energy on (a) quantum well width d and (b) internal electric field F for an (In,Ga)N/GaN QW with an In content of 23 %. The exciton binding energy has been calculated by the variational method.[125] The calculations were performed by P. Corfdir. The typically used thickness for a polar QW (d = 3 nm) is indicated by a vertical line in (a). The exciton binding energy of bulk GaN[108,113–116] is highlighted by horizontal lines in both graphs.

To estimate E_X in our samples, we have performed variational calculations following the approach presented in Ref. 125 for QWs with an In content of 23 %. We note that the trends for the performed calculations are similar for lower In contents. Moreover, even absolute values of E_X are similar (deviation below 5 meV) for QWs with In contents in the range of 10–30 % as shown in Ref. 460. Thus, we estimate the exciton binding energy for all samples from the calculations presented in Fig. 5.4. In Fig. 5.4(a) we show E_X versus the thickness (d) of a QW for two values of the internal electric field F. For nonpolar QWs with d of about 3 nm, E_X can be as high as 50 meV. In contrast, for typical values of F on the order of 2 MV/cm, E_X monotonically decreases for d larger than 1 nm and amounts to $E_X = 32$ meV for conventional 3-nm-thick QWs. In the case of a field-free bulk (In,Ga)N, i. e., $F = 0$ and $d \gg 10$ nm, E_X approaches the values of bulk GaN (i. e., 26 meV [108,113–116]) as the absence of the confinement lowers E_X. Figure 5.4(b), in which we present E_X over F for two values of d, demonstrates that the internal electric field significantly reduces E_X (factor of 1.6 or 2.1 for a 3- or 5-nm-thick QW).

Qualitatively, we estimate the ratio between the exciton binding energy E_X and the localization energy E_{loc} from the shape of the transients presented in Fig. 5.3(b) as summarized in Tab. 5.1. We assume that $E_X < E_{loc}$ for nonpolar QWs, while the opposite is the case for polar QWs. E_X has to be similar to E_{loc} in the polar bulk (In,Ga)N to explain the significant initial exponential part as well as the power law asymptote of the PL decay. As already mentioned at the beginning of this section, we presume $E_{loc} = E_{e,loc} + E_{h,loc}$.

sample	observation and energy relation	estimated E_X (meV)	influence of well-width fluctuations
nonpolar QW	single exponential decay over several orders of magnitude: $\rightarrow E_X > E_{loc}$	42	well-width fluctuations without internal fields: $E_{e,loc} < 5$ meV for a 5-nm-thick QW with 15 % In $\Longrightarrow E_{loc} \approx E_{h,loc}$
polar QW	almost no single exponential part; dominant power law decay: $E_X < E_{loc}$	32	well-width fluctuations with internal fields: $E_{e,loc} \approx 40$ meV for a 3-nm-QW with 15 % In $\Longrightarrow E_{loc} = E_{h,loc} + E_{e,loc}$
polar bulk	single exponential decay over 1–2 orders of magnitude; subsequent steep power law decay: $E_X \approx E_{loc}$	26	no well-width fluctuations: $\Longrightarrow E_{loc} = E_{h,loc}$

Table 5.1: Comparison of the influence of the exciton binding energy E_X and the localization energy E_{loc} for polar and nonpolar (In,Ga)N/GaN QWs as well as polar bulk (In,Ga)N. The values for E_X have been obtained as described in the text. The estimation of well-width fluctuations on E_{loc} is based on one-dimensional Schrödinger-Poisson calculations (see Sec. 3.3) as described in Sec. 2.4.1.

Starting with the assumption that the influence of localized electrons at well-width fluctuation is negligible in polar bulk (In,Ga)N (i. e., $E_{e,loc} = 0$) and that E_X exhibits the same value as bulk GaN, we can approximate the contribution of the holes to the localization energy with $E_{loc} = E_{h,loc} \approx E_X = 26\,meV$. Because the structural quality of the investigated samples is similar as discussed above, we assume $E_{h,loc}$ to be similar for all samples.

In contrast to bulk (In,Ga)N, we have to consider the impact of well-width fluctuations for the samples containing QWs. We use a Schrödinger-Poisson solver[305] to estimate the additional potential for charge carriers created by the well-width fluctuations (see also Secs. 2.4 and 3.3). For a 5-nm-thick nonpolar QW with an In content of 10 %, the additional potential amounts to less than 5 meV, while the additional potential is approximately 40 meV in the sample containing Ga-polar QWs with a similar In content. Consequently, in the case of a nonpolar QWs $E_{loc} \approx E_{h,loc} \approx 26\,meV$. This value is in fair agreement with $E_{loc} = 30\,meV$ determined from the temperature-dependent radiative lifetime of the nonpolar µ-rods in Sec. 5.1. Moreover, $E_X > E_{loc}$ in the nonpolar QW so that excitons form. However, in the Ga-polar QWs, E_{loc} is dominated by the contribution of the electrons, and, because of $E_{loc} > E_X$, the recombination occurs between individual, spatially separated electrons and holes.

5.3 Summary and conclusions

Core/shell GaN/(In,Ga)N µ-rods are a promising alternative to replace planar GaN-based LEDs due to the enhanced active volume per surface area. However, steady-state PL experiments reveal a macroscopic gradient of the In content along the µ-rod causing a rather broad luminescence band and position-dependent PL intensities. Nonetheless, we observe a single exponential decay over several orders of magnitude utilizing time-resolved PL. The temperature dependence of the radiative lifetime, extracted from the PL transients, shows that excitons are localized at low temperatures and delocalized at elevated temperatures ($T > 150\,K$).

From a comparison of nonpolar and Ga-polar QWs with a Ga-polar bulk (In,Ga)N, we estimate the influence of the exciton binding energy and localization energy on the different shapes of the decay. The combination of a low exciton binding energy and a large localization energy of electrons in the polar QWs, both caused by the presence of large internal electric fields, leads to the recombination of spatially separated electrons and holes. In contrast, the formation of excitons with short radiative lifetimes is a consequence of the large exciton binding energy in the field-free nonpolar (In,Ga)N/GaN QWs in the µ-rods. However, the low IQE of the µ-rods, compared to polar reference samples, may be linked to the fact that not only the radiative recombination rate increases, but also the nonradiative rate. Point defects in potential minima (higher In content) may trap charge carriers more efficiently in nonpolar QWs, because electrons and holes are present as an entity (exciton), which is not the case for polar QWs. Thus, a low density of nonradiative defects seems to be more important for QWs grown along the nonpolar crystal direction.

Chapter 6

Impact of an external reverse bias on the recombination mechanism

Applying a reverse bias to a Ga-polar (In,Ga)N/GaN LED, enables us to systematically tune the band profile and reduce the internal electric field in the QWs. We observe a blueshift of the PL band accompanied by a decrease of the integrated PL intensity. Taking thermionic emission and tunneling escape into account, we explain the resulting excitation-energy-dependent photocurrent by an extraction of the charge carriers from the active region before they relax to the ground state. Utilizing time-resolved PL spectroscopy, the decrease of the internal electric fields in the QWs manifests itself by a marked decrease of the radiative PL lifetime (larger overlap of electron and hole wave functions) and a gradual transition from PL transients that asymptotically obey a power law to an exponential decay. Thus, the decay mechanism changes from tunneling recombination of individual, spatially separated electrons and holes to an excitonic recombination. However, not only the radiative rate increases, but also the nonradiative rate, which we attribute to the simultaneous spatial presence of electron-hole pairs.

6.1 General concept and band profile simulation

In the preceding chapter, we have suggested that the internal electric field, influencing the exciton binding energy, is one of the main factors for determining the recombination mechanism. In fact, we observe tunneling recombination of spatially separated electrons and hole in polar and excitonic recombination for nonpolar (In,Ga)N/GaN QWs (see Sec. 5.2). However, this distinct difference may also originate from a different localization strength in these samples (because the crystallographic planes are not equivalent, which may influence the incorporation of In), and it would thus be desirable to study the impact of the internal field on the recombination mechanism in one and the same sample. For this purpose, we apply a reverse bias to the Ga-polar LED emitting in the green spectral range, introduced in Sec. 3.5.2.

Applying a reverse bias to similar samples, results in a blueshift of the PL band and a higher overlap of the electron and hole wave functions that have been attributed to a reduction of the internal piezoelectric fields and hence a reduction of the quantum-confined

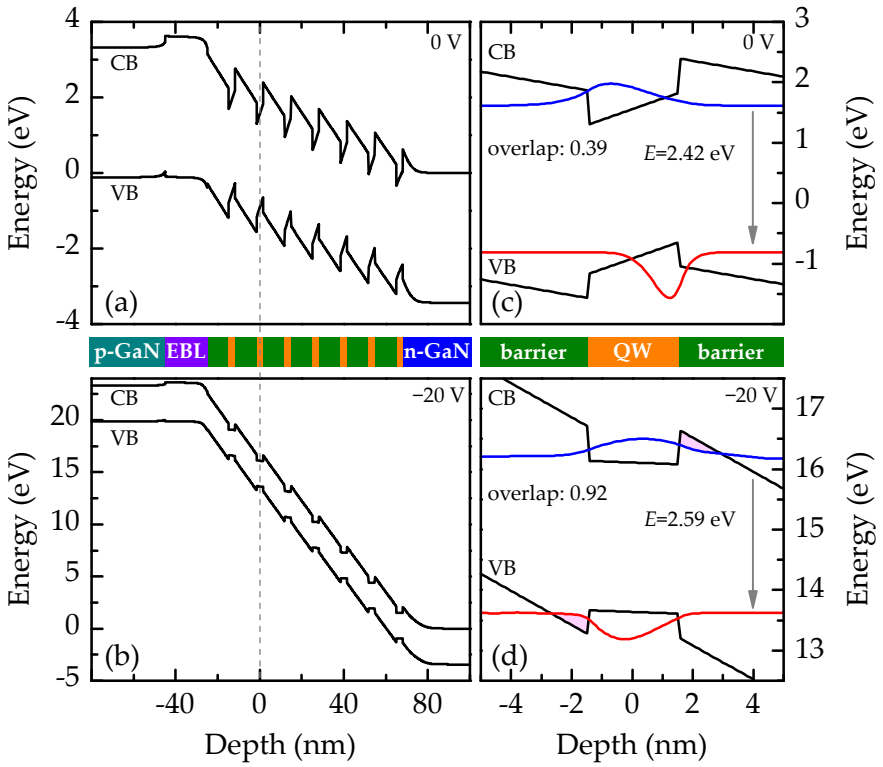

Figure 6.1: Band edge profile of an LED containing seven $In_{0.24}Ga_{0.76}N$ QWs (orange) embedded between GaN barriers (green) simulated with an applied voltage of (a) 0 V and (b) −20 V. The simulated layer sequence with the electron blocking layer (EBL) is explained in the text and schematically depicted between the corresponding graphs. The dashed line marks the QW which is magnified in (c) and (d) for the indicated voltages. The electron (blue) and hole (red) wave functions of the ground state, the overlap of the wave functions, and the transition energy E are shown for the selected QW. Additionally, the reduced effective potential barrier (pink area) for electrons and holes at a bias of −20 V is indicated in (d).

Stark effect.[408,461–465] To theoretically explore the required voltage range to achieve a negligible field in the QW, we have simulated the band profile of the LED as shown in Fig. 6.1. The LED structure consists of the following layer sequence: The p-doped GaN cap has a thickness of 150 nm and a Mg-concentration of 5×10^{19} cm^{-3}. A 20-nm-thick $Al_{0.15}Ga_{0.85}N$ electron blocking layer with similar doping is embedded between the cap and the active region to prevent the overflow of electrons as suggested in Refs. 298–300. The active region consists of an $In_{0.24}Ga_{0.76}N$/GaN multi-QW heterostructure. The nominal QW (barrier) thickness of this custom-made research and development LED sample amounts to 2–4 nm (about 10 nm) with doping concentrations of about 5×10^{16} cm^{-3}. The Si concentration in the n-doped GaN buffer is set to a value of 1×10^{19} cm^{-3}. We consider activation energies of 180 meV[295] and 25 meV[466] for the thermal activation of Mg and Si dopants, respectively.[467] For simplicity, we neglect the complex GaN buffers with short-period superlattices (similar to Ref. 468), which do not influence the band profile of the active region significantly. More details about the simulation software and the parameters can

be found in Sec. 3.3.

In Figs. 6.1(a) and 6.1(b), we show results of one-dimensional Schrödinger-Poisson calculations of the conduction and valence band of the green LED at 0 and −20 V, respectively. We obtain a set of transition energies (2.35 eV at 3.6 V, 2.42 eV at 0 V and 2.59 eV at −20 V), which is consistent with experimental PL and EL data, by adjusting the magnitude of the piezoelectric polarization and the In content. With increasing reverse bias, we observe an increasing potential drop across the active region which in turn increases the electric field F in the barriers [$F(0\,\mathrm{V}) = 0.9\,\mathrm{MV/cm}$ to $F(-20\mathrm{V}) = 2.8\,\mathrm{MV/cm}$], but reduces the fields in the QWs.

In Figs. 6.1(c) and 6.1(d), we present a magnified view of the QW marked by the dashed lines in Figs. 6.1(a) and 6.1(b), respectively. Obviously, the internal electric field in the QW is significantly reduced from 1.8 to 0.2 MV/cm by tuning the applied voltage from 0 to −20 V. According to the diminution of the field in the QW, the overlap of the electron and hole wave functions increases by about a factor of 2 from 0.39 to 0.93. Hence, we not only expect a blueshift, but also a faster (radiative) recombination with increasing reverse bias. Moreover, as the internal fields are lower, the localization energy should not be dominated by the localization of electrons at well-width fluctuations anymore (see Sec. 5.2), and excitons should form due to the increase of the exciton binding energy. Thus, we expect a transition from a PL transient asymptotically obeying a power law to an exponential transient.

6.2 Steady-state photoluminescence spectroscopy under reverse bias

Figures 6.2(a) and 6.2(b) show bias-dependent steady-state µ-PL spectra of the green LED excited with a diode laser ($E_{\mathrm{laser}} = 3.08\,\mathrm{eV}$) and recorded at room temperature at low ($I_{\mathrm{exc}} = 70\,\mathrm{W/cm^2}$) and high excitation intensities ($I_{\mathrm{exc}} = 700\,\mathrm{kW/cm^2}$), respectively. The PL band with a FWHM of about 100 meV is centered at 2.42 eV at 1 V and $70\,\mathrm{W/cm^2}$. The corresponding PL band at $700\,\mathrm{kW/cm^2}$ exhibits a blueshift of 100 meV [arrow in Fig. 6.2(b)]. Obviously, the large number of charge carriers causes band filling (increase of the PL intensity at the high energy side accompanied by a larger FWHM) and a screening of the polarization charges at 1 V, which reduces the quantum-confined Stark effect. With increasing reverse bias, the band blueshifts to 2.57 eV at −20 V for low and high excitation densities. This result implies that the residual internal field at −20 V is close to zero.

In contrast to $I_{\mathrm{exc}} = 70\,\mathrm{W/cm^2}$, for which the PL intensity reduces by more than four orders of magnitude, it reduces only by a factor of four for $700\,\mathrm{kW/cm^2}$ with increasing reverse bias. Hence, a significant amount of charge carriers recombines in the QW even at −20 V. For comparison, we show the µ-EL spectrum of the LED with close to normal operating conditions (3.65 V and 200 mA) in Fig. 6.2(b). The EL band is centered at 2.37 eV. Interestingly, the PL intensity obtained with µ-PL at high I_{exc} is a factor of ten higher than that obtained by µ-EL. Consequently, we achieve comparatively large charge carrier densities in the active region with our excitation of the QWs. For more details

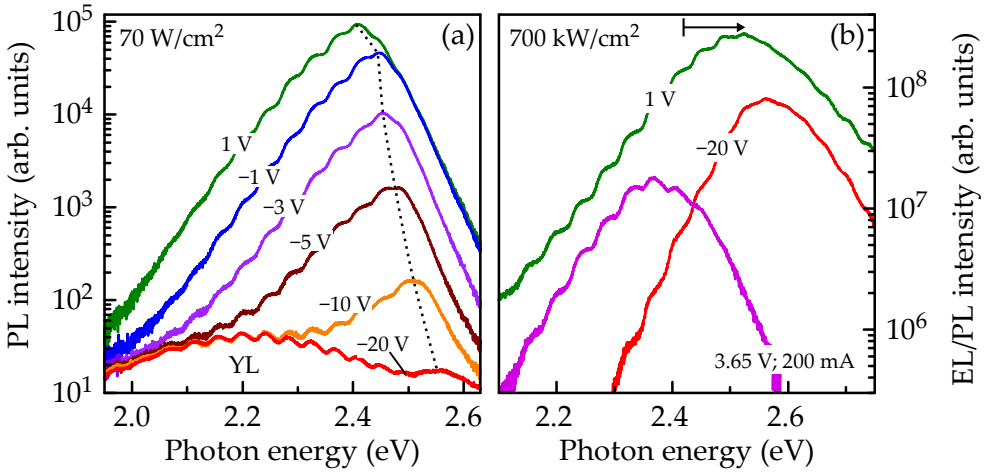

Figure 6.2: Room temperature steady-state PL spectra of the biased LED excited with (a) low and (b) high power density as indicated in the graphs. The PL band blueshifts as indicated by the dotted line. The broad band in (a) centered at 2.2 eV is caused by the yellow luminescence (YL) in GaN.[127] An EL spectrum recorded with settings close to normal operating conditions is shown in (b). The spectra are modulated by thickness interference fringes of the GaN buffer.

about the μ-EL and μ-PL of these type of LED, see Secs. 3.5.2 and A.1.

While the blueshift of the PL is expected for a decreasing quantum-confined Stark effect,[469] the reduction of the PL intensity is counterintuitive, because we expect a higher overlap of electron and hole wave functions from our simulation (see Fig. 6.1) and thus a higher PL intensity. Nonetheless, a reduction of the PL intensity has been observed by other groups too.[234,365,461–465] In conjunction with the reduction of the PL intensity, a photocurrent has been observed—indicating the escape of charge carriers from the active region. More specifically, the reduced effective barrier height for the charge carriers in the QWs at large reverse biases is believed to enhance the probability of tunneling or thermionic processes [see pink area marked in Fig. 6.1(d)].[234,365,463,464]

6.3 Photocurrent measurements and time-resolved photoluminescence spectroscopy

In order to investigate the decrease of the steady-state PL intensity at large reverse biases and to obtain information for the subsequent analysis of the time-resolved PL data, we have recorded the average photocurrent* after pulsed excitation with different energy fluences and excitation energies as shown in Figs. 6.3(a) and 6.3(b), respectively.† The photocurrent saturates at large reverse biases for low and medium excitation densities and at laser energies (E_{laser}) of 3.10 eV. Hence, below −15 V, a further decrease of the voltage

*The photocurrent has been recorded by a lock-in technique. Identical results have been obtained by conventional current measurements with subtracted dark current.

†Results obtained with steady-state excitation are similar.

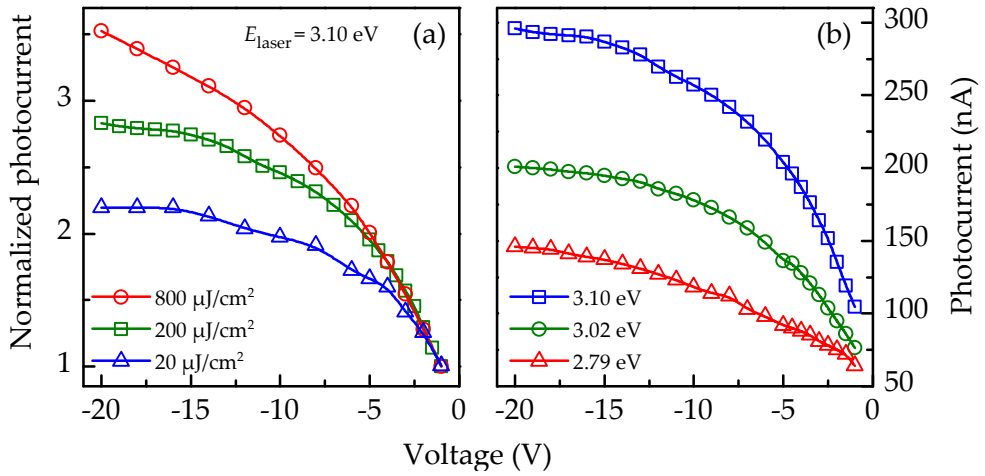

Figure 6.3: Dependence of the photocurrent on the reverse bias for (a) for different energy fluences at a laser energy of E_{laser} = 3.10 eV and (b) various excitation energies at 85 µJ/cm^2. The photocurrent in (a) is normalized to the value at −1 V to account for the excitation-dependent carrier densities. Solid lines are a guide to the eye in both graphs.

does not result in the extraction of a larger amount of charge carriers from the active region. However, for high energy fluences, the photocurrent increases monotonically [see Fig. 6.3(a)]. This observation may be explained by band filling, as charge carriers far above the ground state of the QW are extracted more efficiently from the active region (due to the strong fields in the barriers). Note that the photocurrent only sublinearly becomes larger with increasing fluences, which may be explained by a faster relaxation process of charge carriers to the QW ground state (→ reduced photocurrent) as suggested in Ref. 238. Additionally the photocurrent reduces by a factor of 2, when the excitation energy (excess energy of the photons created by the laser) is decreased from 3.10 to 2.79 eV as shown in Fig. 6.3(b). Based on the results reported by Miller *et al.*,[470] we assume an energy-independent absorption of the excited QWs. In Fig. 6.4, the escape of charge carriers from the excited state (1) or the ground state (0) of a QW at a large reverse bias is schematically depicted. The thermionic emission or the tunneling escape time of the excited charge carriers (red) is much shorter (due to the smaller effective potential barrier) than that of the relaxed ones (blue). The charge carriers are partly able to relax, if the relaxation process (curved arrow) is at least as fast as the escape from the excited state. Thus, we attribute the observed increase of the photocurrent with increasing excitation energy [see Fig. 6.3(b)] to the extraction of excited charge carriers before they relax to the ground state

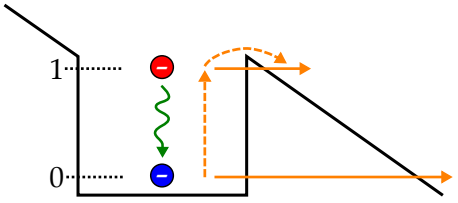

Figure 6.4: Schematic of the tunneling (solid arrows) and the thermionic (dashed arrows) escape of charge carriers either from the excited state (1) or the ground state (0) of a Ga-polar QW at a large reverse bias as in Fig. 6.1(d).

of the QW. Hence, it is beneficial to employ a low excitation energy in the experiment to excite the charge carriers as close as possible to the ground state of the QW. Note that the escape of charge carriers from both levels increases the photocurrent and reduces the integrated PL intensity. For time-resolved PL spectroscopy, however, the loss of charge carriers from the excited states simply reduces the charge carrier density at the QW ground state. This does not influence the shape of the (exponential) transient. In contrast, the escape from the ground state constitutes a nonradiative loss channel competing with the observed radiative recombination. This nonradiative channel decreases the effective PL lifetime and results in an exponential decay. Consequently, the transition from a power law to an exponential decay may either originate from a modification of the recombination mechanism due to the reduced internal field inside the QWs or from the escape of charge carriers relaxed to the ground state.

In a first step, we test our hypothesis of the transition of the recombination mechanism from individual electron and hole to excitonic recombination. For this purpose, we have recorded PL transients with time-correlated single photon counting at room temperature for various reverse biases as shown in the double- and semilogarithmic representation in Figs. 6.5(a) and 6.5(b), respectively. The QWs of the green emitting LED have been excited with 2.79 eV and an energy fluence per pulse of about 85 µJ/cm^2 with the setup described in detail in Sec. 3.4.2. The transients were recorded at the respective peak energies integrated over a spectral range of about 20 meV. As indicated by the dotted line in Fig. 6.5(a), the asymptote of the decay obeys a power law as expected for polar QWs (see also Chap. 4). However, already at −1 V the decay is faster, when compared to open-circuit conditions [pentagons in Fig. 6.5(a)]. Under open-circuit conditions, the time-integrated

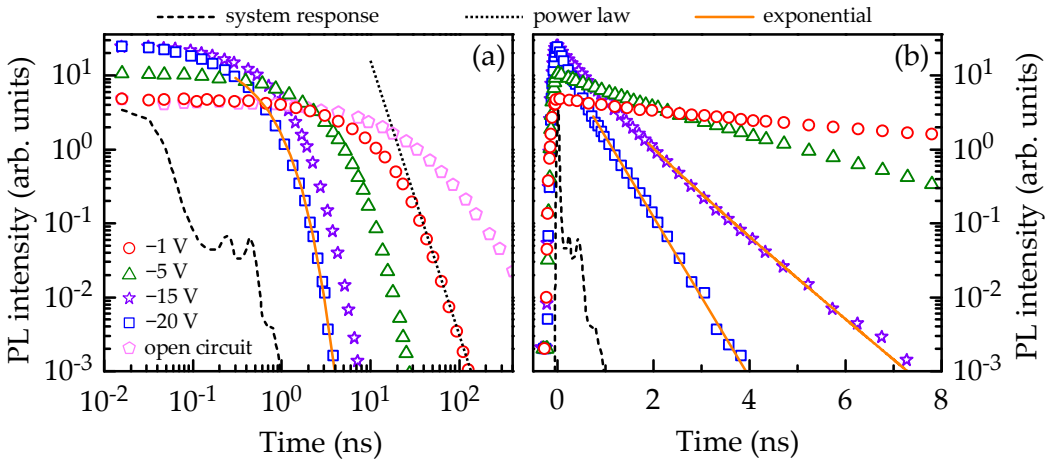

Figure 6.5: (a) Double- and (b) semilogarithmic representation of PL transients of a reverse biased LED emitting in the green spectral range. The response of the system to the laser with an excitation energy of 2.79 eV is shown as a dashed line. While the power law asymptote at small reverse biases (dotted line) can be identified in (a), the asymptote of the decay obeys a single exponential function (solid lines) at −15 and −20 V as indicated in (b).

voltage	asymptote	F_{QW}	$E_{h,loc} + E_{e,loc} = E_{loc}$ (meV)	E_X
0 V	power law	1.8 MV/cm	25 + 55 = 80	33 meV
−15 V	almost exponential	0.3 MV/cm	25 + 25 = 50	47 meV
−20 V	exponential	−0.2 MV/cm	25 + 20 = 45	48 meV

Table 6.1: Voltage dependence of the electric field inside the QW (F_{QW}) as well as the localization (E_{loc}) and the exciton binding energy (E_X) for characteristic asymptotes of the PL transients. According to the uncertainties of the parameters for the simulation, the error for all estimated energies amounts to at least ±5 meV

PL intensity[‡] and the effective PL lifetime increase compared to biased conditions, because of the accumulation of charge carriers at the contacts. Due to the formation of a depletion region, a forward voltage is induced[365] which influences the internal electric fields, leading to longer PL lifetimes. Moreover, the integrated PL intensity is higher because no photocurrent flows.

The rise time of the PL transients is basically identical at −1 and −20 V and amounts to 65 ± 5 ps, which is not limited by the temporal resolution of the system of 47 ± 1 ps (FWHM) as shown in Fig. 6.5(b). For increasing reverse biases, the absolute value of the exponent of the power law becomes larger, until the asymptote of the decay is exponential at about −15 V [see Fig. 6.5(b)], indicating that recombination is excitonic at this and larger reverse biases. The measured excitonic lifetime of 400 ps is in good agreement with the values reported for the lifetimes of excitons in nonpolar (In,Ga)N/GaN or GaN.[408–414] Additionally, we observe that the peak PL intensity increases for larger reverse biases, which excludes the escape of charge carriers from the ground state of the QW and reflects the increase of the radiative recombination rate. This behavior has not been observed in Refs. 463 and 472, but is consistent with the simulations, predicting a larger overlap of the electron and hole wave functions. Thus, we observe clear indications for the bias-induced transition from tunneling recombination of individually, spatially separated electrons and holes to the recombination of excitons in our Ga-polar (In,Ga)N/GaN QWs.

Our interpretation is furthermore supported by the comparison of the localization energy E_{loc} and the exciton binding energy E_X. The results from the preceding chapter suggest that the hole localization energy ($E_{h,loc}$) is in the range of 25 ± 5 meV for a thick Ga-polar (In,Ga)N layer with an In content of about 15 %. Although the In content in the LED is higher, the compositional fluctuations in QWs, representing a random alloy, should result in a similar value of $E_{h,loc}$. Utilizing a Schrödinger-Poisson solver, we determine the localization energy of electrons ($E_{e,loc}$) and the electric field in the QWs as summarized in Tab. 6.1 for various biases. We extract the values of E_X given in the same table from the variational calculations presented in Fig. 5.4(b). A comparison of E_{loc} and E_X reveals that the transients become indeed exponential when $E_X > E_{loc}$. Note that these results are only an approximation, as the macroscopic electric fields are not necessarily equal to the local fields in the random ternary alloy.[386]

[‡]A similar trend has been observed for the steady-state PL intensity in Ref. 471.

6.3.1 Simulation of escape mechanisms

From Fig. 6.5(a), we have deduced that the integrated PL intensity (area under the transient) decreases for increasing reverse biases. To ascribe the change of the transient only to the bias-induced transition of the recombination mechanism, we have to rule out the escape of charge carriers from the QW ground state (see. Fig. 6.4), which would also result in an excitonic decay. For this purpose, we theoretically investigate two well-known escape mechanisms, namely thermionic emission and direct tunneling escape in this subsection.[§]

In unbiased structures, the GaN barriers prevent leakage of charge carriers from the QWs. However, with increasing reverse bias, the electric field inside the barriers increases, leading to a reduction of the effective barrier thickness from about 10 nm to 1–2 nm [see Figs. 6.1(c) and 6.1(d)]. Moreover, the polarity of the reverse bias efficiently extracts the charge carriers from the active region once they leave a QW. Thus, at large reverse biases, electrons and holes may escape the QWs much easier by tunneling or thermionic emission, both constituting additional loss channels resulting in exponential PL transients.

As we excite the charge carriers slightly above the ground state of the QW, they possess kinetic energy and thermalize/relax to the ground state, before recombination at the Γ-point occurs. For investigating the excitation process in our LED, we utilize an eight-band **k·p** model and calculate the band structure for electrons and holes as shown in Fig. 6.6(a). Employing a laser energy of 2.79 eV and following the selection rules,[477] the excitation occurs dominantly from the first valence to the first conduction band near the Γ-point in the K-direction. Due to the small effective mass of the electrons, their excess energy is much larger (150 meV above the band gap and 250 meV above the ground state) than that of the holes (30 meV and 50 meV, respectively). For simplicity, we assume the ratio of the excess energies to be equal at 0 and −20 V.

Combining our results deduced from Figs. 6.1(c), 6.1(d) and 6.6(a), we are able to analyze the thermionic emission and tunneling times for relaxed and excited charge carriers in our QWs. Starting with the thermionic emission time $\tau_{\mathrm{TE},i}$, the values for electrons ($i = e$) and holes ($i = h$) with the respective effective masses m_i are given according to Schneider and v. Klitzing[478] by

$$\tau_{\mathrm{TE},i} = d\sqrt{\frac{2\pi m_i}{k_\mathrm{B}T}}\exp\left(\frac{E_\mathrm{barrier}}{k_\mathrm{B}T}\right) \tag{6.1}$$

with the Boltzmann constant k_B.

In Fig. 6.6(b), we present τ_TE over the effective barrier height E_barrier for a QW with a thickness of $d = 3$ nm at a temperature of $T = 300$ K. E_barrier is smaller for the ground state of the holes at 0 and −20 V due to the band offset ratio of 60 : 40. Hence, the thermionic emission of holes $\tau_{\mathrm{TE},h}$ is the limiting process if both types of charge carriers have relaxed to the ground state. For excited states, τ_TE is determined by the thermal emission of

[§]Note that for modeling the reverse leakage current of (In,Ga)N QDs embedded in GaN nanowires[261] the variable-range hopping,[473] the Poole-Frenkel conduction,[474] and the phonon-assisted tunneling[475,476] have to be taken into account as additional escape mechanisms.

electrons because of the larger excess energy transferred from the exciting photons to the electrons.

It is well-known that relaxation processes in semiconductors are faster than 10 ps in III-nitrides[479,480] which is faster than $\tau_{\mathrm{TE},e}$ from the excited states. Thus, our excited charge carriers thermalize rapidly, and we only have to consider the thermionic emission of holes from the ground state of the QW as an additional loss process. As indicated by the dashed lines, the experimentally determined value of the effective PL lifetimes (τ_{eff}) are shorter than $\tau_{\mathrm{TE},h}$ for 0 and −20 V [see red dotted line in Fig. 6.6(b)]. This result rules out thermionic emission as the origin of the photocurrent, which was also shown experimentally by Meneghini *et al.* [481] for a similar sample.

Next, we examine carrier escape by tunneling. According to Landau and Lifshitz,[482] we formulate the tunneling time $\tau_{\mathrm{T},i}$ ($i = e,\ h$) through a triangular potential barrier with the respective height $U(z)_i$, the energy (κ_i) and mass (m_i) of the particle in the QW in the Wentzel-Kramers-Brillouin approximation. The bias-dependent electric field F of the barrier determines the slope of the triangular potential. Hence, we consider the special

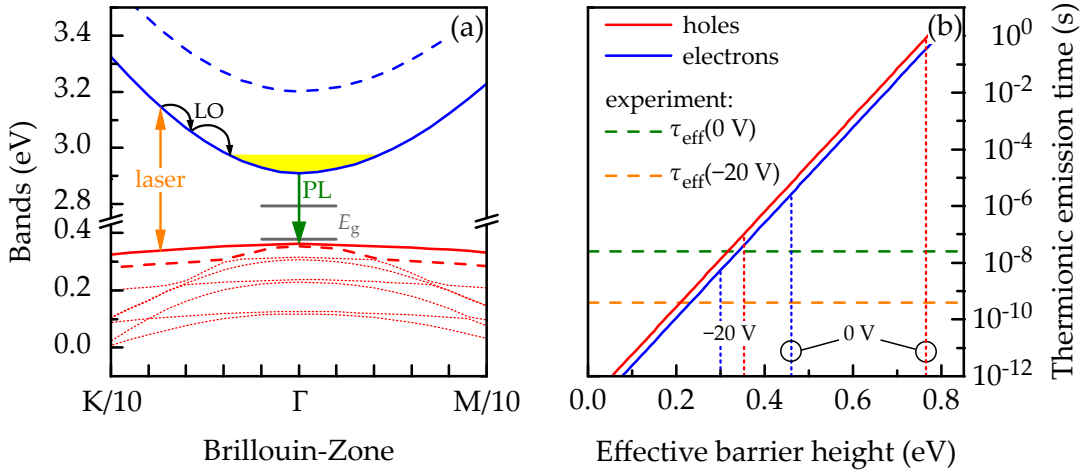

Figure 6.6: (a) Band structure of first (solid lines), second (dashed lines) and higher (dotted lines) states for electrons (blue) and holes (red) of a field free, 3-nm-thick $In_{0.24}Ga_{0.76}N$ QW embedded in GaN barriers calculated with an eight-band $\mathbf{k}\cdot\mathbf{p}$ model with parameters from Ref. 307. The calculations have been performed by O. Marquardt. The (dark) gray solid lines indicate the band gap E_g of the (In,Ga)N/GaN QW at the Γ-point at 300 K. Electron-hole pairs are excited by the laser (orange arrow) with E_{laser} = 2.79 eV. Electrons relax via the emission of longitudinal optical phonons (LO) indicated by curved black arrows until they reach the yellow region, where further relaxation toward the conduction band minimum occurs via the emission of acoustic phonons.[152] The direct transition (green arrow) at the Γ-point can be observed in the PL spectra. (b) Thermionic emission time depicted over the effective barrier height for electrons (blue) and holes (red) for a 3-nm-thick $In_{0.24}Ga_{0.76}N$ QW embedded in GaN barriers at a temperature of 300 K. The colors of the dotted lines indicate the effective barrier height and thermionic emission times of the lifetime-defining species at 0 and −20 V. The experimentally determined effective PL lifetimes (τ_{eff}) are indicated by horizontal lines.

case of Fowler-Nordheim tunneling.[483] Therefore,

$$\tau_{\mathrm{T},i} = \tau_{\mathrm{esc}} \times \exp\left(2\int_{z_0}^{z_1}\sqrt{\frac{2m_i/\hbar^2}{[eF(z)-\kappa_i]}}\mathrm{d}z\right). \tag{6.2}$$

To calculate absolute tunneling times, the collision frequency of the particles with the walls of the confining QW potential has to be calculated.[484] Utilizing the Oppenheimer formalism,[485] we convert the collision / attempt-to-escape frequency of particles in a QW into the escape time τ_{esc} by expressing the velocity of the particles in terms of energy[484,486]

$$\tau_{\mathrm{esc}} = d\left(\frac{\kappa_i}{2m_i}\right)^{-1/2} = \frac{\hbar\pi}{\kappa_i}. \tag{6.3}$$

Inserting Eq. (6.3) into Eq. (6.2) and selecting proper integration limits (i. e., $z_0 = 0$ and $z_1 = (U_0 - \kappa_i)/F$ with $U(z_0 = 0) = U_0$), results in

$$\tau_{\mathrm{T},i} = \frac{\hbar\pi}{\kappa_i}\exp\left[\frac{4\sqrt{2m_i}}{3e\hbar F}(U_0-\kappa_i)^{3/2}\right]. \tag{6.4}$$

Utilizing electric fields and barrier heights from the calculations of the band profiles, we obtain values of $\tau_{\mathrm{T},i}$ as a function of κ_i as shown in Figs. 6.7(a)–6.7(c) for 0 V, −15 V, and −20 V, respectively. Here, we define κ_i as the energy above the band gap. At 0 V, $\tau_{\mathrm{T},e}$ and $\tau_{\mathrm{T},h}$ for relaxed particles are longer than the experimental determined effective PL lifetimes (green dashed line) as shown in Fig. 6.7(a). Although the tunneling time of electrons is only a few ns (i. e., shorter than τ_{eff}), a relaxation process on the order of ps[479,480] prevent significant tunneling from the QW. Hence, we do not expect any tunneling escape at 0 V from the simulations. Consequently, we expect no photocurrent to be present at 0 V (as thermionic emission is not present either), which is in fair agreement with our experimental observations.

For −15 and −20 V the situation is different, because of the strong electric field inside the barriers and the resulting small effective barrier height [see pink area in Fig. 6.1(d)]. In Figs. 6.7(b) and 6.7(c), we observe that $\tau_{\mathrm{T},e}$ is on the order of a few ps even for electrons relaxed to the ground state. The carrier dynamics should thus be completely dominated by the tunneling escape of electrons. In contradiction to this theoretical result, we experimentally detect significant PL intensity and effective PL lifetimes much longer than the few ps at −15 and −20 V expected from Figs. 6.7(b) and 6.7(c) [cf. Figs. 6.2(b) and 6.5(b)]. Martinet *et al.*[486] reported a similar discrepancy for GaAs/(Al,Ga)As QWs and speculated that scattering at defects cause wave vectors being not perpendicular to the QW interfaces. Consequently, they assume a severe reduction of the attempt-to-escape frequency. In (In,Ga)N/GaN, charge carriers scatter at structural defects, rough interfaces or impurities, and most likely at alloy disorder.[487,488] Thus, the classical tunneling escape picture seems not to hold for (In,Ga)N. Furthermore, tight-binding calculations suggest

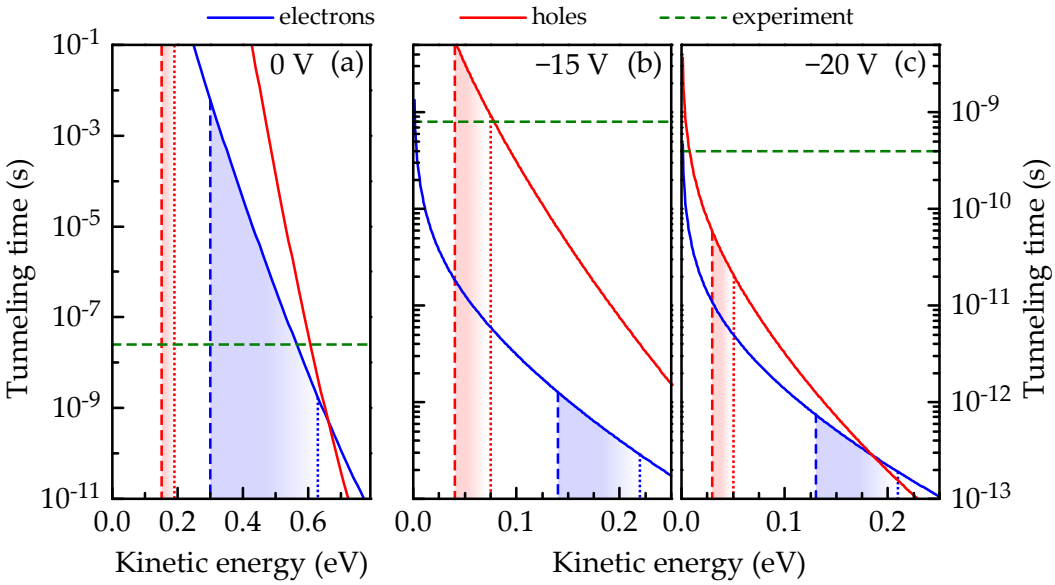

Figure 6.7: Tunneling time as a function of the kinetic energy of electrons (blue) and holes (red) for the $In_{0.24}Ga_{0.76}N/GaN$ QW at (a) 0 V, (b) −15 V, and (c) −20 V. The shaded area mark the kinetic energy for the respective particle ranging from "relaxed to the ground state" (maximum effective barrier thickness; opaque) to "maximum excess energy" (almost transparent). The limits are additionally indicated for ground states and excited states by vertical dashed and dotted lines, respectively. The experimentally measured effective PL lifetimes are indicated by horizontal lines.

strongly localized wave functions of holes at random compositional fluctuations.[68] The localization of holes, however, significantly reduces the probability of direct tunneling which in turn prolongs τ_{esc}. Consequently, the above presented estimation of the classical tunneling escape, with delocalized wave functions, represents the lower limit of τ_T.

Another explanation may originate from the formation of excitons. The Coulomb attraction may counteract the tunneling of the individual particles, because electrons and holes tunnel through opposite barriers of the QW (see, e. g., Ref. 470). Hence, we should not consider electrons and holes individually, but as an entity. We propose to approximate the tunneling escape time of the exciton with that of the holes in a first approximation. For a bias of −15 V, the tunneling escape of excitons is prevented because the escape time of the holes (which "capture" the electrons) is much longer than the measured exponential PL lifetime of the asymptote. However, at −20 V, the tunneling escape time of electrons and holes are significantly shorter than any experimentally determined lifetime [see Fig. 6.7(c)].

Summarizing this subsection, we believe that the experimentally observed photocurrent results predominantly from the tunneling of excited electrons which do not immediately form excitons. Consequently, tunneling escape from the active region does not influence the PL transients of the investigated QWs up to at least −15 V, but reduces the effective excitation density only.

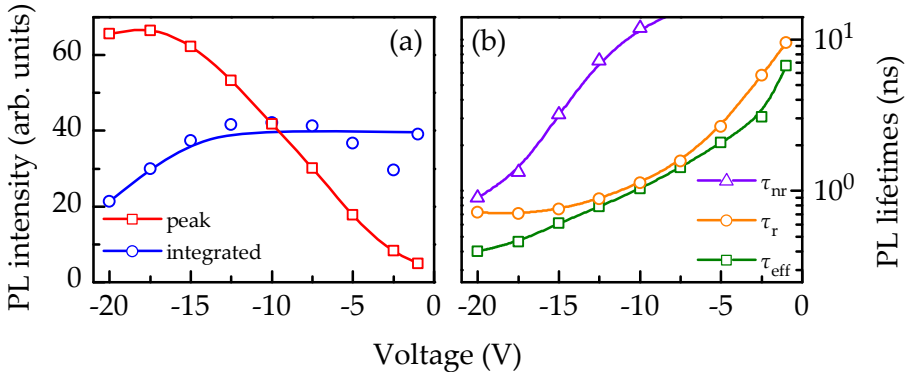

Figure 6.8: Dependence of the (a) peak and time-integrated PL intensity (squares and circles) as well as the (b) effective (τ_{eff}) and radiative (τ_r) PL lifetimes (squares and circles) on the reverse bias. The PL intensities have been corrected for the losses due to the increasing photocurrent and for the spectral response of the detection system. Approximate values for τ_r have been obtained by assuming an IQE of 70 % at −1 V. All solid lines are a guide to the eye.

6.3.2 Quantitative analysis of the photoluminescence transients

The statement that tunneling escape from the active region does not influence the PL transients at least up to −15 V allows us to correct the measured PL intensities for the photocurrent and hence to draw quantitative conclusions. In Fig. 6.8(a) we show the voltage dependence of the corrected peak and integrated intensities of the PL transients shown in Fig. 6.5(a). From this voltage dependence, we obtain two important results.

First, we observe that the corrected peak intensity increases monotonically with increasing reverse bias, before it saturates at about −15 V. Second, the integrated PL intensity is almost constant up to −15 V and decreases thereafter [see Fig. 6.8(a)].[¶] From the first observation, it directly follows that the calculated radiative lifetime (deduced from the inverse peak intensity with the assumption of an IQE of 70 % at −1 V) decreases by a factor of 13 when the reverse voltage is increased from 1 to 15 V, and saturates thereafter as shown in Fig. 6.8(b). From the simulations of the overlap of the electron and hole wave functions, we expect an increase of a factor of about 2 only. However, as the recombining species change from spatially separated electrons and holes to excitons, the radiative rate is not simply proportional to the overlap. For GaN, for example, the radiative rate increases by about one order of magnitude when including Coulomb interactions (formation of excitons) in the simulations.[148]

However, not only the radiative recombination rate increases, but also the nonradiative one [see Fig. 6.8(b)]. Thus, the overall recombination rate becomes faster which is expected for the higher overlap of the wave functions of electrons and holes. In combination with the saturation of τ_r, we explain our second observation, namely, the reduction of the integrated PL intensity for a large reverse bias, by an enhanced nonradiative recombination

[¶]The minor discrepancy of the value at −2.5 V may be due to the adjustment of the spectral position of the detection to follow the blueshift of the PL band.

for excitons in our Ga-polar (In,Ga)N/GaN QWs. Additionally, the shorter effective PL lifetime and the reduced integrated PL intensity [see Fig. 6.8(b)] for reverse biases above −15 V may indicate the escape of excitons, which do not contribute to the photocurrent.

6.4 Summary and conclusions

By applying a reverse bias to a Ga-polar (In,Ga)N/GaN LED, and thereby decreasing the internal electric field in the QWs, we have demonstrated the possibility to tune the recombination mechanism from the decay of individual, spatially separated electrons and holes to the decay of excitons. Once the exciton binding energy exceeds the localization energy, the asymptote of the PL transient does not obey a power law, but follows a single exponential function. Additionally, the transition is accompanied by a decrease of the radiative PL lifetime. Taking into account that tunneling of electrons out of the QW (causing the observed photocurrent) does not influence the shape of the transient, we obtain an increase of the radiative rate by about one order of magnitude. However, also the nonradiative rate increases at a large reverse bias. Consequently, the higher spatial overlap of electrons and holes is not entirely beneficial for (In,Ga)N/GaN, because electrons and holes are present at nonradiative centers simultaneously. Moreover, the increase of the nonradiative recombination rate may be responsible for the lower IQE of nonpolar (In,Ga)N/GaN QWs with comparable structural quality, for which the recombination of excitons is common. Finally, we conclude that the large localization energy and spatial separation of charge carriers, caused by the internal electric fields in Ga-polar (In,Ga)N QWs embedded in GaN, actually enhance the IQE.

Chapter 7

(In,Ga)N/GaN short-period superlattices

This chapter deals with SPSLs composed of In-containing QSs embedded between GaN QBs. These SPSLs are predecessors of digital alloys, made of InN/GaN heterostructures, which are briefly introduced in the beginning of this chapter. The combination of both, in-situ and ex-situ structural characterization techniques, indicates that an In adsorbate structure can be utilized to fabricate SPSLs containing InN QS with sub-ML coverage and lateral ordering. The main focus of this chapter lies on the PL spectroscopy of such structures. We observe an electronic coupling of the QSs embedded between QBs as thin as 6 MLs. However, time-resolved PL reveals asymptotes of the decay that obey a power law at low temperatures. Thus, we conclude that the sub-ML InN QSs act electronically as two-dimensional random alloys such as conventional (In,Ga)N/GaN QWs. At elevated temperatures, not only the vertical separation of electrons and holes along the SPSL, but also an extremely effective nonradiative recombination channel quenches the PL intensity significantly. Parts of this chapter have been published in Ref. 489.

7.1 InN/GaN digital alloys

In the previous chapters, we presented a detailed study of the effect of the localization of charge carriers in the random ternary alloy (In,Ga)N on the PL properties. The high efficiency of light emitters used for solid-state lighting,[20,44] display technologies,[342] and diode lasers[343,490] is believed to be linked to this carrier localization by the inevitable compositional fluctuations occurring on an atomic scale in the random alloy (In,Ga)N (see also Sec. 2.4).[45,56] However, the inhomogeneous broadening of electronic transitions and a strongly retarded recombination dynamics in the (In,Ga)N/GaN QWs are simultaneously caused by the localization at random compositional fluctuations as shown in Chaps. 4 and 5. Both of these effects are detrimental for laser applications.[491,492]

So-called digital alloys have been proposed to avoid localization effects, but to retain the widely tunable band gap of (In,Ga)N for solid-state lighting.[76] In contrast to the ternary compound, these digital alloys are composed of ML-thick alternating layers of the binary compounds InN and GaN. These SPSL are envisioned to eliminate alloy disorder and the

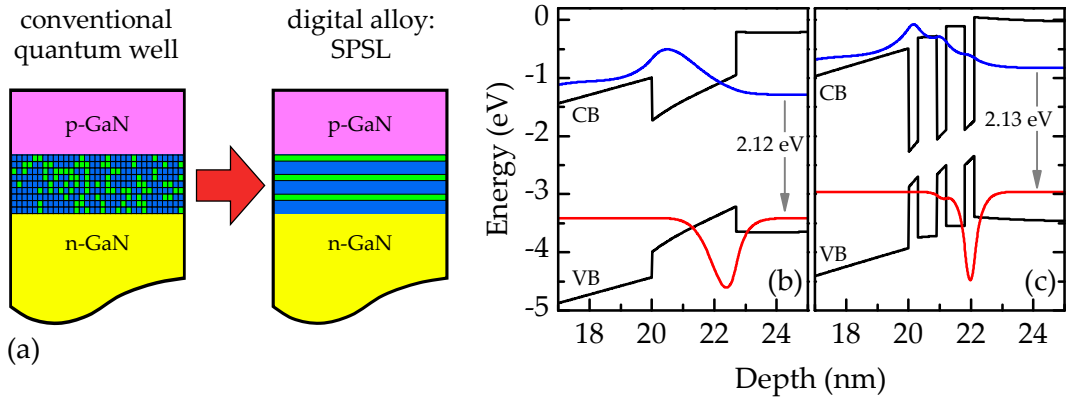

Figure 7.1: (a) Schematic of the replacement of a conventional (In,Ga)N/GaN QW with random In fluctuations by a digital alloy in the form of an SPSL composed of ML-thick layers of the binary compounds InN (green) and GaN (blue). To fabricate a light emitting device, the active regions are embedded between n- and p-doped GaN. Band diagrams and wave functions of electron (blue) and hole (red) ground states of active regions containing (b) an $In_{0.31}Ga_{0.6}N$ QW with a thickness of 2.7 nm and (c) a SPSL consisting of 3 periods of 1 ML InN and 2 MLs GaN. Both active regions are embedded between 20-nm-thick n- and p-doped GaN. Operating the devices at 4 V results in similar transition energies, as indicated by the arrows.

resulting localization phenomena.[76,493–496] For example, these structures are expected to exhibit a reduced inhomogeneous broadening and an enhanced radiative recombination rate, both beneficial for laser applications.[497]

To tune the transition energy in an SPSL, the thickness of the InN QS and of the GaN QB has to be adjusted as shown in detail by Gorczyca *et al.*[78] The coupling of the QSs through the sufficiently thin QBs (i. e., only a few MLs) results in a structure with a transition energy corresponding to a layer with an effective In content. In Fig. 7.1(a), we illustrate the replacement of a conventional (In,Ga)N/GaN single QW with random alloy fluctuations by an SPSL consisting of InN QSs (green) separated by GaN QBs (blue). To obtain emission from an LED at a bias of 4 V in the desired green to yellow spectral range, a single QW has to contain an In content of about 31 % as deduced from Schrödinger-Poisson calculations presented in Fig. 7.1(b). Figure 7.1(c) shows an active region consisting of 3 periods of 1 ML InN and 2 MLs GaN. Coupling between the InN QSs through the thin GaN QBs, i. e., a spreading of the electron and the hole wave functions over the entire SPSL, energetically lowers the electron and hole ground states of the InN QSs (compared to isolated thin InN QSs) and leads to a similar transition energy at 4 V. However, the coupling is weaker than compared to flat-band conditions due to polarization charges at the interfaces.

In contrast to the GaAs/(Al,Ga)As system, for which superlattices have been fabricated by Dingle *et al.*[498] already in 1975,[498] the realization of group-III-nitride superlattices is much more challenging. The growth of digital alloys out of the binary constituents InN and GaN is hampered by the large lattice mismatch between InN and GaN of 11 %[499] and

the tendency of In to segregate on the growth front.[500] Furthermore, the incompatible growth conditions of the binary constituents[501] and the fact that plastic relaxation occurs already during the formation of the first MLs of InN on GaN[502,503] impede the fabrication of these digital alloys.

For GaAs-based superlattices, it has been shown that the miniband, resulting from the coupling of the QWs, splits into a so-called Stark ladder when applying an external electric field.[504,505] Small external fields cause Wannier-Stark localization of charge carriers. However, large external electric fields separates electrons and holes to the opposite sides of the superlattice and cause a vanishing overlap of the electron and hole wave functions,[505] which is detrimental for optical devices. As GaN-based devices are typically grown along the polar direction, the separation of electrons and holes across the SPSL by the internal electric fields limits the maximum vertical extension of SPSLs grown along this direction.

Nonetheless, Yoshikawa *et al.*[76] reported the realization of InN/GaN SPSLs with PL transition energies in the range of 2.9–3.3 eV in 2007. However, a recent microscopic investigation of InN/GaN SPSLs grown under identical conditions demonstrated that the nominal InN MLs in the SPSL exhibit a coverage of only 0.33 MLs.[506] This finding raises the question whether the InN QSs consist of microscopic two-dimensional InN islands, i. e., InN patches with sub-ML coverage, or of a single ML of disordered $In_{0.33}Ga_{0.67}N$.

A third possibility arises from the existence of an In adatom-induced surface reconstruction on GaN(0001) that is expected to be formed by 1/3 MLs of In,[500,507] the same coverage as observed by Suski *et al.*[506] This agreement may be coincidental, but it may also suggest that, under the usual growth conditions, the In coverage in the first ML of InN growth is restricted to the one that constitutes the energetically favorable surface phase, i. e., the $(\sqrt{3}\times\sqrt{3})$R30°-In adsorbate structure. Note that a reconstruction with this symmetry has also been observed for (In,Ga)N by Friedrich *et al.*[508] as well as for pure InN by Himmerlich *et al.*[509] Since this surface phase is self-limiting in thickness to a single ML and is laterally ordered, it may provide a template for the insertion of ordered $InGa_2N_3$ QS in GaN.[510]

7.2 Growth and structural characterization

Here, we focus on the comparison of two samples exhibiting periodically inserted InN QSs with the same nominal coverage, but with a different vertical separation by GaN QBs. The QBs in sample I have a thickness of 6 MLs enabling an electronic coupling of the QSs,[511] while the 50-ML-thick QBs in sample II electronically isolate the QSs from each other. Thus, sample II is used as a reference representing thin and uncoupled QSs. Plasma-assisted molecular beam epitaxy was employed to realize SPSLs with abrupt interfaces.[512],* Details about the growth of this specific structures have been reported by Chèze *et al.*[77] In the following, we will summarize their results to introduce the samples subsequently analyzed by PL.

By monitoring the growth, Chèze *et al.*[77] have ensured that the InN QSs are formed

*Recently, Staszczak *et al.*[513] have demonstrated the growth of similar structures with MOCVD.

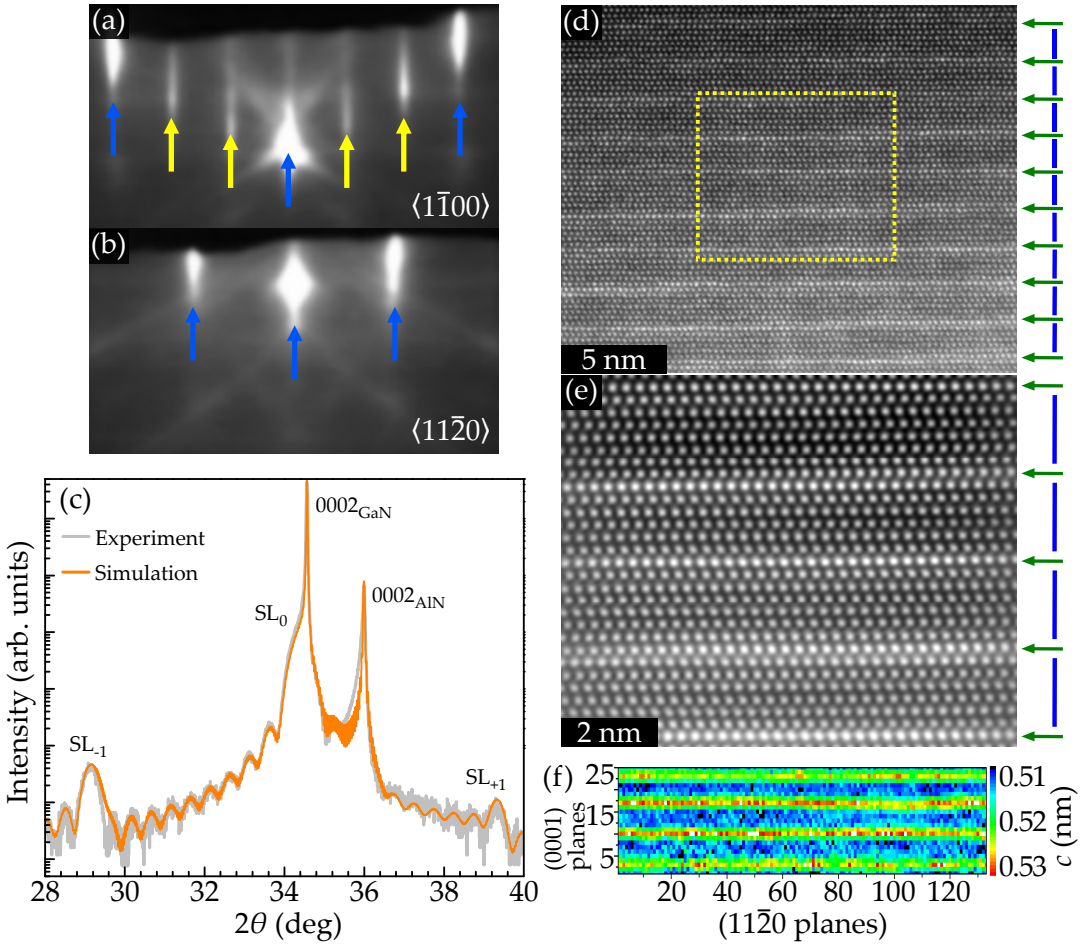

Figure 7.2: Structural characterization of sample I with 6 ML-thick barrier. Reflection high-energy electron diffraction patterns along the (a) ⟨1$\bar{1}$00⟩ and (b) ⟨11$\bar{2}$0⟩ azimuths of the GaN(0001) surface showing the In-induced $(\sqrt{3}\times\sqrt{3})$R30° surface reconstruction during In and N supply. Blue and yellow arrows indicate integer and fractional order reflections, respectively. (c) Semilogarithmic representation of experimental and simulated ω-2θ x-ray diffraction profiles across the 0002 reflection of GaN. Satellite reflections due to the SPSL are labeled $SL_{\pm n}$. The AlN reflection originates from the template. (d) Cross-sectional scanning transmission electron micrograph of the entire SPSL, and (e) magnified view of four periods in the area enclosed by the dotted rectangle in (d). The micrographs were Fourier filtered to remove high-frequency noise. The horizontal green arrows and the vertical blue lines highlight the (In,Ga)N QSs and the 6 ML thick GaN QBs, respectively. (g) Color-coded map of the c lattice parameter deduced from high-resolution transmission electron micrographs for four periods revealing thicknesses of 1 ML and 6 MLs for the QSs and the QBs as well as an In content of 25 %. The figure has been adapted from Ref. 77.

by a $(\sqrt{3}\times\sqrt{3})$R30°-like surface arrangement of the In(N) adlayer [corresponding to a (1×3) reconstruction pattern observed by reflection high-energy electron diffraction] and not by actual InN growth. The heterostructures have been deposited onto commercial GaN/AlN/Al_2O_3(0001) templates at a substrate temperature of 550 °C, i. e., significantly

above the decomposition temperature of InN(0001).[514],† Flushing the GaN(0001) surface with In under the exposure to active nitrogen has led to the reflection high-energy electron diffraction pattern shown in Figs. 7.2(a) and 7.2(b) for each of the QSs. The pattern along the $\langle 1\bar{1}00\rangle$ azimuth was found to exhibit sharp and intense 1/3 order reflections [see Fig. 7.2(a)]. Along the $\langle 11\bar{2}0\rangle$ azimuth, only the periodicity of the unreconstructed surface was detected [see Fig. 7.2(b)]. The formation of the $(\sqrt{3}\times\sqrt{3})$R30°-In adsorbate structure on GaN(0001) was indicated by the simultaneous occurrence of both patterns.[500,507] The supply of an excess of In, i. e., more than the 1/3 ML that was needed to form the adsorbate structure, has led to a liquid In adlayer floating on the surface. This adlayer was found to act as a reservoir that prevents a loss of In from the $(\sqrt{3}\times\sqrt{3})$R30°-In structure when overgrowth is initiated.[516] More details about the growth and monitoring the formation of the In adsorbate structure with line-of-sight quadrupole mass spectrometry can be found in Refs. 77 and 512.

For the structural characterization, triple-axis ω-2θ x-ray diffraction scans performed with $CuK_{\alpha 1}$ radiation in a Panalytical X'Pert™ diffractometer equipped with a Ge(220) hybrid monochromator and a Ge(220) analyzer crystal, as well as high-resolution and scanning transmission electron microscopy in an aberration-corrected FEI Titan™ 80-300 operating at 300 kV were used by Chèze *et al.*[77] to assess the periodicity, the interface abruptness and the composition of both SPSL samples. The distribution of the *c* lattice parameter was deduced from high-resolution transmission electron micrographs as described in Refs. 63 and 506.

Figure 7.2(c) shows an ω-2θ scan across the 0002 reflection of GaN exemplary for sample I. The periodicity of the SPSL is reflected by the scans since clear first-order satellite reflections have been observed. The coherent growth has been confirmed by asymmetric $10\bar{1}5$ reciprocal space maps (not shown). Accounting for the elastic strain, the x-ray diffraction profile[517,518] of sample I as shown in Fig. 7.2(c) has been simulated by using ten periods of 1 ML-thick $In_{0.29}Ga_{0.71}N$ QSs separated by 6 ML-thick GaN QBs. For sample II, the simulation of the x-ray diffraction profiles has indicated QSs with similar properties separated by GaN QBs with a thickness of 50 MLs.

The periodicity of sample I is visualized by the micrograph shown in Fig. 7.2(d). The interfaces were found to stay abrupt and do not deteriorate from the bottom to the top of the structure. The progressively weaker contrast toward the top of the SPSL was explained by a change in thickness of the cross-sectional sample. Figure 7.2(e) depicts the magnified view of the area marked by the dotted line in the micrograph in Fig. 7.2(d). The embedded QSs were found to exhibit monoatomic steps at some of the QS/QB interfaces, and the thickness of the QS thus appears to fluctuate between 1 and 2 MLs. However, the map of the *c* lattice parameter shown in Fig. 7.2(f), deduced from high-resolution transmission electron microscopy on a very thin (10 nm) cross-section, has revealed three increased interplanar distances for each of the QSs, corresponding to a single ML.[506] The magnitude of the distortions of the *c* lattice parameter was found to correspond to an In

†The substrate temperature was measured by a pyrometer. For calibrating the pyrometer, the boundary between the intermediate and the Ga-droplet growth regimes on the GaN(0001) surface was used.[515]

content of about 25 %, which is in fair agreement with the In content deduced from x-ray diffraction. A perfect 1-In/2-Ga repetition in the QS was detected in high-angle, annular dark-field imaging using a scanning transmission electron microscopy (not shown) for small sections.[519] This indicates the formation of an ordered $InGa_2N_3$ phase.

7.3 Photoluminescence spectroscopy of submonolayer InN quantum sheets embedded in GaN

In what follows, we employ temperature-dependent PL spectroscopy under both steady-state and pulsed excitation to explore the electronic properties of samples I and II introduced above. For the basic characterization with steady-state PL spectroscopy, the samples were excited by the 325 nm-line (E_{laser} = 3.814 eV) of a He-Cd laser with an excitation power density of 100 W cm^{-2}. Utilizing time-resolved PL spectroscopy, we have the possibility to discern the PL decay of pure InN islands from the one of (In,Ga)N QSs or ordered In_2Ga_3N. For the time-resolved PL experiments, a photon energy of 3.55 eV was used to create pulses with an energy fluence per pulse of 50 µJ cm^{-2} and a repetition rate of 420 kHz. For detection, time-correlated single photon counting was employed. The transients were recorded at the respective peak energies integrated over a spectral range of about 10 meV. Further details about the experimental setups and techniques can be found in Sec. 3.4.

7.3.1 Temperature-dependent steady-state PL spectroscopy

Figures 7.3(a) and 7.3(b) show temperature-dependent steady-state PL spectra on a semilogarithmic scale of samples I and II, respectively. The PL bands peak at around 3.16 eV for sample I and at 3.25 eV for sample II. These transition energies are close to those reported for nominally complete InN MLs (see, e. g., Refs. 511, 520, and 521 as well as Ref. 506 and references therein). From the results of the structural characterization presented in Sec. 7.2, we have established that these samples exhibit QSs with sub-ML coverage. Hence, the agreement of the PL transition energies suggests that the samples discussed in the literature do not have full InN coverage either. Furthermore, the measured PL transition energies agree very well with the calculated values using density functional theory for SPSLs with an In coverage of 0.33 MLs.[78,506,510,522] In particular, we observe the predicted redshift in the transition energy by Suski *et al.*[506] for thin barriers (sample I) as a result of the electronic coupling predominantly between the electron states in the QSs. Note, however, that the peak energies do not follow the behavior of the monotonically decreasing band gap of (In,Ga)N with increasing temperature as indicated by the dashed lines in Figs. 7.3(a) and 7.3(b). Note further that the line width of the PL band of 60 meV is not expected for emission from an ordered layer, but is rather indicative of disorder although even larger line widths have been reported for InN/GaN samples with nominally complete InN MLs.[520]

Figure 7.4(a) shows the fit procedure to extract the spectral position, the linewidth, and

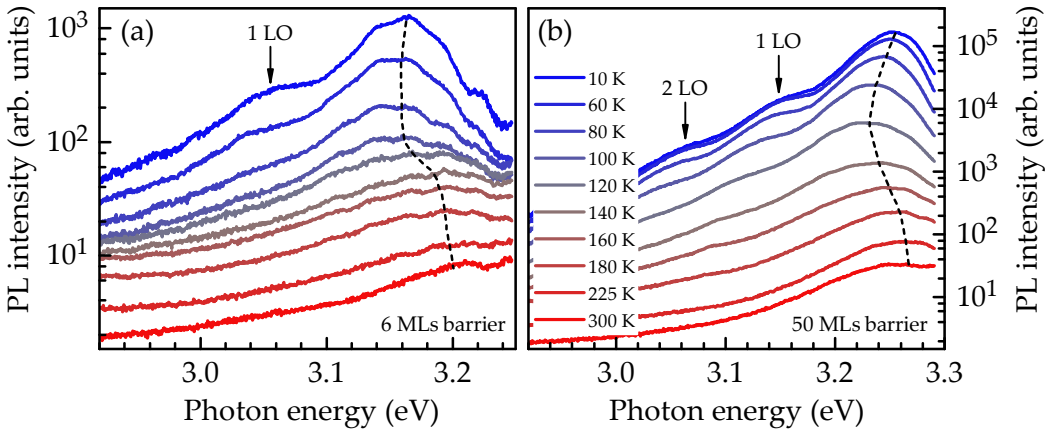

Figure 7.3: Semilogarithmic representation of temperature-dependent steady-state PL spectra of (a) sample I with 6 MLs barrier and (b) (reference) sample II with 50 MLs barrier. The dashed lines indicate the peak position of the QS luminescence and the arrows the first- as well as the second-order longitudinal optical phonon replica (LO).

the integrated intensity of the QS luminescence. The main band labeled by QSs as well as the side-band of the first- and second-order longitudinal optical phonon replica are fit by three Gaussian functions (dashed lines) which are separated by 92 meV, the energy of a longitudinal optical phonon in wurtzite GaN at cryogenic temperatures.[328,329] The extracted results of this line shape analysis of the temperature-dependent steady-state PL spectra are shown in Figs. 7.4(b)–7.4(d). At low temperatures, the emission bands of samples I and II differ significantly not only in the peak PL energy E_{PL}, but also in the integrated intensity I_{PL}. This difference is partly due to the fact that sample II absorbs about 79 % of the incident photons within the total thickness of 132 nm of the 10-period InN/GaN superlattice as compared to 19 % for sample I with its total thickness of only 18 nm. However, this effect accounts only for a factor of four. In fact, the integrated intensity obtained by utilizing an excitation energy of $E_{\mathrm{laser}} = 3.41$ eV, for which the total absorbance of the ten QSs is expected to be very similar for samples I and II, still differs by a factor of 50 (not shown). A stronger influence of surface-induced electric fields for sample I, causing carriers to escape from the QSs and to subsequently recombine at the surface nonradiatively, can be excluded as well, since samples identical to sample I except for a 33-nm-thick cap layer exhibit a comparable PL intensity.[‡] We believe that the large difference in PL intensity between samples I and II originates from the electronic coupling between the QSs in sample I. The redshift of E_{PL} by 90 meV at 10 K [see Fig. 7.4(b)] indicates that this coupling is strong, which in turn means that the electron states are basically delocalized over the entire SPSL. This fact also increases the probability of electrons to reside in the barriers and thus, as we will see below, to suffer from nonradiative recombi-

[‡]Note that the PL energy of the capped sample, which exhibits the same In coverage, is blue-shifted by 60 meV. This may be caused by the different influence of the surface-induced band bending leading to a higher internal electric field and thus to a steeper Stark ladder in the sample without the cap layer. See Ref. 505 for related considerations.

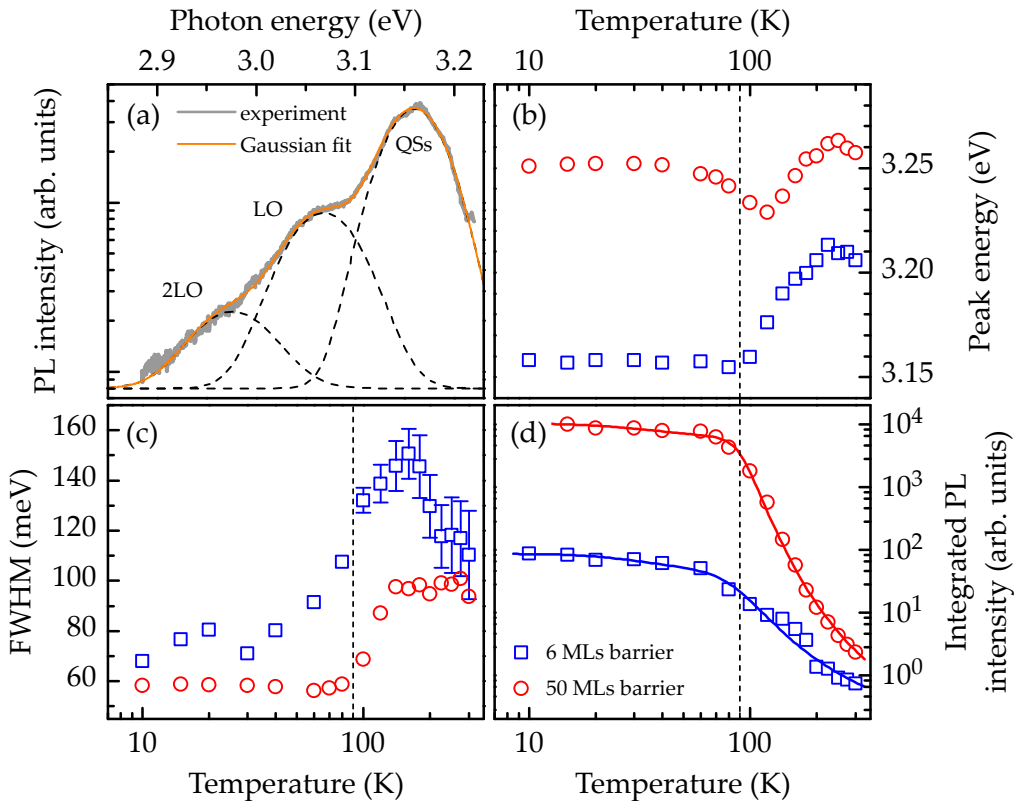

Figure 7.4: (a) Semilogarithmic representation of an exemplary steady-state PL spectrum acquired at 10 K from the sample with 6 MLs barrier recorded at 10 K to illustrate the fit procedure after subtraction of the background for the subsequent peak analysis of the QS luminescence. The orange solid line represents a fit of the spectrum with three Gaussian functions (dashed lines) separated by 92 meV, the energy of a longitudinal optical phonon in wurtzite GaN at cryogenic temperatures.[328,329] Temperature dependence of the (b) peak energy, (c) FWHM and (d) integrated PL intensity of the QS PL band of sample I with 6 MLs barrier (blue squares) and (reference) sample II with 50 MLs barrier (red circles). The dashed lines indicate the threshold temperature at which all three quantities change simultaneously. The solid lines in (d) show fits to the data as discussed in the text.

nation. Furthermore, for an SPSL with a finite number of QSs, the large electrostatic fields within the QSs will not be perfectly balanced by opposing fields in the barriers[103,523] (see also Sec. 2.1), i. e., the heterostructure will exhibit a potential staircase, which in turn will result in a vertical electron-hole separation.

With increasing temperature, E_{PL} redshifts by about 20 meV for sample II with the thicker barriers, before the band blueshifts by 30 meV. In contrast, E_{PL} for sample I with the thinner barriers blueshifts monotonically by about 50 meV. Simultaneously with the change in transition energy, the full width at half maximum ΔE_{PL} increases by about 40 meV (70 meV), and I_{PL} decreases by 2 (3.5) orders of magnitude for sample I (sample II). These simultaneous changes of the three main characteristics of the emission band, highlighted by the dashed lines in Figs. 7.4(b)–7.4(d), suggest that they have a common origin.

The evolution of the transition energy with temperature observed for sample II [see Fig. 7.4(b)] clearly resembles the well-known S-shape commonly observed for random (In,Ga)N alloys.[53] This behavior is most frequently ascribed to carrier localization at low temperatures (see, e. g., Ref. 188 and references therein). At elevated temperatures, carriers are able to relax from shallow to deep states (causing a decrease in the transition energy, such as observed here for E_{PL} around 90 K), while, at even higher temperatures, they are thermally activated to higher energy states (resulting in an increase in E_{PL}) and become mobile within the band of interacting localized states. The latter phenomenon is usually accompanied by an abrupt broadening of the emission band, as also observed here [see Fig. 7.4(c)]. Furthermore, the delocalization of carriers that occurs at this point frequently results in an onset of nonradiative recombination, which manifests itself by an abrupt reduction of the luminous efficiency with increasing temperature.[47] Indeed, the integrated intensities of the PL bands of samples I and II start to decrease at 90 K and are described well by a common three-level Arrhenius-like model of a thermally activated PL quenching[360] with activation energies of (42 ± 10) and (89 ± 15) meV for sample I and II, respectively [see Fig. 7.4(d)].

An alternative explanation for the simultaneous blueshift of the emission band and a quenching of its intensity as observed for (In,Ga)N/GaN(0001) QWs has been recently proposed by Langer *et al.*[170] Their model relies on the exponential variation of the radiative lifetime with transition energy due to the strong piezoelectric fields within the QWs. An activated nonradiative recombination preferentially quenches the longer living transitions, resulting in an effective blueshift of the emission band. Within this interpretation, the activation energy deduced from the data in Fig. 7.4(d) would be related to the activation of nonradiative centers and not to the localization energy of carriers.

7.3.2 Temperature-dependent time-resolved PL spectroscopy

In order to distinguish between these two different interpretations of our steady-state PL data presented at the end of the previous subsection, we performed temperature-dependent time-resolved PL experiments. Additionally, time-resolved PL has the possibility to identify the presence of an ordered phase (i. e., $InGa_2N_3$). Figures 7.5(a) and 7.5(b) show the decay of the PL intensity at the peak energy of the emission band of samples I and II, respectively, in a double logarithmic representation. Regardless of the specific emission energy, the recombination dynamics observed is qualitatively similar for both samples and is characterized by the following three major properties. First, the peak PL intensity of the transient just after the laser pulse I_{max} is almost constant up to 50–70 K and decreases thereafter with increasing temperature. Second, the decay at 10 K is very slow for both samples and actually follows a power law [see Figs. 7.5(a)–7.5(b)]. Third, the decay accelerates with increasing temperature and gradually approaches a single exponential dependence at 150 K [see the corresponding fit indicated by the dotted line in Fig. 7.5(a)]. In the following, we will discuss these three observations in detail.

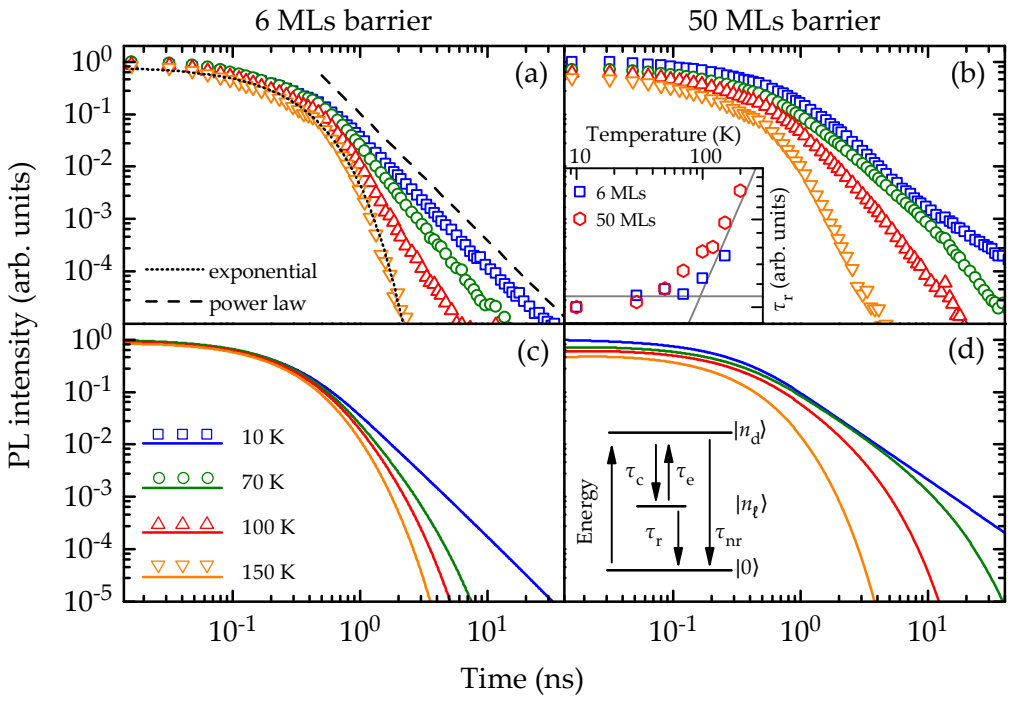

Figure 7.5: Double-logarithmic representation of the experimental PL transients of (a) sample I with 6 MLs barrier and (b) (reference) sample II with 50 MLs barrier at various temperatures as indicated in (c). The dashed and dotted lines in (a) show a comparison with a $t^{-2.4}$ power law and a fit with a single exponential function, respectively. The inset in (b) displays the temperature dependence of the inverse peak intensity of the transient, which is proportional to the radiative lifetime τ_r. The solid lines in the inset are a guide to the eye and highlight the change from constant to linear increasing τ_r with temperature. The corresponding simulated PL transients are shown in (c) and (d). The simulations are based on the rate-equation system (7.1)–(7.2), which is schematically depicted as the inset in (d).

(i) Since I_{max} is proportional to the inverse radiative lifetime,[142] it follows that the radiative lifetime is almost constant up to about 50–70 K as shown in the inset of Fig. 7.5(b). As shown in Sec. 2.3.4, a temperature-independent radiative lifetime is a fingerprint for transitions arising from zero-dimensional states.[372] At higher temperatures, the radiative lifetime approaches the linear increase expected for radiative transitions in two-dimensional systems such as QWs and QSs [see the inset of Fig. 7.5(b)].[372] These results thus support the interpretation of the data shown in Figs. 7.4(c)–7.4(d) in terms of carrier localization at low temperatures followed by delocalization at 70–90 K and not the model of activation of nonradiative centers.

(ii) The power law decay kinetics observed for both samples at 10 K furthermore demonstrates that the recombination is not excitonic, but takes place between individually localized electrons and holes with varying spatial separation[48,49,79] as explained in detail in Chap. 4.

(iii) Together with the acceleration of the decay at elevated temperatures, the time-integrated intensity of the transients decreases significantly, suggesting that both observations are linked by a nonradiative channel made accessible by the delocalization of carriers. To test this hypothesis, let us consider a simple model for the recombination dynamics visualized by the level scheme in the inset in Fig. 7.5(d). We implicitly assume that the recombination is determined by holes populating either localized $|n_\ell\rangle$ or extended/delocalized states $|n_\mathrm{d}\rangle$. These populations are coupled via the relaxation of holes from $|n_\mathrm{d}\rangle$ to $|n_\ell\rangle$ with a time constant τ_c and by their thermally activated emission from $|n_\ell\rangle$ to $|n_\mathrm{d}\rangle$ with a time constant τ_e. To keep the model as simple as possible, we assume that recombination from localized states is purely radiative with a temperature-dependent lifetime $\tau_\mathrm{r}(T)$ as observed experimentally, while the extended states are supposed to be dominated by a nonradiative process with a constant lifetime τ_nr.

These considerations lead to the following coupled system of differential equations

$$\frac{\partial n_\mathrm{d}(T)}{\partial t} = -\frac{n_\mathrm{d}}{\tau_\mathrm{c}} - \frac{n_\mathrm{d}}{\tau_\mathrm{nr}} + \frac{n_\ell}{\tau_\mathrm{e}} \exp\left(-\frac{E_\mathrm{a}}{k_\mathrm{B}T}\right) \tag{7.1}$$

$$\frac{\partial n_\ell(T,t)}{\partial t} = \frac{n_\mathrm{d}}{\tau_\mathrm{c}} - t^{a-1}\frac{n_\ell}{\tau_\mathrm{r}(T)} - \frac{n_\ell}{\tau_\mathrm{e}} \exp\left(-\frac{E_\mathrm{a}}{k_\mathrm{B}T}\right) \tag{7.2}$$

with the activation energy E_a for the emission of holes from localized to extended states. The prefactor t^{a-1} of the radiative term $t^{a-1}n_\ell/\tau_\mathrm{r}$ in Eq. (7.2) results in a stretched exponential decay, but approaches a power law decay for $a \to 0$.

Intensity transients simulated by Eqs. (7.1) and (7.2) are shown in Figs. 7.5(c) and 7.5(d) corresponding to sample I and II, respectively. Evidently, the experimentally observed evolution from a power law to a single exponential decay together with the simultaneous loss in intensity are well reproduced. Our understanding of this phenomenon (namely, that it is solely induced by delocalization) is thus confirmed. Quantitatively, we have assumed activation energies E_a of 16 meV for sample I and 27 meV for sample II to obtain a change with temperature in agreement with the experiments. Both of these values are a factor of about 3 smaller than those derived from our steady-state PL experiments [see Fig. 7.4(d)]. We ascribe this finding to the much higher (two orders of magnitude) excitation density in the time-resolved PL experiments, which is known to significantly increase the actual carrier temperature with respect to the temperature of the lattice.

7.4 Summary, conclusions and outlook

Using time-resolved PL, the sub-ML InN QSs, formed by utilizing the ordered $(\sqrt{3} \times \sqrt{3})$R30°-In adsorbate structure on GaN(0001), have been found to act electronically as two-dimensional random alloys similar to conventional (In,Ga)N/GaN QWs. Especially, a narrow linewidth of the PL transition or exponential PL transients at low temperatures

could not be detected. Since the transition energies observed for our samples are essentially identical to those reported in the literature as InN/GaN digital alloys,[76,521] we suggest that these nominally complete InN MLs are in fact also formed by the energetically favorable In adsorbate structure on GaN(0001), but without detectable lateral ordering.

Obviously, the high degree of lateral ordering evident from the reflection high-energy electron diffraction pattern can be conserved upon overgrowth only partly as detected by transmission electron microscopy.[519,524] Additionally, any deviation from a perfectly ordered state in a two-dimensional system will induce carrier localization.[525] At present, it seems be to unlikely to obtain perfectly ordered $InGa_2N_3$ on a macroscopic scale. Furthermore, the minimal achievable transition energy in a SPSL containing the $(\sqrt{3} \times \sqrt{3})$R30°-In adsorbate structure is limited due to a maximum In content of 33 %.

Hence, the fabrication of InN/GaN digital alloys emitting in the green spectral range may be more difficult than envisioned. The low growth temperatures of the QB, required to embed the sub-ML InN QSs, cause nonradiative recombination and result in a low IQE at room temperature. Moreover, the vertical separation of electrons and holes in the SPSL due to the internal electric fields reduces the radiative recombination rate. To overcome these problems, a radically different growth approach is necessary to realize efficient InN/GaN digital alloys with narrow optical transitions. For example, the growth along the N-polar crystal direction allows the stabilization of InN at higher temperatures which may reduce the point defect density. On the other hand, the growth along the nonpolar direction on bulk GaN substrates eliminates the strong internal electric fields and impedes the vertical separation of electrons and holes. Finally, the growth of QSs with higher In content may be possible for other morphologies. Only recently, spontaneous ordering into alternating In-rich and Ga-rich MLs has been reported for strain-released (In,Ga)N$(000\bar{1})$ nanowires.[526]

Chapter 8

Summary, conclusions, and outlook

In this thesis, we have investigated the influence of the localization of charge carriers on the recombination dynamics in polar and nonpolar (In,Ga)N/GaN QWs by time-resolved PL. We have found that in polar QWs recombination occurs by tunneling between individually localized, spatially separated electrons and holes, but is due to the radiative decay of localized excitons in nonpolar QWs. In conjunction with Monte Carlo simulations, we have analyzed the peculiar power law decay in polar (In,Ga)N/GaN QWs to gain access to the diffusivity and the recombination rates. Furthermore, we have applied our understanding of the recombination processes to evaluate the potential of three alternative concepts for future (In,Ga)N-based light emitters. In this chapter, we briefly summarize and relate the main conclusions drawn from the previous chapters. Finally, we present a general outlook on further investigations as well as on future concepts for (In,Ga)N-based light emitters.

Summary and conclusions

The aim of this thesis was to understand the recombination dynamics of (In,Ga)N/GaN heterostructures and investigate the influence of the localization of charge carriers. Moreover, the gained knowledge on the recombination dynamics was applied to evaluate three different concepts for future (In,Ga)N/GaN light emitters, namely N-polar, axial (In,Ga)N/GaN QDs in GaN nanowires, core/shell GaN/(In,Ga)N μ-rods, and SPSLs containing sub-ML InN QSs embedded between GaN QBs. Utilizing temperature-dependent steady-state and time-resolved PL spectroscopy, we arrived at the following main conclusions:

- Similar to the decay of excitons in GaN, the recombination is excitonic for nonpolar (In,Ga)N/GaN QWs and results in an exponential decay of the PL intensity. In striking contrast, the PL transients of polar (In,Ga)N/GaN QWs asymptotically follow a power law. The peculiar power law shape indicates that recombination occurs by tunneling between individually localized, spatially separated electrons and holes.[51] We explain the distinct difference in the recombination mechanism by considering the balance between the localization and the exciton binding energies,

which are both influenced by the magnitude of the internal electric field in the QWs (see Chap. 5). Moreover, we verify this interpretation by altering the recombination mechanism in one and the same sample, utilizing an external bias to tune its internal electric field (see Chap. 6).

- The recombination of electrons and holes in polar (In,Ga)N/GaN QWs with its power law asymptote cannot by characterized by a unique PL lifetime. Hence, also the concept of a carrier or diffusion length cannot be applied to this case. In addition, a long PL decay does not necessarily correlate with a high IQE, because not only the radiative recombination slows down, but also the nonradiative one. Moreover, the power law decay is preserved despite nonradiative recombination. Thus, the PL transients of polar QWs have to be analyzed more carefully, for example with the recombination model presented in Chap. 4, to extract any useful recombination parameters. For the simulation of the complex shapes of the decay in polar (In,Ga)N/GaN QWs, we utilized a dedicated Monte Carlo algorithm,[79] which efficiently solved the position-dependent diffusion-reaction equations of our model. From the simulations of the experimentally obtained PL transients, we deduced recombination coefficients and diffusivities.[51] From these results, we conclude that the N-polar, axial (In,Ga)N/GaN nanowires suffer from a very efficient capture of charge carriers by nonradiative centers even at low temperatures. The density of these centers, however, is comparable to that of the Ga-polar, planar reference sample, but their capture coefficients are significantly larger. Thus, it is the strong localization at compositional fluctuations that prevents a strong thermal quenching of the PL intensity. Hence, taking this thermal quenching as a measure for the IQE may be entirely misleading.

- The analysis of the exponential PL transients in nonpolar core/shell GaN/(In,Ga)N µ-rods reveals the radiative decay of excitons. This excitonic recombination occurs on the order of ns and is thus much faster than the tunneling recombination in polar QWs which takes place on the order of µs. However, not only the radiative recombination rate increases, but also the nonradiative one as a comparison with lifetimes reported in the literature for similar structures shows (see Chap. 5). Thus, the higher overlap of electron and hole wave functions in these structures does not necessarily result in a higher IQE.

- Temperature-dependent PL spectroscopy of sub-ML InN/GaN SPSL reveals a decay asymptotically following a power law at low temperatures. Hence, individually localized charge carriers with varying in-plane separation in the QSs recombine via tunneling, which is reminiscent of the PL decay in conventional (In,Ga)N/GaN QWs (see Chap. 7). At elevated temperatures, the power law asymptote smoothly approaches an exponential decay. We explain this observation by efficient nonradiative recombination, once delocalization sets in, probably caused by the low growth temperature of the GaN QBs.[489] The high nonradiative rate in conjunction with the low radiative rate, caused by the vertical separation of electrons and holes

in the SPSL, leads to a weak PL intensity at room temperature. Consequently, the replacement of conventional (In,Ga)N/GaN QWs by digital alloys consisting of the binary compounds InN and GaN may be more difficult than envisioned.

Outlook

The presented understanding of the influence of localization of charge carriers on the recombination dynamics in polar (In,Ga)N/GaN QWs enables the systematic and refined analysis of samples grown on substrates with different polarities as well as grown with various geometries and techniques. In the following, we suggest attractive structures to explore the difference between N-polar and Ga-polar (In,Ga)N/GaN QWs grown by MBE, to optimize In-containing SPSLs, and to test our model concerning the balance between the localization and the exciton binding energies. Moreover, we propose an improved experiment to analyze the PL transients of polar (In,Ga)N/GaN QWs at high carrier densities.

- With our understanding of the recombination dynamics and our model for the simulation of PL transients, we have the possibility to accurately characterize the polar (In,Ga)N/GaN heterostructures and give useful feedback for the epitaxy. So far, we have not investigated any N-polar (In,Ga)N/GaN heterostructures grown by MOCVD which might be an interesting test bed for our model concerning the balance between the localization and the exciton binding energies. Due to the reversed direction of the internal electric fields, electrons should reside at the lower interface of the QWs, which is more abrupt in general and does exhibit less frequently monolayer fluctuations. Hence, the localization energy for electrons should be reduced, resulting in an enhanced in-plane diffusivity of electrons and consequently in a faster decay. The reduced localization and the faster decay, though, may not result in an increasing IQE. In addition, the investigation of so-called second generation LEDs,[527] which are fabricated on bulk GaN substrates, might give useful information about the recombination dynamics of highly efficient polar (In,Ga)N/GaN LEDs which may serve as a new reference.
- For meaningful simulations of the recombination dynamics of (In,Ga)N/GaN LEDs, our results imply that it is imperative to consider the omnipresent localization of holes at compositional fluctuations of the random ternary alloy (In,Ga)N. This localization results in excitation-dependent recombination coefficients. Consequently, we suggest to revise conventional drift-diffusion simulations as well as phenomenological models (e. g. the *ABC* model) that use constant recombination coefficients to extract the IQE. The diffusion-reaction equations employed in Chap. 4 constitute a clear physically motivated framework on which a more general model of the recombination dynamics, also including effects for high excitation densities, could be based. A recent atom-to-device simulation framework, paying attention to localization effects in (In,Ga)N/GaN heterostructures, has been established in the DEEPEN

project and can by employed for sophisticated device simulations.[243] Additionally, the group of Weisbuch has introduced the so-called localization landscape theory of disorder in semiconductors, whose results can be directly implemented into a drift-diffusion model of carrier transport and into the calculation of optical transitions.[528] For the investigation of PL transients of polar (In,Ga)N/GaN QWs at high excitation densities, time-resolved PL experiments of biased LEDs (under typical operation conditions) may provide additional insights. The experimental procedure may be similar to the one described in Ref. 220, but the recorded PL transients should exhibit a much higher dynamic range.

- In order to replace conventional (In,Ga)N/GaN QWs with digital alloys for efficient and narrow-linewidth future light-emitting devices, the width of the QBs has to be reduced from 6 MLs to 1–2 MLs. Utilizing the *ordered* $(\sqrt{3} \times \sqrt{3})$R30°-In adsorbate structure with an In content of 33 % grown on Ga-polar GaN at high temperatures may enable the realization of superior blue laser diodes for Blu-ray™ applications. To achieve green emission, the fundamental problem to deposit pure InN QSs or to realize ordered QSs with an In content higher than 33 % in a GaN matrix has to be solved. A higher incorporation of In at higher growth temperatures may be possible along the N-polar direction of GaN. A possible structure may contain 3 periods of 1 ML InN and 3 MLs GaN embedded between GaN or even (Al,Ga)N barriers. In addition, the growth along the nonpolar direction is an attractive alternative to eliminate the internal electric fields in the SPSL stack. However, the absence of the quantum-confined Stark effect demands a higher In content for transition energies to be comparable to the polar ones.

Appendix A

Analysis of the contrast pattern in µ-electroluminescence maps

Localization and the recombination of individual, spatially separated charge carriers in polar (In,Ga)N not only constitute interesting physical phenomena, but also have implications on real-world applications. In this appendix, we extend our study of the diffusivity to normal operation conditions of LEDs and discuss the influence of the diffusion on µ-EL patterns of (In,Ga)N/GaN LEDs. The comparison of µ-EL patterns with drift-diffusion simulations suggests a limited diffusivity even under normal operating conditions. Moreover, the correlation analysis of the µ-EL pattern reveals that the distribution of In content and point defects cause the microscopic luminescence intensity pattern. This result questions the applicability of conventional drift-diffusion simulations for (In,Ga)N/GaN QWs.

A.1 µ-electroluminescence spectroscopy of (In,Ga)N/GaN LEDs

Because of carrier localization in the fluctuating potential landscape of the random alloy of (In,Ga)N, the carrier diffusivity is low in polar (In,Ga)N/GaN QW at the low excitation densities employed for the time-resolved PL measurements presented in Chap. 4. This situation might change if the density of charge carriers is as high as under normal operation conditions of LEDs (in the range of $2.5 \times 10^{12}\,\mathrm{cm}^{-2}$). Commonly, a filling of localization centers[529] and the subsequent increase of the diffusion[530] are assumed to occur.

In this section, we conduct µ-EL measurements of polar (In,Ga)N/GaN LEDs, emitting in the blue or green spectral range. All measurements have been performed at room temperature. The LEDs have been introduced and characterized in Sec. 3.5.2 and investigated under reverse bias in Chap. 6. With electrical injection, we have the possibility to achieve very high sheet carrier densities and to analyze the diffusion under operating conditions. The EL of the LEDs was collected utilizing an 100× objective with a numerical aperture of 0.7. Employing a monochromator and confocal microscopy, we achieve spectral and spatial resolutions of about 1 meV and 250 nm, respectively (for more details see Sec. 3.4).

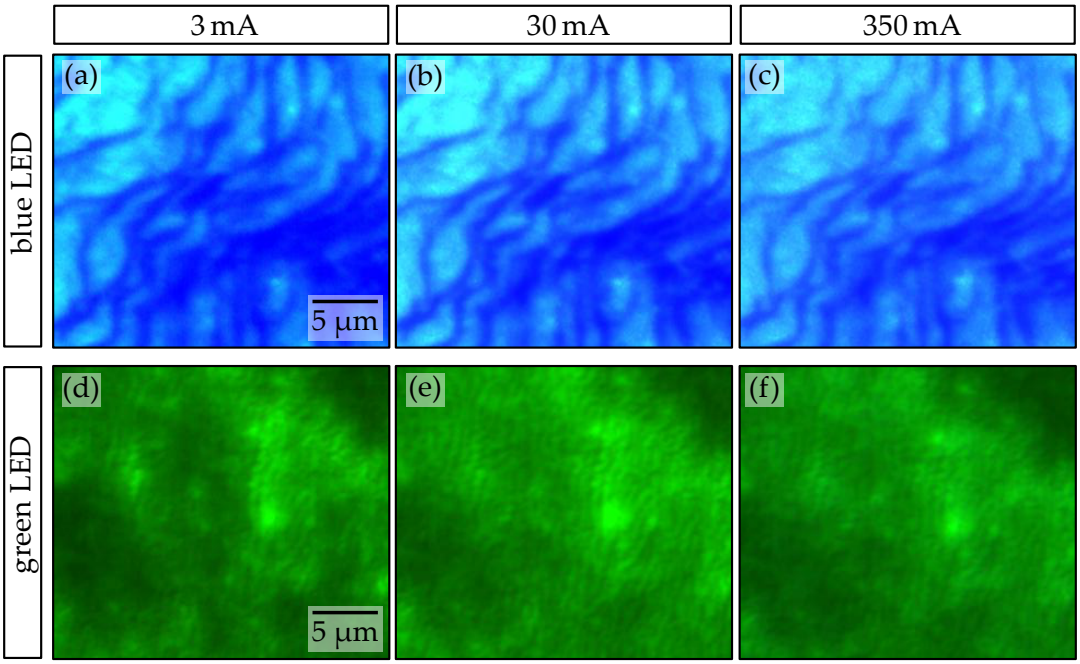

Figure A.1: EL micrographs of a blue (a)–(c) and a green (d)–(f) LED. The current varies over two orders of magnitude ranging from 3 mA (a, d) over 30 mA (b, e) to 350 mA (c, f). The brightness of the true color micrographs represents the EL intensity of the different areas in the LED.

At first, we took EL optical micrographs of a blue and a green LED with the current varying over more than two orders of magnitude. The true-color micrographs are shown in Fig. A.1 and represent the active region of the LED. While 3 mA represent a current just slightly above the threshold of the LED, 30 mA is close to the value at which the LEDs achieve their maximum EQE. The droop (a reduction of the EQE with increasing current densities) reduces the EQE by approximately 20 % for the blue and 35 % for the green LED at standard operating conditions of 350 mA [see Fig. 3.7(f) in Sec. 3.5.2]. We observe two important facts from the micrographs in Fig. A.1. First, the distribution of the EL looks the same regardless of the applied current for one specific color of the LED. Especially no blurring of the contrast is observed with increasing current. Minor differences may be due to different exposure times and slight changes of the focal plane while recording the micrographs. Second, comparing the blue and the green LED, the distribution of the luminescence intensity in the blue LED has a much coarser pattern* than in the green one. Note that the distribution of the EL does not correlate with features at the polished surface of the LED as verified by atomic force microscopy (not shown), which could lead to a different extraction of the light. In addition, focusing the microscope objective, the EL intensity is maximal, when the contrast is maximal. Consequently, the EL pattern originates from the active region of the LED.

On the basis of treating (In,Ga)N as a random alloy with localization phenomena,

*The pattern of the blue-emitting LED is similar to the one observed for (In,Ga)N layers. [531]

it is conceivable to observe a patterned EL distribution at low current densities. Parts with higher In content or regions with larger QW width (well-width fluctuations) attract charge carriers due to the lower band gap. Hence, areas with a lower peak energy should correlate with areas with a higher EL intensity. However, these fluctuations occur on an atomic to a nanometer scale in (In,Ga)N.[157] Additionally, increasing the current density should lead to a saturation of localization sites and thus an enhanced portion of mobile charge carriers.[530] Particularly, for a homogeneous pumping of the active region, as it is the case for the investigated samples, we expect to observe a blurring of the contrast at high current densities.

The much finer contrast pattern of the green LED [see Figs. A.1(d)–A.1(f)] seems to reflect major differences in the growth of the active region. The different luminescence distribution may be directly linked to the reduced efficiency, because in contrast to the blue LED no large bright areas exist, but only small spots. This may indicate that defects (i. e., nonradiative recombination centers) cause the different contrast patterns in blue and green LEDs.

In order to investigate the above mentioned correlation of peak energy and intensity, we have mounted the samples on the x-y scanning stage of the LABRAM EVOLUTION setup (see Sec. 3.4.1) and acquired 20×20 μm^2 μ-PL and μ-EL maps with a scanning increment of

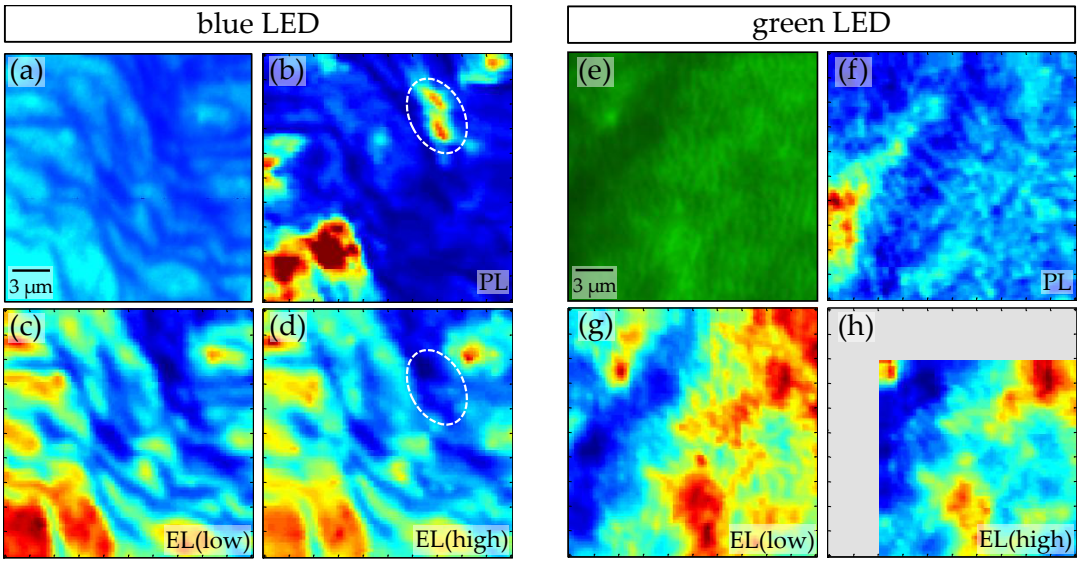

Figure A.2: Comparison of EL micrographs, μ-PL and μ-EL intensity maps for two LEDs with different emission color. The color-coded integrated intensity of the maps ranges from low intensity (blue) to high intensity (red). The EL micrographs (a) and (e), the μ-PL maps (b) and (f) as well as the μ-EL maps (c, d) and (g, h) of the blue and the green LED are acquired at the same position. The gray area in (h) has not been recorded due to an offset in the position. The μ-EL maps label with low (high) have been recorded with a current of 30 mA (360 mA). For the PL measurements, we used E_{laser} = 3.06 eV and with an excitation power density of 15 kW/cm^2. The dashed ellipses mark an exemplary region where PL and EL intensity are inverted. The size of the μ-EL maps amounts to 20×20 μm^2 with a step increment of 0.25 μm.

0.25 µm for the blue [see Figs. A.2(b)–A.2(d)] and the green [see Figs. A.2(f)–A.2(h)] LED. The µ-PL and µ-EL maps have been recorded at the same position for the respective LED. We have integrated the intensity over a spectral range from 2.23–2.46 eV and 2.60–2.93 eV for the green- and blue-emitting LEDs, respectively. The corresponding EL micrographs of the investigated areas are shown in Figs. A.2(a) and A.2(e), respectively.

Comparing the luminescence patterns for each LED, slight differences between the EL micrograph, the µ-PL, and the µ-EL maps are visible. In particular, the resolution of the micrograph of the green LED seems to be higher than the corresponding maps. We attribute this to a combination of the long acquisition time of the maps (1 h compared to 500 ms for a micrograph) and a thermally induced drift due to the current flow. As we are investigating the active region of a polar LED, the PL in the unbiased device is sensitive to minimal changes of the internal electric fields (induced, for example, by inhomogeneities in doping or strain), which may explain the differences of the µ-PL and the µ-EL maps [see area marked by the dashed circles in Figs. A.2(b) and A.2(d)]. Nonetheless, the µ-PL map and the µ-EL maps reveal similar luminescence intensity distributions, indicating that an enhanced density of charge carriers does not significantly change the spatial distribution of the EL intensity. Utilizing the Michelson contrast[532]

$$\frac{I_{\mathrm{min}} - I_{\mathrm{max}}}{I_{\mathrm{min}} + I_{\mathrm{max}}} \tag{A.1}$$

for the minimum (I_{min}) and maximum (I_{max}) integrated EL intensities to quantify the contrast, we obtain 0.65 (0.64) and 0.54 (0.47) for blue and green LED at low (high) current densities, respectively. We note that determining the intensity with the high accuracy of 3 % results already in an estimated error of about ±0.03 for the Michelson contrast.

A.2 Drift-diffusion simulations

In the following, we will discuss the observed luminescence pattern in the standard framework of drift and diffusion of excitons in a potential landscape. In this picture, excitons will drift into potential minima causing a high contrast in the resulting distribution of the luminescence intensity (decay of the excitons). In contrast, diffusion will level/smooth the distribution of excitons and thus the contrast. For a qualitative comparison of the contrast for different diffusivities, we have carried out two-dimensional drift-diffusion simulations by solving the equation

$$0 = \frac{\partial^2 n(x,y)}{\partial t} = G(x,y) + D\Delta n(x,y) + \mu^* \vec{\nabla}\left[\left(\vec{\nabla} E_{\mathrm{g}}(x,y)\right) n(x,y)\right] - \frac{n(x,y)}{\tau_{\mathrm{eff}}} \tag{A.2}$$

for excitons with n, $\tau_{\mathrm{eff}} = 100\,\mathrm{ns}$, $\mu^* = 50\,\mathrm{cm}^2/(\mathrm{V\,s})$, and D being their density, effective lifetime, mobility, and diffusivity, respectively. We place a potential minimum in the middle of a given area [see Fig. A.3(a)]. Steady-state excitation conditions with a Gaussian laser pulse $G(x,y)$ have been used for the simulation in the potential landscape $E_{\mathrm{g}}(x,y)$. The remaining parameters for the simulations are related to the experiment and shown

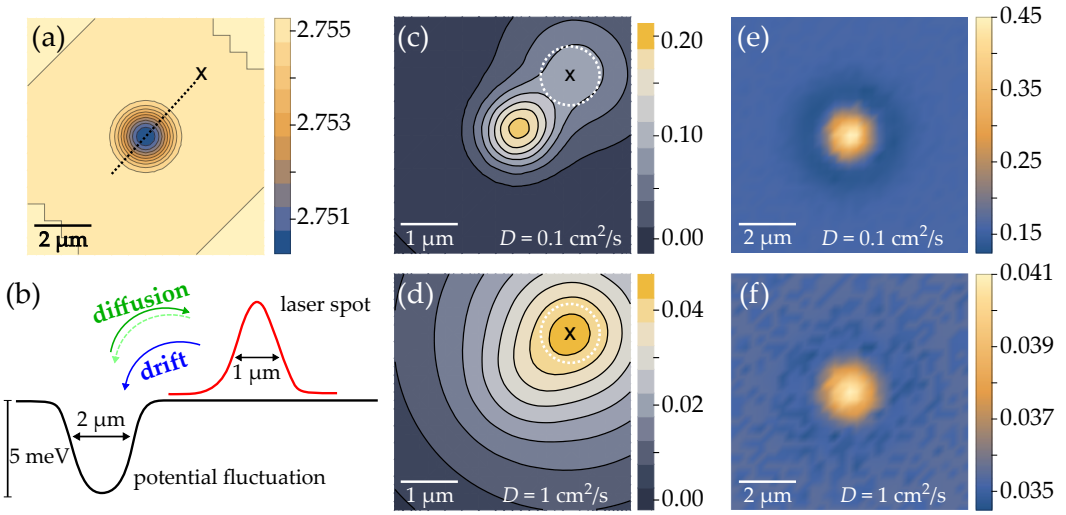

Figure A.3: (a) Potential landscape with color-coded energy in eV. (b) Schematic of drift and diffusion of excitons along the dotted line in (a). The excitons are created optically with a laser with a given spatial distribution. Exemplary simulated intensity distribution (color-coded) with diffusivities of (c) $D = 0.1$ cm^2/s and (d) $D = 1$ cm^2/s (Note the different scales.). The position of the laser spot is marked by an X, and the dotted circle represents the area used for the determination of the integrated intensity shown in (e) and (f). Resulting distribution of the integrated intensity for (e) $D = 0.1$ cm^2/s and (f) $D = 1$ cm^2/s for scanning the laser spot over the area in (a) with a step increment of 0.25 µm.

in the schematic in Fig. A.3(b). First, we calculate the intensity distribution for a given position of the exciting laser spot for diffusivities of $D = 0.1$ cm^2/s [see Fig. A.3(c)] and $D = 1$ cm^2/s [see Fig. A.3(d)].

Second, we scan the laser in the simulation over an area of 8×8 µm^2 around the potential minimum with a scanning increment of the laser spot of 0.25 µm. The resulting map of the integrated intensity around *each* position of the laser spot [see dotted line in Fig. A.3(c)] exhibit a maximum at the center of the potential minimum for low ($D = 0.1$ cm^2/s) [see Fig. A.3(e)] and high ($D = 1$ cm^2/s) [Fig. A.3(f)] diffusivities. However, the contrast of the images significantly blurs from values of the contrast of 0.55 for $D = 0.1$ cm^2/s to 0.09 for $D = 1$ cm^2/s. Thus, according to our simulations, we expect a pronounced blurring of the drift-induced contrast in the experiments, if the diffusion is enhanced.

A.3 Correlation of peak energy and intensity

To evaluate only the contrast of the EL intensities may be an oversimplification if the luminescence pattern is affected by processes in addition to drift and diffusion. To overcome the problem of evaluating the contrast only, we analyze the Pearson correlation coefficient ρ of the peak energy and the integrated intensity of the µ-EL maps. To assess the peak energy, we have automatically processed the spectra as shown in Sec. 3.4.1. The Pearson correlation coefficient ρ of N points of the integrated intensity I and the peak

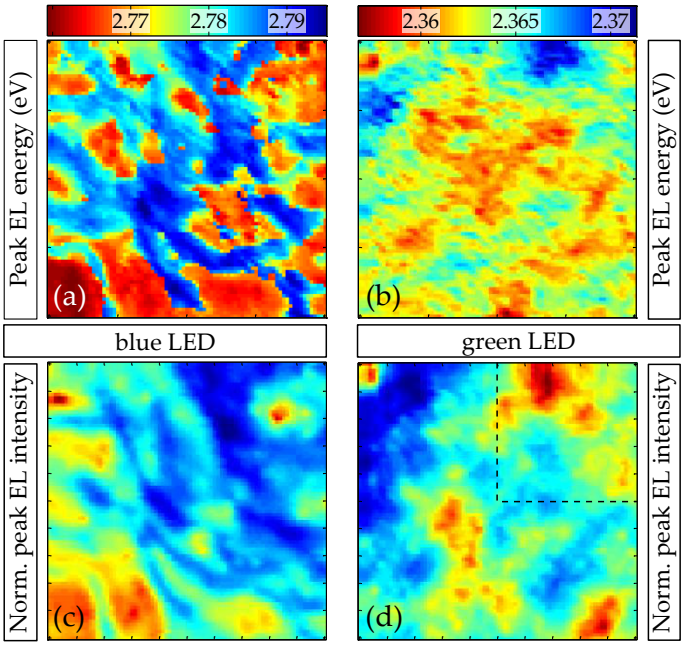

Figure A.4: µ-EL maps of the peak photon energy in eV of the (a) blue and (b) green LED operated at 360 mA. The integrated µ-EL intensity for the (c) blue and (d) green LED ranges from low intensity (blue) to high intensity (red). The dashed square marks an area with a positive correlation coefficient, which is explained in more detail in the text. The size of the µ-EL maps amounts to 20×20 µm^2 with a step increment of 0.25 µm.

energy E with their respective mean values $\bar{\mu}$ and standard deviations σ is defined as

$$\rho(E,I) = \frac{1}{N-1}\sum_{i=1}^{N}\left(\frac{E_i-\bar{\mu}_E}{\sigma_E}\right)\left(\frac{I_i-\bar{\mu}_I}{\sigma_I}\right). \tag{A.3}$$

From the two-dimensional drift-diffusion simulations, we deduce that for negligible diffusion a potential fluctuation is associated with a strict anti-correlation (high intensity correlates with low peak energy; $\rho = -1$) as confirmed by Fig. A.3(c). As carriers are distributed more uniformly for high diffusivities, we expect an experimental correlation coefficient in the range $-1 \leq \rho \ll 0$.

In Figure A.4, we show exemplary µ-EL maps of the peak energy and the integrated EL intensity for a blue and a green LED recorded at standard LED operating conditions. Scanning over a comparably large area of 20×20 µm^2, the difference of the maximum and the minimum peak energy covers the range from 10 to 40 meV. Generally, the blue LED seems to exhibit a slightly larger distribution of peak energies. This behavior appears to be rather general, as we observe it not only in µ-EL, but also in µ-PL maps of undoped blue and green single-QW samples (not shown). The contrast of the EL intensity amounts to 0.64 and 0.47 for the blue and green LED, respectively [see Figs. A.4(c) and A.4(d)].

For the µ-EL map of the blue LED [see Figs. A.4(a) and A.4(c)], we obtain $\rho \approx -0.6$,

i. e., an anti-correlation. Figure A.5(a) exemplary shows the distribution of peak energy and peak intensity which exhibit a negative correlation indicated by the red line. The combination of the anti-correlation with the contrast pattern indicates a small diffusivity for the blue LED. In contrast, the µ-EL map of the green LED [see Figs. A.4(b) and A.4(d)] reveals a correlation coefficient of $\rho \approx 0$. However, if we analyze the smaller area (5×5 µm) surrounded by the dashed line in Fig. A.4(d), we achieve a correlation with a (positive) correlation coefficient of $\rho \approx 0.8$. A correlation, however, cannot be explained in the framework of drift and diffusion alone.

The analysis of a larger number of µ-EL maps (from various areas of a 0.8 mm^2 LED chip) reveals Pearson correlation coefficients of $-0.7 \leq \rho \leq 0.2$ for blue LEDs and values of $0 \leq \rho \leq 0.8$ for green LEDs as shown in Fig. A.5(b). Additionally, we present µ-PL maps from similar (In,Ga)N/GaN heterostructures in the same graph. The scattering of the correlation coefficient to values closer to zero for the PL experiments compared to the EL experiments may be explained by the higher sensitivity of the PL intensity to the internal electric fields of the unbiased samples. However, the finding of a positive correlation coefficient in the green LEDs underlines that the contrast pattern cannot be a result of drift and diffusion.

A.4 Correlation between photoluminescence intensity and structural defects

Based on cathodoluminescence measurements, Pozina *et al.* [533] proposed that structural defects, such as dislocations, are at the origin of the contrast pattern in CL maps from (In,Ga)N/GaN heterostructures. Kaneta *et al.* [534] suggest a model for which they assume

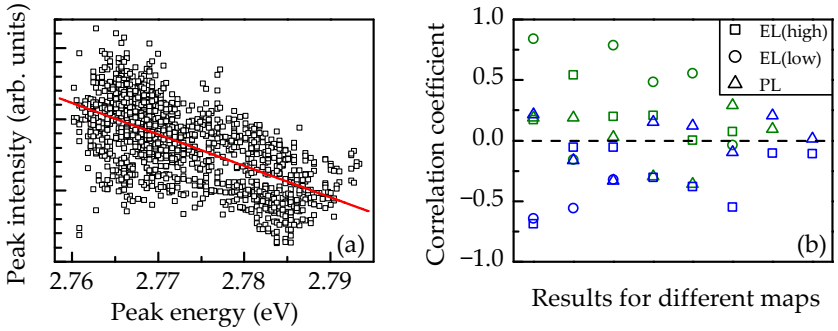

Figure A.5: (a) Example of a µ-EL map with 6561 data points where only every sixth point is shown. The correlation coefficient of such as map is calculated by means of Eq. (A.3). The solid line highlights the anti-correlation with a value of $\rho \approx -0.6$. (b) Compilation of the Pearson correlation coefficients of µ-PL maps (triangles), µ-EL maps recorded at low current densities (circles), and µ-EL maps recorded at high current densities (squares). Blue- or green-emitting LEDs are represented by the corresponding color. A correlation coefficient of $\rho = 1$ denotes correlation (high intensity at high peak energy), while anti-correlation (high intensity at low peak energy) is indicated by in a correlation coefficient of $\rho = -1$.

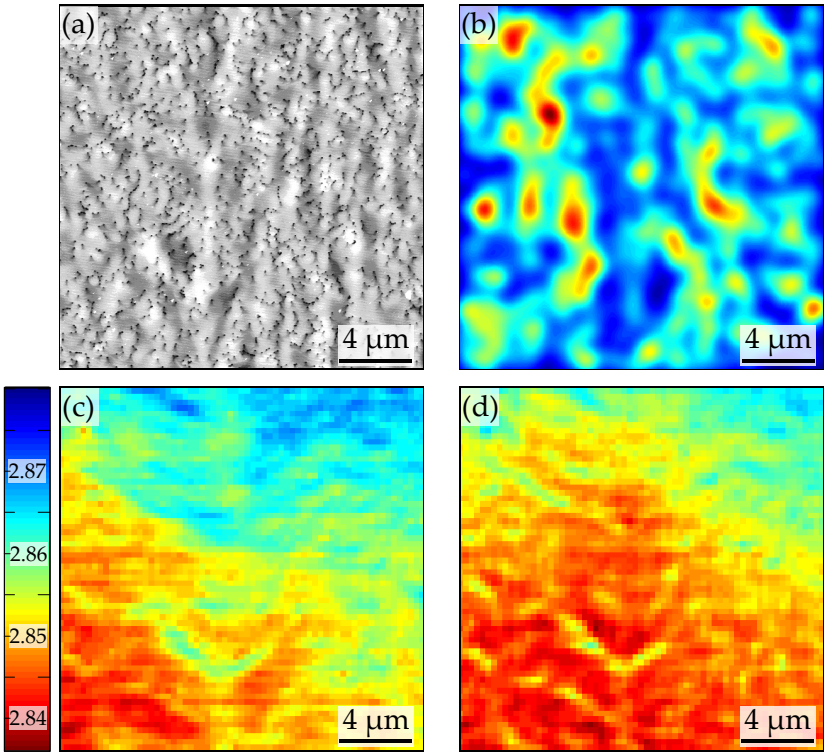

Figure A.6: (a) Atomic force micrograph of an undoped blue single-QW sample. The V-pits, forming at the outcrops of threading dislocations, are visible as black spots. (b) Convolution of the dislocations with Gaussian functions with a full width at half maximum of 800 nm. The intensity represents the assumed impact of nonradiative recombination and is color-coded ranging from low (blue) to high (red) impact of nonradiative recombination. Color-coded (c) peak energy in eV and (d) peak intensity (blue: low intensity, red: high intensity) of the μ-PL recorded at the same position as the micrograph in (a).

a higher number of point defects accumulating in the regions of higher In content in green LEDs.[†] Thus, charge carriers are attracted by these regions, but recombine preferentially nonradiatively.[534,536–540] Both models support the idea that the luminescence pattern of polar (In,Ga)N/GaN LEDs grown on foreign substrates is not necessarily determined by drift and diffusion of charge carriers, but by the distribution of nonradiative centers.

To estimate a possible influence of structural defects, we analyze an atomic force micrograph[‡] of a blue (In,Ga)N/GaN single QW of similar structural quality as the blue LED [see Fig. A.6(a)]. The V-pits, forming at the outcrops of threading dislocations, are visible as black spots. It is possible that dislocations attract nonradiative centers due to their strain field (Cottrell atmosphere).[542] However, more important is the change of the band gap due to the strain field (several meV per μm).[543] If we assume a Gaussian distribution of the impact of nonradiative recombination around threading dislocations with a full

[†]A similar idea has been proposed by Vierheilig *et al.*[535] by combining spatially resolved measurements of PL and photocurrent.

[‡]Acquired with a Veeco Dimension 3100 and analyzed with Gwyddion.[541]

width at half maximum of 800 nm and convolute this distribution with the dislocations, we obtain a color-coded map of the impact of nonradiative defects as shown in Fig. A.6(b). The obtained distribution of areas with a high impact of nonradiative recombination exhibits a pattern qualitatively similar to the maps obtained by μ-PL. However, a map of the PL peak energy [see Fig. A.6(c)] and PL peak intensity [see Fig. A.6(d)] recorded at the same position as the atomic force micrograph shows a luminescence pattern that differs from our simulation. Thus, the microscopic fluctuations in the luminescence pattern are not linked to the V-pits, in contrast to the observations reported in Ref. 544, but may be caused by a correlation of the In content and the density of nonradiative point defects.

A.5 Summary and conclusions

We have not observed an enhanced diffusivity of charge carriers under operating conditions by combining drift-diffusion simulations with μ-EL intensity patterns of LEDs. Moreover, the μ-EL patterns of LEDs cannot be explained in the framework of drift and diffusion without taking additional effects into account such as, for example, the distribution of nonradiative recombination centers (in particular, point defects).

Appendix B

Anti-Stokes photoluminescence

In this appendix, we investigate the temperature- and excitation-dependent intense anti-Stokes luminescence of (In,Ga)N/GaN QWs, which we found to originate from a two-step two-photon absorption process of localized charge carriers. We suggest this mechanism to contribute to the leakage of charge carriers from the active region in (In,Ga)N/GaN.

B.1 Two-step two-photon absorption

Nowadays, Auger recombination is believed to be (more or less exclusively) responsible for the droop in GaN-based LEDs (see also Sec. 2.6).[25,28] However, direct experimental indications of Auger recombination processes have been reported only by Iveland *et al.* [252] using electron emission spectroscopy and by Binder *et al.* [254] utilizing PL excitation of a specially designed (In,Ga)N/GaN structure containing QWs with low and high In content. Although Binder *et al.* [254] only excited the QWs with high In content (low peak energy), they observe luminescence from the QWs with low In content (high peak energy) and propose electron-electron-hole as well as electron-hole-hole Auger processes to explain the upconversion of the photon energy.[254] Similar, but more sophisticated experiments for (In,Ga)N/GaN QWs have been reported already in 2000 by Satake *et al.* [545] Considering localization of charge carriers, Satake *et al.* [545] explain the observed, so-called anti-Stokes PL not by an Auger process, but by a so-called two-step TPA[546] process.* Due to localization of the charge carriers in real space, their wave functions in k-space exhibit contributions from all k states in the Brillouin zone.[547] Thus, long-living carriers are able to absorb photons directly without the participation of phonons.[547,548]

For other material systems exhibiting localization and spatially separated charge carriers, intense anti-Stokes PL has been reported already in the 1990s.[547,549] Initially, theoretical calculations by Zegrya and Kharchenko[550] suggest a cold Auger process which was used to describe the experimental observations in Refs. 549 and 551. However, in the majority of publications, the intense anti-Stokes PL is attributed to a two-step TPA

*This sequential TPA process is also referred to as two-step absorption.

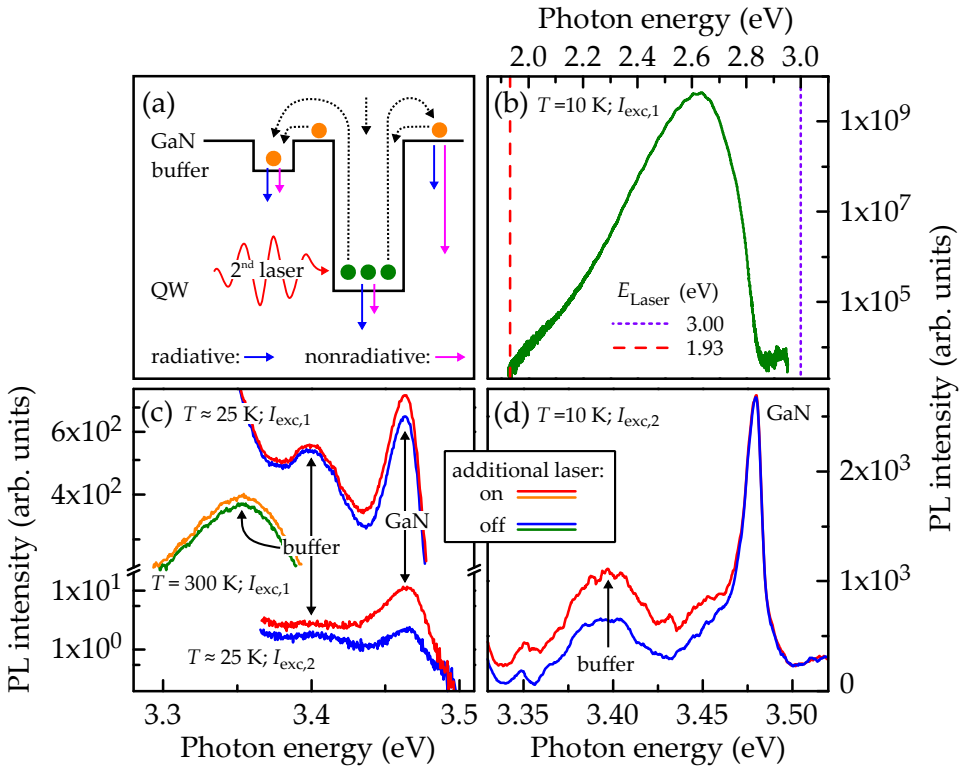

Figure B.1: (a) Schematic of the two-step TPA in (In,Ga)N/GaN. Localized charge carriers [here shown for electrons (green circles)] are able to reabsorb photons from the actual QW transition, the laser, or from an additional laser source (2nd laser) with a photon energy below the band gap of the QW. The excited charge carriers (orange circles) may relax into the surrounding GaN barrier, the In-containing buffer, or be captured by the QW (dashed arrows). From either of these three levels, the charge carriers recombine radiatively (blue arrow) or nonradiatively (violet arrow). (b) Exemplary low-temperature steady-state PL spectrum of the (In,Ga)N/GaN multi QW excited with $E_{\text{laser}} = 3.00\,\text{eV}$ (dotted line) and additionally with $E_{\text{laser}} = 1.93\,\text{eV}$ (dashed line). (c) Temperature- and excitation-dependent anti-Stokes luminescence spectra of the same sample as used in (b) without and with additional excitation with $E_{\text{laser}} = 1.93\,\text{eV}$ as indicated. $I_{\text{exc},1} = 400\,\text{kW/cm}^2$ and $I_{\text{exc},2} = 10\,\text{kW/cm}^2$. (d) Anti-Stokes luminescence spectra of the same sample recorded at 10 K, but with additional excitation at $E_{\text{laser}} = 1.16\,\text{eV}$. The luminescence signal from the buffer at around 3.4 eV as well as the GaN peak at 3.48 eV at low temperatures are indicated in (c) and (d).

process, which was found to fully account for the experimental results.[545–548,552]

The investigated polar (In,Ga)N/GaN heterostructure is similar to the one used by Binder *et al.*[254] and was also grown by OSRAM Opto Semiconductors GmbH. Our sample contains three (In,Ga)N/GaN QWs and an In-containing buffer emitting in the green and the UV spectral range, respectively. According to the results in Ref. 545, we expect a two-step TPA process as depicted schematically in Fig. B.1(a) when utilizing a laser to excite only the QWs with the higher In content (emitting in the green spectral range). Initially, charge carriers are excited inside these QW by the (first) laser. Due to localization and the spatial separation of charge carriers in polar (In,Ga)N/GaN heterostructures (see results in

Chap. 4), their wave vectors and lifetimes are sufficient to absorb a second photon [either from the first laser, a photon emitted from the QW (comparable to self-absorption[85]) or from a second laser with a photon energy smaller than the band gap of the QW]. Depending on the electric fields in the barriers surrounding the QW (not shown), the so-called up-converted charge carriers may relax into to the GaN barrier and/or the In-containing buffer. Besides direct recombination in the GaN barriers, the up-converted charge carriers may also drift and relax either into the In-containing buffer or the QW. In general, normal or up-converted charge carriers recombine radiatively (blue arrows) or nonradiatively (violet arrows) from their respective levels as schematically depicted in Fig. B.1(a).

B.2 Photoluminescence analysis

In what follows, we demonstrate that the emission observed in the UV for our sample is indeed a *photon*-mediated process (i. e., a two-step TPA) involving localized charge carriers and is not caused by Auger recombination[252,254] or excitation-induced dephasing.[263] We present an exemplary spectrum of the Stokes-PL emission of the green (In,Ga)N/GaN multi-QW sample recorded at low temperatures in Fig. B.1(b). The exciting laser with a photon energy of 3.00 eV is indicated by a dotted line, while the additional laser with a photon energy of $E_{\mathrm{laser}} = 1.93$ eV is shown by a dashed line. The rather broad Stokes-PL band peaks at about 2.65 eV. Figure B.1(c) shows steady-state PL spectra of the investigated sample recorded on the anti-Stokes side at excitation densities and temperatures as indicated. Obviously, we detect the PL bands of the GaN and the In-containing buffer at low temperatures and moderate steady-state excitation densities, which are insufficient for classical TPA or Auger recombination. At room temperature, the PL emission originates from the In-containing buffer only.

Exciting the sample not only at 3.00 eV, but additionally with a laser emitting at 1.93 eV (5 kW/cm^2) results in an increase of the anti-Stokes PL intensity at low and high temperatures [see Fig. B.1(c)]. Thus, photons from the laser become absorbed in the active region although their energy is well below the interband energy of the QW states. Thus, we observe an intraband absorption process of photons, which subsequently excite charge carriers from the QWs. The excited charge carriers subsequently recombine in the GaN or In-containing buffer as schematically depicted in Fig. B.1(a). To ensure that we do not excite any deep levels at 1.93 eV in this structure, we conduct additional experiments with an even lower photon energy of the second laser. Utilizing a photon energy of the second laser of 1.16 eV (1 kW/cm^2) results in an increase of the anti-Stokes PL recorded at 10 K as presented in Fig. B.1(d). In contrast to the additional excitation with photons with an energy of 1.93 eV, for which the anti-Stokes PL of the GaN is predominantly enhanced, the anti-Stokes PL intensity of the In-containing buffer increases only for $E_{\mathrm{laser}} = 1.16$ eV [see Figs. B.1(c) and B.1(d)]. This observation may be explained as follows: Preferentially, deeply localized charge carriers undergo the upconversion process. To populate the GaN barrier after reabsorption of a second photon requires a photon energy of > 1.2 eV.

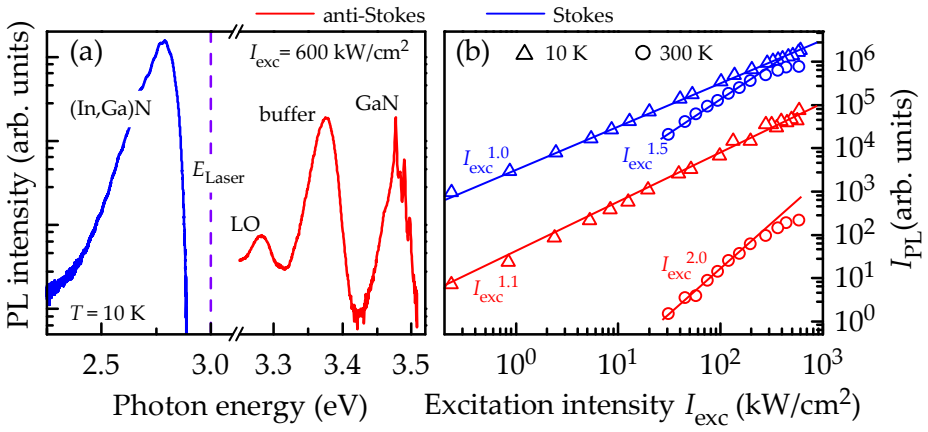

Figure B.2: (a) Exemplary Stokes (blue) and anti-Stokes (red) PL spectrum of the (In,Ga)N/GaN single QW on an In-containing buffer on GaN excited with E_{laser} = 3.00 eV at 10 K. (b) Corresponding, excitation-dependent integrated Stokes (blue) and anti-Stokes (red) PL intensity (I_{PL}) recorded at 10 K (squares) and 300 K (circles). The solid lines indicate fits whose slopes are indicated.

To quantify the efficiency of the upconversion, we investigate an (In,Ga)N/GaN single QW on an In-containing buffer on GaN, whose exemplary Stokes and anti-Stokes PL spectra recorded at 10 K are depicted in Fig. B.2(a). In Fig B.2(b), we show the numerically integrated Stokes and anti-Stokes PL intensity at 10 and 300 K over the excitation power density (I_{exc}). Both, Stokes and anti-Stokes PL intensity, increase linearly with the excitation density over four orders of magnitude at 10 K [see triangles in Fig. B.2(b)]. Thus, we safely exclude conventional TPA or Auger processes as their dependence on excitation density is not linear.[251,553–555] At 300 K, the Stokes PL intensity increases with $I_{exc}^{1.5}$ [see Fig. B.2(b)].[†] Despite the large excitation densities, we may attribute the superlinear slope at 300 K to the saturation of nonradiative centers and an increasing overlap of electron and hole wave functions (due to screening of the large piezoelectric field) in the single-QW sample. We note that an identical heterostructure, but containing a single QW with a higher In content (Stokes emission in the green spectral range), exhibits a slope of the Stokes PL intensity that results in $I_{exc}^{2.5}$.

The anti-Stokes PL intensity is about two (four) orders of magnitude lower than the Stokes PL intensity at 10 K (300 K). To explain the large difference between Stokes and anti-Stokes PL intensity, especially at room temperature, we have to consider the efficient nonradiative recombination in the surrounding GaN barriers[‡], whose PL intensity quenches over several orders of magnitude with increasing temperature. Additionally, we

[†]The decrease of the slope of Stokes and anti-Stokes PL intensity at the high excitation densities is due to band filling and spectral broadening of the Stokes spectrum which exceeds the energy of the photons emitted from the laser. (See, e. g., Ref. 67 for related considerations.)

[‡]While the nonradiative recombination of charge carriers at dislocations (density on the order of 10^8 cm^{-2}) is efficiently screened by V-pits in the (In,Ga)N/GaN QWs,[269] up-converted charge carriers in the GaN barriers reach these nonradiative centers easily because no energy barrier exists. Moreover, the diffusivity of charge carriers in GaN is much larger than in (In,Ga)N.

have to take into account that charge carriers may partly delocalize at room temperature (see Chap. 4) and, thus, that the two-step TPA is less efficient.

We note that we have observed anti-Stokes PL emission not only in the test structures, but also in the nanowires characterized and investigated in Sec. 3.5.1 and Chap. 4 as well as in the LED investigated in Sec. 3.5.2 and Chap. 6. However, we do not detect any anti-Stokes luminescence by using only electrical injection in the LED. This might be mainly due to two reasons: First, the active region of the LED is buried deeply in the sample. Hence, we do not expect to observe a signal from GaN because of reabsorption (despite the fact that the GaN signal is weak anyway at room temperature). And second and most likely, the voltage-induced band bending attracts the electrons to the p-doped region, and no carriers reach the In-containing buffer. However, the absence of anti-Stokes luminescence does not automatically indicate an absence of the two-step TPA process.

B.3 Summary and conclusions

We have analyzed the intense anti-Stokes PL emission in polar (In,Ga)N/GaN heterostructures. Although the upconversion of photons or the emission of high energy electrons have been ascribed to an Auger process,[252,254] our experiments indicate that both effects may instead originate from the two-step TPA, in agreement with the results from Ref. 545. The reduction of the efficiency of polar (In,Ga)N/GaN heterostructures in PL experiments with excitation of the QWs may be partly attributed to the two-step TPA. Moreover, the energy upconversion of localized charge carriers by the reabsorption of photons and the subsequent nonradiative recombination in the GaN barriers may constitute an additional loss channel in polar (In,Ga)N/GaN heterostructures—similar to a *photon*-assisted Auger process.

Appendix C

List of samples

sample	structure; growth	PL emission	Lab-ID	chapter
planar reference	planar (In,Ga)N/GaN QWs; MOCVD	blue	NAE_02042f	3, 4
nanowires	(In,Ga)N QDs in GaN nanowires on Si; MBE	green	M81310	4
blue LED	planar (In,Ga)N/GaN LED with polished surface; MOCVD	blue	HOEPL412	3, A
green LED	similar to blue LED	green	HOEPL413	3, 6, A
µ-rods	GaN/(In,Ga)N core/shell µ-rods with a QW; MOCVD	violet	–	5
(In,Ga)N layer	40-nm-thick (In,Ga)N layer on Al_2O_3; MOCVD	violet	S4	5
SPSL I	SPSL with thin QBs; MBE	UV	M1497	7
SPSL II	SPSL with thick QBs; MBE	UV	M1491	7
Anti-Stokes I	planar (In,Ga)N/GaN QWs with In-containing buffer; MOCVD	green	NAE_05090	B
Anti-Stokes II	similar to Anti-Stokes I, but with a single QW	blue	NAE_05117	B

Table C.1: List of samples investigated in this thesis.

Bibliography

[1] P. J. Mohr, D. B. Newell, and B. N. Taylor, *CODATA Recommended Values of the Fundamental Physical Constants: 2014*, J. Phys. Chem. Ref. Data **45**, 043102 (2016).

[2] W. C. Johnson, J. B. Parson, and M. C. Crew, *NITROGEN COMPOUNDS OF GALLIUM III. Gallic Nitride*, J. Phys. Chem. **36**, 2651 (1932).

[3] R. Juza and F. Hund, *Die ternären Nitride Li_3AlN_2 und Li_3GaN_2*, Z. Anorg. Allg. Chem. **257**, 13 (1948).

[4] A. Addamiano, *On the Preparation of the Nitrides of Aluminum and Gallium*, J. Electrochem. Soc. **108**, 1072 (1961).

[5] M. R. Lorenz and B. B. Binkowski, *Preparation, Stability, and Luminescence of Gallium Nitride*, J. Electrochem. Soc. **109**, 24 (1962).

[6] J. Pastrňák and L. Součková, *Herstellung dünner Schichten von Aluminium-, Gallium- sowie Indiumnitrid unter einer Gasentladung*, Phys. Status Solidi **3**, K71 (1963).

[7] H. P. Maruska and J. J. Tietjen, *THE PREPARATION AND PROPERTIES OF VAPOR-DEPOSITED SINGLE-CRYSTALLINE GaN*, Appl. Phys. Lett. **15**, 327 (1969).

[8] B. B. Kosicki and D. Kahng, *Preparation and Structural Properties of GaN Thin Films*, J. Vac. Sci. Technol. **6**, 593 (1969).

[9] H. Maruska, D. Stevenson, and J. Pankove, *Violet luminescence of Mg-doped GaN*, Appl. Phys. Lett. **22**, 303 (1973).

[10] H. M. Manasevit, F. M. Erdmann, and W. I. Simpson, *The Use of Metalorganics in the Preparation of Semiconductor Materials IV. The Nitrides of Aluminum and Gallium*, J. Electrochem. Soc. **118**, 1864 (1971).

[11] C. Weyrich, *Light emitting diodes for the visible spectrum*, Festkörperprobleme **XVIII**, 265 (1978).

[12] C. Weyrich and M. Plihal, *Halbleiterlichtquellen*, Phys. Bl. **36**, 137 (1980).

[13] H. P. Maruska and W. C. Rhines, *A modern perspective on the history of semiconductor nitride blue light sources*, Solid State Electron. **111**, 32 (2015).

[14] H. Amano, N. Sawaki, I. Akasaki, and Y. Toyoda, *Metalorganic vapor phase epitaxial growth of a high quality GaN film using an AlN buffer layer*, Appl. Phys. Lett. **48**, 353

(1986).

[15] H. Amano, M. Kito, K. Hiramatsu, and I. Akasaki, *P-Type Conduction in Mg-Doped GaN Treated with Low-Energy Electron Beam Irradiation (LEEBI)*, Jpn. J. Appl. Phys. **28**, L2112 (1989).

[16] S. Nakamura, T. Mukai, M. Senoh, and N. Iwasa, *Thermal Annealing Effects on P-Type Mg-Doped GaN Films*, Jpn. J. Appl. Phys. **31**, L139 (1992).

[17] S. Nakamura, N. Iwasa, M. Senoh, and T. Mukai, *Hole Compensation Mechanism of P-Type GaN Films*, Jpn. J. Appl. Phys. **31**, 1258 (1992).

[18] J. Neugebauer and C. G. Van de Walle, *Hydrogen in GaN: Novel Aspects of a Common Impurity*, Phys. Rev. Lett. **75**, 4452 (1995).

[19] S. Nakamura, M. Senoh, and T. Mukai, *P-GaN/N-InGaN/N-GaN Double-Heterostructure Blue-Light-Emitting Diodes*, Jpn. J. Appl. Phys. **32**, L8 (1993).

[20] Y. Narukawa, M. Ichikawa, D. Sanga, M. Sano, and T. Mukai, *White light emitting diodes with super-high luminous efficacy*, J. Phys. D: Appl. Phys. **43**, 354002 (2010).

[21] Press Release of the Royal Swedish Academy of Sciences: Nobel Prize in Physics, https://www.nobelprize.org/nobel_prizes/physics/laureates/2014/press.pdf, 7/10/2014.

[22] Strategies-Unlimited®: Global packaged LED market to reach $22 billion by 2019 from 05/05/2015, http://www.strategies-u.com/articles/press-releases/global-packaged-led-market-to-reach-22-billion-by-2019.html, 31/07/2017.

[23] Google Patents, https://patents.google.com/?q=(In%2cGa)N,InGaN, 31/07/2017.

[24] Web of Science, https://www.webofknowledge.com, 24/07/2017.

[25] J. Piprek, *Efficiency droop in nitride-based light-emitting diodes*, Phys. Status Solidi A **207**, 2217 (2010).

[26] D. Schiavon, *Analysis of the green gap problem in III–nitride LEDs*, PhD thesis, Universität Ulm (2014).

[27] J. Hader, J. V. Moloney, and S. W. Koch, *Density-activated defect recombination as a possible explanation for the efficiency droop in GaN-based diodes*, Appl. Phys. Lett. **96**, 221106 (2010).

[28] J. Piprek, *How to decide between competing efficiency droop models for GaN-based light-emitting diodes*, Appl. Phys. Lett. **107**, 031101 (2015).

[29] M. Auf der Maur, A. Pecchia, G. Penazzi, W. Rodrigues, and A. Di Carlo, *Efficiency Drop in Green InGaN/GaN Light Emitting Diodes: The Role of Random Alloy Fluctuations*, Phys. Rev. Lett. **116**, 027401 (2016).

[30] S. Y. Karpov, *Carrier localization in InGaN by composition fluctuations: implication to the "green gap"*, Photonics Res. **5**, A7 (2017).

[31] Y. C. Shen, G. O. Mueller, S. Watanabe, N. F. Gardner, A. Munkholm, and M. R. Krames, *Auger recombination in InGaN measured by photoluminescence*, Appl. Phys. Lett. **91**, 141101 (2007).

[32] R. Singh, D. Doppalapudi, T. Moustakas, and L. Romano, *Phase separation in InGaN thick films and formation of InGaN/GaN double heterostructures in the entire alloy composition*, Appl. Phys. Lett. **70**, 1089 (1997).

[33] Q. Dai, M. F. Schubert, M. H. Kim, J. K. Kim, E. F. Schubert, D. D. Koleske, M. H. Crawford, S. R. Lee, A. J. Fischer, G. Thaler, and M. A. Banas, *Internal quantum efficiency and nonradiative recombination coefficient of GaInN/GaN multiple quantum wells with different dislocation densities*, Appl. Phys. Lett. **94**, 111109 (2009).

[34] T. Langer, H. Jönen, A. Kruse, H. Bremers, U. Rossow, and A. Hangleiter, *Strain-induced defects as nonradiative recombination centers in green-emitting GaInN/GaN quantum well structures*, Appl. Phys. Lett. **103**, 022108 (2013).

[35] A. M. Armstrong, M. H. Crawford, and D. D. Koleske, *Contribution of deep-level defects to decreasing radiative efficiency of InGaN/GaN quantum wells with increasing emission wavelength*, Appl. Phys. Express **7**, 032101 (2014).

[36] M. Takashi, Y. Motokazu, and S. Nakamura, *Current and Temperature Dependences of Electroluminescence of InGaN-Based UV / Blue / Green Light-Emitting Diodes*, Jpn. J. Appl. Phys. **37**, L1358 (1998).

[37] K. T. Delaney, P. Rinke, and C. G. Van De Walle, *Auger recombination rates in nitrides from first principles*, Appl. Phys. Lett. **94**, 191109 (2009).

[38] E. Kioupakis, D. Steiauf, P. Rinke, K. T. Delaney, and C. G. Van de Walle, *First-principles calculations of indirect Auger recombination in nitride semiconductors*, Phys. Rev. B **92**, 035207 (2015).

[39] M. Shahmohammadi, W. Liu, G. Rossbach, L. Lahourcade, A. Dussaigne, C. Bougerol, R. Butté, N. Grandjean, B. Deveaud, and G. Jacopin, *Enhancement of Auger recombination induced by carrier localization in InGaN/GaN quantum wells*, Phys. Rev. B **95**, 125314 (2017).

[40] H. Schömig, S. Halm, A. Forchel, G. Bacher, J. Off, and F. Scholz, *Probing Individual Localization Centers in an InGaN/GaN Quantum Well*, Phys. Rev. Lett. **92**, 106802 (2004).

[41] S. Kalliakos, P. Lefebvre, X. B. Zhang, T. Taliercio, B. Gil, N. Grandjean, B. Damilano, and J. Massies, *The effects of localization and of electric fields on LO-phonon-exciton coupling in InGaN/GaN quantum wells and quantum boxes*, Phys. Status Solidi A **190**, 149 (2002).

[42] S. Kalliakos, X. B. Zhang, T. Taliercio, P. Lefebvre, B. Gil, N. Grandjean, B. Damilano, and J. Massies, *Large size dependence of exciton-longitudinal-optical-phonon coupling in nitride-based quantum wells and quantum boxes*, Appl. Phys. Lett. **80**, 428 (2002).

[43] J. Lähnemann, C. Hauswald, M. Wölz, U. Jahn, M. Hanke, L. Geelhaar, and O. Brandt, *Localization and defects in axial (In,Ga)N/GaN nanowire heterostructures investigated by spatially resolved luminescence spectroscopy*, J. Phys. D: Appl. Phys. **47**, 394010 (2014).

[44] S. Nakamura, *The Roles of Structural Imperfections in InGaN-Based Blue Light-Emitting Diodes and Laser Diodes*, Science **281**, 956 (1998).

[45] S. F. Chichibu, A. Uedono, T. Onuma, B. A. Haskell, A. Chakraborty, T. Koyama, P. T. Fini, S. Keller, S. P. DenBaars, J. S. Speck, U. K. Mishra, S. Nakamura, S. Yamaguchi, S. Kamiyama, H. Amano, I. Akasaki, J. Han, and T. Sota, *Origin of defect-insensitive emission probability in In-containing (Al,In,Ga)N alloy semiconductors*, Nat. Mater. **5**, 810 (2006).

[46] Y.-H. Cho, G. H. Gainer, A. J. Fischer, J. J. Song, S. Keller, U. K. Mishra, and S. P. DenBaars, *"S-shaped" temperature-dependent emission shift and carrier dynamics in InGaN/GaN multiple quantum wells*, Appl. Phys. Lett. **73**, 1370 (1998).

[47] S. Dhar, U. Jahn, O. Brandt, P. Waltereit, and K. H. Ploog, *Influence of exciton localization on the quantum efficiency of GaN/(In,Ga)N multiple quantum wells grown by molecular-beam epitaxy*, Appl. Phys. Lett. **81**, 673 (2002).

[48] A. Morel, P. Lefebvre, S. Kalliakos, T. Taliercio, T. Bretagnon, and B. Gil, *Donor-acceptor-like behavior of electron-hole pair recombinations in low-dimensional (Ga,In)N/GaN systems*, Phys. Rev. B **68**, 045331 (2003).

[49] C.-N. Brosseau, M. Perrin, C. Silva, and R. Leonelli, *Carrier recombination dynamics in In_xGa_{1-x}/GaN multiple quantum wells*, Phys. Rev. B **82**, 085305 (2010).

[50] D. Watson-Parris, M. J. Godfrey, P. Dawson, R. A. Oliver, M. J. Galtrey, M. J. Kappers, and C. J. Humphreys, *Carrier localization mechanisms in $In_xGa_{1-x}N$/GaN quantum wells*, Phys. Rev. B **83**, 115321 (2011).

[51] F. Feix, T. Flissikowski, K. K. Sabelfeld, V. M. Kaganer, M. Wölz, L. Geelhaar, H. T. Grahn, and O. Brandt, *Ga-polar (In,Ga)N/GaN quantum wells versus N-polar (In,Ga)N quantum disks in GaN nanowires: A comparative analysis of carrier recombination, diffusion, and radiative efficiency*, Phys. Rev. Applied **8**, 014032 (2017).

[52] S. Chichibu, T. Azuhata, T. Sota, and S. Nakamura, *Spontaneous emission of localized excitons in InGaN single and multiquantum well structures*, Appl. Phys. Lett. **69**, 4188 (1996).

[53] P. G. Eliseev, P. Perlin, J. Lee, and M. Osiński, *"Blue" temperature-induced shift and band-tail emission in InGaN-based light sources*, Appl. Phys. Lett. **71**, 569 (1997).

[54] U. Jahn, S. Dhar, O. Brandt, H. T. Grahn, K. H. Ploog, and I. M. Watson, *Exciton localization and quantum efficiency – A comparative cathodoluminescence study of (In,Ga)N/GaN and GaN/(Al,Ga)N quantum wells*, J. Appl. Phys. **93**, 1048 (2003).

[55] T. Bartel, M. Dworzak, M. Strassburg, A. Hoffmann, A. Strittmatter, and D. Bimberg, *Recombination dynamics of localized excitons in InGaN quantum dots*, Appl. Phys. Lett. **85**, 1946 (2004).

[56] O. Brandt and K. H. Ploog, *Solid-state lighting: The benefit of disorder*, Nat. Mater. **5**, 769 (2006).

[57] T. M. Smeeton, M. J. Kappers, J. S. Barnard, M. E. Vickers, and C. J. Humphreys, *Electron-beam-induced strain within InGaN quantum wells: False indium "cluster" detection in the transmission electron microscope*, Appl. Phys. Lett. **83**, 5419 (2003).

[58] D. Watson-Parris, *Carrier Localization in InGaN/GaN Quantum Wells*, PhD thesis, University of Manchester (2011).

[59] M. J. Galtrey, R. A. Oliver, M. J. Kappers, C. J. Humphreys, P. H. Clifton, D. Larson, D. W. Saxey, and A. Cerezo, *Three-dimensional atom probe analysis of green- and blue-emitting $In_xGa_{1-x}N$/GaN multiple quantum well structures*, J. Appl. Phys. **104**, 013524 (2008).

[60] V. B. Özdöl, C. T. Koch, and P. A. van Aken, *A nondamaging electron microscopy approach to map In distribution in InGaN light-emitting diodes*, J. Appl. Phys. **108**, 056103 (2010).

[61] T. Schulz, T. Remmele, T. Markurt, M. Korytov, and M. Albrecht, *Analysis of statistical compositional alloy fluctuations in InGaN from aberration corrected transmission electron microscopy image series*, J. Appl. Phys. **112**, 033106 (2012).

[62] K. H. Baloch, A. C. Johnston-Peck, K. Kisslinger, E. A. Stach, and S. Gradečak, *Revisiting the "In-clustering" question in InGaN through the use of aberration-corrected electron microscopy below the knock-on threshold*, Appl. Phys. Lett. **102**, 191910 (2013).

[63] T. Schulz, A. Duff, T. Remmele, M. Korytov, T. Markurt, M. Albrecht, L. Lymperakis, J. Neugebauer, C. Chèze, and C. Skierbiszewski, *Separating strain from composition in unit cell parameter maps obtained from aberration corrected high resolution transmission electron microscopy imaging*, J. Appl. Phys. **115**, 33113 (2014).

[64] K. Song, C. T. Koch, J. K. Lee, D. Y. Kim, J. K. Kim, A. Parvizi, W. Y. Jung, C. G. Park, H. J. Jeong, H. S. Kim, Y. Cao, T. Yang, L.-Q. Chen, and S. H. Oh, *Correlative High-Resolution Mapping of Strain and Charge Density in a Strained Piezoelectric Multilayer*, Adv. Mater. Interfaces **2**, 1400281 (2015).

[65] C. J. Humphreys, J. T. Griffiths, F. Tang, F. Oehler, S. D. Findlay, C. Zheng, J. Etheridge, T. L. Martin, P. A. Bagot, M. P. Moody, D. Sutherland, P. Dawson, S. Schulz, S. Zhang, W. Y. Fu, T. Zhu, M. J. Kappers, and R. A. Oliver, *The atomic structure of polar and non-polar InGaN quantum wells and the green gap problem*, Ultramicroscopy **176**, 93 (2017).

[66] A. Hangleiter, D. Fuhrmann, M. Grewe, F. Hitzel, G. Klewer, S. Lahmann, C. Netzel, N. Riedel, and U. Rossow, *Towards understanding the emission efficiency of nitride quantum wells*, Phys. Status Solidi C **1**, 2808 (2004).

[67] T. Langer, A. Chernikov, D. Kalincev, M. Gerhard, H. Bremers, U. Rossow, M. Koch, and A. Hangleiter, *Room temperature excitonic recombination in GaInN/GaN quantum wells*, Appl. Phys. Lett. **103**, 202106 (2013).

[68] S. Schulz, M. A. Caro, C. Coughlan, and E. P. O'Reilly, *Atomistic analysis of the impact of alloy and well-width fluctuations on the electronic and optical properties of InGaN/GaN quantum wells*, Phys. Rev. B **91**, 035439 (2015).

[69] M. Wölz, J. Lähnemann, O. Brandt, V. M. Kaganer, M. Ramsteiner, C. Pfüller, C. Hauswald, C. N. Huang, L. Geelhaar, and H. Riechert, *Correlation between In content and emission wavelength of InGaN/GaN nanowire heterostructures*, Nanotechnology **23**, 455203 (2012).

[70] F. Glas, *Critical dimensions for the plastic relaxation of strained axial heterostructures in free-standing nanowires*, Phys. Rev. B **74**, 121302 (2006).

[71] M. Wölz, M. Ramsteiner, V. M. Kaganer, O. Brandt, L. Geelhaar, and H. Riechert,

Strain Engineering of Nanowire Multi-Quantum Well Demonstrated by Raman Spectroscopy, Nano Lett. **13**, 4053 (2013).

[72] T. Krause, M. Hanke, O. Brandt, and A. Trampert, *Counterintuitive strain distribution in axial (In,Ga)N/GaN nanowires*, Appl. Phys. Lett. **108**, 032103 (2016).

[73] C. Hauswald, I. Giuntoni, T. Flissikowski, T. Gotschke, R. Calarco, H. T. Grahn, L. Geelhaar, and O. Brandt, *Luminous Efficiency of Ordered Arrays of GaN Nanowires with Subwavelength Diameters*, ACS Photonics **4**, 52 (2017).

[74] M. S. Mohajerani, M. Müller, J. Hartmann, H. Zhou, H.-H. Wehmann, P. Veit, F. Bertram, J. Christen, and A. Waag, *Direct correlations of structural and optical properties of three-dimensional GaN/InGaN core/shell micro-light emitting diodes*, Jpn. J. Appl. Phys. **55**, 05FJ09 (2016).

[75] T. Schimpke, H.-J. Lugauer, A. Avramescu, T. Varghese, A. Koller, J. Hartmann, J. Ledig, A. Waag, and M. Strassburg, *Position-controlled MOVPE growth and electro-optical characterization of core-shell InGaN/GaN microrod LEDs*, Proc. SPIE **9768**, 97680T (2016).

[76] A. Yoshikawa, S. B. Che, W. Yamaguchi, H. Saito, X. Q. Wang, Y. Ishitani, and E. S. Hwang, *Proposal and achievement of novel structure InN/GaN multiple quantum wells consisting of 1 ML and fractional monolayer InN wells inserted in GaN matrix*, Appl. Phys. Lett. **90**, 073101 (2007).

[77] C. Chèze, F. Feix, M. Anikeeva, T. Schulz, M. Albrecht, H. Riechert, O. Brandt, and R. Calarco, *In/GaN(0001)-$\left(\sqrt{3}\times\sqrt{3}\right)R30°$ adsorbate structure as a template for embedded (In,Ga)N/GaN monolayers and short-period superlattices*, Appl. Phys. Lett. **110**, 072104 (2017).

[78] I. Gorczyca, K. Skrobas, T. Suski, N. E. Christensen, and A. Svane, *Band gaps in InN/GaN superlattices: Nonpolar and polar growth directions*, J. Appl. Phys. **114**, 223102 (2013).

[79] K. K. Sabelfeld, O. Brandt, and V. M. Kaganer, *Stochastic model for the fluctuation-limited reaction–diffusion kinetics in inhomogeneous media based on the nonlinear Smoluchowski equations*, J. Math. Chem. **53**, 651 (2015).

[80] C. Kittel, *Einführung in die Festkörperphysik*, Oldenbourg, München (2006).

[81] N. Ashcroft and N. Mermin, *Festkörperphysik*, Oldenbourg, München (2005).

[82] S. Hunklinger, *Festkörperphysik*, Oldenbourg, München (2007).

[83] H. Morkoç, *Handbook of Nitride Semiconductors and Devices: Materials Properties, Physics and Growth, Volume 1*, Wiley-VCH Verlag, Weinheim (2008).

[84] H. Morkoç, *Handbook of Nitride Semiconductors and Devices: Electronic and Optical Processes in Nitrides, Volume 2*, Wiley-VCH Verlag, Weinheim (2008).

[85] H. Morkoç, *Handbook of Nitride Semiconductors and Devices: GaN-Based Optical and Electronic Devices, Volume 3*, Wiley-VCH Verlag, Weinheim (2008).

[86] J. C. Phillips, *Ionicity of the chemical bond in crystals*, Rev. Mod. Phys. **42**, 317 (1970).

[87] P. Lawaetz, *Stability of the Wurtzite Structure*, Phys. Rev. B **5**, 4039 (1972).

[88] H. Schulz and K. Thiemann, *Crystal structure refinement of AlN and GaN*, Solid State Commun. **23**, 815 (1977).

[89] M. A. Moram and M. E. Vickers, *X-ray diffraction of III-nitrides*, Rep. Prog. Phys. **72**, 036502 (2009).

[90] O. Ambacher, J. Majewski, C. Miskys, A. Link, M. Hermann, M. Eickhoff, M. Stutzmann, F. Bernardini, V. Fiorentini, V. Tilak, B. Schaff, and L. F. Eastman, *Pyroelectric properties of Al(In)GaN/GaN hetero- and quantum well structures*, J. Phys. Condens. Matter **14**, 3399 (2002).

[91] J. Zúñiga-Pérez, V. Consonni, L. Lymperakis, X. Kong, A. Trampert, S. Fernández-Garrido, O. Brandt, H. Renevier, S. Keller, K. Hestroffer, M. R. Wagner, J. S. Reparaz, F. Akyol, S. Rajan, S. Rennesson, T. Palacios, and G. Feuillet, *Polarity in GaN and ZnO: Theory, measurement, growth, and devices*, Appl. Phys. Rev. **3**, 041303 (2016).

[92] J. Jerphagnon and H. W. Newkirk, *OPTICAL NONLINEAR SUSCEPTIBILITIES OF BERYLLIUM OXIDE*, Appl. Phys. Lett. **18**, 245 (1971).

[93] A. Belabbes, J. Furthmüller, and F. Bechstedt, *Relation between spontaneous polarization and crystal field from first principles*, Phys. Rev. B **87**, 035305 (2013).

[94] F. Bernardini, V. Fiorentini, and D. Vanderbilt, *Spontaneous polarization and piezoelectric constants of III-V nitrides*, Phys. Rev. B **56**, R10024 (1997).

[95] R. D. King-Smith and D. Vanderbilt, *Theory of polarization of crystalline solids*, Phys. Rev. B **47**, 1651 (1993).

[96] C. E. Dreyer, A. Janotti, C. G. Van de Walle, and D. Vanderbilt, *Correct Implementation of Polarization Constants in Wurtzite Materials and Impact on III-Nitrides*, Phys. Rev. X **6**, 021038 (2016).

[97] W. Ludwig, *Festkörperphysik*, Akademische Verlagsgesellschaft, Wiesbaden (1978).

[98] S. Haussühl, *Kristallphysik*, Physik-Verlag, Weinheim (1983).

[99] A. Polian, M. Grimsditch, and I. Grzegory, *Elastic constants of gallium nitride*, J. Appl. Phys. **79**, 3343 (1996).

[100] K. Kim, W. R. L. Lambrecht, and B. Segall, *Elastic constants and related properties of tetrahedrally bonded BN, AlN, GaN, and InN*, Phys. Rev. B **53**, 16310 (1996).

[101] A. F. Wright, *Elastic properties of zinc-blende and wurtzite AlN, GaN, and InN*, J. Appl. Phys. **82**, 2833 (1997).

[102] F. Bernardini, V. Fiorentini, and D. Vanderbilt, *Polarization-Based Calculation of the Dielectric Tensor of Polar Crystals*, Phys. Rev. Lett. **79**, 3958 (1997).

[103] V. Fiorentini, F. Bernardini, F. Della Sala, A. Di Carlo, and P. Lugli, *Effects of macroscopic polarization in III-V nitride multiple quantum wells*, Phys. Rev. B **60**, 8849 (1999).

[104] F. Bernardini and V. Fiorentini, *Spontaneous versus Piezoelectric Polarization in III±V Nitrides: Conceptual Aspects and Practical Consequences*, Phys. Status Solidi B **216**, 391 (1999).

[105] F. Bernardini and V. Fiorentini, *Polarization fields in nitride nanostructures: 10 Points*

to think about, Appl. Surf. Sci. **166**, 23 (2000).

[106] R. Kudrawiec, L. Janicki, M. Gladysiewicz, J. Misiewicz, G. Cywinski, M. Boćkowski, G. Muzioł, C. Chèze, M. Sawicka, and C. Skierbiszewski, *Contactless electroreflectance studies of surface potential barrier for N- and Ga-face epilayers grown by molecular beam epitaxy*, Appl. Phys. Lett. **103**, 052107 (2013).

[107] E. Hanamura, *Rapid radiative decay and enhanced optical nonlinearity of excitons in a quantum well*, Phys. Rev. B **38**, 1228 (1988).

[108] W. Shan, B. D. Little, A. J. Fischer, J. J. Song, B. Goldenberg, W. G. Perry, M. D. Bremser, and R. F. Davis, *Binding energy for the intrinsic excitons in wurtzite GaN*, Phys. Rev. B **54**, 16369 (1996).

[109] M. Pope and C. Swenberg, *Electronic Processes in Organic Crystals and Polymers*, Oxford University Press (1999).

[110] X.-F. He, *Excitons in anisotropic solids: The model of fractional-dimensional space*, Phys. Rev. B **43**, 2063 (1991).

[111] M. Dvorak, S.-H. Wei, and Z. Wu, *Origin of the Variation of Exciton Binding Energy in Semiconductors*, Phys. Rev. Lett. **110**, 016402 (2013).

[112] I. Vurgaftman and J. R. Meyer, *Band parameters for nitrogen-containing semiconductors*, J. Appl. Phys. **94**, 3675 (2003).

[113] D. Volm, K. Oettinger, T. Streibl, D. Kovalev, M. Ben-Chorin, J. Diener, B. K. Meyer, J. Majewski, L. Eckey, A. Hoffmann, H. Amano, I. Akasaki, K. Hiramatsu, and T. Detchprohm, *Exciton fine structure in undoped GaN epitaxial films*, Phys. Rev. B **53**, 16543 (1996).

[114] A. K. Viswanath, J. I. Lee, D. Kim, C. R. Lee, and J. Y. Leem, *Exciton-phonon interactions, exciton binding energy, and their importance in the realization of room-temperature semiconductor lasers based on GaN*, Phys. Rev. B **58**, 16333 (1998).

[115] K. Reimann, M. Steube, D. Fröhlich, and S. Clarke, *Exciton binding energies and band gaps in GaN bulk crystals*, J. Cryst. Growth **189**, 652 (1998).

[116] A. V. Rodina, M. Dietrich, A. Göldner, L. Eckey, A. Hoffmann, A. L. Efros, M. Rosen, and B. K. Meyer, *Free excitons in wurtzite GaN*, Phys. Rev. B **64**, 115204 (2001).

[117] T. J. Badcock, P. Dawson, M. J. Kappers, C. McAleese, J. L. Hollander, C. F. Johnston, D. V. Sridhara Rao, A. M. Sanchez, and C. J. Humphreys, *Optical polarization anisotropy of a-plane GaN/AlGaN multiple quantum well structures grown on r-plane sapphire substrates*, J. Appl. Phys. **105**, 123112 (2009).

[118] R. P. Leavitt and J. W. Little, *Simple method for calculating exciton binding energies in quantum-confined semiconductor structures*, Phys. Rev. B **42**, 11774 (1990).

[119] H. Mathieu, P. Lefebvre, and P. Christol, *Simple analytical method for calculating exciton binding energies in semiconductor quantum wells*, Phys. Rev. B **46**, 4092 (1992).

[120] L. C. Andreani and A. Pasquarello, *Accurate theory of excitons in GaAs-$Ga_{1-x}Al_xAs$ quantum wells*, Phys. Rev. B **42**, 8928 (1990).

[121] R. C. Miller, D. A. Kleinman, W. T. Tsang, and A. C. Gossard, *Observation of the*

excited level of excitons in GaAs quantum wells, Phys. Rev. B **24**, 1134 (1981).

[122] G. Bastard, E. E. Mendez, L. L. Chang, and L. Esaki, *Exciton binding energy in quantum wells*, Phys. Rev. B **26**, 1974 (1982).

[123] R. L. Greene, K. K. Bajaj, and D. E. Phelps, *Energy levels of Wannier excitons in GaAs-$Ga_{1-x}Al_xAs$ quantum-well structures*, Phys. Rev. B **29**, 1807 (1984).

[124] A. Bellabchara, P. Lefebvre, P. Christol, and H. Mathieu, *Improved modeling of excitons in type-II semiconductor heterostructures by use of a three-dimensional variational function*, Phys. Rev. B **50**, 11840 (1994).

[125] P. Corfdir and P. Lefebvre, *Importance of excitonic effects and the question of internal electric fields in stacking faults and crystal phase quantum discs: The model-case of GaN*, J. Appl. Phys. **112**, 053512 (2012).

[126] P. Corfdir, J. K. Zettler, C. Hauswald, S. Fernández-Garrido, O. Brandt, and P. Lefebvre, *Sub-meV linewidth in GaN nanowire ensembles: Absence of surface excitons due to the field ionization of donors*, Phys. Rev. B **90**, 205301 (2014).

[127] M. A. Reshchikov and H. Morkoç, *Luminescence properties of defects in GaN*, J. Appl. Phys. **97**, 061301 (2005).

[128] O. Brandt, J. Ringling, K. H. Ploog, H.-J. Wünsche, and F. Henneberger, *Temperature dependence of the radiative lifetime in GaN*, Phys. Rev. B **58**, R15977 (1998).

[129] E. I. Rashba and G. E. Gurgenishvili, *Edge absorption theory in semiconductors*, Sov. Phys. Solid State **4**, 759 (1962).

[130] C. H. Henry and K. Nassau, *Lifetimes of Bound Excitons in CdS*, Phys. Rev. B **1**, 1628 (1970).

[131] G. W. 't Hooft, W. A. J. A. van der Poel, L. W. Molenkamp, and C. T. Foxon, *Giant oscillator strength of free excitons in GaAs*, Phys. Rev. B **35**, 8281 (1987).

[132] K. Kornitzer, T. Ebner, K. Thonke, R. Sauer, C. Kirchner, V. Schwegler, M. Kamp, M. Leszczynski, I. Grzegory, and S. Porowski, *Photoluminescence and reflectance spectroscopy of excitonic transitions in high-quality homoepitaxial GaN films*, Phys. Rev. B **60**, 1471 (1999).

[133] B. Deveaud, F. Clérot, N. Roy, K. Satzke, B. Sermage, and D. S. Katzer, *Enhanced radiative recombination of free excitons in GaAs quantum wells*, Phys. Rev. Lett. **67**, 2355 (1991).

[134] O. Brandt, G. C. La Rocca, A. Heberle, A. Ruiz, and K. Ploog, *Evidence for superradiant decay of excitons in InAs quantum sheets*, Phys. Rev. B **45**, 3803 (1992).

[135] R. H. Dicke, *Coherence in Spontaneous Radiation Processes*, Phys. Rev. **93**, 99 (1954).

[136] P. Corfdir, C. Hauswald, O. Marquardt, T. Flissikowski, J. K. Zettler, S. Fernández-Garrido, L. Geelhaar, H. T. Grahn, and O. Brandt, *Crystal-phase quantum dots in GaN quantum wires*, Phys. Rev. B **93**, 115305 (2016).

[137] D. S. Citrin, *Radiative lifetimes of exciton in quantum wells: localization and phase-coherence effects*, Phys. Rev. B **47**, 3832 (1993).

[138] A. V. Kavokin, *Exciton oscillator strength in quantum wells: From localized to free resonant*

states, Phys. Rev. B **50**, 8000 (1994).

[139] J. Feldmann, G. Peter, E. O. Göbel, P. Dawson, K. Moore, C. Foxon, and R. J. Elliott, *Linewidth dependence of radiative exciton lifetimes in quantum wells*, Phys. Rev. Lett. **59**, 2337 (1987).

[140] O. Brandt, H. Lage, and K. Ploog, *Excitons in InAs/GaAs submonolayer quantum wells*, Phys. Rev. B **43**, 14285 (1991).

[141] W. Shockley and W. T. Read, *Statistics of the Recombination of Holes and Electrons*, Phys. Rev. **87**, 835 (1952).

[142] O. Brandt, H. Yang, and K. H. Ploog, *Impact of recombination centers on the spontaneous emission of semiconductors under steady-state and transient conditions*, Phys. Rev. B **54**, R5215 (1996).

[143] P. A. M. Dirac, *The Quantum Theory of the Emission and Absorption of Radiation*, P. Roy. Soc. Lond. A: Mat. **114**, 243 (1927).

[144] E. Fermi, *Nuclear Physics: Course Notes Compiled by J. Orear, A. H. Rosenfeld, and R. A. Schuster*, University of Chicago Press, Chicago (1950).

[145] H. B. Bebb and E. W. Williams, *Transport and Optical Phenomena: Photoluminescence I: Theory*, Vol. 8 of *Semiconductors and Semimetals*, Academic Press, New York (1972).

[146] L. Brillouin, *Wave Propagation and Group Velocity*, Academic Press, New York (1960).

[147] W. van Roosbroeck and W. Shockley, *Photon-Radiative Recombination of Electrons and Holes in Germanium*, Phys. Rev. **94**, 1558 (1954).

[148] O. Brandt, H.-J. Wünsche, H. Yang, R. Klann, J. Müllhäuser, and K. Ploog, *Recombination dynamics in GaN*, J. Cryst. Growth **189/190**, 790 (1998).

[149] L. C. Andreani, F. Tassone, and F. Bassani, *Radiative Lifetime of Free Excitons in Quantum Wells*, Solid State Commun. **77**, 641 (1991).

[150] P. Lefebvre, J. Allègre, B. Gil, A. Kavokine, H. Mathieu, W. Kim, A. Salvador, A. Botchkarev, and H. Morkoç, *Recombination dynamics of free and localized excitons in GaN/$Ga_{0.93}Al_{0.07}N$ quantum wells*, Phys. Rev. B **57**, R9447 (1998).

[151] D. Rosales, T. Bretagnon, B. Gil, A. Kahouli, J. Brault, B. Damilano, J. Massies, M. V. Durnev, and A. V. Kavokin, *Excitons in nitride heterostructures: From zero- to one-dimensional behavior*, Phys. Rev. B **88**, 125437 (2013).

[152] J. Hopfield, *Theory of the Contribution of Excitons to the Complex Dielectric Constant of Crystals*, Phys. Rev. **112**, 1555 (1958).

[153] Y. Narukawa, Y. Kawakami, M. Funato, S. Fujita, S. Fujita, and S. Nakamura, *Role of self-formed InGaN quantum dots for exciton localization in the purple laser diode emitting at 420 nm*, Appl. Phys. Lett. **70**, 981 (1997).

[154] L.-W. Wang, *Calculations of carrier localization in $In_xGa_{1-x}N$*, Phys. Rev. B **63**, 245107 (2001).

[155] I.-h. Ho and G. B. Stringfellow, *Solid phase immiscibility in GaInN*, Appl. Phys. Lett. **69**, 2701 (1996).

[156] S. Y. Karpov, *Suppression of phase separation in InGaN due to elastic strain*, MRS Internet J. Nitride Semicond. Res. **3**, 16 (1998).

[157] R. A. Oliver, S. E. Bennett, T. Zhu, D. J. Beesley, M. J. Kappers, D. W. Saxey, A. Cerezo, and C. J. Humphreys, *Microstructural origins of localization in InGaN quantum wells*, J. Phys. D: Appl. Phys. **43**, 354003 (2010).

[158] S. Schulz, O. Marquardt, C. Coughlan, M. A. Caro, O. Brandt, and E. P. O'Reilly, *Atomistic description of wave function localization effects in $In_xGa_{1-x}N$ alloys and quantum wells*, Proc. SPIE **9357**, 93570C (2015).

[159] N. K. van der Laak, R. A. Oliver, M. J. Kappers, and C. J. Humphreys, *Role of gross well-width fluctuations in bright, green-emitting single InGaN/GaN quantum well structures*, Appl. Phys. Lett. **90**, 121911 (2007).

[160] R. A. Oliver, F. C. P. Massabuau, M. J. Kappers, W. A. Phillips, E. J. Thrush, C. C. Tartan, W. E. Blenkhorn, T. J. Badcock, P. Dawson, M. A. Hopkins, D. W. E. Allsopp, and C. J. Humphreys, *The impact of gross well width fluctuations on the efficiency of GaN-based light emitting diodes*, Appl. Phys. Lett. **103**, 141114 (2013).

[161] D. M. Graham, A. Soltani-Vala, P. Dawson, M. J. Godfrey, T. M. Smeeton, J. S. Barnard, M. J. Kappers, C. J. Humphreys, and E. J. Thrush, *Optical and microstructural studies of InGaN/GaN single-quantum-well structures*, J. Appl. Phys. **97**, 103508 (2005).

[162] J. Lähnemann, P. Corfdir, F. Feix, J. Kamimura, T. Flissikowski, H. T. Grahn, L. Geelhaar, and O. Brandt, *Radial Stark Effect in (In,Ga)N Nanowires*, Nano Lett. **16**, 917 (2016).

[163] R. Calarco, M. Marso, T. Richter, A. I. Aykanat, R. Meijers, A. v.d. Hart, T. Stoica, and H. Lüth, *Size-dependent Photoconductivity in MBE-Grown GaN–Nanowires*, Nano Lett. **5**, 981 (2005).

[164] M. H. M. van Weert, O. Wunnicke, A. L. Roest, T. J. Eijkemans, A. Yu Silov, J. E. M. Haverkort, G. W. 't Hooft, and E. P. A. M. Bakkers, *Large redshift in photoluminescence of p-doped InP nanowires induced by Fermi-level pinning*, Appl. Phys. Lett. **88**, 043109 (2006).

[165] O. Marquardt, C. Hauswald, M. Woelz, L. Geelhaar, and O. Brandt, *Luminous efficiency of axial $In_xGa_{1-x}N$/GaN nanowire heterostructures: interplay of polarization and surface potentials*, Nano Lett. **13**, 3298 (2013).

[166] O. Marquardt, L. Geelhaar, and O. Brandt, *Minimizing the impact of surface potentials in axial In_xGa_{1-x} N/GaN nanowire heterostructures by reducing their diameter*, J. Phys. D: Appl. Phys. **47**, 394007 (2014).

[167] J. Kamimura, M. Ramsteiner, L. Geelhaar, and H. Riechert, *Si doping effects on (In,Ga)N nanowires*, J. Appl. Phys. **116**, 244310 (2014).

[168] J. Kamimura, P. Bogdanoff, J. Lähnemann, C. Hauswald, L. Geelhaar, S. Fiechter, and H. Riechert, *Photoelectrochemical Properties of (In,Ga)N Nanowires for Water Splitting Investigated by in Situ Electrochemical Mass Spectroscopy*, J. Am. Chem. Soc. **235**, 10242 (2013).

[169] J. Kamimura, P. Bogdanoff, P. Corfdir, O. Brandt, H. Riechert, and L. Geelhaar,

Broad Band Light Absorption and High Photocurrent of (In,Ga)N Nanowire Photoanodes Resulting from a Radial Stark Effect, ACS Appl. Mater. Interfaces **8**, 34490 (2016).

[170] T. Langer, H.-G. Pietscher, F. A. Ketzer, H. Jönen, H. Bremers, U. Rossow, D. Menzel, and A. Hangleiter, *S shape in polar GaInN/GaN quantum wells: Piezoelectric-field-induced blue shift driven by onset of nonradiative recombination*, Phys. Rev. B **90**, 205302 (2014).

[171] S. D. Baranovskii, R. Eichmann, and P. Thomas, *Temperature-dependent exciton luminescence in quantum wells by computer simulation*, Phys. Rev. B **58**, 13081 (1998).

[172] Y. Varshni, *Temperature dependence of the energy gap in semiconductors*, Physica **34**, 149 (1967).

[173] A. Radkowsky, *Temperature dependence of electron energy levels in solids*, Phys. Rev. **73**, 749 (1948).

[174] H. Y. Fan, *Temperature dependence of the energy gap in semiconductors*, Phys. Rev. **82**, 900 (1951).

[175] K. P. Korona, A. Wysmołek, K. Pakuła, R. Stępniewski, J. M. Baranowski, I. Grzegory, B. Łucznik, M. Wróblewski, and S. Porowski, *Exciton region reflectance of homoepitaxial GaN layers*, Appl. Phys. Lett. **69**, 788 (1996).

[176] R. Pässler, *Basic model relations for temperature dependencies of fundamental energy gaps in semiconductors*, Phys. Status Solidi B **200**, 155 (1997).

[177] R. Pässler, *Semi-empirical descriptions of temperature dependences of band gaps in semiconductors*, Phys. Status Solidi B **236**, 710 (2003).

[178] P. Corfdir, J. Levrat, A. Dussaigne, P. Lefebvre, H. Teisseyre, I. Grzegory, T. Suski, J.-D. Ganière, N. Grandjean, and B. Deveaud-Plédran, *Intrinsic dynamics of weakly and strongly confined excitons in nonpolar nitride-based heterostructures*, Phys. Rev. B **83**, 245326 (2011).

[179] P. Corfdir, C. Hauswald, J. K. Zettler, T. Flissikowski, J. Lähnemann, S. Fernández-Garrido, L. Geelhaar, H. T. Grahn, and O. Brandt, *Stacking faults as quantum wells in nanowires: Density of states, oscillator strength and radiative efficiency*, Phys. Rev. B **90**, 195309 (2014).

[180] O. Brandt, P. Waltereit, S. Dhar, U. Jahn, Y. J. Sun, A. Trampert, K. H. Ploog, M. A. Tagliente, and L. Tapfer, *Properties of (In,Ga)N/GaN quantum wells grown by plasma-assisted molecular beam epitaxy*, J. Vac. Sci. Technol. B **20**, 1626 (2002).

[181] B. Hahn, B. Galler, and K. Engl, *Development of high-efficiency and high-power vertical light emitting diodes*, Jpn. J. Appl. Phys. **53**, 100208 (2014).

[182] A. V. Lobanova, A. L. Kolesnikova, A. E. Romanov, S. Y. Karpov, M. E. Rudinsky, and E. V. Yakovlev, *Mechanism of stress relaxation in (0001) InGaN/GaN via formation of V-shaped dislocation half-loops*, Appl. Phys. Lett. **103**, 152106 (2013).

[183] I.-L. Lu, Y.-R. Wu, and J. Singh, *Study of carrier dynamics and radiative efficiency in InGaN/GaN LEDs with Monte Carlo method*, Phys. Status Solidi C **8**, 2393 (2011).

[184] C.-K. Wu, C.-K. Li, and Y.-R. Wu, *Percolation transport study in nitride based LED by considering the random alloy fluctuation*, J. Comput. Electron. **14**, 416 (2015).

[185] C.-K. Li, C.-K. Wu, C.-C. Hsu, L.-S. Lu, H. Li, T.-C. Lu, and Y.-R. Wu, *3D numerical modeling of the carrier transport and radiative efficiency for InGaN/GaN light emitting diodes with V-shaped pits*, AIP Adv. **6**, 055208 (2016).

[186] J. R. Haynes and W. Shockley, *Investigation of Hole Injection in Transistor Action*, Phys. Rev. **75**, 691 (1949).

[187] J. Danhof, *Local charge carrier diffusion and recombination in InGaN quantum wells*, PhD thesis, Albert-Ludwigs-Universität Freiburg im Breisgau (2013).

[188] S. Hammersley, D. Watson-Parris, P. Dawson, M. J. Godfrey, T. J. Badcock, M. J. Kappers, C. McAleese, R. A. Oliver, and C. J. Humphreys, *The consequences of high injected carrier densities on carrier localization and efficiency droop in InGaN/GaN quantum well structures*, J. Appl. Phys. **111**, 083512 (2012).

[189] Y. Roichman and N. Tessler, *Generalized Einstein relation for disordered semiconductors–implications for device performance*, Appl. Phys. Lett. **80**, 1948 (2002).

[190] G. A. H. Wetzelaer, L. J. A. Koster, and P. W. M. Blom, *Validity of the Einstein Relation in Disordered Organic Semiconductors*, Phys. Rev. Lett. **107**, 066605 (2011).

[191] S. Krasavin, *Electron scattering due to dislocation wall strain field in GaN layers*, J. Appl. Phys. **105**, 126104 (2009).

[192] O. Laboutin, Y. Cao, W. Johnson, R. Wang, G. Li, D. Jena, and H. Xing, *InGaN channel high electron mobility transistor structures grown by metal organic chemical vapor deposition*, Appl. Phys. Lett. **100**, 121909 (2012).

[193] R. Aleksiejūnas, M. Sūdžius, V. Gudelis, T. Malinauskas, K. Jarašiūnas, Q. Fareed, R. Gaska, M. S. Shur, J. Zhang, J. Yang, E. Kuokštis, and M. A. Khan, *Carrier transport and recombination in InGaN/GaN heterostructures, studied by optical four-wave mixing technique*, Phys. Status Solidi C **0**, 2686 (2003).

[194] S. Chichibu, K. Wada, and S. Nakamura, *Spatially resolved cathodoluminescence spectra of InGaN quantum wells*, Appl. Phys. Lett. **71**, 2346 (1997).

[195] K. Kumakura, T. Makimoto, N. Kobayashi, T. Hashizume, T. Fukui, and H. Hasegawa, *Minority carrier diffusion length in GaN: Dislocation density and doping concentration dependence*, Appl. Phys. Lett. **86**, 052105 (2005).

[196] K. Okamoto, A. Kaneta, K. Inoue, Y. Kawakami, M. Terazima, G. Shinomiya, T. Mukai, and S. Fujita, *Carrier Dynamics in InGaN/GaN SQW Structure Probed by the Transient Grating Method with Subpicosecond Pulsed Laser*, Phys. Status Solidi B **228**, 81 (2001).

[197] H.-M. Solowan, J. Danhof, and U. T. Schwarz, *Direct Observation of Charge Carrier Diffusion and Localization in an InGaN Multi Quantum Well*, Jpn. J. Appl. Phys. **52**, 08JK07 (2013).

[198] A. Vertikov, I. Ozden, and A. V. Nurmikko, *Diffusion and relaxation of excess carriers in InGaN quantum wells in localized versus extended states*, J. Appl. Phys. **86**, 4697 (1999).

[199] Z. Z. Bandić, P. M. Bridger, E. C. Piquette, and T. C. McGill, *Minority carrier diffusion length and lifetime in GaN*, Appl. Phys. Lett. **72**, 3166 (1998).

[200] S. Y. Karpov and Y. N. Makarov, *Dislocation effect on light emission efficiency in gallium*

nitride, Appl. Phys. Lett. **81**, 4721 (2003).

[201] R. J. Kaplar, S. R. Kurtz, and D. D. Koleske, *Optical and electrical step-recovery study of minority-carrier transport in an InGaN/GaN quantum-well light-emitting diode grown on sapphire*, Appl. Phys. Lett. **85**, 5436 (2004).

[202] K. Kumakura, T. Makimoto, N. Kobayashi, T. Hashizume, T. Fukui, and H. Hasegawa, *Minority carrier diffusion lengths in MOVPE-grown n- and p-InGaN and performance of AlGaN/InGaN/GaN double heterojunction bipolar transistors*, J. Cryst. Growth **298**, 787 (2007).

[203] T. Malinauskas, R. Aleksiejūnas, K. Jarašiūnas, B. Beaumont, P. Gibart, A. Kakanakova-Georgieva, E. Janzen, D. Gogova, B. Monemar, and M. Heuken, *All-optical characterization of carrier lifetimes and diffusion lengths in MOCVD-, ELO-, and HVPE- grown GaN*, J. Cryst. Growth **300**, 223 (2007).

[204] N. Pauc, M. R. Phillips, V. Aimez, and D. Drouin, *Carrier recombination near threading dislocations in GaN epilayers by low voltage cathodoluminescence*, Appl. Phys. Lett. **89**, 161905 (2006).

[205] N. Ino and N. Yamamoto, *Low temperature diffusion length of excitons in gallium nitride measured by cathodoluminescence technique*, Appl. Phys. Lett. **93**, 232103 (2008).

[206] S. Hafiz, F. Zhang, M. Monavarian, V. Avrutin, H. Morkoç, Ü. Özgür, S. Metzner, F. Bertram, J. Christen, and B. Gil, *Determination of carrier diffusion length in GaN*, J. Appl. Phys. **117**, 013106 (2015).

[207] M. Hocker, P. Maier, L. Jerg, I. Tischer, G. Neusser, C. Kranz, M. Pristovsek, C. J. Humphreys, R. A. R. Leute, D. Heinz, O. Rettig, F. Scholz, and K. Thonke, *Determination of axial and lateral exciton diffusion length in GaN by electron energy dependent cathodoluminescence*, J. Appl. Phys. **120**, 085703 (2016).

[208] Z. Z. Bandić, P. M. Bridger, E. C. Piquette, and T. C. McGill, *The values of minority carrier diffusion lengths and lifetimes in GaN and their implications for bipolar devices*, Solid State Electron. **44**, 221 (2000).

[209] L. Lymperakis, J. Neugebauer, M. Albrecht, T. Remmele, and H. P. Strunk, *Strain Induced Deep Electronic States around Threading Dislocations in GaN*, Phys. Rev. Lett. **93**, 196401 (2004).

[210] G. Maciejewski, S. Kret, and P. Ruterana, *Piezoelectric field around threading dislocation in GaN determined on the basis of high-resolution transmission electron microscopy image*, J. Microsc. **223**, 212 (2006).

[211] R. Sakaguchi, T. Akiyama, K. Nakamura, and T. Ito, *Theoretical investigations of compositional inhomogeneity around threading dislocations in III–nitride semiconductor alloys*, Jpn. J. Appl. Phys. **55**, 05FM05 (2016).

[212] J. Danhof, U. T. Schwarz, A. Kaneta, and Y. Kawakami, *Time-of-flight measurements of charge carrier diffusion in $In_xGa_{1-x}N$/GaN quantum wells*, Phys. Rev. B **84**, 035324 (2011).

[213] J. Danhof, H.-M. Solowan, U. T. Schwarz, A. Kaneta, Y. Kawakami, D. Schiavon, T. Meyer, and M. Peter, *Lateral charge carrier diffusion in InGaN quantum wells*, Phys.

Status Solidi B **249**, 480 (2012).

[214] S. Sonderegger, E. Feltin, M. Merano, A. Crottini, J. F. Carlin, R. Sachot, B. Deveaud, N. Grandjean, and J. D. Ganière, *High spatial resolution picosecond cathodoluminescence of InGaN quantum wells*, Appl. Phys. Lett. **89**, 232109 (2006).

[215] A. Vertikov, I. Ozden, and A. V. Nurmikko, *Investigation of excess carrier diffusion in nitride semiconductors with near-field optical microscopy*, Appl. Phys. Lett. **74**, 850 (1999).

[216] C. Vierheilig, H. Braun, U. T. Schwarz, W. Wegscheider, E. Baur, U. Strauß, and V. Härle, *Lateral diffusion of photogenerated carriers in InGaN/GaN heterostructures observed by PL measurements*, Phys. Status Solidi C **4**, 2362 (2007).

[217] Y.-C. Huang, J.-C. Liang, C.-K. Sun, A. Abare, and S. P. DenBaars, *Piezoelectric-field-enhanced lateral ambipolar diffusion coefficient in InGaN/GaN multiple quantum wells*, Appl. Phys. Lett. **78**, 928 (2001).

[218] K. Nomeika, R. Aleksiejūnas, S. Miasojedovas, R. Tomašiūnas, K. Jarašiūnas, I. Pietzonka, M. Strassburg, and H.-J. Lugauer, *Impact of carrier localization and diffusion on photoluminescence in highly excited cyan and green InGaN LED structures*, J. Lumin. **188**, 301 (2017).

[219] B. Hahn, *Closing the Green Efficiency Gap... Status and recent approaches*, https://energy.gov/sites/prod/files/2016/02/f29/hahn_leddroop_raleigh2016.pdf, DOE SSL R&D Workshop, Raleigh (2016).

[220] F. Nippert, S. Y. Karpov, G. Callsen, B. Galler, T. Kure, C. Nenstiel, M. R. Wagner, M. Straßburg, H. J. Lugauer, and A. Hoffmann, *Temperature-dependent recombination coefficients in InGaN light-emitting diodes: Hole localization, Auger processes, and the green gap*, Appl. Phys. Lett. **109**, 161103 (2016).

[221] A. David and M. J. Grundmann, *Influence of polarization fields on carrier lifetime and recombination rates in InGaN-based light-emitting diodes*, Appl. Phys. Lett. **97**, 033501 (2010).

[222] M. Pristovsek, A. Bao, R. A. Oliver, T. Badcock, M. Ali, and A. Shields, *Effects of Wavelength and Defect Density on the Efficiency of (In,Ga)N-Based Light-Emitting Diodes*, Phys. Rev. Applied **7**, 064007 (2017).

[223] O. B. Shchekin, P. J. Schmidt, F. Jin, N. Lawrence, K. J. Vampola, H. Bechtel, D. R. Chamberlin, R. Mueller-Mach, and G. O. Mueller, *Excitation dependent quenching of luminescence in LED phosphors*, Phys. Status Solidi RRL **10**, 310 (2016).

[224] S. Watanabe, N. Yamada, M. Nagashima, Y. Ueki, C. Sasaki, Y. Yamada, T. Taguchi, K. Tadatomo, H. Okagawa, and H. Kudo, *Internal quantum efficiency of highly-efficient $In_xGa_{1-x}N$-based near-ultraviolet light-emitting diodes*, Appl. Phys. Lett. **83**, 4906 (2003).

[225] W. Guo, M. Zhang, P. Bhattacharya, and J. Heo, *Auger Recombination in III-Nitride Nanowires and Its Effect on Nanowire Light-Emitting Diode Characteristics*, Nano Lett. **11**, 1434 (2011).

[226] H. P. T. Nguyen, K. Cui, S. Zhang, M. Djavid, A. Korinek, G. A. Botton, and Z. Mi, *Controlling Electron Overflow in Phosphor-Free InGaN/GaN Nanowire White*

Light-Emitting Diodes, Nano Lett. **12**, 1317 (2012).

[227] S. Jahangir, T. Schimpke, M. Strassburg, K. A. Grossklaus, J. M. Millunchick, and P. Bhattacharya, *Red-Emitting (λ = 610 nm) $In_{0.51}Ga_{0.49}N$/GaN Disk-in-Nanowire Light Emitting Diodes on Silicon*, IEEE J. Quantum Electron. **50**, 530 (2014).

[228] A. T. M. Sarwar Golam, S. D. Carnevale, F. Yang, T. F. Kent, J. J. Jamison, D. W. McComb, and R. C. Myers, *Semiconductor Nanowire Light-Emitting Diodes Grown on Metal: A Direction Toward Large-Scale Fabrication of Nanowire Devices*, Small **11**, 5402 (2015).

[229] N. Alfaraj, S. Mitra, F. Wu, I. A. Ajia, B. Janjua, A. Prabaswara, R. A. Aljefri, H. Sun, T. Khee Ng, B. S. Ooi, I. S. Roqan, and X. Li, *Photoinduced entropy of InGaN/GaN p-i-n double-heterostructure nanowires*, Appl. Phys. Lett. **110**, 161110 (2017).

[230] R. Westphäling, P. Ullrich, J. Hoffmann, H. Kalt, C. Klingshirn, K. Ohkawa, and D. Hommel, *Measurements of the absolute external luminescence quantum efficiency in ZnSe/ZnMgSSe multiple quantum wells as a function of temperature*, J. Appl. Phys. **84**, 6871 (1998).

[231] K. Kojima, T. Ohtomo, K.-i. Ikemura, Y. Yamazaki, M. Saito, H. Ikeda, K. Fujito, and S. F. Chichibu, *Determination of absolute value of quantum efficiency of radiation in high quality GaN single crystals using an integrating sphere*, J. Appl. Phys. **120**, 015704 (2016).

[232] P. G. Eliseev, M. Osin'ski, H. Li, and I. V. Akimova, *Recombination balance in green-light-emitting GaN/InGaN/AlGaN quantum wells*, Appl. Phys. Lett. **75**, 3838 (1999).

[233] A. David and M. J. Grundmann, *Droop in InGaN light-emitting diodes: A differential carrier lifetime analysis*, Appl. Phys. Lett. **96**, 103504 (2010).

[234] C. Mounir and U. T. Schwarz, *Determination of the radiative efficiency of GaN-based light-emitting diodes via bias dependent resonant photoluminescence*, Appl. Phys. Lett. **110**, 011106 (2017).

[235] C. E. Martinez, N. M. Stanton, A. J. Kent, D. M. Graham, P. Dawson, M. J. Kappers, and C. J. Humphreys, *Determination of relative internal quantum efficiency in InGaN/GaN quantum wells*, J. Appl. Phys. **98**, 053509 (2005).

[236] T. Nakano, K. Kawakami, and A. A. Yamaguchi, *Determination of internal quantum efficiency in GaN by simultaneous measurements of photoluminescence and photo-acoustic signals*, SPIE Proceeding **9748**, 97481W (2016).

[237] S. Karpov, *ABC-model for interpretation of internal quantum efficiency and its droop in III-nitride LEDs: a review*, Opt. Quant. Electron. **47**, 1293 (2015).

[238] A. David, C. A. Hurni, N. G. Young, and M. D. Craven, *Carrier dynamics and Coulomb-enhanced capture in III-nitride quantum heterostructures*, Appl. Phys. Lett. **109**, 033504 (2016).

[239] M. Vallone, M. Goano, F. Bertazzi, and G. Ghione, *Carrier capture in InGaN/GaN quantum wells: Role of electron-electron scattering*, J. Appl. Phys. **121**, 123107 (2017).

[240] V. A. Jhalani, J.-J. Zhou, and M. Bernardi, *Ultrafast Hot Carrier Dynamics in GaN and Its Impact on the Efficiency Droop*, Nano Lett. **17**, 5012 (2017).

[241] Y.-R. Wu, R. Shivaraman, K.-C. Wang, and J. S. Speck, *Analyzing the physical properties of InGaN multiple quantum well light emitting diodes from nano scale structure*, Appl. Phys. Lett. **101**, 083505 (2012).

[242] T.-J. Yang, R. Shivaraman, J. S. Speck, and Y.-R. Wu, *The influence of random indium alloy fluctuations in indium gallium nitride quantum wells on the device behavior*, J. Appl. Phys. **116**, 113104 (2014).

[243] DEEPEN: Atom-to-Device Explicit simulation Environment for Photonics and Electronics Nanostructures, http://www.nmp-deepen.eu/about-us, 10/11/2016.

[244] DEEPEN: D6.9 – Modelling of transport and EL properties validated for systematic variations in LED design, http://www.nmp-deepen.eu/contentfiles/D6.9.pdf, 29/12/2016.

[245] D.-P. Han, J.-I. Shim, and D.-S. Shin, *Factors Determining the Carrier Distribution in InGaN/GaN Multiple-Quantum-Well Light-Emitting Diodes*, arXiv p. 1705.09559 (2017).

[246] D. Barettin, M. Auf der Maur, A. di Carlo, A. Pecchia, A. F. Tsatsulnikov, W. V. Lundin, A. V. Sakharov, A. E. Nikolaev, M. Korytov, N. Cherkashin, M. J. Hÿtch, and S. Y. Karpov, *Carrier transport and emission efficiency in InGaN quantum-dot based light-emitting diodes*, Nanotechnology **28**, 275201 (2017).

[247] J. Hader, *Auger as Reason for Droop?*, https://nusod.wordpress.com/2015/06/10/auger-as-reason-for-droop/, NUSOD (2015).

[248] A. Haug, *Auger recombination in direct-gap semiconductors: band-structure effects*, J. Phys. C: Solid State Phys. **16**, 4159 (1983).

[249] K. T. Delaney, P. Rinke, and C. G. Van de Walle, *Erratum: "Auger recombination rates in nitrides from first principles" [Appl. Phys. Lett. 94, 191109 (2009)]*, Appl. Phys. Lett. **108**, 259901 (2016).

[250] E. Kioupakis, P. Rinke, K. T. Delaney, and C. G. Van de Walle, *Indirect Auger recombination as a cause of efficiency droop in nitride light-emitting diodes*, Appl. Phys. Lett. **98**, 161107 (2011).

[251] E. Kioupakis, Q. Yan, D. Steiauf, and C. G. Van de Walle, *Temperature and carrier-density dependence of Auger and radiative recombination in nitride optoelectronic devices*, New J. Phys. **15**, 125006 (2013).

[252] J. Iveland, L. Martinelli, J. Peretti, J. S. Speck, and C. Weisbuch, *Direct Measurement of Auger Electrons Emitted from a Semiconductor Light-Emitting Diode under Electrical Injection: Identification of the Dominant Mechanism for Efficiency Droop*, Phys. Rev. Lett. **110**, 177406 (2013).

[253] J. Iveland, M. Piccardo, L. Martinelli, J. Peretti, J. W. Choi, N. Young, S. Nakamura, J. S. Speck, and C. Weisbuch, *Origin of electrons emitted into vacuum from InGaN light emitting diodes*, Appl. Phys. Lett. **105**, 052103 (2014).

[254] M. Binder, A. Nirschl, R. Zeisel, T. Hager, H.-J. Lugauer, M. Sabathil, D. Bougeard, J. Wagner, and B. Galler, *Identification of nnp and npp Auger recombination as significant contributor to the efficiency droop in (GaIn)N quantum wells by visualization of hot carriers*

in photoluminescence, Appl. Phys. Lett. **103**, 071108 (2013).

[255] F. Bertazzi, M. Goano, X. Zhou, M. Calciati, G. Ghione, M. Matsubara, and E. Bellotti, *Comment on "Direct Measurement of Auger Electrons Emitted from a Semiconductor Light-Emitting Diode under Electrical Injection: Identification of the Dominant Mechanism for Efficiency Droop" [Phys. Rev. Lett. 110, 177406 (2013)]*, arXiv p. 1305.2512 (2013).

[256] M.-H. Kim, M. F. Schubert, Q. Dai, J. K. Kim, E. F. Schubert, J. Piprek, and Y. Park, *Origin of efficiency droop in GaN-based light-emitting diodes*, Appl. Phys. Lett. **91**, 183507 (2007).

[257] G.-B. Lin, D. Meyaard, J. Cho, E. Fred Schubert, H. Shim, and C. Sone, *Analytic model for the efficiency droop in semiconductors with asymmetric carrier-transport properties based on drift-induced reduction of injection efficiency*, Appl. Phys. Lett. **100**, 161106 (2012).

[258] T. Kim, T. Y. Seong, and O. Kwon, *Investigating the origin of efficiency droop by profiling the voltage across the multi-quantum well of an operating light-emitting diode*, Appl. Phys. Lett. **108**, 231101 (2016).

[259] M. Auf der Maur, B. Galler, I. Pietzonka, M. Strassburg, H. Lugauer, and A. Di Carlo, *Trap-assisted tunneling in InGaN/GaN single-quantum-well light-emitting diodes*, Appl. Phys. Lett. **105**, 133504 (2014).

[260] M. Mandurrino, G. Verzellesi, M. Goano, M. Vallone, F. Bertazzi, G. Ghione, M. Meneghini, G. Meneghesso, and E. Zanoni, *Physics-based modeling and experimental implications of trap-assisted tunneling in InGaN/GaN light-emitting diodes*, Phys. Status Solidi A **212**, 947 (2015).

[261] M. Musolino, D. van Treeck, A. Tahraoui, L. Scarparo, C. De Santi, M. Meneghini, E. Zanoni, L. Geelhaar, and H. Riechert, *A physical model for the reverse leakage current in (In,Ga)N/GaN light-emitting diodes based on nanowires*, J. Appl. Phys. **119**, 044502 (2016).

[262] E. Kioupakis, P. Rinke, A. Schleife, F. Bechstedt, and C. G. Van de Walle, *Free-carrier absorption in nitrides from first principles*, Phys. Rev. B **81**, 241201 (2010).

[263] J. Hader, J. V. Moloney, and S. W. Koch, *Optical excitation dependent emission properties of InGaN quantum wells*, J. Comput. Electron. **14**, 425 (2015).

[264] A. Laubsch, M. Sabathil, W. Bergbauer, M. Strassburg, H. Lugauer, M. Peter, S. Lutgen, N. Linder, K. Streubel, J. Hader, J. V. Moloney, B. Pasenow, and S. W. Koch, *On the origin of IQE-'droop' in InGaN LEDs*, Phys. Status Solidi C **6**, S913 (2009).

[265] K. Fujiwara, H. Jimi, and K. Kaneda, *Temperature-dependent droop of electroluminescence efficiency in blue (In,Ga)N quantum-well diodes*, Phys. Status Solidi C **6**, S814 (2009).

[266] D. P. Han, D. G. Zheng, C. H. Oh, H. Kim, J. I. Shim, D. S. Shin, and K. S. Kim, *Nonradiative recombination mechanisms in InGaN/GaN-based light-emitting diodes investigated by temperature-dependent measurements*, Appl. Phys. Lett. **104**, 151108 (2014).

[267] J. Hader, J. V. Moloney, and S. W. Koch, *Temperature-dependence of the internal efficiency droop in GaN-based diodes*, Appl. Phys. Lett. **99**, 181127 (2011).

[268] B. Monemar and B. E. Sernelius, *Defect related issues in the "current roll-off" in InGaN*

based light emitting diodes, Appl. Phys. Lett. **91**, 181103 (2007).

[269] A. Hangleiter, F. Hitzel, C. Netzel, D. Fuhrmann, U. Rossow, G. Ade, and P. Hinze, *Suppression of Nonradiative Recombination by V-Shaped Pits in GaInN/GaN Quantum Wells Produces a Large Increase in the Light Emission Efficiency*, Phys. Rev. Lett. **95**, 127402 (2005).

[270] Z. Quan, J. Liu, F. Fang, G. Wang, and F. Jiang, *A new interpretation for performance improvement of high-efficiency vertical blue light-emitting diodes by InGaN/GaN superlattices*, J. Appl. Phys. **118**, 193102 (2015).

[271] C.-Y. Chang, H. Li, Y.-T. Shih, and T.-C. Lu, *Manipulation of nanoscale V-pits to optimize internal quantum efficiency of InGaN multiple quantum wells*, Appl. Phys. Lett. **106**, 091104 (2015).

[272] T. J. Badcock, M. Ali, T. Zhu, M. Pristovsek, R. A. Oliver, and A. J. Shields, *Radiative recombination mechanisms in polar and non-polar InGaN/GaN quantum well LED structures*, Appl. Phys. Lett. **109**, 151110 (2016).

[273] B. Galler, H.-J. Lugauer, M. Binder, R. Hollweck, Y. Folwill, A. Nirschl, A. Gomez-Iglesias, B. Hahn, J. Wagner, and M. Sabathil, *Experimental Determination of the Dominant Type of Auger Recombination in InGaN Quantum Wells*, Appl. Phys. Express **6**, 112101 (2013).

[274] F. Römer and B. Witzigmann, *Effect of Auger recombination and leakage on the droop in InGaN/GaN quantum well LEDs*, Opt. Express **22**, A1440 (2014).

[275] A. David, N. G. Young, C. A. Hurni, and M. D. Craven, *All-optical measurements of carrier dynamics in bulk-GaN LEDs: Beyond the ABC approximation*, Appl. Phys. Lett. **110**, 253504 (2017).

[276] F. Della Sala, A. Di Carlo, P. Lugli, F. Bernardini, V. Fiorentini, R. Scholz, and J.-M. Jancu, *Free-carrier screening of polarization fields in wurtzite GaN/InGaN laser structures*, Appl. Phys. Lett. **74**, 2002 (1999).

[277] E. Kioupakis, Q. Yan, and C. G. Van De Walle, *Interplay of polarization fields and Auger recombination in the efficiency droop of nitride light-emitting diodes*, Appl. Phys. Lett. **101**, 231107 (2012).

[278] G. Rossbach, J. Levrat, G. Jacopin, M. Shahmohammadi, J.-F. Carlin, J.-D. Ganière, R. Butté, B. Deveaud, and N. Grandjean, *High-temperature Mott transition in wide-band-gap semiconductor quantum wells*, Phys. Rev. B **90**, 201308 (2014).

[279] J. Hader, J. V. Moloney, and S. W. Koch, *Supression of carrier recombination in semiconductor lasers by phase-space filling*, Appl. Phys. Lett. **87**, 201112 (2005).

[280] T. Malinauskas, K. Jarasiunas, M. Heuken, F. Scholz, and P. Brückner, *Diffusion and recombination of degenerate carrier plasma in GaN*, Phys. Status Solidi C **6**, 743 (2009).

[281] D.-P. Han, J.-I. Shim, and D.-S. Shin, *Analysis of carrier recombination dynamics in InGaN-based light-emitting diodes by differential carrier lifetime measurement*, Appl. Phys. Express **10**, 052101 (2017).

[282] G. Koblmüller, C. S. Gallinat, and J. S. Speck, *Surface kinetics and thermal instability of N-face InN grown by plasma-assisted molecular beam epitaxy*, J. Appl. Phys. **101**, 083516

(2007).

[283] D. N. Nath, E. Gür, S. A. Ringel, and S. Rajan, *Molecular beam epitaxy of N-polar InGaN*, Appl. Phys. Lett. **97**, 071903 (2010).

[284] S.-H. Han, D.-Y. Lee, J.-Y. Lim, J. W. Lee, D.-J. Kim, Y. S. Kim, S.-T. Kim, and S.-J. Park, *Effect of Internal Electric Field in Well Layer of InGaN/GaN Multiple Quantum Well Light-Emitting Diodes on Efficiency Droop*, Jpn. J. Appl. Phys. **51**, 100201 (2012).

[285] P. D. Dapkus, *Metalorganic Chemical Vapor Deposition*, Annu. Rev. Mater. Sci. **12**, 243 (1982).

[286] K. Ploog, *Molecular Beam Epitaxy of III-V Compounds: Technology and Growth Process*, Annu. Rev. Mater. Sci. **11**, 171 (1981).

[287] P. D. Dapkus, *A critical comparison of MOCVD and MBE for heterojunction devices*, J. Cryst. Growth **68**, 345 (1984).

[288] M. Johnson, Z. Yu, J. Brown, F. Koeck, N. El-Masry, H. Kong, J. Edmond, J. Cook, and J. Schetzina, *A Critical Comparison Between MOVPE and MBE Growth of III-V Nitride Semiconductor Materials for Opto-Electronic Device Applications*, MRS Internet J. Nitride Semicond. Res. **4**, 594 (1999).

[289] D. Schiavon, M. Binder, M. Peter, B. Galler, P. Drechsel, and F. Scholz, *Wavelength-dependent determination of the recombination rate coefficients in single-quantum-well GaInN/GaN light emitting diodes*, Phys. Status Solidi B **250**, 283 (2013).

[290] M. Musolino, A. Tahraoui, F. Limbach, J. Lähnemann, U. Jahn, O. Brandt, L. Geelhaar, and H. Riechert, *Understanding peculiarities in the optoelectronic characteristics of light emitting diodes based on (In,Ga)N/GaN nanowires*, Appl. Phys. Lett. **105**, 083505 (2014).

[291] Y. Nakagawa, M. Haraguchi, M. Fukui, S. Tanaka, A. Sakaki, K. Kususe, N. Hosokawa, T. Takehara, Y. Morioka, H. Iijima, M. Kubota, M. Abe, T. Mukai, H. Takagi, and G. I. Shinomiya, *Hydrogen Dissociation from Mg-doped GaN*, Jpn. J. Appl. Phys. **43**, 23 (2004).

[292] S. Nakamura, T. Mukai, and M. Senoh, *Si- and Ge-Doped GaN Films Grown with GaN Buffer Layers*, Jpn. J. Appl. Phys. **31**, 2883 (1992).

[293] S. Fritze, A. Dadgar, H. Witte, M. Bügler, A. Rohrbeck, J. Bläsing, A. Hoffmann, and A. Krost, *High Si and Ge n-type doping of GaN doping - Limits and impact on stress*, Appl. Phys. Lett. **100**, 122104 (2012).

[294] H. Obloh, K. Bachem, U. Kaufmann, M. Kunzer, M. Maier, A. Ramakrishnan, and P. Schlotter, *Self-compensation in Mg doped p-type GaN grown by MOCVD*, J. Cryst. Growth **195**, 270 (1998).

[295] D. J. Kim, D. Y. Ryu, N. A. Bojarczuk, J. Karasinski, S. Guha, S. H. Lee, and J. H. Lee, *Thermal activation energies of Mg in GaN:Mg measured by the Hall effect and admittance spectroscopy*, J. Appl. Phys. **88**, 2564 (2000).

[296] K. S. Kim, C. S. Oh, W. H. Lee, K. J. Lee, G. M. Yang, C. H. Hong, E. K. Suh, K. Y. Lim, H. J. Lee, and D. J. Byun, *Comparative analysis of characteristics of Si, Mg, and undoped GaN*, J. Cryst. Growth **210**, 505 (2000).

[297] I. S. Romanov, I. A. Prudaev, V. V. Kopyev, A. A. Marmalyuk, V. A. Kureshov, D. R. Sabitov, and A. V. Mazalov, *Effect of growth temperature of GaN:Mg layer on internal quantum efficiency of LED structures with InGaN/GaN quantum wells*, J. Phys. Conf. Ser. **541**, 012083 (2014).

[298] S. Nakamura, M. Senoh, S. ichi Nagahama, N. Iwasa, T. Yamada, T. Matsushita, H. Kiyoku, and Y. Sugimoto, *InGaN-Based Multi-Quantum-Well-Structure Laser Diodes*, Jpn. J. Appl. Phys. **35**, L74 (1996).

[299] M. Ikeda and S. Uchida, *Blue-Violet Laser Diodes Suitable for Blu-ray Disk*, Phys. Status Solidi A **194**, 407 (2002).

[300] S.-H. Han, D.-Y. Lee, S.-J. Lee, C.-Y. Cho, M.-K. Kwon, S. P. Lee, D. Y. Noh, D.-J. Kim, Y. C. Kim, and S.-J. Park, *Effect of electron blocking layer on efficiency droop in InGaN/GaN multiple quantum well light-emitting diodes*, Appl. Phys. Lett. **94**, 231123 (2009).

[301] G. Snider, *One-dimensional self-consistent Poisson and Schrödinger solver*, http://www3.nd.edu/ gsnider/, University of Notre Dame, Indiana (2014).

[302] I. Tan, G. L. Snider, L. D. Chang, and E. L. Hu, *A self-consistent solution of Schrödinger-Poisson equations using a nonuniform mesh*, J. Appl. Phys. **68**, 4071 (1990).

[303] G. Snider, I. Tan, and E. Hu, *Electron states in mesa-etched one-dimensional quantum well wires*, J. Appl. Phys. **68**, 2849 (1990).

[304] D. Winston and R. Hayes, *SimWindows: A New Simulator for Studying Quantum Well Optoelectronic Devices*, Proc. Intern. Symp. on Compound Semic. , IPO Publishing, San-Diego CA, 747, (1994).

[305] Y. Wu, *One Dimensional Poisson, Drift-Diffusion, and Schrödinger Solver (1D-DDCC)*, http://yrwu-wk.ee.ntu.edu.tw/, National Taiwan University, Taipei (2017).

[306] Silvaco: Atlas Device Simulation Framework, https://www.silvaco.com/products/tcad/device_simulation/atlas/atlas.html, 10/07/2017.

[307] P. Rinke, M. Winkelnkemper, A. Qteish, D. Bimberg, J. Neugebauer, and M. Scheffler, *Consistent set of band parameters for the group-III nitrides AlN, GaN, and InN*, Phys. Rev. B **77**, 075202 (2008).

[308] L. Vegard, *Die Konstitution der Mischkristalle und die Raumfüllung der Atome*, Zeitschrift für Phys. **5**, 17 (1921).

[309] T. Inushima, T. Shiraishi, and V. Y. Davydov, *Phonon structure of InN grown by atomic layer epitaxy*, Solid State Commun. **110**, 491 (1999).

[310] P. Schley, R. Goldhahn, A. T. Winzer, G. Gobsch, V. Cimalla, O. Ambacher, H. Lu, W. J. Schaff, M. Kurouchi, Y. Nanishi, M. Rakel, C. Cobet, and N. Esser, *Dielectric function and Van Hove singularities for In-rich $In_xGa_{1-x}N$ alloys: Comparison of N- and metal-face materials*, Phys. Rev. B **75**, 205204 (2007).

[311] C. Persson, A. Ferreira da Silva, R. Ahuja, and B. Johansson, *First-principle calculations of the dielectric function of zinc-blende and wurtzite InN*, J. Phys. Condens. Matter **13**, 8945 (2001).

[312] C. S. Gallinat, G. Koblmüller, J. S. Brown, S. Bernardis, J. S. Speck, G. D. Chern, E. D.

Readinger, H. Shen, and M. Wraback, *In-polar InN grown by plasma-assisted molecular beam epitaxy*, Appl. Phys. Lett. **89**, 032109 (2006).

[313] G. Martin, A. Botchkarev, A. Rockett, and H. Morkoç, *Valence-band discontinuities of wurtzite GaN, AlN, and InN heterojunctions measured by x-ray photoemission spectroscopy*, Appl. Phys. Lett. **68**, 2541 (1996).

[314] P. D. C. King, T. D. Veal, C. E. Kendrick, L. R. Bailey, S. M. Durbin, and C. F. McConville, *InN/GaN valence band offset: High-resolution x-ray photoemission spectroscopy measurements*, Phys. Rev. B **78**, 033308 (2008).

[315] P. G. Moses and C. G. Van de Walle, *Band bowing and band alignment in InGaN alloys*, Appl. Phys. Lett. **96**, 021908 (2010).

[316] L. Dong, J. V. Mantese, V. Avrutin, Ü. Özgür, H. Morkoç, and S. P. Alpay, *Strain induced variations in band offsets and built-in electric fields in InGaN/GaN multiple quantum wells*, J. Appl. Phys. **114**, 043715 (2013).

[317] V. Fiorentini, F. Bernardini, and O. Ambacher, *Evidence for nonlinear macroscopic polarization in III-V nitride alloy heterostructures*, Appl. Phys. Lett. **80**, 1204 (2002).

[318] F. Renner, P. Kiesel, G. H. Döhler, M. Kneissl, C. G. Van de Walle, and N. M. Johnson, *Quantitative analysis of the polarization fields and absorption changes in InGaN/GaN quantum wells with electroabsorption spectroscopy*, Appl. Phys. Lett. **81**, 490 (2002).

[319] H. Zhang, E. J. Miller, E. T. Yu, C. Poblenz, and J. S. Speck, *Measurement of polarization charge and conduction-band offset at $In_xGa_{1-x}N$/GaN heterojunction interfaces*, Appl. Phys. Lett. **84**, 4644 (2004).

[320] M.-C. Tsai, S.-H. Yen, S.-H. Chang, and Y.-K. Kuo, *Effect of spontaneous and piezoelectric polarization on optical characteristics of ultraviolet AlGaInN light-emitting diodes*, Opt. Commun. **282**, 1589 (2009).

[321] C. Böcklin, R. G. Veprek, S. Steiger, and B. Witzigmann, *Computational study of an InGaN/GaN nanocolumn light-emitting diode*, Phys. Rev. B **81**, 155306 (2010).

[322] F. Zhang, M. Ikeda, S.-M. Zhang, J.-P. Liu, A.-Q. Tian, P.-Y. Wen, Y. Cheng, and H. Yang, *Reduction of Polarization Field Strength in Fully Strained c-Plane InGaN/(In)GaN Multiple Quantum Wells Grown by MOCVD*, Nanoscale Res. Lett. **11**, 519 (2016).

[323] P. E. Ciddor, *Refractive index of air: new equations for the visible and near infrared*, Appl. Opt. **35**, 1566 (1996).

[324] B. Amos, G. McConnell, and T. Wilson, *Confocal Microscopy*, Vol. 2 of *Handbook of Comprehensive Biophysics*, Elsevier, Amsterdam (2012).

[325] E. Luna, R. Hey, and A. Trampert, *Interface properties of (In,Ga)As/GaAs quantum wells grown by solid-phase epitaxy*, J. Vac. Sci. Technol. B **30**, 02B108 (2012).

[326] HAMAMATSU PHOTONICS K.K., Systems Division, *A guide to streak cameras*, http://www.hamamatsu.com/resources/pdf/sys/SHSS0006E_STREAK.pdf, Hamamatsu City, Japan (2008).

[327] D. V. O'Connor and D. Phillips, *Time-Correlated Single Photon Counting*, Academic Press, London (1984).

[328] A. S. Barker and M. Ilegems, *Infrared Lattice Vibrations and Free-Electron Dispersion in GaN*, Phys. Rev. B **7**, 743 (1973).

[329] V. Y. Davydov, Y. E. Kitaev, I. N. Goncharuk, A. N. Smirnov, J. Graul, O. Semchinova, D. Uffmann, M. B. Smirnov, A. P. Mirgorodsky, and R. A. Evarestov, *Phonon dispersion and Raman scattering in hexagonal GaN and AlN*, Phys. Rev. B **58**, 12899 (1998).

[330] J. Lee, E. S. Koteles, and M. O. Vassell, *Luminescence linewidths of excitons in GaAs quantum wells below 150 K*, Phys. Rev. B **33**, 5512 (1986).

[331] S. Rudin, T. L. Reinecke, and B. Segall, *Temperature-dependent exciton linewidths in semiconductors*, Phys. Rev. B **42**, 11218 (1990).

[332] G. Steude, B. K. Meyer, A. Göldner, A. Hoffmann, F. Bertram, J. Christen, H. Amano, and I. Akasaki, *Optical investigations of AlGaN on GaN epitaxial films*, Appl. Phys. Lett. **74**, 2456 (1999).

[333] J. Lähnemann, O. Brandt, C. Pfüller, T. Flissikowski, U. Jahn, E. Luna, M. Hanke, M. Knelangen, A. Trampert, and H. T. Grahn, *Coexistence of quantum-confined Stark effect and localized states in an (In,Ga)N/GaN nanowire heterostructure*, Phys. Rev. B **84**, 155303 (2011).

[334] A. Laubsch, M. Sabathil, J. Baur, M. Peter, and B. Hahn, *High-Power and High-Efficiency InGaN-Based Light Emitters*, IEEE Trans. Electron Devices **57**, 79 (2010).

[335] M. Peter, A. Laubsch, W. Bergbauer, T. Meyer, M. Sabathil, J. Baur, and B. Hahn, *New developments in green LEDs*, Phys. Status Solidi A **206**, 1125 (2009).

[336] J. Danhof, C. Vierheilig, U. T. Schwarz, T. Meyer, M. Peter, and B. Hahn, *Temperature-dependent photoluminescence measurements on a sub-micrometer length scale on green light emitting InGaN/GaN quantum wells*, Phys. Status Solidi B **248**, 1270 (2011).

[337] W. Liu, D. Zhao, D. Jiang, P. Chen, Z. Liu, J. Zhu, X. Li, F. Liang, J. Liu, L. Zhang, H. Yang, Y. Zhang, and G. Du, *Shockley–Read–Hall recombination and efficiency droop in InGaN/GaN multiple-quantum-well green light-emitting diodes*, J. Phys. D: Appl. Phys. **49**, 145104 (2016).

[338] S. Nakamura, M. Senoh, N. Iwasa, and S.-i. Nagahama, *High-Brightness InGaN Blue, Green and Yellow Light-Emitting Diodes with Quantum Well Structures*, Jpn. J. Appl. Phys. **34**, L797 (1995).

[339] T. Mukai, M. Yamada, and S. Nakamura, *Characteristics of InGaN-Based UV/Blue/Green/Amber/Red Light-Emitting Diodes*, Jpn. J. Appl. Phys. **38**, 3976 (1999).

[340] C. A. Hurni, A. David, M. J. Cich, R. I. Aldaz, B. Ellis, K. Huang, A. Tyagi, R. A. DeLille, M. D. Craven, F. M. Steranka, and M. R. Krames, *Bulk GaN flip-chip violet light-emitting diodes with optimized efficiency for high-power operation*, Appl. Phys. Lett. **106**, 031101 (2015).

[341] S. Nakamura, T. Mukai, and M. Senoh, *Candela-class high-brightness InGaN/AlGaN double-heterostructure blue-light-emitting diodes*, Appl. Phys. Lett. **64**, 1687 (1994).

[342] P. Pust, P. J. Schmidt, and W. Schnick, *A revolution in lighting*, Nat. Mater. **14**, 454 (2015).

[343] S. Nakamura, M. Senoh, S. Nagahama, N. Iwasa, T. Yamada, T. Matsushita, Y. Sug-

imoto, and H. Kiyoku, *Room-temperature continuous-wave operation of InGaN multi-quantum-well structure laser diodes*, Appl. Phys. Lett. **69**, 4056 (1996).

[344] E. Taylor, P. R. Edwards, and R. W. Martin, *Colorimetry and efficiency of white LEDs: Spectral width dependence*, Phys. Status Solidi A **209**, 461 (2012).

[345] Y.-H. Ra, R. Wang, S. Y. Woo, M. Djavid, S. M. Sadaf, J. Lee, G. A. Botton, and Z. Mi, *Full-Color Single Nanowire Pixels for Projection Displays*, Nano Lett. **16**, 4608 (2016).

[346] N. Bardsley, S. Bland, M. Hansen, L. Pattison, M. Pattison, K. Stober, and M. Yamada, *Solid-State Lighting R&D Plan*, http://energy.gov/sites/prod/files/2015/06/f22/ssl_rd-plan_may2015_0.pdf, U.S. Department of Energy, Office of Energy Efficiency and Renewable Energy, Washington (2015).

[347] K. A. Bulashevich, A. V. Kulik, and S. Y. Karpov, *Optimal ways of colour mixing for high-quality white-light LED sources*, Phys. Status Solidi A **212**, 914 (2015).

[348] C. Weisbuch, M. Piccardo, L. Martinelli, J. Iveland, J. Peretti, and J. S. Speck, *The efficiency challenge of nitride light-emitting diodes for lighting*, Phys. Status Solidi A **212**, 899 (2015).

[349] S. Fernández-Garrido, X. Kong, T. Gotschke, R. Calarco, L. Geelhaar, A. Trampert, and O. Brandt, *Spontaneous Nucleation and Growth of GaN Nanowires: The Fundamental Role of Crystal Polarity*, Nano Lett. **12**, 6119 (2012).

[350] O. Romanyuk, S. Fernández-Garrido, P. Jiříček, I. Bartoš, L. Geelhaar, O. Brandt, and T. Paskova, *Non-destructive assessment of the polarity of GaN nanowire ensembles using low-energy electron diffraction and x-ray photoelectron diffraction*, Appl. Phys. Lett. **106**, 021602 (2015).

[351] B. J. May, A. T. M. Sarwar Golam, and R. C. Myers, *Nanowire LEDs Grown Directly on Flexible Metal Foil*, Appl. Phys. Lett. **108**, 141103 (2016).

[352] G. Calabrese, P. Corfdir, G. Gao, C. Pfüller, A. Trampert, O. Brandt, L. Geelhaar, and S. Fernández-Garrido, *Molecular beam epitaxy of single crystalline GaN nanowires on a flexible Ti foil*, Appl. Phys. Lett. **108**, 202101 (2016).

[353] M. Musolino, A. Tahraoui, L. Geelhaar, F. Sacconi, F. Panetta, C. De Santi, M. Meneghini, and E. Zanoni, *Effect of Varying Three-Dimensional Strain on the Emission Properties of Light-Emitting Diodes Based on (In,Ga)N/GaN Nanowires*, Phys. Rev. Applied **7**, 044014 (2017).

[354] B. Janjua, T. K. Ng, C. Zhao, A. Prabaswara, G. B. Consiglio, D. Priante, C. Shen, R. T. Elafandy, D. H. Anjum, A. A. Alhamoud, A. A. Alatawi, Y. Yang, A. Y. Alyamani, M. M. El-Desouki, and B. S. Ooi, *True Yellow Light-Emitting Diodes as Phosphor for Tunable Color-Rendering Index Laser-Based White Light*, ACS Photonics **3**, 2089 (2016).

[355] M. Wölz, V. M. Kaganer, O. Brandt, L. Geelhaar, and H. Riechert, *Analyzing the growth of $In_xGa_{1-x}N$/GaN superlattices in self-induced GaN nanowires by x-ray diffraction*, Appl. Phys. Lett. **98**, 261907 (2011).

[356] M. Wölz, V. M. Kaganer, O. Brandt, L. Geelhaar, and H. Riechert, *Erratum: "Analyzing the growth of $In_xGa_{1-x}N$/GaN superlattices in self-induced GaN nanowires by x-ray diffraction" [Appl. Phys. Lett. 98, 261907 (2011)]*, Appl. Phys. Lett. **100**, 179902 (2012).

[357] C. Pfüller, M. Ramsteiner, O. Brandt, F. Grosse, A. Rathsfeld, G. Schmidt, L. Geelhaar, and H. Riechert, *Raman spectroscopy as a probe for the coupling of light into ensembles of sub-wavelength-sized nanowires*, Appl. Phys. Lett. **101**, 083104 (2012).

[358] K. C. Zeng, M. Smith, J. Y. Lin, and H. X. Jiang, *Collective effects of interface roughness and alloy disorder in $In_xGa_{1-x}N$/GaN multiple quantum wells*, Appl. Phys. Lett. **73**, 1724 (1998).

[359] M. Leroux, N. Grandjean, B. Beaumont, G. Nataf, F. Semond, J. Massies, and P. Gibart, *Temperature quenching of photoluminescence intensities in undoped and doped GaN*, J. Appl. Phys. **86**, 3721 (1999).

[360] D. Bimberg, M. Sondergeld, and E. Grobe, *Thermal Dissociation of Excitons Bounds to Neutral Acceptors in High-Purity GaAs*, Phys. Rev. B **4**, 3451 (1971).

[361] W. Guo, M. Zhang, A. Banerjee, and P. Bhattacharya, *Catalyst-free InGaN/GaN nanowire light emitting diodes grown on (001) silicon by molecular beam epitaxy*, Nano Lett. **10**, 3355 (2010).

[362] S. Hammersley, M. J. Kappers, F. C.-P. Massabuau, S.-L. Sahonta, P. Dawson, R. A. Oliver, and C. J. Humphreys, *Effects of quantum well growth temperature on the recombination efficiency of InGaN/GaN multiple quantum wells that emit in the green and blue spectral regions*, Appl. Phys. Lett. **107**, 132106 (2015).

[363] H. P. T. Nguyen, S. Zhang, K. Cui, X. Han, S. Fathololoumi, M. Couillard, G. A. Botton, and Z. Mi, *p-Type modulation doped InGaN/GaN dot-in-a-wire white-light-emitting diodes monolithically grown on Si(111)*, Nano Lett. **11**, 1919 (2011).

[364] M. A. Reshchikov, A. J. Olsen, M. F. Bishop, and T. McMullen, *Superlinear increase of photoluminescence with excitation intensity in Zn-doped GaN*, Phys. Rev. B **88**, 075204 (2013).

[365] M. F. Schubert, J. Xu, Q. Dai, F. W. Mont, J. K. Kim, and E. F. Schubert, *On resonant optical excitation and carrier escape in GaInN/GaN quantum wells*, Appl. Phys. Lett. **94**, 081114 (2009).

[366] C. Hauswald, P. Corfdir, J. K. Zettler, V. M. Kaganer, K. K. Sabelfeld, S. Fernández-Garrido, T. Flissikowski, V. Consonni, T. Gotschke, H. T. Grahn, L. Geelhaar, and O. Brandt, *Origin of the nonradiative decay of bound excitons in GaN nanowires*, Phys. Rev. B **90**, 165304 (2014).

[367] T. Langer, A. Kruse, F. A. Ketzer, A. Schwiegel, L. Hoffmann, H. Jönen, H. Bremers, U. Rossow, and A. Hangleiter, *Origin of the "green gap": Increasing nonradiative recombination in indium-rich GaInN/GaN quantum well structures*, Phys. Status Solidi C **8**, 2170 (2011).

[368] S. Schulz, D. P. Tanner, E. P. O'Reilly, M. A. Caro, T. L. Martin, P. A. J. Bagot, M. P. Moody, F. Tang, J. T. Griffiths, F. Oehler, M. J. Kappers, R. A. Oliver, C. J. Humphreys, D. Sutherland, M. J. Davies, and P. Dawson, *Structural, electronic, and optical properties of* m*-plane InGaN/GaN quantum wells: Insights from experiment and atomistic theory*, Phys. Rev. B **92**, 235419 (2015).

[369] H. Murotani, Y. Yamada, Y. Honda, and H. Amano, *Excitation density dependence of radiative and nonradiative recombination lifetimes in InGaN/GaN multiple quantum wells*,

Phys. Status Solidi B **252**, 940 (2015).

[370] M. Pophristic, F. H. Long, C. Tran, I. T. Ferguson, and R. F. Karlicek, *Time-resolved photoluminescence measurements of InGaN light-emitting diodes*, Appl. Phys. Lett. **73**, 3550 (1998).

[371] R. Aleksiejūnas, K. Gelžinytė, S. Nargelas, K. Jarašiūnas, M. Vengris, E. A. Armour, D. P. Byrnes, R. A. Arif, S. M. Lee, and G. D. Papasouliotis, *Diffusion-driven and excitation-dependent recombination rate in blue InGaN/GaN quantum well structures*, Appl. Phys. Lett. **104**, 022114 (2014).

[372] P. Waltereit, O. Brandt, J. Ringling, and K. H. Ploog, *Electrostatic fields and compositional fluctuations in (In,Ga)N/GaN multiple quantum wells grown by plasma-assisted molecular-beam epitaxy*, Phys. Rev. B **64**, 245305 (2001).

[373] D. G. Thomas, J. J. Hopfield, and W. M. Augustyniak, *Kinetics of Radiative Recombination at Randomly Distributed Donors and Acceptors*, Phys. Rev. **140**, A202 (1965).

[374] P. H. Sher, J. M. Smith, P. A. Dalgarno, R. J. Warburton, X. Chen, P. J. Dobson, S. M. Daniels, N. L. Pickett, and P. O'Brien, *Power law carrier dynamics in semiconductor nanocrystals at nanosecond timescales*, Appl. Phys. Lett. **92**, 101111 (2008).

[375] V. Cardin, L. I. Dion-Bertrand, P. Grégoire, H. P. T. Nguyen, M. Sakowicz, Z. Mi, C. Silva, and R. Leonelli, *Recombination dynamics in InGaN/GaN nanowire heterostructures on Si(111)*, Nanotechnology **24**, 045702 (2013).

[376] A. K. Jonscher and A. de Polignac, *The time dependence of luminescence in solids*, J. Phys. C: Solid State Phys. **17**, 6493 (1984).

[377] C. Tsang and R. A. Street, *Recombination in plasma-deposited amorphous Si:H. Luminescence decay*, Phys. Rev. B **19**, 3027 (1979).

[378] J. Noolandi, K. M. Hong, and R. A. Street, *A geminate recombination model for photoluminescence decay in plasma-deposited amorphous Si:H*, Solid State Commun. **34**, 45 (1980).

[379] K. M. Hong, J. Noolandi, and R. A. Street, *Theory of radiative recombination by diffusion and tunneling in amorphous Si:H*, Phys. Rev. B **23**, 2967 (1981).

[380] A. B. Doktorov and E. Kotomin, *Theory of tunneling recombination of defects stimulated by their motion I. General formalism*, Phys. Status Solidi B **114**, 9 (1982).

[381] C. Gourdon and P. Lavallard, *Exciton Transfer between Localized States in $CdS_{1-x}Se_x$ Alloys*, Phys. Status Solidi B **153**, 641 (1989).

[382] X. Chen, B. Henderson, and K. P. O'Donnell, *Luminescence decay in disordered low-dimensional semiconductors*, Appl. Phys. Lett. **60**, 2672 (1992).

[383] D. J. Huntley, *An explanation of the power-law decay of luminescence*, J. Phys.: Condens. Matter **18**, 1359 (2006).

[384] K. Seki, M. Wojcik, and M. Tachiya, *Dispersive-diffusion-controlled distance-dependent recombination in amorphous semiconductors*, J. Chem. Phys. **124**, 044702 (2006).

[385] M. J. Galtrey, R. A. Oliver, M. J. Kappers, C. J. Humphreys, D. J. Stokes, P. H. Clifton, and A. Cerezo, *Three-dimensional atom probe studies of an $In_xGa_{1-x}N$/GaN multiple*

quantum well structure: Assessment of possible indium clustering, Appl. Phys. Lett. **90**, 061903 (2007).

[386] M. A. Caro, S. Schulz, and E. P. O'Reilly, *Theory of local electric polarization and its relation to internal strain: Impact on polarization potential and electronic properties of group-III nitrides*, Phys. Rev. B **88**, 214103 (2013).

[387] R. K. Ahrenkiel, *Minority Carriers In III-V Semiconductors: Physics and Applications*, Vol. 39 of *Semiconductors and Semimetals*, Academic Press, New York (1993).

[388] M. Smoluchowski, *Drei Vorträge über Diffusion, Brownsche Molekularbewegung und Koagulation von Kolloidteilchen*, Phys. Z. **17**, 557, ibid. 585 (1916).

[389] O. Tange, *Gnu parallel - the command-line power tool*, ;login: The USENIX Magazine **36**, 42 (2011).

[390] E. M. Conwell, *Impurity Band Conduction in Germanium and Silicon*, Phys. Rev. **103**, 51 (1956).

[391] N. F. Mott, *ON THE TRANSITION TO METALLIC CONDUCTION IN SEMICONDUCTORS*, Can. J. Phys. **34**, 1356 (1956).

[392] M. Kuik, G.-J. A. H. Wetzelaer, H. T. Nicolai, N. I. Craciun, D. M. De Leeuw, and P. W. M. Blom, *25th Anniversary Article: Charge Transport and Recombination in Polymer Light-Emitting Diodes*, Adv. Mater. **26**, 512 (2014).

[393] M. Agostini *et al.* (Borexino Collaboration), *Test of Electric Charge Conservation with Borexino*, Phys. Rev. Lett. **115**, 231802 (2015).

[394] K. K. Sabelfeld, private communication, 13/02/2015.

[395] Y. Arakawa, H. Sakaki, M. Nishioka, J. Yoshino, and T. Kamiya, *Recombination lifetime of carriers in GaAs-GaAlAs quantum wells near room temperature*, Appl. Phys. Lett. **46**, 519 (1985).

[396] J. Christen and D. Bimberg, *Line shapes of intersubband and excitonic recombination in quantum wells: Influence of final-state interaction, statistical broadening, and momentum conservation*, Phys. Rev. B **42**, 7213 (1990).

[397] L. E. Oliveira and M. de Dios-Leyva, *Radiative lifetimes, quasi-Fermi-levels, and carrier densities in GaAs-(Ga,Al)As quantum-well photoluminescence under steady-state excitation conditions*, Phys. Rev. B **48**, 15092 (1993).

[398] O. Brandt, K. Kanamoto, M. Gotoda, T. Isu, and N. Tsukada, *Recombination processes and photoluminescence intensity in quantum wells under steady-state and transient conditions*, Phys. Rev. B **51**, 7029 (1995).

[399] C. Zhao, T. K. Ng, N. Wei, A. Prabaswara, M. S. Alias, B. Janjua, C. Shen, and B. S. Ooi, *Facile Formation of High-Quality InGaN/GaN Quantum-Disks-in-Nanowires on Bulk-Metal Substrates for High-Power Light-Emitters*, Nano Lett. **16**, 1056 (2016).

[400] C. Zhao, T. K. Ng, R. T. ElAfandy, A. Prabaswara, G. B. Consiglio, I. A. Ajia, I. S. Roqan, B. Janjua, C. Shen, J. Eid, A. Y. Alyamani, M. M. El-Desouki, and B. S. Ooi, *Droop-Free, Reliable, and High-Power InGaN/GaN Nanowire Light-Emitting Diodes for Monolithic Metal-Optoelectronics*, Nano Lett. **16**, 4616 (2016).

[401] M. Musolino, *Growth, fabrication, and investigation of light-emitting diodes based on GaN nanowires*, PhD thesis, Humboldt-Universität zu Berlin (2015).

[402] S. Fernández-Garrido, J. Lähnemann, C. Hauswald, M. Korytov, M. Albrecht, C. Chèze, C. Skierbiszewski, and O. Brandt, *Comparison of the Luminous Efficiencies of Ga- and N-Polar $In_xGa_{1-x}N/In_yGa_{1-y}N$ Quantum Wells Grown by Plasma-Assisted Molecular Beam Epitaxy*, Phys. Rev. Applied **6**, 034017 (2016).

[403] E. C. Young, N. Grandjean, T. E. Mates, and J. S. Speck, *Calcium impurity as a source of non-radiative recombination in (In,Ga)N layers grown by molecular beam epitaxy*, Appl. Phys. Lett. **109**, 212103 (2016).

[404] J.-X. Shen, D. Wickramaratne, C. E. Dreyer, A. Alkauskas, E. Young, J. S. Speck, and C. G. Van de Walle, *Calcium as a nonradiative recombination center in InGaN*, Appl. Phys. Express **10**, 021001 (2017).

[405] J. Cho, E. F. Schubert, and J. K. Kim, *Efficiency droop in light-emitting diodes: Challenges and countermeasures*, Laser Photon. Rev. **7**, 4081 (2013).

[406] P. Waltereit, O. Brandt, A. Trampert, H. T. Grahn, J. Menniger, M. Ramsteiner, M. Reiche, and K. H. Ploog, *Nitride semiconductors free of electrostatic fields for efficient white light-emitting diodes*, Nature **406**, 865 (2000).

[407] P. Waltereit, O. Brandt, M. Ramsteiner, R. Uecker, P. Reiche, and K. H. Ploog, *Growth of M-plane GaN*$(1\bar{1}00)$ *on* γ*-LiAlO*$_2$ *(100)*, J. Cryst. Growth **218**, 143 (2000).

[408] T. Onuma, H. Amaike, M. Kubota, K. Okamoto, H. Ohta, J. Ichihara, H. Takasu, and S. F. Chichibu, *Quantum-confined Stark effects in the m-plane $In_{0.15}Ga_{0.85}N$/GaN multiple quantum well blue light-emitting diode fabricated on low defect density freestanding GaN substrate*, Appl. Phys. Lett. **91**, 181903 (2007).

[409] V. Liuolia, S. Marcinkevičius, Y.-D. Lin, H. Ohta, S. P. DenBaars, and S. Nakamura, *Dynamics of polarized photoluminescence in m-plane InGaN/GaN quantum wells*, J. Appl. Phys. **108**, 023101 (2010).

[410] M. Shahmohammadi, J.-D. Ganière, H. Zhang, R. Ciechonski, G. Vescovi, O. Kryliouk, M. Tchernycheva, and G. Jacopin, *Excitonic Diffusion in InGaN/GaN Core–Shell Nanowires*, Nano Lett. **16**, 243 (2016).

[411] W. Liu, R. Butté, A. Dussaigne, N. Grandjean, B. Deveaud, and G. Jacopin, *Carrier-density-dependent recombination dynamics of excitons and electron-hole plasma in m-plane InGaN/GaN quantum wells*, Phys. Rev. B **94**, 195411 (2016).

[412] T. J. Puchtler, T. Wang, C. X. Ren, F. Tang, R. A. Oliver, R. A. Taylor, and T. Zhu, *Ultrafast, Polarized, Single-Photon Emission from m-Plane InGaN Quantum Dots on GaN Nanowires*, Nano Lett. **16**, 7779 (2016).

[413] T. Zhu, D. Gachet, F. Tang, W. Y. Fu, F. Oehler, M. J. Kappers, P. Dawson, C. J. Humphreys, and R. A. Oliver, *Local carrier recombination and associated dynamics in m-plane InGaN/GaN quantum wells probed by picosecond cathodoluminescence*, Appl. Phys. Lett. **109**, 232103 (2016).

[414] R. Ivanov, S. Marcinkevičius, T. K. Uždavinys, L. Y. Kuritzky, S. Nakamura, and J. S. Speck, *Scanning near-field microscopy of carrier lifetimes in m-plane InGaN quantum*

wells, Appl. Phys. Lett. **110**, 031109 (2017).

[415] K. Motoki, T. Okahisa, S. Nakahata, N. Matsumoto, H. Kimura, H. Kasai, K. Takemoto, K. Uematsu, M. Ueno, Y. Kumagai, A. Koukitu, and H. Seki, *Growth and characterization of freestanding GaN substrates*, J. Cryst. Growth **237-239**, 912 (2002).

[416] K. Fujito, K. Kiyomi, T. Mochizuki, H. Oota, H. Namita, S. Nagao, and I. Fujimura, *High-quality nonpolar m-plane GaN substrates grown by HVPE*, Phys. Status Solidi A **205**, 1056 (2008).

[417] A. Chakraborty, B. A. Haskell, S. Keller, J. S. Speck, S. P. Denbaars, S. Nakamura, and U. K. Mishra, *Demonstration of nonpolar m-plane InGaN/GaN light-emitting diodes on free-standing m-plane GaN substrates*, Jpn. J. Appl. Phys. **44**, L173 (2005).

[418] K. Okamoto, H. Ohta, D. Nakagawa, M. Sonobe, J. Ichihara, and H. Takasu, *Dislocation-Free m-Plane InGaN/GaN Light-Emitting Diodes on m-Plane GaN Single Crystals*, Jpn. J. Appl. Phys. **45**, L1197 (2006).

[419] M. C. Schmidt, K.-C. Kim, R. M. Farrell, D. F. Feezell, D. A. Cohen, M. Saito, K. Fujito, J. S. Speck, S. P. DenBaars, and S. Nakamura, *Demonstration of Nonpolar m-Plane InGaN/GaN Laser Diodes*, Jpn. J. Appl. Phys. **46**, L190 (2007).

[420] D. Sutherland, T. Zhu, J. T. Griffiths, F. Tang, P. Dawson, D. Kundys, F. Oehler, M. J. Kappers, C. J. Humphreys, and R. A. Oliver, *Optical studies of non-polar m-plane ($1\bar{1}00$) InGaN/GaN multi-quantum wells grown on freestanding bulk GaN*, Phys. Status Solidi B **252**, 965 (2015).

[421] T. Langer, M. Klisch, F. Alexej Ketzer, H. Jünen, H. Bremers, U. Rossow, T. Meisch, F. Scholz, and A. Hangleiter, *Radiative and nonradiative recombination mechanisms in nonpolar and semipolar GaInN/GaN quantum wells*, Phys. Status Solidi B **253**, 133 (2016).

[422] P. Horenburg, E. R. Buß, U. Rossow, H. Bremers, F. A. Ketzer, and A. Hangleiter, *Strain dependence of In incorporation in m-oriented GaInN/GaN multi quantum well structures*, Appl. Phys. Lett. **108**, 102105 (2016).

[423] B. Neubert, F. Habel, P. Brückner, F. Scholz, M. Schirra, M. Feneberg, K. Thonke, T. Riemann, J. Christen, M. Beer, J. Zweck, G. Moutchnik, and M. Jetter, *Investigations on local Ga and In incorporation of GaInN quantum wells on facets of selectively grown GaN stripes*, Phys. Status Solidi C **3**, 1587 (2006).

[424] K. Y. Lai, T. Paskova, V. D. Wheeler, T. Y. Chung, J. A. Grenko, M. A. L. Johnson, K. Udwary, E. A. Preble, and K. R. Evans, *Indium incorporation in InGaN/GaN quantum wells grown on m-plane GaN substrate and c-plane sapphire*, Phys. Status Solidi A **209**, 559 (2012).

[425] Y. Zhao, Q. Yan, C.-Y. Huang, S.-C. Huang, P. Shan Hsu, S. Tanaka, C.-C. Pan, Y. Kawaguchi, K. Fujito, C. G. Van de Walle, J. S. Speck, S. P. DenBaars, S. Nakamura, and D. Feezell, *Indium incorporation and emission properties of nonpolar and semipolar InGaN quantum wells*, Appl. Phys. Lett. **100**, 201108 (2012).

[426] Y. Wang, R. Shimma, T. Yamamoto, H. Hayashi, K. I. Shiohama, K. Kurihara, R. Hasegawa, and K. Ohkawa, *The effect of plane orientation on indium incorporation into InGaN/GaN quantum wells fabricated by MOVPE*, J. Cryst. Growth **416**, 164

(2015).

[427] H. Jönen, U. Rossow, H. Bremers, L. Hoffmann, M. Brendel, A. D. Dräger, S. Metzner, F. Bertram, J. Christen, S. Schwaiger, F. Scholz, J. Thalmair, J. Zweck, and A. Hangleiter, *Indium incorporation in GaInN/GaN quantum well structures on polar and nonpolar surfaces*, Phys. Status Solidi B **248**, 600 (2011).

[428] H. Jönen, H. Bremers, U. Rossow, T. Langer, A. Kruse, L. Hoffmann, J. Thalmair, J. Zweck, S. Schwaiger, F. Scholz, and A. Hangleiter, *Analysis of indium incorporation in non- and semipolar GaInN QW structures: comparing x-ray diffraction and optical properties*, Semicond. Sci. Technol. **27**, 024013 (2012).

[429] T. Wernicke, L. Schade, C. Netzel, J. Rass, V. Hoffmann, S. Ploch, A. Knauer, M. Weyers, U. Schwarz, and M. Kneissl, *Indium incorporation and emission wavelength of polar, nonpolar and semipolar InGaN quantum wells*, Semicond. Sci. Technol. **27**, 024014 (2012).

[430] R. Bhat and G. M. Guryanov, *Experimental study of the orientation dependence of indium incorporation in GaInN*, J. Cryst. Growth **433**, 7 (2016).

[431] M. J. Davies, P. Dawson, S. Hammersley, T. Zhu, M. J. Kappers, C. J. Humphreys, and R. A. Oliver, *Comparative studies of efficiency droop in polar and non-polar InGaN quantum wells*, Appl. Phys. Lett. **108**, 252101 (2016).

[432] M. J. Cich, R. I. Aldaz, A. Chakraborty, A. David, M. J. Grundmann, A. Tyagi, M. Zhang, F. M. Steranka, and M. R. Krames, *Bulk GaN based violet light-emitting diodes with high efficiency at very high current density*, Appl. Phys. Lett. **101**, 223509 (2012).

[433] X. Wang, S. Li, M. S. Mohajerani, J. Ledig, H.-H. Wehmann, M. Mandl, M. Strassburg, U. Steegmüller, U. Jahn, J. Lähnemann, H. Riechert, I. Griffiths, D. Cherns, and A. Waag, *Continuous-Flow MOVPE of Ga-Polar GaN Column Arrays and Core-Shell LED Structures*, Cryst. Growth Des. **13**, 3475 (2013).

[434] J. Ledig, X. Wang, S. Fündling, H. Schuhmann, M. Seibt, U. Jahn, H.-H. Wehmann, and A. Waag, *Characterization of the internal properties of InGaN/GaN core-shell LEDs*, Phys. Status Solidi A **8**, 11 (2015).

[435] Y.-H. Ra, R. Navamathavan, J.-H. Park, and C.-R. Lee, *Coaxial $In_xGa_{1-x}N$/GaN Multiple Quantum Well Nanowire Arrays on Si(111) Substrate for High-Performance Light-Emitting Diodes*, Nano Lett. **13**, 3506 (2013).

[436] J. J. Wierer Jr, Q. Li, D. D. Koleske, S. R. Lee, and G. T. Wang, *III-nitride core-shell nanowire arrayed solar cells*, Nanotechnology **23**, 194007 (2012).

[437] S. L. Howell, S. Padalkar, K. Yoon, Q. Li, D. D. Koleske, J. J. Wierer, G. T. Wang, and L. J. Lauhon, *Spatial Mapping of Efficiency of GaN/InGaN Nanowire Array Solar Cells Using Scanning Photocurrent Microscopy*, Nano Lett. **13**, 5123 (2013).

[438] J. D. Eshelby, *Screw Dislocations in Thin Rods*, J. Appl. Phys. **24**, 176 (1953).

[439] T. Schimpke, M. Mandl, I. Stoll, B. Pohl-Klein, D. Bichler, F. Zwaschka, J. Strube-Knyrim, B. Huckenbeck, B. Max, M. Müller, P. Veit, F. Bertram, J. Christen, J. Hartmann, A. Waag, H.-J. Lugauer, and M. Strassburg, *Phosphor-converted white light from*

blue-emitting InGaN microrod LEDs, Phys. Status Solidi A **213**, 1577 (2016).

[440] S. Albert, A. Bengoechea-Encabo, J. Ledig, T. Schimpke, M. A. Sánchez-Garcia, M. Strassburg, A. Waag, and E. Calleja, *Demonstration of (In,Ga)N/GaN Core–Shell Micro Light-Emitting Diodes Grown by Molecular Beam Epitaxy on Ordered MOVPE GaN Pillars*, Cryst. Growth Des. **15**, 3661 (2015).

[441] S. Li and A. Waag, *GaN based nanorods for solid state lighting*, J. Appl. Phys. **111**, 071101 (2012).

[442] H. Sekiguchi, K. Kishino, and A. Kikuchi, *Emission color control from blue to red with nanocolumn diameter of InGaN/GaN nanocolumn arrays grown on same substrate*, Appl. Phys. Lett. **96**, 231104 (2010).

[443] glō® technology, http://www.glo.se/technology.html, 10/03/2017.

[444] C. Mounir, T. Schimpke, G. Rossbach, A. Avramescu, M. Strassburg, and U. T. Schwarz, *Optical properties and internal quantum efficiency of InGaN/GaN core-shell microrods for solid state lighting*, J. Appl. Phys. **120**, 155702 (2016).

[445] C. Mounir, T. Schimpke, G. Rossbach, A. Avramescu, M. Strassburg, and U. T. Schwarz, *Polarization-resolved micro-photoluminescence investigation of InGaN/GaN core-shell microrods*, J. Appl. Phys. **121**, 025701 (2017).

[446] J. R. Riley, S. Padalkar, Q. Li, P. Lu, D. D. Koleske, J. J. Wierer, G. T. Wang, and L. J. Lauhon, *Three-Dimensional Mapping of Quantum Wells in a GaN/InGaN Core–Shell Nanowire Light-Emitting Diode Array*, Nano Lett. **13**, 4317 (2013).

[447] M. Tchernycheva, P. Lavenus, H. Zhang, A. V. Babichev, G. Jacopin, M. Shahmohammadi, F. H. Julien, R. Ciechonski, G. Vescovi, and O. Kryliouk, *InGaN/GaN Core–Shell Single Nanowire Light Emitting Diodes with Graphene-Based P-Contact*, Nano Lett. **14**, 2456 (2014).

[448] M. Müller, P. Veit, F. F. Krause, T. Schimpke, S. Metzner, F. Bertram, T. Mehrtens, K. Müller-Caspary, A. Avramescu, M. Strassburg, A. Rosenauer, and J. Christen, *Nanoscopic Insights into InGaN/GaN Core–Shell Nanorods: Structure, Composition, and Luminescence*, Nano Lett. **16**, 5340 (2016).

[449] T. Krause, M. Hanke, Z. Cheng, M. Niehle, A. Trampert, M. Rosenthal, M. Burghammer, J. Ledig, J. Hartmann, H. Zhou, H.-H. Wehmann, and A. Waag, *Nanofocus x-ray diffraction and cathodoluminescence investigations into individual core–shell (In,Ga)N/GaN rod light-emitting diodes*, Nanotechnology **27**, 325707 (2016).

[450] T. Krause, M. Hanke, L. Nicolai, Z. Cheng, M. Niehle, A. Trampert, M. Kahnt, G. Falkenberg, C. G. Schroer, J. Hartmann, H. Zhou, H.-H. Wehmann, and A. Waag, *Structure and Composition of Isolated Core-Shell (In,Ga)N/GaN Rods Based on Nanofocus X-Ray Diffraction and Scanning Transmission Electron Microscopy*, Phys. Rev. Applied **7**, 024033 (2017).

[451] P. Dawson, S. Schulz, R. A. Oliver, M. J. Kappers, and C. J. Humphreys, *The nature of carrier localisation in polar and nonpolar InGaN/GaN quantum wells*, J. Appl. Phys. **119**, 181505 (2016).

[452] D. P. Tanner, M. A. Caro, E. P. O'Reilly, and S. Schulz, *Atomistic analysis of the*

electronic structure of m-plane InGaN/GaN quantum wells: Carrier localization effects in ground and excited states due to random alloy fluctuations, Phys. Status Solidi B **253**, 853 (2016).

[453] D. S. P. Tanner, M. A. Caro, E. P. O'Reilly, and S. Schulz, *Random alloy fluctuations and structural inhomogeneities in c-plane $In_xGa_{1-x}N$ quantum wells: theory of ground and excited electron and hole states*, RSC Adv. **6**, 64513 (2016).

[454] J. A. Kash, *Exciton tunneling inhibited by disorder in $GaAs_{1-x}P_x$:N*, Phys. Rev. B **29**, 7069 (1984).

[455] A. Müller and M. Grundmann, *Tunneling dynamics of excitons in random semiconductor alloys*, Phys. Rev. B **87**, 035134 (2013).

[456] O. Rubel, S. D. Baranovskii, K. Hantke, J. D. Heber, J. Koch, P. Thomas, J. M. Marshall, W. Stolz, and W. W. Rühle, *On the theoretical description of photoluminescence in disordered quantum structures*, J. Optoelectron. Adv. M. **7**, 115 (2005).

[457] Y. J. Wang, S. J. Xu, D. G. Zhao, J. J. Zhu, H. Yang, X. D. Shan, and D. P. Yu, *Non-exponential photoluminescence decay dynamics of localized carriers in disordered InGaN/GaN quantum wells: the role of localization length.*, Opt. Express **14**, 13151 (2006).

[458] U. Jahn, O. Brandt, E. Luna, X. Sun, H. Wang, D. S. Jiang, L. F. Bian, and H. Yang, *Carrier capture by threading dislocations in (In,Ga)N/GaN heteroepitaxial layers*, Phys. Rev. B **81**, 125314 (2010).

[459] G. Orsal, Y. El Gmili, N. Fressengeas, J. Streque, R. Djerboub, T. Moudakir, S. Sundaram, A. Ougazzaden, and J. Salvestrini, *Bandgap energy bowing parameter of strained and relaxed InGaN layers*, Opt. Mater. Express **4**, 1030 (2014).

[460] M. Funato and Y. Kawakami, *Excitonic properties of polar, semipolar, and nonpolar InGaNGaN strained quantum wells with potential fluctuations*, J. Appl. Phys. **103**, 093501 (2008).

[461] S. F. Chichibu, T. Azuhata, T. Sota, T. Mukai, and S. Nakamura, *Localized quantum well excitons in InGaN single-quantum-well amber light-emitting diodes*, J. Appl. Phys. **88**, 5153 (2000).

[462] Y. D. Jho, J. S. Yahng, E. Oh, and D. S. Kim, *Measurement of piezoelectric field and tunneling times in strongly biased InGan/GaN quantum wells*, Appl. Phys. Lett. **79**, 1130 (2001).

[463] Y. D. Jho, J. S. Yahng, E. Oh, and D. S. Kim, *Field-dependent carrier decay dynamics in strained $In_xGa_{1-x}N$/GaN quantum wells*, Phys. Rev. B **66**, 035334 (2002).

[464] M. Sabathil, A. Laubsch, and N. Linder, *Self-consistent modeling of resonant PL in InGaN SQW LED-structure*, Proc. SPIE **6486**, 64860V (2007).

[465] A. Laubsch, M. Sabathil, G. Bruederl, J. Wagner, M. Strassburg, E. Baur, H. Braun, U. T. Schwarz, A. Lell, S. Lutgen, N. Linder, R. Oberschmid, and B. Hahn, *Measurement of the internal quantum efficiency of InGaN quantum wells*, Proc. SPIE **6486**, 64860J (2007).

[466] W. Götz, N. M. Johnson, C. Chen, H. Liu, C. Kuo, and W. Imler, *Activation energies of Si donors in GaN*, Appl. Phys. Lett. **68**, 3144 (1996).

[467] P. Pampili and P. J. Parbrook, *Doping of III-nitride materials*, Mater. Sci. Semicond. Process. **62**, 180 (2017).

[468] L. Zhang, W.-S. Tan, S. Westwater, A. Pujol, A. Pinos, S. Mezouari, K. Stribley, J. Whiteman, J. Shannon, and K. Strickland, *High Brightness GaN-on-Si Based Blue LEDs Grown on 150 mm Si Substrates Using Thin Buffer Layer Technology*, IEEE J. Electron Devices Soc. **3**, 457 (2015).

[469] D. A. B. Miller, D. S. Chemla, T. C. Damen, A. C. Gossard, W. Wiegmann, T. H. Wood, and C. A. Burrus, *Band-Edge Electroabsorption in Quantum Well Structures: The Quantum-Confined Stark Effect*, Phys. Rev. Lett. **53**, 2173 (1984).

[470] D. A. B. Miller, D. S. Chemla, T. C. Damen, A. C. Gossard, W. Wiegmann, T. H. Wood, and C. A. Burrus, *Electric field dependence of optical absorption near the band gap of quantum-well structures*, Phys. Rev. B **32**, 1043 (1985).

[471] M. F. Schubert, Q. Dai, J. Xu, J. K. Kim, and E. F. Schubert, *Electroluminescence induced by photoluminescence excitation in GaInN/GaN light-emitting diodes*, Appl. Phys. Lett. **95**, 191105 (2009).

[472] T. Onuma, S. F. Chichibu, T. Aoyama, K. Nakajima, P. Ahmet, T. Azuhata, T. Chikyow, T. Sota, S.-i. Nagahama, and T. Mukai, *Influence of Internal Electric Field on the Recombination Dynamics of Localized Excitons in an InGaN Double-Quantum-Well Laser Diode Wafer Operated at 450 nm*, Jpn. J. Appl. Phys. **42**, 7276 (2003).

[473] R. M. Hill, *Hopping conduction in amorphous solids*, Philos. Mag. **24**, 1307 (1971).

[474] R. M. Hill, *Poole-Frenkel conduction in amorphous solids*, Philos. Mag. **23**, 59 (1971).

[475] W. Dumke, P. Miller, and R. Haering, *Theory of polar phonon assisted tunneling*, J. Phys. Chem. Solids **23**, 501 (1962).

[476] G. Vincent, A. Chantre, and D. Bois, *Electric field effect on the thermal emission of traps in semiconductor junctions*, J. Appl. Phys. **50**, 5484 (1979).

[477] E. Burstein and C. Weisbuch, *Confined Electrons and Photons: New Physics and Applications*, Vol. 340 of *NATO ASI Series*, Springer, New York (1995).

[478] H. Schneider and K. v. Klitzing, *Thermionic emission and Gaussian transport of holes in a GaAs/$Al_xGa_{1-x}As$ multiple-quantum-well structure*, Phys. Rev. B **38**, 6160 (1988).

[479] C.-K. Sun, F. Vallée, S. Keller, J. E. Bowers, and S. P. DenBaars, *Femtosecond studies of carrier dynamics in InGaN*, Appl. Phys. Lett. **70**, 2004 (1997).

[480] Ü. Özgür, M. J. Bergmann, H. C. Casey, H. O. Everitt, A. C. Abare, S. Keller, and S. P. DenBaars, *Ultrafast optical characterization of carrier capture times in $In_xGa_{1-x}N$ multiple quantum wells*, Appl. Phys. Lett. **77**, 109 (2000).

[481] M. Meneghini, N. Trivellin, M. Pavesi, M. Manfredi, U. Zehnder, B. Hahn, G. Meneghesso, and E. Zanoni, *Leakage current and reverse-bias luminescence in InGaN-based light-emitting diodes*, Appl. Phys. Lett. **95**, 173507 (2009).

[482] L. D. Landau and E. M. Lifshitz, *Quantum Mechanics Non-relativistic Theory*, Pergamon Press Ltd., Oxford, 2nd edition (1965).

[483] R. H. Fowler and L. Nordheim, *Electron Emission in Intense Electric Fields*, Proc. R.

Soc. A **119**, 173 (1928).

[484] K. Köhler, H.-J. Polland, L. Schultheis, and C. W. Tu, *Photoluminescence of two-dimensional excitons in an electric field: Lifetime enhancement and field ionization in GaAs quantum wells*, Phys. Rev. B **38**, 5496 (1988).

[485] J. R. Oppenheimer, *Three Notes on the Quantum Theory of Aperiodic Effects*, Phys. Rev. **31**, 66 (1928).

[486] E. Martinet, E. Rosencher, F. Chevoir, J. Nagle, and P. Bois, *Direct determination of the electron-tunneling escape time from a GaAs/Al_xGa_{1-x}As quantum well by transient-capacitance spectroscopy*, Phys. Rev. B **44**, 3157 (1991).

[487] E. Bellotti, F. Bertazzi, and M. Goano, *Alloy scattering in AlGaN and InGaN: A numerical study*, J. Appl. Phys. **101**, 123706 (2007).

[488] S. Gökden, R. Tülek, A. Teke, J. H. Leach, Q. Fan, J. Xie, Ü. Özgür, H. Morkoç, S. B. Lisesivdin, and E. Özbay, *Mobility limiting scattering mechanisms in nitride-based two-dimensional heterostructures with the InGaN channel*, Semicond. Sci. Technol. **25**, 045024 (2010).

[489] F. Feix, T. Flissikowski, C. Chèze, R. Calarco, H. T. Grahn, and O. Brandt, *Individual electron and hole localization in submonolayer InN quantum sheets embedded in GaN*, Appl. Phys. Lett. **109**, 042104 (2016).

[490] S. Izumi, N. Fuutagawa, T. Hamaguchi, M. Murayama, M. Kuramoto, and H. Narui, *Room-temperature continuous-wave operation of GaN-based vertical-cavity surface-emitting lasers fabricated using epitaxial lateral overgrowth*, Appl. Phys. Express **8**, 062702 (2015).

[491] W. W. Chow, A. F. Wright, A. Girndt, F. Jahnke, and S. W. Koch, *Microscopic theory of gain for an InGaN/AlGaN quantum well laser*, Appl. Phys. Lett. **71**, 2608 (1997).

[492] B. Witzigmann, V. Laino, M. Luisier, U. T. Schwarz, G. Feicht, W. Wegscheider, K. Engl, M. Furitsch, A. Leber, A. Lell, and V. Härle, *Microscopic analysis of optical gain in InGaN/GaN quantum wells*, Appl. Phys. Lett. **88**, 021104 (2006).

[493] M. E. Lin, F. Y. Huang, and H. Morkoç, *Nonalloyed ohmic contacts on GaN using InN/GaN short-period superlattices*, Appl. Phys. Lett. **64**, 2557 (1994).

[494] P. Ruterana and F. Deniel, *Observation of ordering and phase separation in $In_xGa_{1-x}N$ layers*, Mater. Sci. Eng. B **59**, 186 (1999).

[495] H. K. Cho, D. C. Kim, B. H. Kong, K. H. Lee, J. T. Oh, S. Kim, D. J. Kim, J. W. Kim, and S. K. Hong, *Nanostructure formation and emission characterization of blue emission InN/GaN quantum well with thin InN well layers*, J. Cryst. Growth **281**, 349 (2005).

[496] E. Dimakis, A. Yu. Nikiforov, C. Thomidis, L. Zhou, D. J. Smith, J. Abell, C.-K. Kao, and T. D. Moustakas, *Growth and properties of near-UV light emitting diodes based on InN/GaN quantum wells*, Phys. Status Solidi A **205**, 1070 (2008).

[497] K. Kusakabe and A. Yoshikawa, *III-Nitride Semiconductor Optoelectronics*, Vol. 96 of *Semiconductors and Semimetals*, Elsevier Science, New York (2017).

[498] R. Dingle, A. C. Gossard, and W. Wiegmann, *Direct Observation of Superlattice Formation in a Semiconductor Heterostructure*, Phys. Rev. Lett. **34**, 1327 (1975).

[499] S. Yamaguchi, M. Kariya, S. Nitta, T. Takeuchi, C. Wetzel, H. Amano, and I. Akasaki, *Structural properties of InN on GaN grown by metalorganic vapor-phase epitaxy*, J. Appl. Phys. **85**, 7682 (1999).

[500] P. Waltereit, O. Brandt, K. H. Ploog, M. A. Tagliente, and L. Tapfer, *In surface segregation during growth of (In,Ga)N/GaN multiple quantum wells by plasma-assisted molecular beam epitaxy*, Phys. Rev. B **66**, 165322 (2002).

[501] O. Ambacher, *Growth and applications of Group III-nitrides*, J. Phys. D: Appl. Phys. **31**, 2653 (1998).

[502] Y. F. Ng, Y. G. Cao, M. H. Xie, X. L. Wang, and S. Y. Tong, *Growth mode and strain evolution during InN growth on GaN(0001) by molecular-beam epitaxy*, Appl. Phys. Lett. **81**, 3960 (2002).

[503] E. Bellet-Amalric, C. Adelmann, E. Sarigiannidou, J. L. Rouvière, G. Feuillet, E. Monroy, and B. Daudin, *Plastic strain relaxation of nitride heterostructures*, J. Appl. Phys. **95**, 1127 (2004).

[504] E. E. Mendez, F. Agulló-Rueda, and J. M. Hong, *Stark Localization in GaAs-GaAlAs Superlattices under an Electric Field*, Phys. Rev. Lett. **60**, 2426 (1988).

[505] K. Fujiwara, *Room-Temperature Observation of Stark Ladder Formation in a Short-Period GaAs / AlAs Superlattice under an Electric Field*, Jpn. J. Appl. Phys. **28**, L1718 (1989).

[506] T. Suski, T. Schulz, M. Albrecht, X. Q. Wang, I. Gorczyca, K. Skrobas, N. E. Christensen, and A. Svane, *The discrepancies between theory and experiment in the optical emission of monolayer In(Ga)N quantum wells revisited by transmission electron microscopy*, Appl. Phys. Lett. **104**, 182103 (2014).

[507] H. Chen, R. M. Feenstra, J. E. Northrup, T. Zywietz, J. Neugebauer, and D. W. Greve, *Surface structures and growth kinetics of InGaN(0001) grown by molecular beam epitaxy*, J. Vac. Sci. Technol. B **18**, 2284 (2000).

[508] C. Friedrich, A. Biermann, V. Hoffmann, M. Kneissl, N. Esser, and P. Vogt, *Preparation and atomic structure of reconstructed (0001) InGaN surfaces*, J. Appl. Phys. **112**, 033509 (2012).

[509] M. Himmerlich, A. Eisenhardt, J. A. Schaefer, and S. Krischok, *PAMBE growth and in-situ characterisation of clean (2×2) and ($\sqrt{3}\times\sqrt{3}$) R30° reconstructed InN(0001) thin films*, Phys. Status Solidi B **246**, 1173 (2009).

[510] I. Gorczyca, K. Skrobas, T. Suski, N. E. Christensen, and A. Svane, *Influence of internal electric fields on band gaps in short period GaN/GaAlN and InGaN/GaN polar superlattices*, J. Appl. Phys. **118**, 075702 (2015).

[511] K. Kusakabe, D. Imai, K. Wang, and A. Yoshikawa, *InN/GaN short-period superlattices as ordered InGaN ternary alloys*, Phys. Status Solidi C **13**, 205 (2016).

[512] C. Chèze, M. Siekacz, F. Isa, B. Jenichen, F. Feix, J. Buller, T. Schulz, M. Albrecht, C. Skierbiszewski, R. Calarco, and H. Riechert, *Investigation of interface abruptness and In content in (In,Ga)N/GaN superlattices*, J. Appl. Phys. **120**, 125307 (2016).

[513] G. Staszczak, I. Gorczyca, E. Grzanka, J. Smalc-Koziorowska, G. Targowski, R. Czernecki, M. Siekacz, S. Grzanka, C. Skierbiszewski, T. Schulz, N. E. Christensen,

and T. Suski, *Bandgap behavior of InGaN/GaN short period superlattices grown by metal-organic vapor phase epitaxy*, Phys. Status Solidi B **254**, 1600710 (2017).

[514] C. S. Gallinat, G. Koblmüller, J. S. Brown, and J. S. Speck, *A growth diagram for plasma-assisted molecular beam epitaxy of In-face InN*, J. Appl. Phys. **102**, 064907 (2007).

[515] B. Heying, R. Averbeck, L. F. Chen, E. Haus, H. Riechert, and J. S. Speck, *Control of GaN surface morphologies using plasma-assisted molecular beam epitaxy*, J. Appl. Phys. **88**, 1855 (2000).

[516] H. Chen, R. M. Feenstra, J. E. Northrup, T. Zywietz, and J. Neugebauer, *Spontaneous Formation of Indium-Rich Nanostructures on InGaN(0001) Surfaces*, Phys. Rev. Lett. **85**, 1902 (2000).

[517] O. Brandt, P. Waltereit, and K. H. Ploog, *Determination of strain state and composition of highly mismatched group-III nitride heterostructures by x-ray diffraction*, J. Phys. D: Appl. Phys. **35**, 577 (2002).

[518] M. E. Vickers, M. J. Kappers, T. M. Smeeton, E. J. Thrush, J. S. Barnard, and C. J. Humphreys, *Determination of the indium content and layer thicknesses in InGaN/GaN quantum wells by x-ray scattering*, J. Appl. Phys. **94**, 1565 (2003).

[519] T. Markurt, T. Schulz, X. Q. Wang, X. T. Zheng, D. Y. Ma, and M. Albrecht, *Anomalous contrast behavior for STEM HAADF imaging of ordered $In_{0.33}Ga_{0.67}N$ monolayers*, Eur. Microsc. Congr. 2016 Proc., p. 628 (2016).

[520] G. Staszczak, I. Gorczyca, T. Suski, X. Q. Wang, N. E. Christensen, A. Svane, E. Dimakis, and T. D. Moustakas, *Photoluminescence and pressure effects in short period InN/nGaN superlattices*, J. Appl. Phys. **113**, 123101 (2013).

[521] A. Yoshikawa, K. Kusakabe, N. Hashimoto, E.-S. Hwang, D. Imai, and T. Itoi, *Systematic study on dynamic atomic layer epitaxy of InN on/in +c-GaN matrix and fabrication of fine-structure InN/GaN quantum wells: Role of high growth temperature*, J. Appl. Phys. **120**, 225303 (2016).

[522] M. Ribeiro and M. Marques, *Theoretical study of InN/GaN short period superlattices to mimic disordered alloys*, J. Appl. Phys. **115**, 223708 (2014).

[523] F. Bernardini and V. Fiorentini, *Macroscopic polarization and band offsets at nitride heterojunctions*, Phys. Rev. B **57**, R9427 (1998).

[524] T. Schulz, private communication, 24/02/2016.

[525] E. Abrahams, P. W. Anderson, D. C. Licciardello, and T. V. Ramakrishnan, *Scaling Theory of Localization: Absence of Quantum Diffusion in Two Dimensions*, Phys. Rev. Lett. **42**, 673 (1979).

[526] X. Zhang, H. Lourenço-Martins, S. Meuret, M. Kociak, B. Haas, J.-L. Rouvière, P.-H. Jouneau, C. Bougerol, T. Auzelle, D. Jalabert, X. Biquard, B. Gayral, and B. Daudin, *InGaN nanowires with high InN molar fraction: growth, structural and optical properties*, Nanotechnology **27**, 195704 (2016).

[527] S. Nakamura and M. R. Krames, *History of Gallium–Nitride-Based Light-Emitting Diodes for Illumination*, Proc. IEEE **101**, 2211 (2013).

[528] M. Filoche, M. Piccardo, Y.-R. Wu, C.-K. Li, C. Weisbuch, and S. Mayboroda, *Local-*

ization landscape theory of disorder in semiconductors. I. Theory and modeling, Phys. Rev. B **95**, 144204 (2017).

[529] H. Wang, Z. Ji, S. Qu, G. Wang, Y. Jiang, B. Liu, X. Xu, and H. Mino, *Influence of excitation power and temperature on photoluminescence in InGaN/GaN multiple quantum wells*, Opt. Express **20**, 3932 (2012).

[530] F. Yang, C. Zhang, C. Shi, M. Joo Park, J. Seop Kwak, S. Jung, Y.-H. Choi, X. Wu, X. Wang, and M. Xiao, *Defect recombination induced by density-activated carrier diffusion in nonpolar InGaN quantum wells*, Appl. Phys. Lett. **103**, 123506 (2013).

[531] H. Koch, F. Bertram, I. Pietzonka, J.-P. Ahl, M. Strassburg, O. August, J. Christen, H. Kalisch, A. Vescan, and H.-J. Lugauer, *InGaN: Direct correlation of nanoscopic morphology features with optical and structural properties*, Appl. Phys. Lett. **105**, 072108 (2014).

[532] A. A. Michelson, *Studies in Optics*, University of Chicago Press (1927).

[533] G. Pozina, R. Ciechonski, Z. Bi, L. Samuelson, and B. Monemar, *Dislocation related droop in InGaN/GaN light emitting diodes investigated via cathodoluminescence*, Appl. Phys. Lett. **107**, 251106 (2015).

[534] A. Kaneta, M. Funato, and Y. Kawakami, *Nanoscopic recombination processes in InGaN/GaN quantum wells emitting violet, blue, and green spectra*, Phys. Rev. B **78**, 125317 (2008).

[535] C. Vierheilig, U. T. Schwarz, N. Gmeinwieser, A. Laubsch, and B. Hahn, *Bias dependent spatially resolved photoluminescence spectroscopy and photocurrent measurements of InGaN/GaN LED structures*, Phys. Status Solidi C **6**, S755 (2009).

[536] A. Kaneta, T. Hashimoto, K. Nishimura, M. Funato, and Y. Kawakami, *Visualization of the Local Carrier Dynamics in an InGaN Quantum Well Using Dual-Probe Scanning Near-Field Optical Microscopy*, Appl. Phys. Express **3**, 102102 (2010).

[537] A. Kaneta, R. Fujimoto, T. Hashimoto, K. Nishimura, M. Funato, and Y. Kawakami, *Instrumentation for dual-probe scanning near-field optical microscopy*, Rev. Sci. Instrum. **83**, 083709 (2012).

[538] A. Kaneta, T. Mutoh, Y. Kawakami, S. Fujita, G. Marutsuki, Y. Narukawa, and T. Mukai, *Discrimination of local radiative and nonradiative recombination processes in an InGaN/GaN single-quantum-well structure by a time-resolved multimode scanning near-field optical microscopy*, Appl. Phys. Lett. **83**, 3462 (2003).

[539] A. Kaneta, K. Okamoto, Y. Kawakami, S. Fujita, G. Marutsuki, Y. Narukawa, and T. Mukai, *Spatial and temporal luminescence dynamics in an $In_xGa_{1-x}N$ single quantum well probed by near-field optical microscopy*, Appl. Phys. Lett. **81**, 4353 (2002).

[540] Y. Kawakami, A. Kaneta, A. Hashiya, and M. Funato, *Impact of Radiative and Nonradiative Recombination Processes on the Efficiency-Droop Phenomenon in $In_xGa_{1-x}N$ Single Quantum Wells Studied by Scanning Near-Field Optical Microscopy*, Phys. Rev. Applied **6**, 044018 (2016).

[541] D. Nečas and P. Klapetek, *Gwyddion: an open-source software for SPM data analysis*, Cent. Eur. J. Phys. **10**, 181 (2012).

[542] T. Sekiguchi and K. Sumino, *Interaction between Dislocations and Non-Radiative Recombination Centers in GaAs*, Jpn. J. Appl. Phys. **26**, L179 (1987).

[543] F. C.-P. Massabuau, P. Chen, M. K. Horton, S. L. Rhode, C. X. Ren, T. J. O'Hanlon, A. Kovács, M. J. Kappers, C. J. Humphreys, R. E. Dunin-Borkowski, and R. A. Oliver, *Carrier localization in the vicinity of dislocations in InGaN*, J. Appl. Phys. **121**, 013104 (2017).

[544] T. Meyer, M. Peter, J. Danhof, U. T. Schwarz, and B. Hahn, *Micro-electroluminescence of cyan InGaN-based multiple quantum well structures*, Phys. Status Solidi A **208**, 1523 (2011).

[545] A. Satake, Y. Masumoto, T. Miyajima, T. Asatsuma, and T. Hino, *Ultraviolet anti-Stokes photoluminescence in $In_xGa_{1-x}N/GaN$ quantum-well structures*, Phys. Rev. B **61**, 12654 (2000).

[546] R. Cingolani and K. Ploog, *Frequency and density dependent radiative recombination processes in III–V semiconductor quantum wells and superlattices*, Adv. Phys. **40**, 535 (1991).

[547] R. Hellmann, A. Euteneuer, S. G. Hense, J. Feldmann, P. Thomas, E. O. Göbel, D. R. Yakovlev, A. Waag, and G. Landwehr, *Low-temperature anti-Stokes luminescence mediated by disorder in semiconductor quantum-well structures*, Phys. Rev. B **51**, 18053 (1995).

[548] Y.-H. Cho, D. S. Kim, B.-D. Choe, H. Lim, J. I. Lee, and D. Kim, *Dynamics of anti-Stokes photoluminescence in type-II Al_x Ga_{1-x} As-$GaInP_2$ heterostructures: The important role of long-lived carriers near the interface*, Phys. Rev. B **56**, R4375 (1997).

[549] W. Seidel, A. Titkov, J. P. André, P. Voisin, and M. Voos, *High-efficiency energy up-conversion by an "Auger fountain" at an InP-AlInas type-II heterojunction*, Phys. Rev. Lett. **73**, 2356 (1994).

[550] G. Zegrya and V. Kharchenko, *New mechanism of Auger recombination of nonequilibrium current carriers in semiconductor heterostructures*, J. Exp. Theor. Phys. **74**, 173 (1992).

[551] F. A. J. M. Driessen, H. M. Cheong, A. Mascarenhas, S. K. Deb, P. R. Hageman, G. J. Bauhuis, and L. J. Giling, *Interface-induced conversion of infrared to visible light at semiconductor interfaces*, Phys. Rev. B **54**, R5263 (1996).

[552] Z. P. Su, K. L. Teo, P. Y. Yu, and K. Uchida, *Mechanisms of photoluminescence upconversion at the GaAs/(ordered) $GaInP_2$ interface*, Solid State Commun. **99**, 933 (1996).

[553] M. Göppert-Mayer, *Über Elementarakte mit zwei Quantensprüngen*, Ann. Phys. **401**, 273 (1931).

[554] W. Kaiser and C. Garrett, *Two-Photon Excitation in CaF_2:Eu^{2+}*, Phys. Rev. Lett. **7**, 229 (1961).

[555] A. Haug, *Carrier density dependence of Auger recombination*, Solid State Electron. **21**, 1281 (1978).

List of Figures

List of Tables

Danksagung

Die vorliegende Arbeit wäre in ihrer jetzigen Form nicht ohne die Unterstützung zahlreicher Personen entstanden. Dafür möchte ich den direkt oder indirekt Beteiligten an dieser Stelle von ganzem Herzen danken.

- Meinem Doktorvater, dem Direktor des Paul-Drude-Instituts für Festkörperelektronik Berlin, Herrn Prof. Dr. H. Riechert, danke ich, dass er es mir ermöglicht hat, am Paul-Drude-Institut zu promovieren. Zudem gebührt ihm sowie den anderen Gutachtern mein Dank für die Erstellung der Gutachten zu dieser Arbeit.

- Ebenso möchte ich mich bei Herrn Dr. L. Geelhaar bedanken, der mich im Rahmen des Projekts der Europäischen Union „Deepen“ als Doktorand angestellt und in die Obhut meines Abteilungsleiters Herrn Prof. Dr. H. T. Grahn übergeben hat. Beiden möchte ich herzlich dafür danken, dass sie mich immer unterstützt haben und dass ich von ihrem reichhaltigem Wissen profitieren konnte.

- Allergrößter Dank gebührt Herrn Dr. O. Brandt, meinem direkten Betreuer, der mich mit seinem immensen Wissen und seinen cleveren Anregungen immer angeleitet, unterstützt und gefördert hat. Ihm verdanke ich auch zahlreiche Lehrstunden in der Kunst des wissenschaftlichen Publizierens.

- Für herausragende experimentelle Unterstützung und Erklärungen möchte ich Herrn Dr. T. Flissikowski, Herrn Dr. M. Ramsteiner, Herrn Dr. P. Corfdir und Herrn Dr. C. Hauswald danken. Ein großer Dank für hilfreiche Diskussionen und die Durchführung von Simulationen und Berechnungen geht an Herrn Dr. K. K. Sabelfeld, Herrn Dr. V. M. Kaganer und Herrn Dr. O. Marquardt. Herrn Dr. K. K. Sabelfeld danke ich außerdem für die Entwicklung und Bereitstellung des Monte Carlo Algorithmus, der in der vorliegenden Arbeit genutzt und weiterentwickelt wurde.

- An dieser Stelle möchte ich OSRAM Opto Semiconductors GmbH, namentlich Herrn Dr. A. Gomez-Iglesias und Herrn Dr. A. Avramescu, für die Bereitstellung von planaren (In,Ga)N/GaN-Quantengräben, (In,Ga)N/GaN-Leuchtdioden und (In,Ga)N/GaN-Mikrodrähte danken. Des Weiteren gilt mein Dank Frau Dr. C. Chèze, Herrn Dr. S. Fernández-Garrido, Herrn Dr. M. Wölz, Herrn Dr. M. Musolino sowie Herrn

D. van Treeck für das Wachstum von kurzperiodigen Übergittern und (In,Ga)N/GaN-Nanodrähten. Den in diesem Abschnitt genannten Personen danke ich ebenfalls für die vielfältigen aufschlussreichen Diskussionen und Erklärungen.

- Für Kathodolumineszenzmessungen sowie lehrreiche wissenschaftliche und technische Diskussionen danke ich Herrn Dr. C. Pfüller, Herrn Dr. J. Lähnemann und Herrn Dr. U. Jahn.

- Für die Erstellung von transmissionsmikroskopischen Aufnahmen und die Einführung in dieses Fachgebiet danke ich Herrn Dr. A. Trampert, Herrn L. Nicolai, Herrn Dr. J. Bartolomé Vílchez, Herrn Dr. T. Schulz und Herrn Dr. M. Albrecht sowie den Technikern und Technikerinnen, die an der Präparation der Proben beteiligt waren.

- Frau A. Riedel und Herrn Dr. M. Hempel danke ich für die Kontaktierung der Leuchtdioden. Für die Herstellung von Lithographiemasken, die anschließende Prozessierung und die Erläuterung der technischen Details danke ich Herrn W. Seidel, Herrn B. Drescher und Herrn Dr. A. Tahraoui.

- Für die Beratung in technischen Dingen sowie in der Verwaltung danke ich Herrn G. Paris, Herrn Dr. B. Pakulat, Frau A. Holldack und Herrn A. Hartung. Frau D. Dormeyer danke ich für die Beschaffung von Literatur und Herrn J. Pfeiffer stellvertretend für seine Kollegen, die an der Erstellung spezieller Probenhalter beteiligt waren.

- Für das Korrekturlesen bedanke ich mich herzlich bei Herrn Dr. O. Brandt, Herrn Prof. Dr. H. T. Grahn, Herrn D. van Treeck, Herrn B. Röben, Frau Dr. C. Chèze, Herrn Dr. T. Flissikowski, Herrn Dr. J. Lähnemann, Herrn Dr. M. Hempel und Frau Dr. C. Sinito.

- Die Arbeit wurde zum Teil durch die Europäische Union im Rahmen des Projekts „Deepen“ finanziert (FP7-NMP-2013-SMALL-7 unter der Kennziffer 604416).